

Nucleon Structure Functions from ν_μ -Fe Interactions and a Study of the Valence Quark Distribution

Thesis by
Milind Vasant Purohit

In Partial Fulfillment of the Requirements
for the Degree of
Doctor of Philosophy

California Institute of Technology
Pasadena, California

1984
(Submitted October 6, 1983)

Acknowledgements

All the members of the CCFRR collaboration contributed to these results and to them I am most grateful for their splendid efforts. My principal association has been with Dave MacFarlane who produced the twin thesis and with Mike Shaevitz and Frank Sciulli, my adviser. I am deeply indebted to both the professors for their guidance over the years and insightful help with the analysis. I would also like to thank them, especially Frank Sciulli, for reading this thesis and their comments on it. I consider myself lucky to have had Dave for a colleague; his abilities and good cheer make an excellent combination.

The rest of this group has always been very cooperative, in particular Bob Blair by his patient explanations and by blazing the trail. Petros Rapidis was a good mentor during the ion chamber calibration run, as also Keith Jenkins. I have also benefited much from contacts with Gene Fisk, Arie Bodek and Taka Kondo on various occasions. I wish to thank Dr. R.M. Barnett of SLAC and Dr. J.F. Owens and his colleagues at Florida State for providing us with their QCD-fit programs and counsel.

I also wish to thank my friends and all the people at Caltech, Fermilab and Nevis Labs who have gone out of their way to help make my itinerant graduate education easier. Prof. David Hitlin very kindly agreed to act as surrogate adviser at Caltech. Preparation of my thesis was aided tremendously by the Nevis staff, in particular Mr. A. Vermeulen and Ms. J. Therrien. I am grateful to Caltech for financial support during my Ph.D. years and the American taxpayer who, through the good offices of the U.S. DOE and NSF, made most of this research possible.

Most of all, I thank my parents for their encouraging, patient support of the endeavours of a son so far away and my sister for her dependable hospitality and intimate friendship.

Abstract

Data were taken in 1979-80 by the CCFRR high energy neutrino experiment at Fermilab. A total of 150,000 neutrino and 23,000 antineutrino charged current events in the approximate energy range $25 < E_\nu < 250\text{GeV}$ are measured and analyzed. The structure functions F_2 and xF_3 are extracted for three assumptions about σ_L/σ_T : $R=0.$, $R=0.1$ and $R=$ a QCD based expression. Systematic errors are estimated and their significance is discussed. Comparisons of the x and Q^2 behaviour of the structure functions with results from other experiments are made.

We find that statistical errors currently dominate our knowledge of the valence quark distribution, which is studied in this thesis. xF_3 from different experiments has, within errors and apart from level differences, the same dependence on x and Q^2 , except for the HPWF results. The CDHS F_2 shows a clear fall-off at low- x from the CCFRR and EMC results, again apart from level differences which are calculable from cross-sections.

The result for the the GLS rule is found to be $2.83 \pm .15 \pm .09 \pm .10$ where the first error is statistical, the second is an overall level error and the third covers the rest of the systematic errors. QCD studies of xF_3 to leading and second order have been done. The QCD evolution of xF_3 , which is independent of R and the strange sea, does not depend on the gluon distribution and fits yield

$$\Lambda_{LO} = 88_{-78}^{+163} \quad -_{70}^{+113} \text{ MeV}$$

The systematic errors are smaller than the statistical errors. Second order fits give somewhat different values of Λ , although α_S (at $Q_0^2 = 12.6 \text{ GeV}^2$) is not so different.

A fit using the better determined F_2 in place of xF_3 for $x > 0.4$ i.e., assuming $\bar{q} = 0$ in that region, gives

$$\Lambda_{LO} = 266_{-104}^{+114} \quad -_{79}^{+85} \text{ MeV}$$

Again, the statistical errors are larger than the systematic errors. An attempt to measure R was made and the measurements are described. Utilizing the inequality $\bar{q}(x) \geq 0$ we find that in the region $x > .4$ R is less than 0.55 at the 90% confidence level.

To my parents

Contents

	Page
Chapter 1. Introduction	1
1.1 Motivation and Physics	1
1.2 Experiment E616	6
1.3 Organization of Thesis	6
Chapter 2. The Neutrino Beam	8
2.1 The Dichromatic Beam	8
2.2 Beam Flux Monitors	13
2.3 Ion Chamber Calibration	17
2.4 The Čerenkov Counter	26
Chapter 3. Flux Analysis	34
3.1 WBB Parametrization	34
3.2 Beam Centering and Other Cuts	36
3.3 The Beam Monte Carlo	36
3.4 Flux Parametrization	36

Chapter 4. The Lab E Detector	39
4.1 Requirements	39
4.2 Layout, Fiducial Volume and Alignment	39
4.3 Spark Chambers	41
4.4 Scintillation Counters	43
4.5 E_{HAD} Calibration	47
4.6 Electronics	47
4.7 Triggers	47
Chapter 5. Event Analysis	51
5.1 E_μ	51
5.2 θ_μ	61
5.3 E_{had}	62
5.4 Vertex, θ_h , Acceptance, etc.	63
Chapter 6. Extraction of Structure Functions	66
6.1 An Overview of the Physics	66
6.2 Total Cross Sections	67
6.3 Cuts, Resolutions and Binning:	70
6.4 Method of Extraction	73
6.5 Corrections	75
6.6 Systematic Errors	90
6.7 Results and Comparisons	95
Chapter 7. Physics Analysis and Conclusions	107
7.1 Weak Interactions	107
7.2 The Parton Model	109
7.3 Quantum Chromodynamics	115

7.4 Tests of the Quark-parton Model	120
7.4.1 F_2 Comparisons	120
7.4.2 The Gross-Llewellyn-Smith Sum Rule	122
7.5 QCD Analysis	126
7.5.1 Leading Order Non-singlet Analysis	126
7.5.2 \overline{MS} Non-singlet Analysis	134
7.5.3 Non-singlet Analysis Summary	137
7.5.4 Singlet Analysis	137
7.5.5 Comparison with Other Experiments	139
7.6 Extraction of R	140
7.6.1 R from y -dependence of Differential Cross-sections	140
7.6.2 Limit on R	143
7.7 Conclusions	143
Appendix A. Beam Kinematics	146
Appendix B. Event Kinematics	152
Appendix C. Differential Cross-sections	154
Appendix D. Multiple Scattering	159
Appendix E. Event Counting for Total Cross-sections	161
Appendix F. Models for Fitting Structure Functions	165
Appendix G. $R=0.1$ Structure Functions	168
Appendix H. Tables of Statistical and Systematic Errors	170
Appendix I. List of Collaborators	178
References	179

§1.1 Motivation and Physics

Just as Rutherford's experiments proved that the positive charge in the atom is concentrated in the nucleus, electron experiments have shown that charge in the proton is not uniformly diffused over the nucleus but instead is concentrated in very small regions. These experiments were pioneered by Hofstadter and others at SLAC and MIT. The electron is a good probe because it is a point particle and is well understood in the framework of the highly successful theory, QED⁽¹⁾. In 1967, a SLAC-MIT collaborative effort began which used the SLAC linac to study the scattering of electrons from nucleons at different energies and angles⁽²⁾. The incident electron beam had energies ranging from 4.5 GeV to 20 GeV. The incident beam energy spread was less than 0.5%. Two spectrometers were used to scan the scattered beam in energy at fixed angles. As the sampled energy was decreased at fixed angle, the cross section did go through an elastics peak and resonances as expected. The elastics peak had the characteristic $1/q^4$ dependence expected from the photon propagator; in addition it showed a rapid fall with q^2 ascribed to a form factor. Beyond the resonances was found the deep inelastic scattering cross section, which was surprisingly flat in q^2 except for the $1/q^4$ from the propagator. Such a cross section suggests a point scatterer since the form factor is the Fourier transform of the charge density of scatterers.

Such behaviour of the cross section has since come to be known as "scaling" and was first explained by Bjorken and Paschos⁽⁴⁾ and by Feynman⁽³⁾. Since then interest in the structure of the nucleon has grown considerably, especially with the identification of these point scatterers, or partons, with quarks. The behaviour of quarks within the nucleus is expected to tell us more about QCD, the heir-apparent to the mantle of theory of strong interactions. It is also expected that experiments performed with leptons as probes of the nucleus will further confirm the by now accepted Weinberg-Salam-Glashow theory of electroweak interactions.

It is precisely because we have so much faith in the theory of weak interactions that leptons are used as probes of the nucleus. And because, as far as is known, leptons are point

particles. Charged leptons suffer from the disadvantage that their interactions with quarks are principally electromagnetic, giving rise to the $1/q^4$ photon propagator. On the other hand, they are easier to use as a tool since momentum selection of charged particle beams is simpler. The experiment described in this thesis utilized neutrinos as probes instead; this was facilitated by the advent of energy-selected neutrino beams first suggested by Sciulli⁽⁵⁾, Peterson⁽⁶⁾ and others. Neutrinos have no electric or colour charge and consequently interact only weakly with the quarks in a nucleon, a fact that enables us to study the Q^2 behaviour of nucleon structure without the large $1/Q^4$ modulating effect of the photon propagator.

Neutrino interactions with the nucleon are shown in figure 1.1. The standard model of electroweak interactions describes the lepton vertex completely, the hadron vertex is unknown. By studying the x -distributions of cross sections we hope to learn more about the nucleon. For example, the integral of the structure function $2xF_1 (=q + \bar{q})$, is approximately 1/2. This leads us to believe that the remaining half of the nucleon momentum is carried by something other than quark-partons and these particles are expected to be the colour force carrying gluons. Since there are three valence quarks in the nucleon according to standard hadron spectroscopy, we expect the valence quark structure function, xF_3 , to peak at roughly a third of the available momentum, i.e., around 1/6. This indeed seems to be the case.

In the picture accepted now, valence quarks are accompanied by gluons that bind them and a sea of quark-antiquark pairs that are constantly being created and annihilated. Figure 1.3 illustrates these structure functions. The scaling hypothesis is violated by QCD processes shown in figure 1.2. They change the relative momentum fractions carried by the valence quarks, sea and gluons as the nucleon is probed to shorter and shorter distances (Q^2 increases: see fig. 1.2). It is the aim of this experiment to study the structure of the nucleon well.

An introduction to the theories relevant to neutrino-induced charged current interactions is presented in the first part of Chapter 7. Briefly, in the quark-parton model point-like quarks are confined by forces within nucleons but behave as though they are free when probed by high energy particles. Quantum numbers of the quarks are assigned in a way that explains the spectrum of hadrons. To simplify calculations the quarks are frequently assumed to be massless; this cannot be done for the more massive quarks (charm and beyond). QCD attempts to explain the interactions between quarks on the basis of a property known as "colour". Colour charge is responsible for the attractive forces between quarks and their consequent confinement within hadrons. The property of asymptotic freedom explains the basic parton model assumption of interactions with free quarks. Thus, deviations from the parton-model predictions are small corrections at high energies. Quantitatively, the predictions about charged current analysis that can be tested are:

- i. From the quark-parton model:
 - a. The total cross section should be linearly proportional to the incident neutrino energy, E_ν .
 - b. The y -dependence of the differential cross-sections is dictated by spin considerations (see Appendix C). For example, the differential cross section for antineutrinos on quarks is

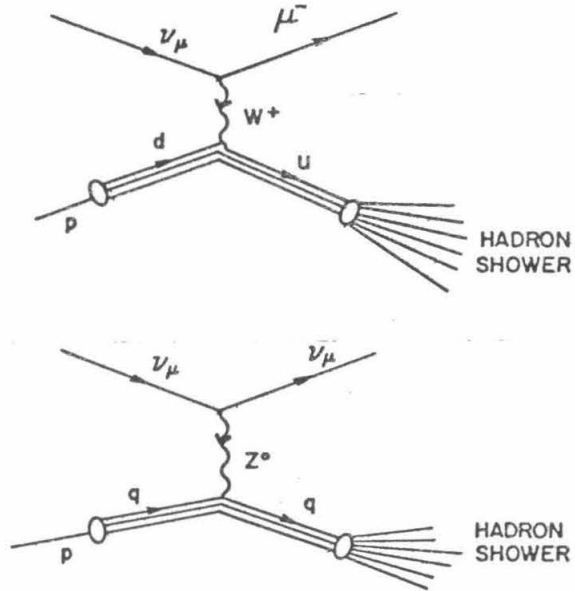


Figure 1.1. Neutrino-nucleon interactions

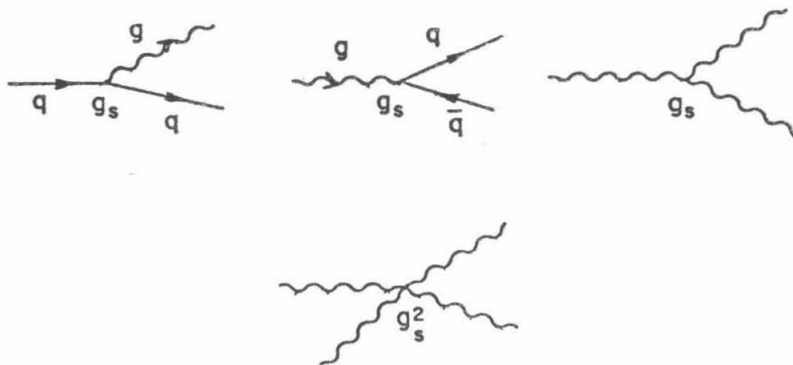


Figure 1.2. Basic QCD processes

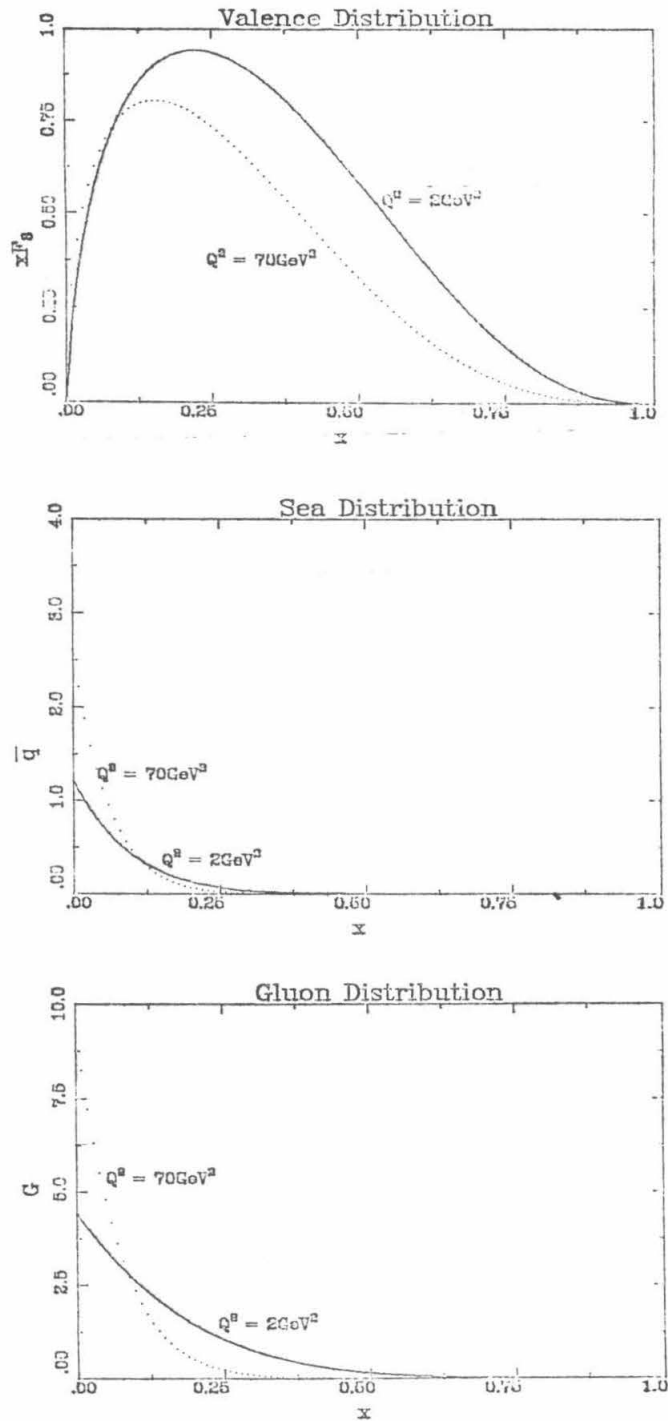


Figure 1.3. Structure functions

$$\frac{d^2\sigma^{\bar{\nu}}}{dx dy} = \frac{G^2 s}{\pi} \cdot x q(x) \cdot (1-y)^2 \quad (1.1)$$

- c. There are no spin-zero constituents in the nucleon, therefore $2xF_1$ ($= q + \bar{q}$) is equal to F_2 ($\approx q + \bar{q} + 2k$). The only contribution to R , defined by

$$F_2 = \frac{(1+R)}{(1+4m_p^2 x^2/Q^2)} 2xF_1 \quad (1.2)$$

comes from target mass, transverse momentum and binding effects, and $R \sim 1/Q^2$, i.e.,⁽³⁾

$$R \approx 4 \frac{(m_p^2 x^2 + p_T^2 \pm \Delta)}{(Q^2 + 2p_T^2)} \quad (1.3)$$

- d. The total number of quarks in a proton is 3 (the Gross-Llewellyn Smith sum rule):

$$\int_0^1 F_3 dx = 3 \quad (1.4)$$

- e. The scaling hypothesis^(3,4) i.e., the structure functions are functions of x alone, not x and Q^2 .
- f. F_2 in electron and muon scattering experiments is not $q + \bar{q}$ since the virtual particle exchanged there is the photon. The photon coupling amplitude is proportional to the charge of the quark, hence

$$F_2^{em} = F_2^{wk} \frac{5}{18} \left\{ 1 - \frac{3s + \bar{s}}{5q + \bar{q}} \right\} \quad (1.5)$$

5/18 is the mean square charge of quarks in a nucleon. The factor in curly brackets is a small correction.

ii. From QCD:

- a. The structure functions depend on Q^2 as well as x ; to leading logs in the perturbative expansion the dependence is like $1/\ln(Q^2)$. QCD prescribes the evolution of structure functions (see chapter 7). The evolution of xF_3 is described by an independent integro-differential equation while that of F_2 is coupled to the (as yet unknown) gluon structure function.

$$\frac{\partial xF_3}{\partial \ln Q^2} = f(xF_3) \quad (1.6)$$

$$\left. \begin{aligned} \frac{\partial F_2}{\partial \ln Q^2} &= g_1(F_2, G) \\ \frac{\partial G}{\partial \ln Q^2} &= g_2(F_2, G) \end{aligned} \right\} \quad (1.7)$$

b. R , to leading order, behaves as $1/\ln Q^2$, is large at small x and small at large x :

$$R = \frac{1}{(2xF_1)\beta_0 \ln Q^2/\Lambda^2} \int_x^1 \frac{dy}{y} \frac{x^2}{y^2} \left[\frac{16}{3} F_2(y, Q^2) + 8n_f \left(1 - \frac{x}{y}\right) y G(y, Q^2) \right] \quad (1.8)$$

In addition to the above, Regge theory predicts that as x tends to zero $x F_3$ behaves like \sqrt{x} .

§1.2 Experiment E616

This experiment was done at the Fermi National Accelerator Laboratory located in Batavia, Illinois (near Chicago). The experiment consisted of a large steel target on which were impinged neutrinos and antineutrinos of energies ranging from 30 GeV to 300 GeV. Charged current interactions change the neutrinos to muons when they leave a nucleon and also produce a shower of hadrons. The neutrinos can also interact without transforming into a muon, the study of these so-called "neutral-current" interactions is vast and complicated by itself and does not form part of this thesis. Thanks to some earlier experiments⁽⁷⁾ done by this group at FNAL, the detector was essentially completely built by the time the run started in early June 1979. In the 8 months that followed we used a total of 5.87×10^{18} protons from the main ring. The neutrinos produced from the decay of secondary pions and kaons created by the interaction of the proton beam with a target gave rise to approximately 150,000 charged current neutrino events, the antineutrinos producing a smaller total of 23,000 events.

The antineutrino data and about half the neutrino data have already been subjected to analysis for purposes of measurement of the total cross section – this work is described in an earlier thesis⁽⁸⁾. Since E616 is a high statistics experiment with a dichromatic beam the data not only yield normalized cross-sections, but can also be exploited for a relatively accurate measurement of structure functions. While this data set was being analysed our group carried out another experiment to investigate the possibility of neutrino oscillations.⁽¹⁰⁹⁾ Another experiment is planned for the Tevatron at Fermilab, it will, in main, study structure functions at the much higher energies possible there. Combined with E616 data all these data add up to an invaluable bank for the study of the nucleon and QCD.

§1.3 Organization of Thesis

As mentioned earlier, a whole Ph.D. thesis has been written on the measurement of total cross sections in E616. An earlier experiment (E356) by the same group has also produced a thesis⁽⁹⁾. Consequently the description of the apparatus for the detector and the monitors requires no more repetition and can be looked up in the above-mentioned references. This thesis will state the bare minimum in these areas except to describe recent advances in understanding (such as with the \check{C} -counter) and to emphasize those aspects of the beam monitoring that are particularly relevant to structure function analysis and/or have not received adequate treatment

elsewhere. Also included is a discussion of the calibration of our ion chamber, in which the author played a major role.

Another thesis⁽¹⁰⁾ is being written on similar material from E616. Much of the analysis has been done in common and it is not possible to unambiguously divide it in two. Two methods of analysis were used by this group with this author consistently preferring maximum likelihood techniques. This applies to the extraction of structure functions and extraction of R . For the Gross-Llewellyn Smith sum rule and QCD analysis we restrict ourselves to xF_3 . The reader may find more detailed descriptions of some topics in one thesis as opposed to the other, reflecting the history of the analysis. Most of the topics are clearly outlined in the table of contents and the reader should be able to navigate his/her way through with facility.

The Neutrino Beam

§2.1 The Dichromatic Beam

High energy neutrino beams can be produced by the decay of charged pions and kaons generated in the interaction of hadrons with hadrons. At Fermilab part of the 400 GeV proton beam in the main ring is extracted and impinges on a BeO target 10.5 in thick. Typical intensities during the E616 running period were around 10^{13} protons per pulse. The proton beam was extracted in two spills: in a fast spill of ~ 2 ms and a slow spill of ~ 500 ms. We used only the fast spill (which minimizes cosmic ray events) for antineutrino running, the data taking not being rate limited there. Typical per pulse secondary beam intensities were about 5×10^9 for negative settings and 2×10^{10} for the positive settings. The proton beam and the dichromatic train are shown in figure 2.1. Listed below are total proton and secondary beam intensities achieved during the ten energy settings at which we took data.

The proton beam produces many charged hadrons on interaction with the target, chiefly pions, kaons and protons. Charged pions decay 99.97% of the time into muons and muon neutrinos; charged kaons do the same only 63.5% of the time. More interesting is the fact that these are two-body decays, so the energies of the decay products are fixed in the centre-of-mass frame. Therefore we isolate pions and kaons in a narrow momentum range to obtain neutrinos in a narrow energy range. The desirability of a thin momentum slice must be balanced against high-flux requirements. Since neutrinos from kaon decays have much higher energies than those from pion decays (see App. A), the neutrino beam is really dichromatic. The pions and kaons are removed by a 20 ft steel and aluminum beam dump, the muons range out in 930m of steel and earth.

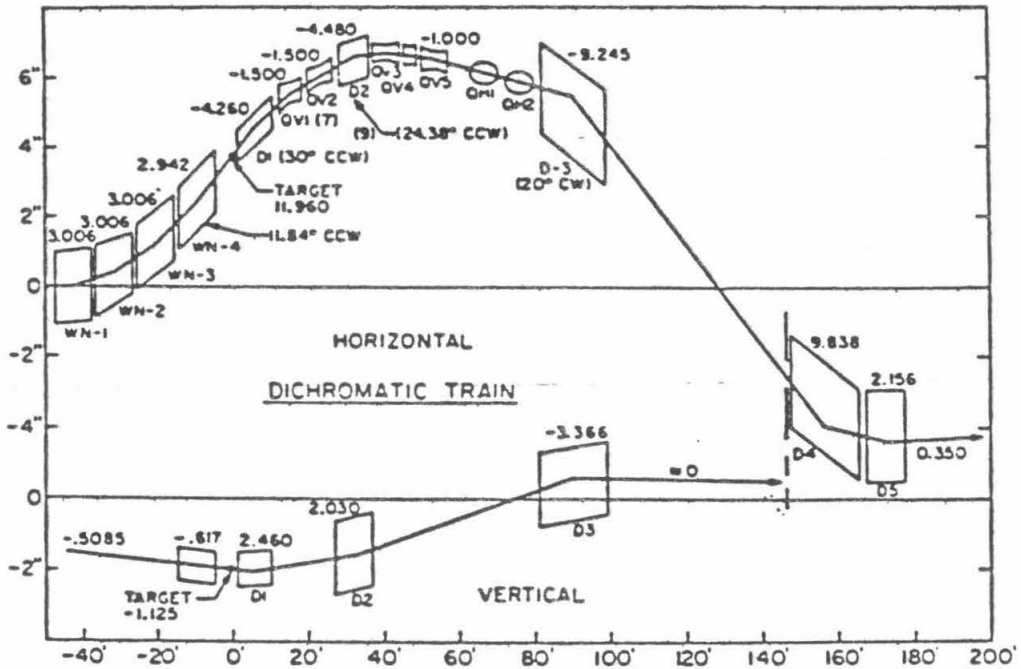


Figure 2.1. The proton beam target and dichromatic train.

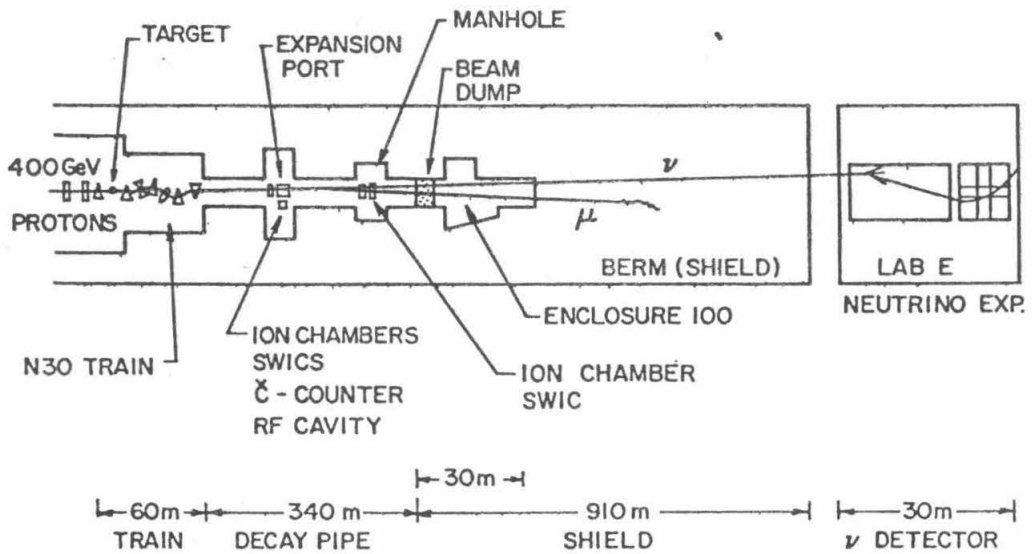


Figure 2.2. Secondary beam line.

E_{SET} (GeV)	Fast Spill			Slow spill		
	Open slit		Cl. Slit	Open Slit		Cl. Slit
	Protons ($\times 10^{12}$)	Secondaries ($\times 10^9$)	Protons ($\times 10^{12}$)	Protons ($\times 10^{12}$)	Secondaries ($\times 10^9$)	Protons ($\times 10^{12}$)
-250	1121000	202000	93800	0	0	0
-200	531000	264000	25600	0	0	0
-165	379000	270000	22700	0	0	0
-140	288000	283000	32800	0	0	0
-120	199000	232000	15500	0	0	0
120	110000	484000	17000	151000	642000	17600
140	138000	673000	11600	187000	837000	12900
165	207000	1155000	15100	295000	1641000	15100
200	301000	2068000	45800	353000	2444000	44500
250	556000	5243000	56700	542000	4894000	42100
Total -ves	2516000	1252000	181000	0	0	0
Total +ves	1312000	9623000	146000	1529000	10460000	132000
Total	3828000	10880000	327000	1529000	10460000	132000

Table 2.1. Accumulated beam intensities over running period

Here it seems appropriate to mention different kinds of neutrino beams.⁽¹²⁾ The simplest kind of beam, of course, would be one in which no attempt is made to select the sign, momentum or direction of the decaying mesons. Such a beam is clearly not very useful for any precise normalized measurements. Examples of beams that sign-select but still manage to use most of the flux of mesons are horn and quadrupole triplet beams. Simple focussing magnets can be used to collect more mesons into the forward direction than with a bare target beam. This improves the neutrino flux. Horn focussed beams have good sign selection and high flux, but have a relatively high flux of low energy neutrinos. The quad-triplet beam on the other hand compromises flux and sign selection in order to improve the relative content of higher energy particles.

Our dichromatic beam (fig. 2.2) is sign-selected in a narrow momentum bite ($\Delta p/p \approx \pm 9\%$) and has an angular divergence of $\pm 15\text{mrad}$ in the horizontal and $\pm 18\text{mrad}$ in the vertical direction. The secondaries are then allowed to decay in an evacuated decay-pipe 340m in length. As shown in appendix A, neutrinos from a thin monochromatic beam of secondaries will have a fixed, known energy for a given angle of decay. This means that as one goes away from the centre of the neutrino detector in Lab E, the energy of neutrinos falls off as a known function of transverse direction (see Appendix A). Such a dichromatic beam is very desirable since it is easy to measure its flux. Increasing the length of the decay pipe, the momentum spread or the angular spread all increase the flux at the price of uncertainty in knowledge of the intensity as a function of energy and radius.

Shown in figure 2.3 is a scatter-plot of neutrinos observed as a function of radius and

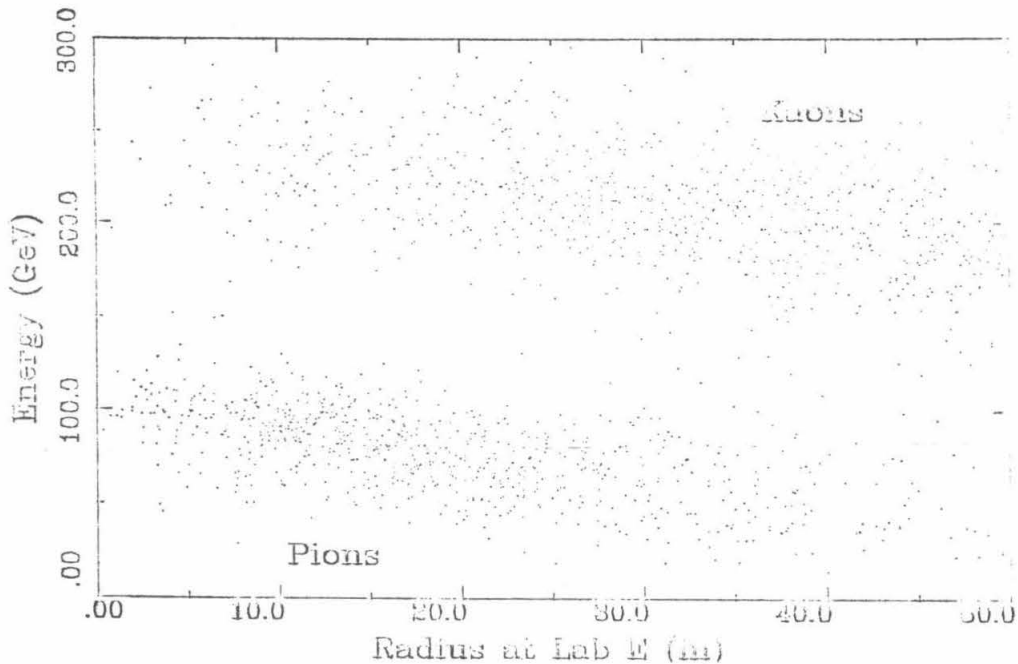


Figure 2.3

E vs. r scatter plot; 1500 events at 250 GeV. Only 1500 events are displayed.

energy with the E616 secondary beam set at 250 GeV/c at Lab E (muon triggers). Notice the clean separation of neutrinos from pion and kaon decay. Figure 2.4 is a projection of this scatter-plot at a fixed radius (10 in $< r < 20$ in), showing again the separation. For details beyond those in appendix A the reader is encouraged to read references 9 and 12. Particle production by a 400 GeV beam is described in ref.13 which includes the particle content of the secondary beam (pions dominate negative energy settings and the lower positive energies, gradually giving way to protons at higher positive settings).

Pion and kaon production cross-sections fall off steeply going away from 0^0 , while their relative content does not show as sharp a variation. For this reason the production angle in the E616 beam is zero degrees. In order to minimize background from the decay of secondaries before sign and momentum selection, the proton beam strikes the target at an angle of 12.01mrad . This background, called the wide band background is therefore mainly at low energies (hadrons produced at $\approx 12\text{mrad}$ have lower energies). There is a like background from the large-angle decays of forward going hadrons. Measurement of these wide-band backgrounds is easily accomplished: one simply cuts off the secondary beam by closing a slit and the wide-band neutrinos are the only ones to reach the detector. Their flux can be estimated well by using the neutrino cross-section measured by this and earlier experiments.^(7,9,30)

Another background arises from 3-body decays of kaons ($K_{\mu 3}$ and $K_{e 3}$: $K^\pm \rightarrow \mu^\pm \bar{\nu}_\mu \pi^0$,

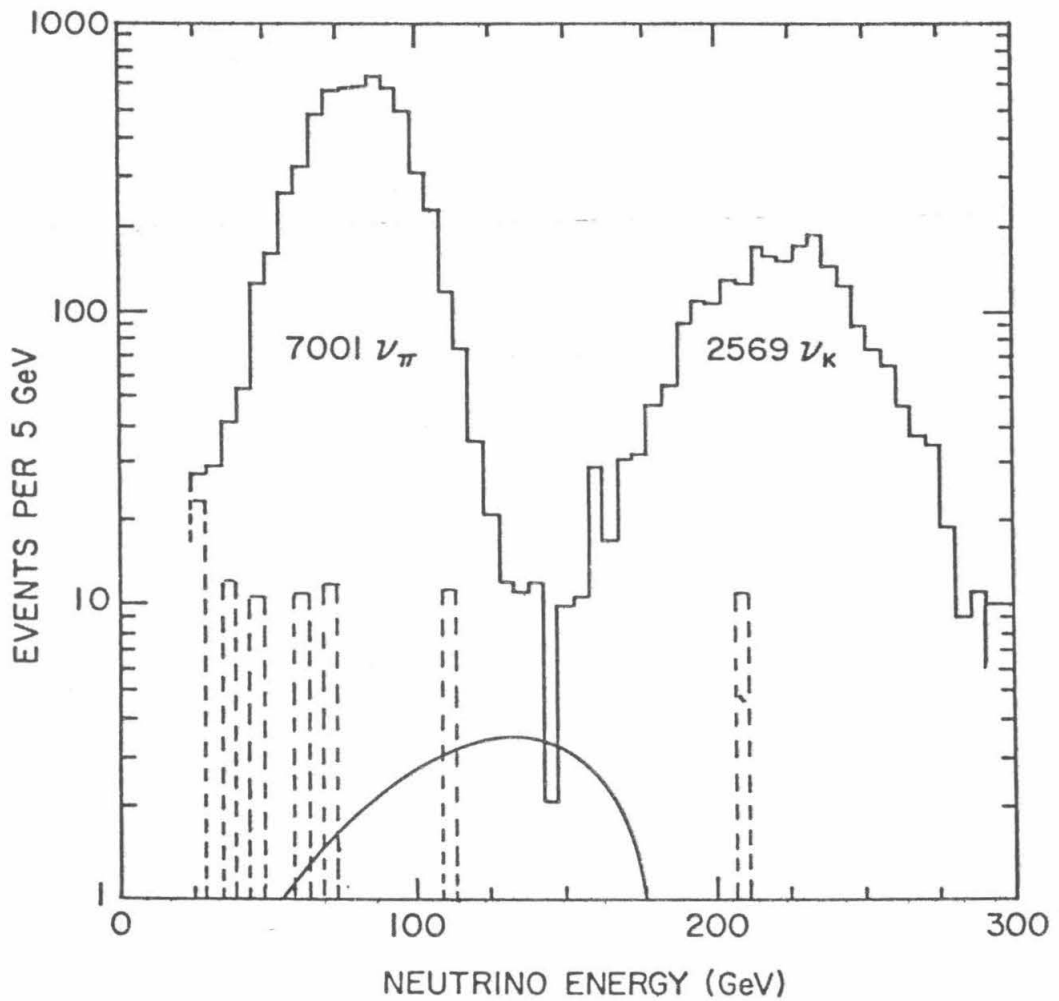


Figure 2.4. 10 in $\langle r \rangle < 20$ in Energy histogram; 250 GeV setting.

$K^\pm \rightarrow e^\pm (\bar{\nu}_e) \pi^0$). This background is small, lower in energy with a larger spread and is estimated via linkage to the main neutrino flux by a Monte Carlo program.

§2.2 Beam Flux Monitors

As mentioned earlier, one of the better distinctions of a dichromatic beam lies in our ability to measure its flux with relative ease. This may be accomplished either by the measurement of the secondary beam flux or by the measurement of the decay muons produced along with the neutrinos. The latter approach did not prove to be consistent and accurate, at least to the level at which it was pursued, and will not be discussed further. Both methods involve tying threads of information about total flux, mean momentum, angular dispersion, beam composition, direction and background together into one consistent unit. Several devices were used to monitor one or more of these quantities, the dependence of the final flux as a function of energy and radius at Lab E being predicted by a Monte Carlo program that utilized all available information. Other programs were used to perform cross-checks and to estimate the total cross-section. Calibration (esp. of the ion-chamber) and analysis (particularly that of the Čerenkov counter) of all the devices was done by yet other programs. It is not possible, as mentioned earlier in the introduction, to go into every detail here – the cross-section theses^(8,9) are again to be referred to.

As is usually the case, one of several devices used to measure a quantity ends up being its primary monitor, the rest serving as useful checks. The total flux comes primarily from the ion chambers at the expansion port (fig. 2.5) which is just before the decay pipe (see fig. 2.2), and the target manhole (towards the end of the decay pipe). It was mainly the expansion port ion chamber that was used, with the manhole ion chamber acting as a backup.

The expansion port ion chamber (fig. 2.6) consists of three ion chambers in one: one to measure the total flux, one to monitor the beam direction, and a third for calibration purposes. All three consist of a central high voltage plate 18 in in diameter (the beam is contained within a 4 in radius at the expansion port and within an 8 in radius at the manhole) flanked by two similar signal plates. In the case of the calibration chamber the HV plate is separated from its neighbours by an inch; the HV plate in the flux-measuring chamber being separated by a 1/4 in from the signal plates. The signal plates in the beam-direction monitoring chamber are split in two at lines through their centres, with one plate split into top and bottom halves and another into east and west halves. The idea, similar to tracking devices in telescopes, is to ensure spill by spill that both halves receive equal amounts of charge and the beam is thus centered. The larger the gap, the more the signal collected, a total gap of 1/2 in being sufficient for regular flux monitoring. The inner diameter of the chamber plates is 16 in as opposed to 22 in for the manhole ion chamber (which has an outer diameter of 30 in). The manhole ion chamber has a total flux gap of 1/4 in. The operating voltage on the expansion port ion chamber is 600 V. The plates are .003 in aluminum foils. There is also a 2 in gap containing an Americium source for relative calibration due to temperature and pressure fluctuations.

In order to calibrate the ion chamber using particle counting techniques one must go to lower beam intensities than those of the real beam (typical secondary beam intensity varies

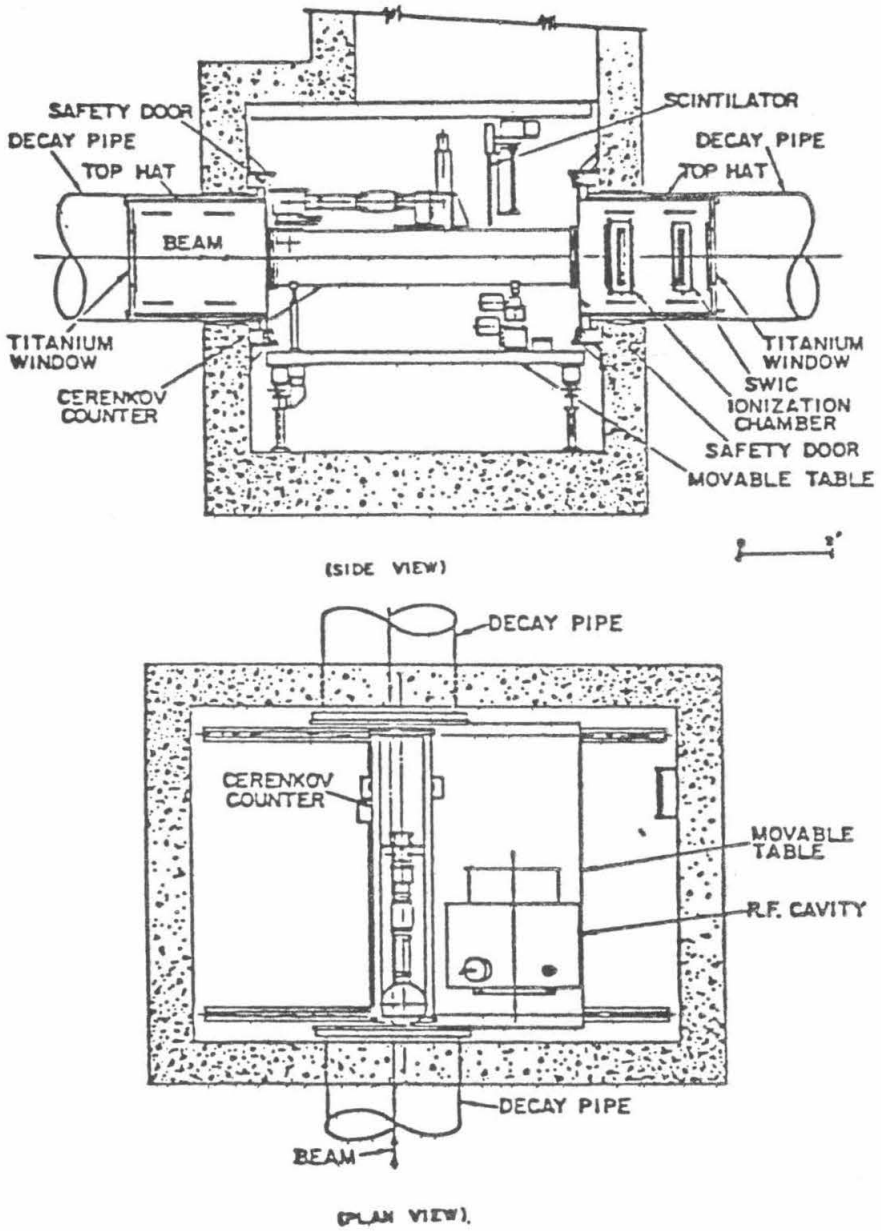


Figure 2.5. The expansion port.

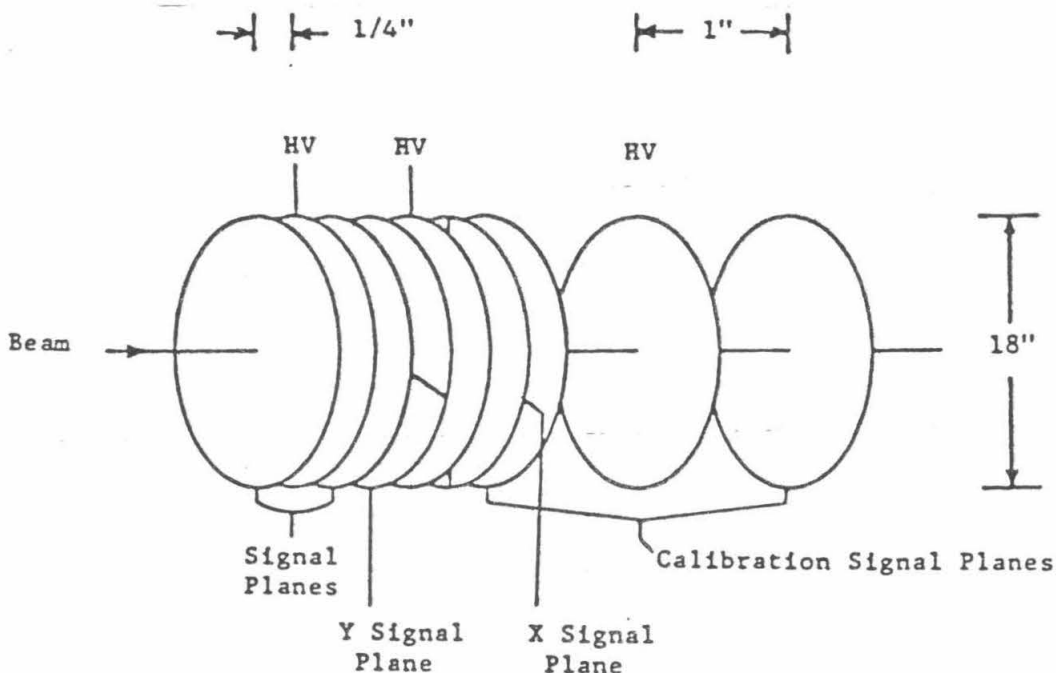


Figure 2.6. The expansion port ion chamber.

between 2 and 40 times 10^9 particles/pulse). Since one cannot use the total flux planes for calibration anyway (at low intensities noise is sufficiently high for them), it was decided to use a small model ion chamber instead. But more about ion chamber calibration later.

The other major total flux monitors are the RF cavity at the expansion port (fig. 2.5) and the toroid in the proton beam. These were primarily used as checks on the ion chambers, with plots of the ion chamber vs. the RF cavity (XR) and the toroid (NT) showing a remarkable linearity (figs. 2.7,2.8). It is also relevant to point out that the expansion port and manhole ion chambers tracked each other to within 2%, a fine example of how well these devices work (fig. 2.9). A current transformer in the beam was not used because of its sensitivity to halo particles in the beam.

The RF cavity is a resonant cavity through which the beam passes. Since the beam is accelerated in the main ring by RF cavities, it has an RF structure, i.e., it comes in pulses separated by 19 ns, corresponding to a frequency of about 53 MHz to which the cavity is tuned. The cavity may be used to calibrate the ion chamber because its response is calculable directly from Maxwell's equations. In practice however the observed stability and the readout electronics limit this to 5%.

Another major parameter of the beam is its angular dispersion. This is measured by two segmented wire ion chambers (SWICs), one at the expansion port and another at the manhole. These provided projections of the secondary beam in x and y views at two points

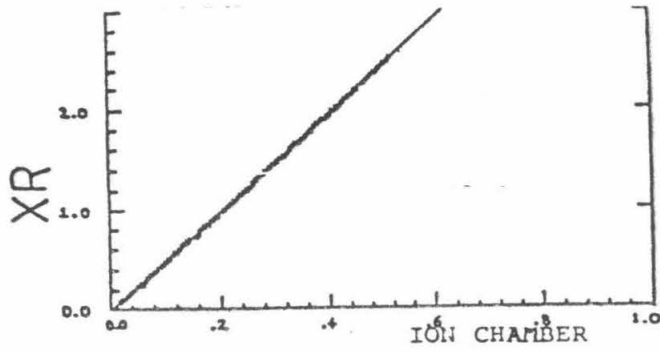


Figure 2.7. Linearity of XR vs XI

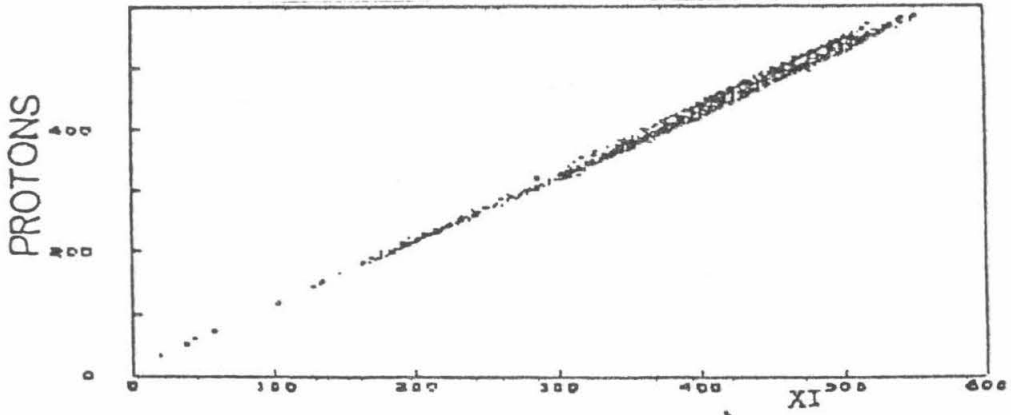


Figure 2.8. Linearity of NT vs XI

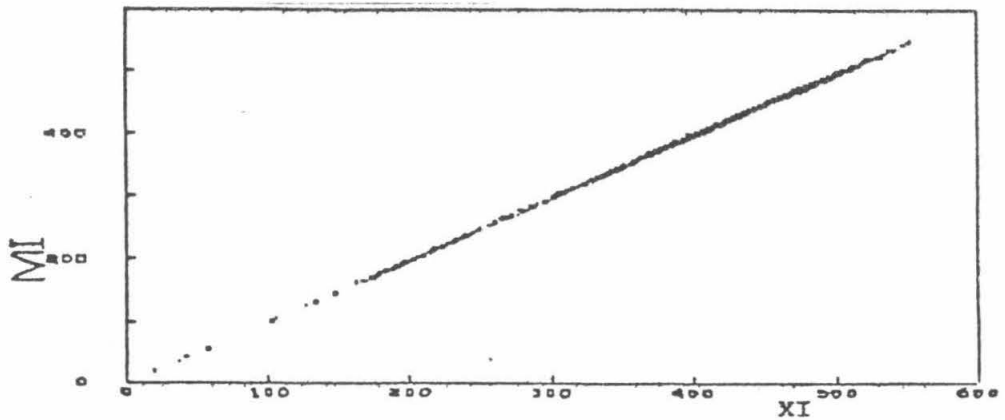


Figure 2.9. Linearity of MI vs XI

separated by 154m (fig. 2.10). The increase in width can be related to the angular dispersion of the beam. A check on the SWIC profile is the small 1/4 in x 1/4 in scintillation counter in the expansion port. It could be placed at different positions in the beam, enabling us to spatially sample the beam.

For a detailed description of all the flux devices and the accuracies to which one determines beam properties the reader is referred to ref.8, particularly its appendix A. We continue with the ion chamber calibration and the Čerenkov counter analysis.

§2.3 Ion Chamber Calibration

The ion chamber was calibrated in several ways. One technique employed was to irradiate a copper foil, place it in the decay pipe and measure its residual radioactivity. For this purpose a 200 GeV proton beam was sent through the decay pipe with the target removed. After about 10^{13} protons the foil was removed and this led to a calibration constant of $(3.45 \pm .22) \times 10^{-18}$ Coulombs/particle. An old calibration against a 275 GeV pion beam using particle counting gave a result of $(3.57 \pm .18) \times 10^{-18}$ Coulombs/particle.

A better calibration can be obtained from the RF Cavity. As mentioned earlier, this device has an accuracy of about 5%. The calibration constant varies from $(3.31 \pm .17) \times 10^{-18}$ for negatives to numbers around 3.7×10^{-18} for positives. This systematically larger constant (about 10%) for positives puzzled us. One clue was the difference in proton content (zero for negatives; between 25% at +90 GeV and 92% at +250 GeV for positives). The dE/dx energy loss due to protons is slightly different from that due to pions, *however the energy loss from pions is a little greater*. This means that the observed difference is *opposite* to that expected from dE/dx losses. This phenomenon clearly presented a puzzle and a particle counting measurement was planned, this time with 1% accuracy.

Using the expansion port ion chamber itself was out of the question, since its large size and G-10 separated gaps lead to leakage and noise levels incompatible with a 1% measurement at low intensities. A fairly similar ion chamber was built with 1/4 in gaps like the expansion port ion chamber, except for the use of ceramic spacers instead of G-10 and the smaller diameter (6 in). The signal plates were still made of .003 in thick aluminum foil. The windows were made of .022 in of titanium.

The ion chamber (fig. 2.11) was put in the M2 beam line of the meson lab at FNAL in May, 1982. This meson beam was operated at different energy settings and with positively and negatively charged particles selected. The initial proton beam impinged on a 15 in target and particles were extracted at a production angle of 2.1 mrad. The beam composition of course varied with energy setting and sign selection and is tabulated below.

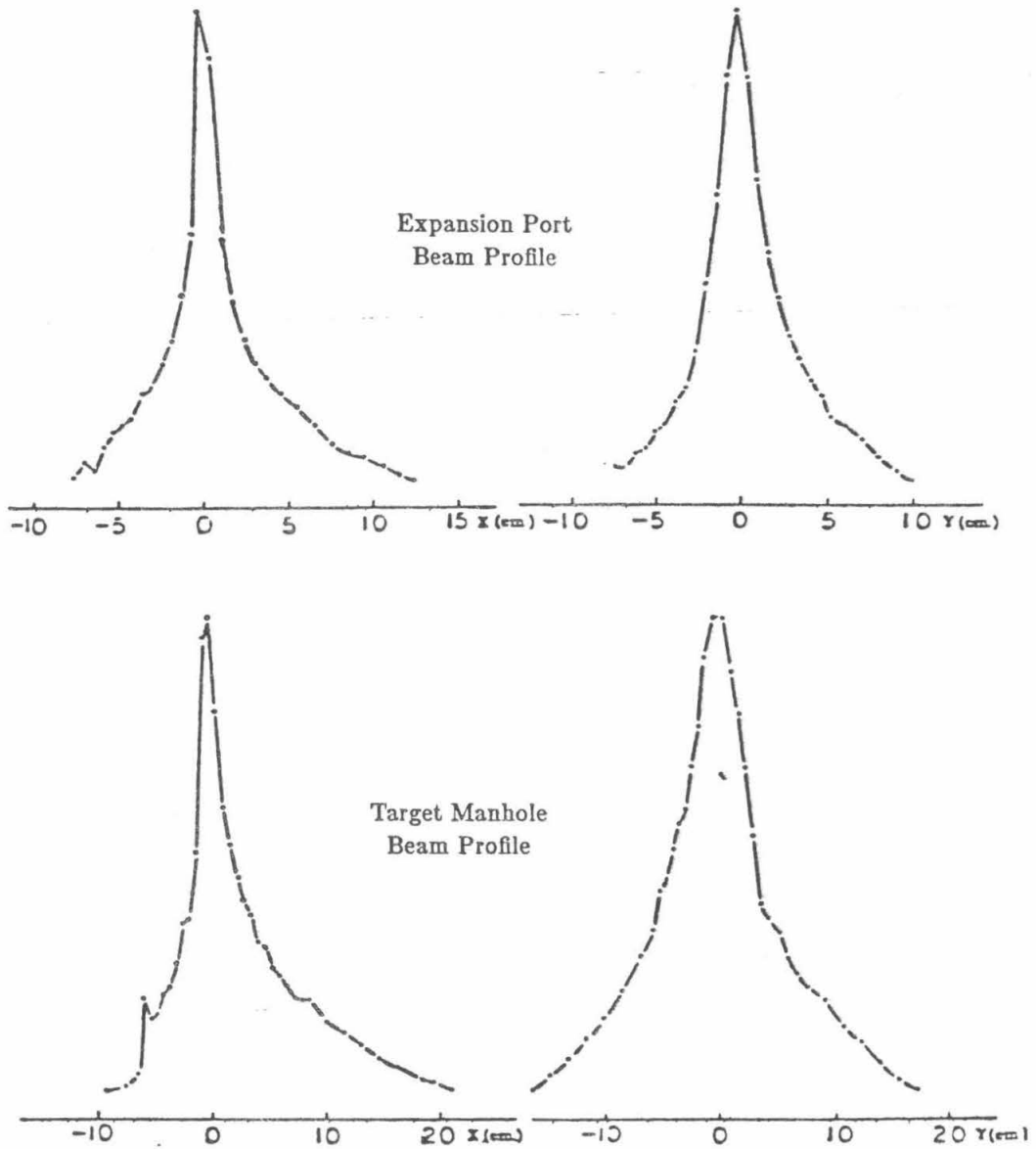


Figure 2.10. SWIC profiles.

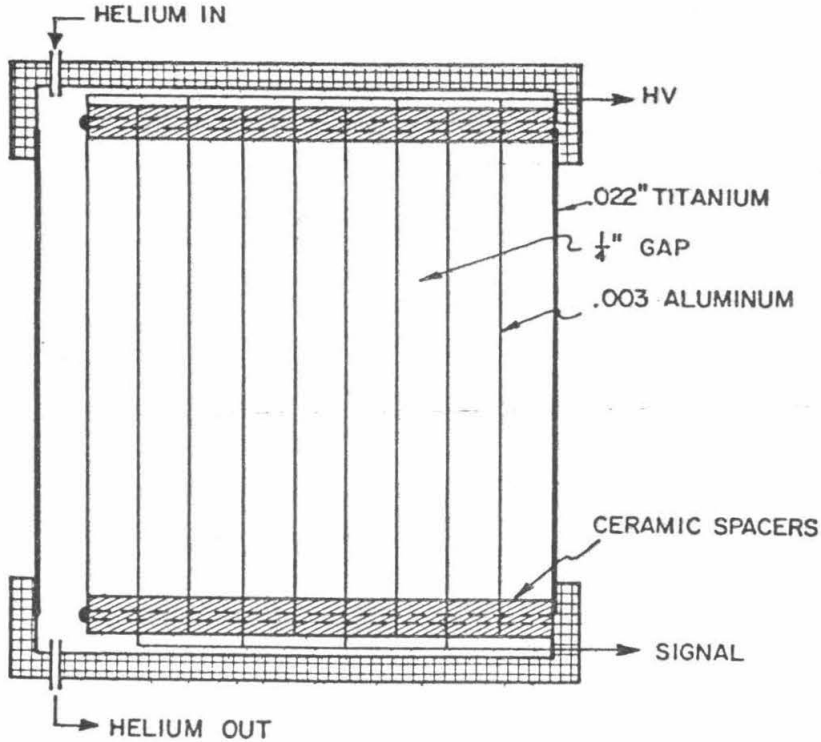


Figure 2.11. The M2 line ion chamber.

E_{SET} (GeV)	Proton Fraction	Calibration Constant ($10^{-18}C/particle$)	Averaged Cal. Const. ($10^{-18}C/particle$)
+90	29%	$3.468 \pm .050$	
+90	29%	$3.468 \pm .063$	$3.468 \pm .039$
+140	53%	$3.448 \pm .050$	$3.448 \pm .050$
+200	82%	$3.468 \pm .127$	
+200	82%	$3.619 \pm .050$	
+200	82%	$3.679 \pm .059$	$3.630 \pm .037$
+300	97%	$3.569 \pm .050$	$3.569 \pm .050$
-90	$\sim 0\%$	$3.380 \pm .050$	
-200	$\sim 0\%$	$3.385 \pm .050$	$3.383 \pm .035$

Table 2.2. M2 line beam composition and ICH calibration results

After toying with various combinations of counters we settled on the configuration shown in fig. 2.13. The ion chamber was placed upstream of all the counters in order to

count only primary particles. The scintillation counters were of varying thickness, with the fat counter (F) being used as input to a QVT analyzer. The beam spot size as seen in Polaroid film exposed to the beam was used to centre the various pieces of apparatus. The counter was situated 10 ft downstream of the .005 in thick beam pipe window in an effort to simulate actual conditions in the expansion port.

The counters were plateaued and discriminator levels set to be above noise levels. The fat counter output went to a QVT analyzer which was triggered by a coincidence pulse. The idea was to try and determine the fraction of particles that arrived in pairs or higher-order bunches. A typical pulse height analysis by the QVT is shown in figure 2.12. (If 2 or more particles arrive in a single RF bucket of ≈ 2 ns duration, the counters with a width of 25 ns counted them as one). As suspected, the number of such coincidences never exceeded 1%, at least at the intensities used (from 2K to 800K particles per pulse). Helium gas was slowly injected into the chamber and bubbled out. A record of pressure was kept at all times.

Output from the ion chamber itself was integrated and the total charge collected across a capacitor was converted into a voltage which was then amplified and input into an ADC. This ADC was sampled by sending interrupts between 80 to 100 times every spill from an on-line PDP 11/45 computer. Data acquisition and on-line analysis were also handled by this computer. The ADC, when calibrated against a very accurate DC voltage calibrator, was found to be extremely linear. The ion chamber calibration consisted, of course, of measuring the drop of the ADC output due to the passage of a beam pulse through the chamber and comparing it with the counted number of particles corrected for RF-bucket pairing, randoms and counter inefficiencies.

We know from coincidence rates that counter efficiencies were all always greater than 0.9995. Singles and coincidence rates suffice to extract the randoms rate; this small correction was applied to all the data.

Ideally, if one plotted the charge from the ion chamber as a function of time (fig. 2.14) the curve should be flat before and after the beam spill, with the slope of the drop in between being proportional to the beam intensity. Noise, leakage and even possibly pickup from magnet currents ramped in the vicinity lead to slight slopes for the curve before and after every spill (fig. 2.15). The true charge collected during a beam spill must be determined. At least three different ways of doing this were tried: fitting straight lines to the portions before and after the beam spill, subtracting an averaged no-beam curve and subtracting a "no-beam" fit to the curve spill by spill.

Let ΔV be the measured voltage difference in volts (see fig. 2.14) and

$$\begin{aligned} x &= \text{the number of ion pairs/cm/particle,} \\ D &= \text{the gap size for the M2 ion chamber,} \\ d &= \text{the gap size for the exp. port ion chamber,} \\ Q &= \text{the total charge collected at the ion chamber,} \\ f &= \text{the cal. const. in pCoul./}10^6 \text{ particles.} \end{aligned}$$

Then,

$$Q = (nxD)1.6 \times 10^{-19} C = .16nxD \times 10^{-6} pC. \quad (2.1)$$

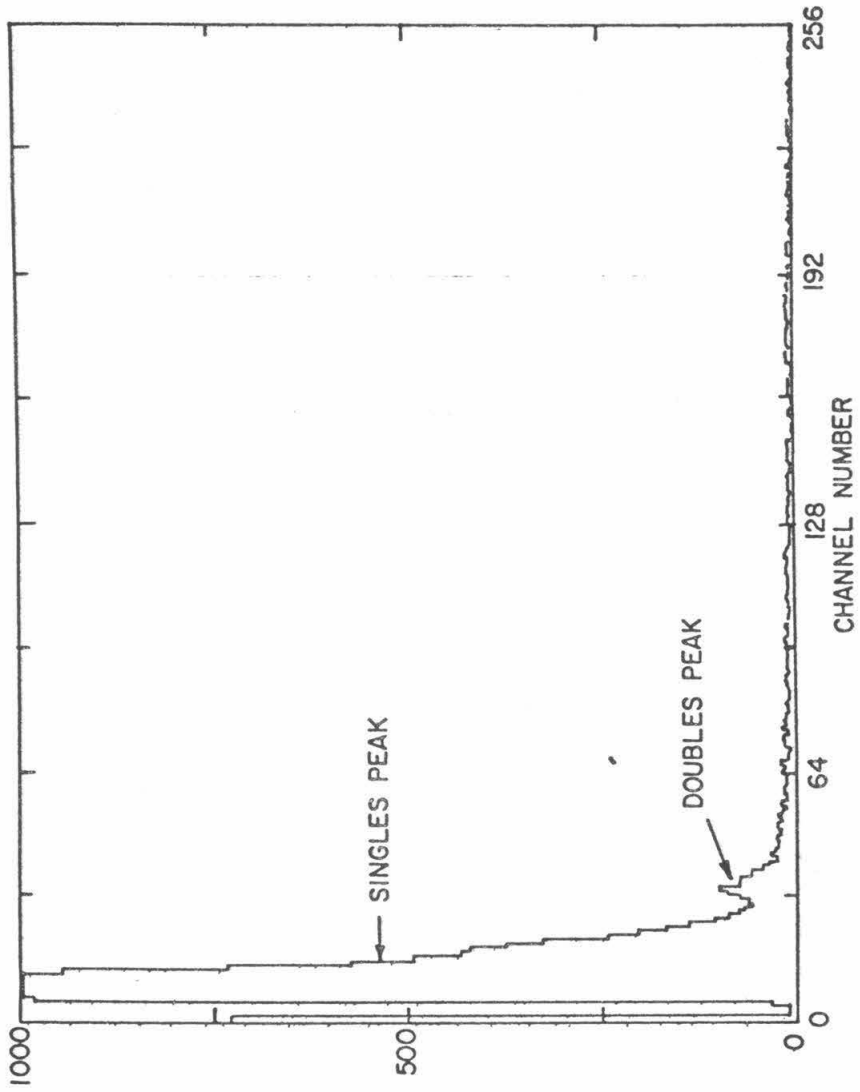


Figure 2.12. Typical QVT analysis of one pulse.

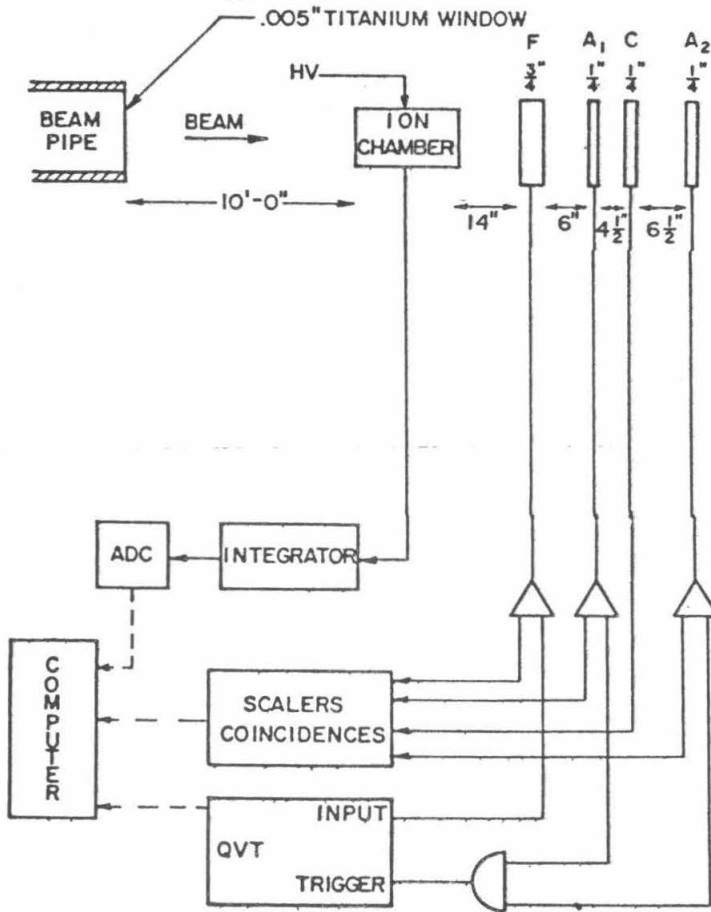


Figure 2.13. The calibration run set-up.

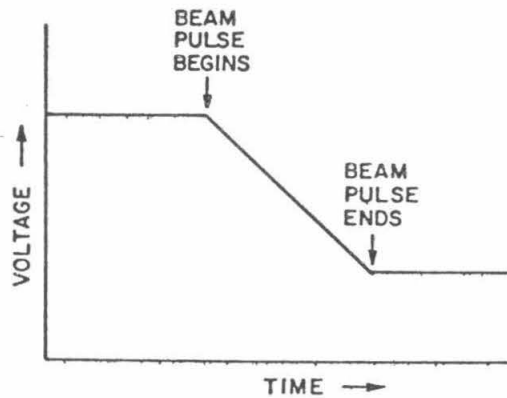


Figure 2.14. An ideal ion chamber voltage vs time curve.

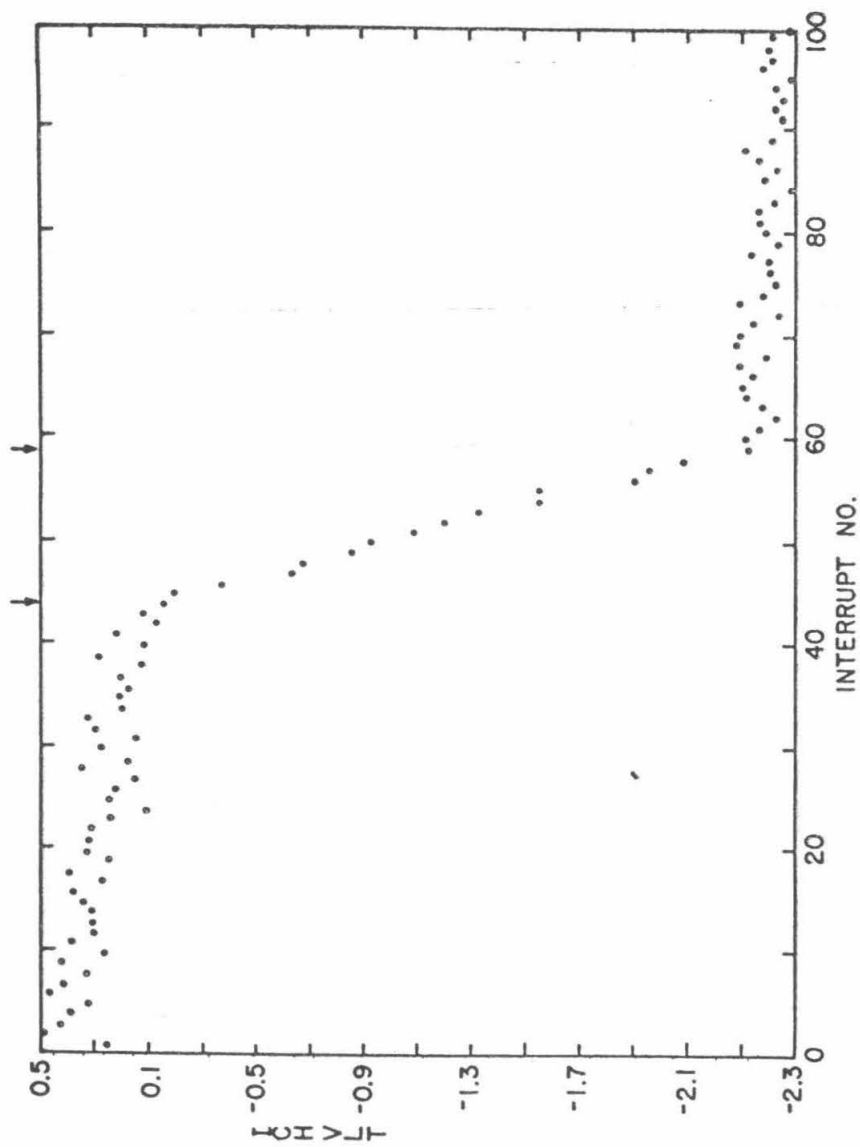


Figure 2.15. An actual ion chamber voltage vs time curve.

$$\Rightarrow f = \frac{Q}{(D/d)(n/10^6)} = .16zd \quad (2.2)$$

Since the charge is collected across a capacitor of 995 pF and since the voltage generated is amplified by 500.3 before measurement,

$$Q = \frac{995 \times 10^{-12} F \times \Delta V}{500.3} = 1.989 \Delta V \text{ pC.} \quad (2.3)$$

Thus, combining (2.1),(2.2) and (2.3),

$$f = \frac{0.4975 \Delta V}{(n/10^6)}. \quad (2.4)$$

Also note that if

$$\begin{aligned} P_x &= \text{pressure of gas in the X I.Ch.} \\ P_M &= \text{pressure of gas in the M2 I.Ch.} \\ T_x &= \text{temperature of gas in the X I.Ch.} \\ T_M &= \text{temperature of gas in the M2 I.Ch.} \end{aligned}$$

then

$$f = \frac{0.4975 \Delta V}{(n/10^6)} \cdot \frac{P_x}{P_M} \cdot \frac{T_M}{T_x} \quad (2.5)$$

The mean pressures and temperatures are used to effect the above conversion for Lab E purposes; the pressure variation during the calibration run is also incorporated in the analysis. Since both the X I.Ch. and the M2 I.Ch. were deep inside "caves", the temperatures varied very little.

There were slight differences in the ΔV as obtained by the three different methods. Our suspicion fell on a spurious pedestal coming from noise, making ΔV depend on the intensity I in the form $(aI + b)$ where the first term is the true ΔV and the b the noise that varied from method to method. Clearly, this problem could be solved by extrapolating $a = (\Delta V - b)/I$ to infinite intensity ($1/I=0$) and indeed, all three methods tend to converge on one calibration constant.

The QVT is a hardware histogramming device (a multichannel analyzer) that was triggered on the coincidence of the two channels A1 and A2. Fig. 2.12 shows the typical QVT response to a pulse of beam. There is a small second peak due to 2 particles in one gate. These pairs may occur because 2 RF buckets occur in one 25ns period, because there may be 2 particles within a single bucket or because of the interaction of a particle with the beam pipe window or the 10 ft of air upstream of the chamber. In any case, the scintillation counters count them as one particle and a correction must be applied. The number of extra particles to be added can be expected to be proportional to the intensity itself for any of the above effects, and indeed a fit of the form $(1.177 \times 10^{-8} I^2 + 153.7)$ was added to the intensity I .

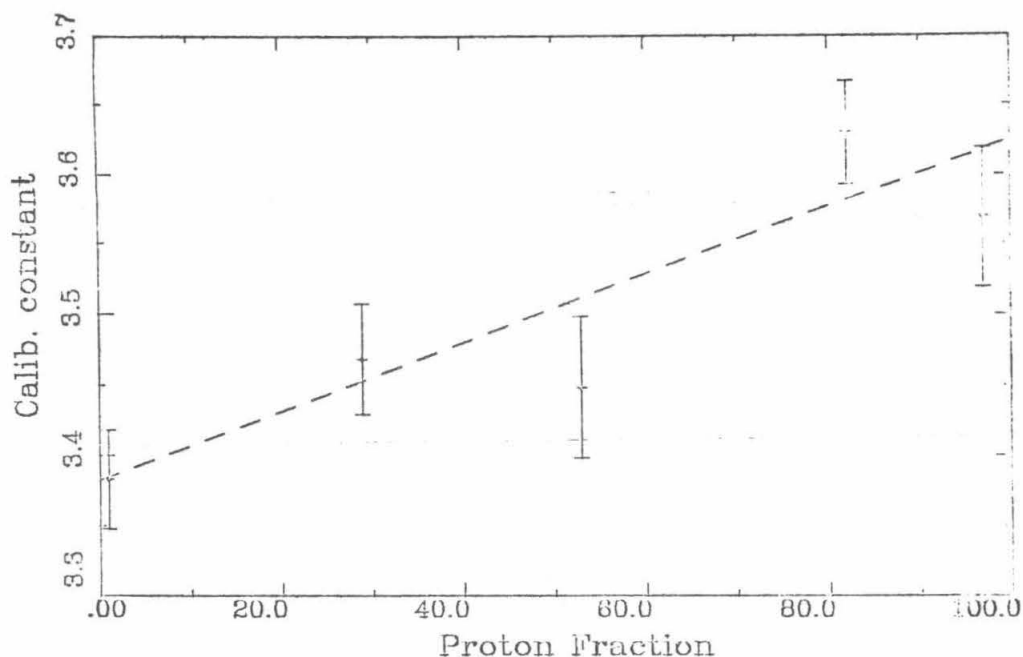


Figure 2.16

The ion chamber calibration constant as a function of proton content.

Finally, extra material (.042 in of titanium) was placed upstream of the ion chamber for 2 energy settings, +90 and +200 GeV/c, to see if any interactions with the material caused a change in the calibration constant. The final results of the analysis are tabulated in table 2.2. There is no measurable difference between material "in" and "out" for the two energy settings at which the effect was studied. This cannot explain the approximately 10% effects seen with the RF cavity. The only explanation that meets the bill is a proton-pion difference in the calibration constant.

When the results of table 2.2 are plotted (fig. 2.16) as a function of proton content, one sees a definite increase in the calibration constant as the number of pions in the beam decreases. This is attributed to the lower cross-section of interaction for a pion as opposed to the proton (at approx. 200 GeV, the πp cross-section is $\approx 24\text{mb}$, the $pp \approx 42\text{mb}$). The low energy particles created in interactions ($\approx 17\text{ MeV}$) ionize very heavily due to their low velocity. Thus, one can conclude that protons have an $\approx 6\frac{1}{2}\%$ higher response than pions in helium-filled ion chambers, and the calibration constants used for protons and pions are $(3.63 \pm .06)$ and $(3.38 \pm .05) \times 10^{-18}\text{ C/particle}$ respectively.

§2.4 The Čerenkov Counter

The Čerenkov counter is a veritable cornucopia of information. In principle it is capable of telling us the total flux, the flux due to each particle type, the mean momentum of each particle type and even information on the momentum and angular dispersion of the beam. We shall see in this section how it is used to provide information about all but the total flux, for which this particular Čerenkov counter cannot be used while simultaneously measuring the other quantities of interest.

The principle of operation of a Čerenkov counter is simple; if a charged particle of speed β goes through a medium of refractive index n , and if β is greater than $1/n$, coherent light is emitted at an angle θ_c with respect to the direction of motion of the particle, where θ_c is given by

$$\cos \theta_c = \frac{1}{\beta n}. \quad (2.6)$$

For the highly relativistic particles we are considering,

$$\beta \approx 1 - \frac{m^2}{2p^2}. \quad (2.7)$$

The refractive index of gases is related to their pressure P by

$$n \approx 1 + \kappa P. \quad (2.8)$$

κ for helium has been measured to be $4.37 \times 10^{-8}/mmHg$. Combining (2.7) and (2.8) with (2.6) gives, for small angles ($\cos \theta_c \approx 1 - \theta_c^2/2$),

$$\theta_c^2 = 2\kappa P - \frac{m^2}{p^2}. \quad (2.9)$$

Many important consequences follow from this central relation, as we shall shortly discover.

The secondary beam consists of different particle types all at the same momentum. From (2.9) we see that at a fixed pressure, P , and a fixed momentum, p , the lightest particles have the largest angles. If a lens or focussing mirror is used to focus this light, one obtains rings of different radii corresponding to each particle type. The angular separation of two particle types of masses m_1 and m_2 is obtained by differentiating (2.9) to yield

$$\Delta \theta_c = \frac{m_1^2 - m_2^2}{2\theta_c p^2}. \quad (2.10)$$

Thus, in order to obtain as wide a separation as possible, it is best to minimize θ_c . The ring imaging possibility also gives us a means of clearly separating particle types: in the ring image plane is an annular iris that permits only one ring at a time, the light that passes through being measured by a phototube. Instead of varying the annulus, we vary the pressure of the gas (Helium), with a fixed annulus.

The counter is shown in fig. 2.17. At one end is a spherical mirror of focal length 119.02 in and 10 in in diameter. It is tilted slightly and the Čerenkov light is reflected off

a couple of plane mirrors before going through the iris after which it is reflected off a fourth mirror (also plane) and goes through a lens and enters the phototube. An alternate transducer, the photodiode, can be used with the help of a light splitting mirror. Since the typical number of particles in a pulse is very large, a weak signal is definitely not a problem (Čerenkov counters are capable of detecting single particles). Consequently the counter is short, with a radiative medium of length 74.3 in. The phototube accepts light roughly within the limits 3300 Å and 5000 Å with a mean accepted wavelength of ≈ 4400 Å. The iris has several apertures of which, for ring imaging, we used the annular aperture from .7 to 1. mrad (at the focal plane of the primary mirror). Baffles before the iris cut down stray light and a shutter between the second and third mirrors can be closed to measure background light. Helium gas is used in the counter as the Čerenkov medium. Its pressure is constantly monitored by a pressure gauge.

The ray optics of the counter in a plane containing the optic axis is shown in fig. 2.18. From the figure it is clear that if the beam were parallel to the axis but shifted a small distance from it, light would still be focussed at the same ring in the focal plane. Consequently not much attention is paid to the precise coincidence of the beam and optic axes. The counter is placed on a movable table and may be moved in and out of the beam (see fig. 2.5). The alignment of the *directions* of the optic and beam axes is, of course, very important and is done before every pressure curve is taken by remotely adjusting two orientations of the counter until the signal goes through a maximum, where the counter is then set. A Čerenkov curve is then taken by varying the pressure from zero by filling the counter with helium. A typical Čerenkov curve is shown in fig. 2.21. The number of photons emitted by a particle in a length L of medium in a wavelength range $[\lambda, \lambda + d\lambda]$ is given by

$$dN = L \cdot \frac{2\pi\alpha}{\lambda^2} \cdot \sin^2\theta_c d\lambda. \quad (2.11)$$

Not surprisingly, the amount of light is proportional to the length, L . At small angles, it is also proportional to θ_c^2 . From (2.9), we can plot the Čerenkov counter response with respect to θ_c^2 or, equivalently, pressure and the area under each of the bumps will, apart from diffraction effects, be proportional to the number of particles of the corresponding type. Before this is done however, various backgrounds must be subtracted, a procedure discussed later in this section.

The Čerenkov rings may be broadened for several reasons. There is chromatic dispersion in the gas which produces an angular broadening $\Delta\theta \approx \frac{1}{2}\theta_c\omega$ where ω is a constant of the gas. Helium was chosen because it has a fairly small ω (4.5%), does not scintillate and has the right magnitude of gas constant for our counter and iris dimensions. Another cause of broadening is the $\sim 10\%$ momentum bite of the beam. $\Delta\theta$ due to this is given by

$$\frac{\Delta\theta}{\theta} = \frac{m^2}{p^2\theta_c^2} \cdot \frac{\Delta p}{p} = \frac{1}{\gamma^2\theta_c^2} \cdot \frac{\Delta p}{p}. \quad (2.12)$$

For our counter, $1/\theta_c^2 \approx 1.37 \times 10^8$ which means $\Delta\theta/\theta = \Delta p/p (= 10\%)$ for $\gamma \approx 1170$. Clearly, $\Delta\theta/\theta$ can be very large for kaons and protons (see table in Appendix A for typical values of γ). From (2.10) we see that the momentum broadening and the angular separation maintain a fixed ratio. Angular dispersion of the beam causes a fixed broadening $\sim .18$ mrad, which is the magnitude of the dispersion. In order to minimize this effect the angular separation of the particle types must be made large i.e., the Čerenkov angle θ_c must be made small.

Before the Čerenkov curves can be analyzed they must be corrected for various experimental effects. Since any pressure scan extends over many beam spills, the spill-to-spill

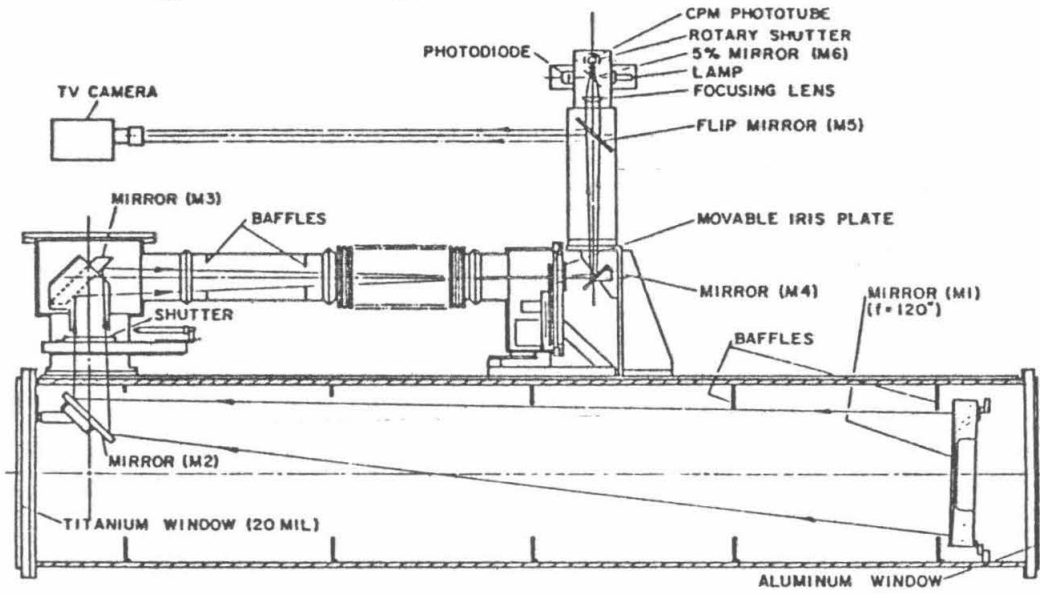


Figure 2.17. The E616 Čerenkov counter.

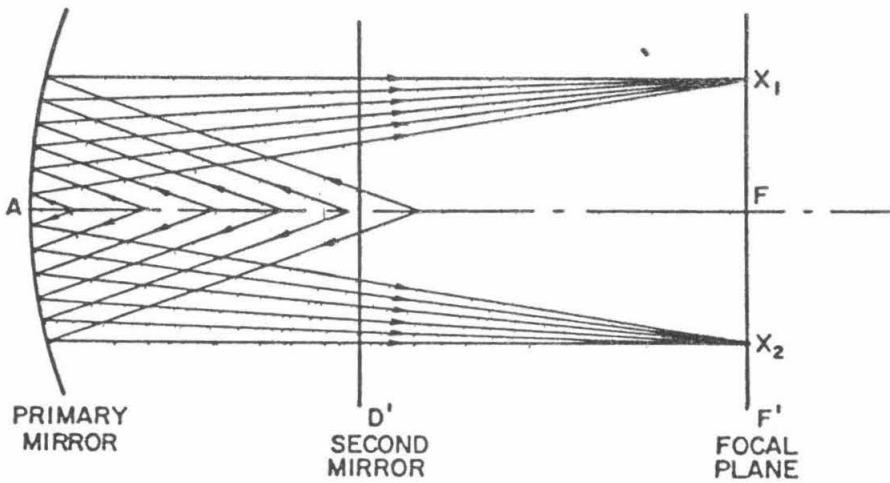


Figure 2.18. Ray optics of the Čerenkov counter.

variations must be relatively normalized by one of the ion chambers. The expansion port ion chamber is so close to the Čerenkov counter that it was feared that the halo of secondaries produced by beam-primary mirror interactions would make it unreliable. Consequently, the downstream manhole ion chamber was used. Another variable that can affect analysis is temperature. At 300K, a 3°C variation can cause κ to change by 1%. However, the counter was in a cavity buried fairly deep and consequently temperature variations were not severe. They were monitored by a thermocouple affixed to the counter itself.

One unfortunate consequence of pressure changes in the counter was a variation in alignment of the iris with respect to the central axis. This effect was measured after the run by a theodolite through a transparent hole in the beam window aimed at a cross-hair on the iris plate. The deflection $\Delta\theta_{\text{iris}}$ in milliradians was fairly linear with pressure and could be parametrized as $\Delta\theta_{\text{iris}}(\text{mr}) = (.001318 \pm .000050)P$, P being in mm of mercury. Such a pressure dependent alignment can cause a very significant change in the amount of light collected, especially at high pressures. Since the correction can be easily calculated, this effect is safely accounted for. Studies were also made of the calibration of the pressure and total response of the counter. The counter is filled by opening a valve for a fixed short time repeatedly. This procedure can be shown to make the counter pressure

$$P = P_0(1 - e^{-\alpha n}), \quad (2.13)$$

where P_0 is the (fixed) pressure of the gas before the valve and n is the number of fills. This relation was directly checked against a pressure gauge that monitors the counter pressure and the two agree to less than 0.8%.

After the end of the data taking run, a 200 GeV beam from the accelerator with an extremely small momentum dispersion ($\approx 0.1\%$) was fed through the train, with the target removed. The iris of 0.7 mrad to 1.0 mrad aperture was replaced by a circular hole of 2.0 mrad aperture. In this mode, the counter functioned as a total light measuring device, and when its response was plotted against the manhole ion chamber, the linearity of the phototube and digitizer was checked and found good to 0.6%. The primary 200 GeV beam intensity was varied by almost an order of magnitude for this test. Inverting (2.9), one can also use the 200 GeV beam to measure κ . The value thus obtained is $4.37 \times 10^{-8}/\text{mm Hg}$, very close to the book value of $4.35 \times 10^{-8}/\text{mm Hg}$. Another method of obtaining κ is to measure the threshold pressure at which light is emitted for the 200 GeV proton beam; κ can be obtained by solving (2.9) for $\theta_c = 0$. κ obtained this way agrees with the above method and is included in the average.

Once the Čerenkov curves have been corrected for all the effects mentioned above, there are still some backgrounds to be subtracted:

(1) Shutter-closed background:

Interactions outside the main body of the counter e.g., near the iris or phototube can cause extra Čerenkov light. This light is easily isolated by closing the shutter and taking Čerenkov curves. Such a Čerenkov curve is shown as the lower curve in fig. 2.19, and is subtracted from all raw curves.

(2) Beam-material interaction background:

Upstream of the gas is the counter window which is made of .020 in thick titanium. Including air and other material, there was an equivalent of .080 in of titanium upstream of the gas. Interaction of the beam with all this material produces additional particles

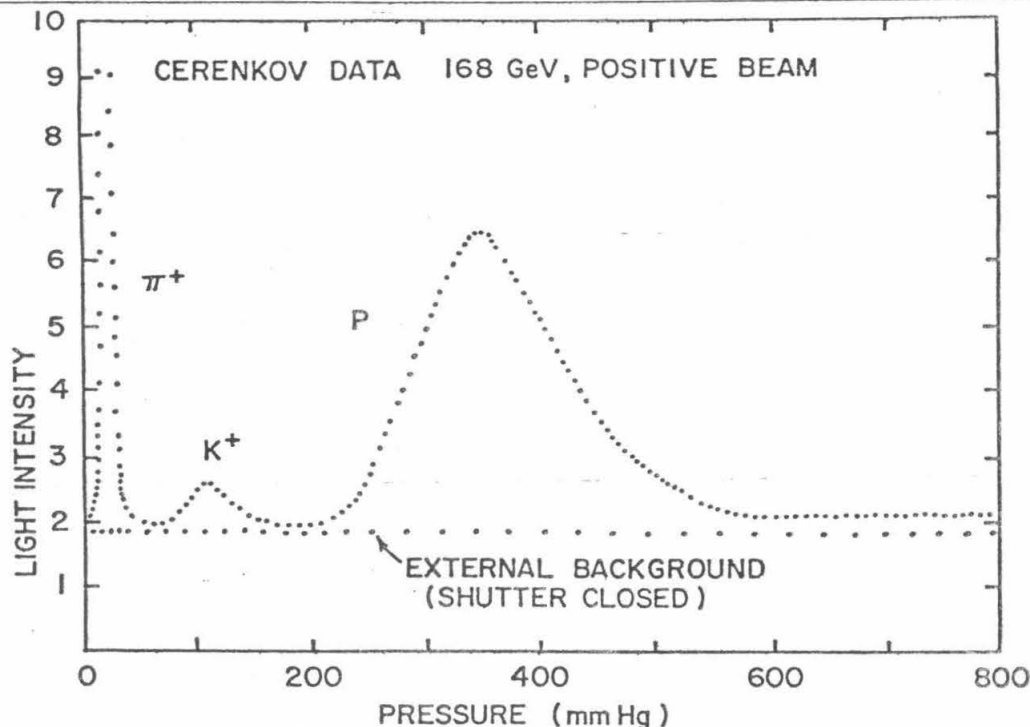


Figure 2.19. Čerenkov curve with a shutter-closed curve underneath.

which in turn give rise to extra Čerenkov light. The easiest way to account for this is to add even more material, obtain another curve and subtract the properly normalized difference as a background correction to the Čerenkov curves. Unfortunately beam-material curves were not taken at all energy settings and some interpolation had to be performed.

(3) Light-scattering Background:

After subtracting the above backgrounds it is found that some background light persists. One possibility was scattering of light off dust on some mirror. Evidence for this possibility came from the monotonic increase with time of this background, observation of dust on the second mirror and a dramatic decrease in the background when the second mirror was cleaned with a nitrogen jet. It is possible in theory to accurately calculate this background (if the position, size, amount and albedo of dust were well known) by applying the optics of diffraction and scattering. Such an attempt was made⁽¹⁷⁾ and the qualitative conclusion was a background that rises from zero at zero pressure and ultimately flattens out, being dominated at high pressures by scattering. Since our knowledge of the quantity and properties of dust in the counter are necessarily limited, it was decided to try the simple form shown in fig. 2.20. P_0 is held fixed for all energy settings, L is allowed to vary from setting to setting. The resulting fits are then subtracted from each energy setting.

(4) Counter Diffraction:

The broadening of the Čerenkov ring due to diffraction (the counter has an effective

aperture of $L\theta_c$ where L is the counter length) is approximately

$$\Delta\theta_{diff} = \frac{\lambda}{L\theta_c} = 0.27 \text{ mrad.} \quad (2.14)$$

This is obviously significant for our counter and in fact is the dominant broadening effect for the lighter particles (pions, muons, electrons). The number of photons in the range $[\lambda, \lambda + d\lambda)$ and $[\theta, \theta + d\theta)$ where θ is the angle with the beam direction is given by⁽¹⁸⁾

$$\frac{dN}{d\lambda d\cos\theta} = \frac{2\pi\alpha}{\lambda} \left(\frac{L}{\lambda}\right)^2 \sin^2\theta \left(\frac{\sin\psi}{\psi}\right)^2 \quad (2.15)$$

where

$$\psi(\theta) = \frac{\pi L}{2\lambda} [1 - \beta^2 + \theta^2 - 2\kappa P]. \quad (2.16)$$

In the limit $(L/\lambda) \rightarrow \infty$, (2.15) reduces to (2.12). It is clear from (2.15) and (2.16) that there will be some Čerenkov light *even below* the Čerenkov threshold. This is due to transition radiation when the beam crosses the counter windows and is the correct explanation for the mysterious zero pressure background that plagued earlier Čerenkov analyses.⁽⁹⁾

After the shutter-closed and beam-material backgrounds are accounted for and removed, a Čerenkov curve looks like the one shown in fig. 2.21. Apart from diffracted light, particle fractions are directly proportional to the areas under their respective peaks. There is a small contribution to Čerenkov light from electrons (or positrons) at the lowest pressures. These arise due to π^0 production at the target with the π^0 s subsequently decaying into two photons which then pair-produce. Corrections are made to the particle fractions for this effect and also for the small changes in fractions due to decays before the counter (fractions are quoted at the target). The final results are to be found in table 2.3. Since the kaon and proton peaks are dominated by the momentum bite, their peaks can be translated into momentum probability distributions and their mean momentum is thus obtained. The pion peaks are broadened by iris acceptance, diffraction and angular dispersion. Consequently the energy of neutrinos from pion decays as measured in Lab E is used to estimate the mean momentum of the pions rather than the Čerenkov data. The final mean momenta are tabulated in table 2.3 below.

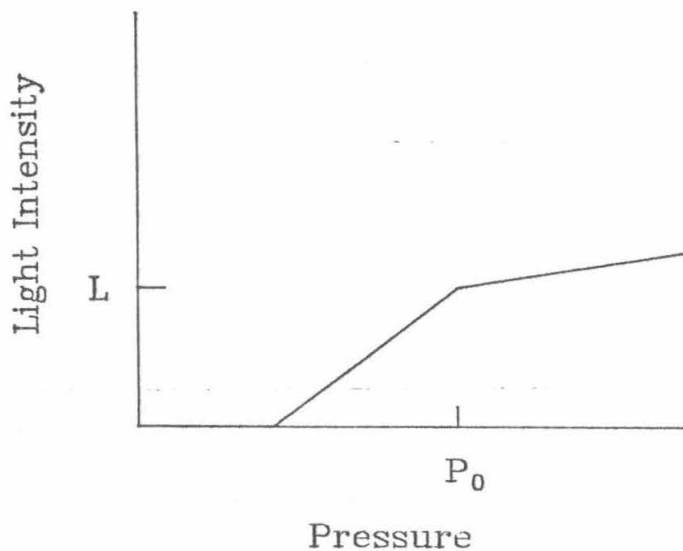


Figure 2.20. Form of the light scattering background.

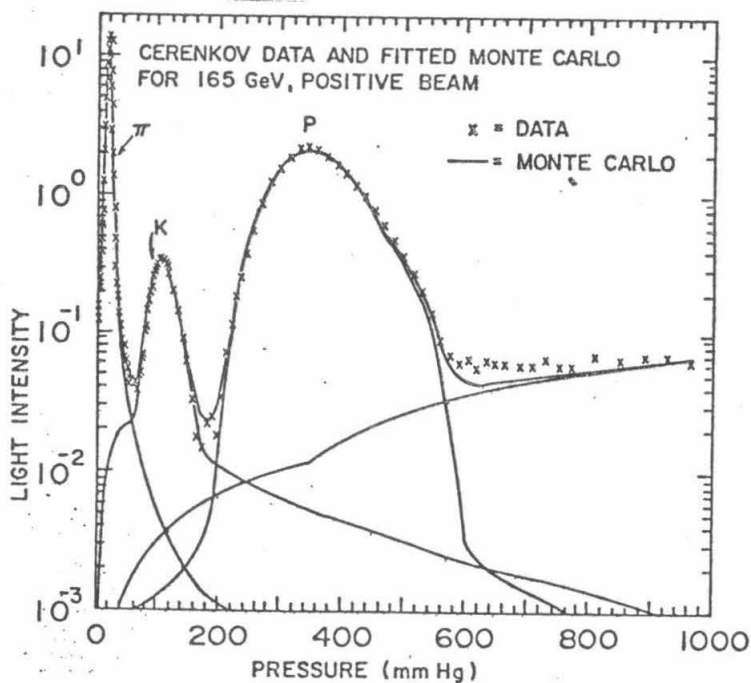


Figure 2.21

Final Čerenkov curve with fits to individual particle type and light scattering background indicated.

E_{SET}	π /total	K /total	π mean p	K mean p	$\sqrt{\langle \theta_x^2 \rangle}$	$\sqrt{\langle \theta_y^2 \rangle}$	σ_p/p
(GeV)			(GeV/c)	(GeV/c)	(mrad)	(mrad)	(%)
-250	.954 \pm .006	.0419 \pm .0018	239.0	238.0	.16	.20	8.7
-200	.939 \pm .009	.0486 \pm .0018	194.0	194.6	.15	.20	9.2
-165	.915 \pm .009	.0615 \pm .0019	164.3	165.3	.13	.20	9.5
-140	.891 \pm .012	.0647 \pm .0025	137.8	138.9	.15	.21	9.4
-120	.881 \pm .014	.0600 \pm .0032	118.4	119.6	.16	.23	9.7
+120	.529 \pm .022	.0545 \pm .0033	119.5	122.4	.16	.23	10.1
+140	.424 \pm .014	.0485 \pm .0024	139.2	142.2	.15	.21	9.9
+165	.313 \pm .012	.0388 \pm .0018	166.3	169.8	.13	.20	10.0
+200	.193 \pm .007	.0263 \pm .0013	197.0	200.6	.15	.20	9.6
+250	.0773 \pm .0027	.0124 \pm .0007	243.8	247.0	.16	.20	9.4

Table 2.9. Particle fractions, momenta and dispersions

In this chapter we shall discuss how data from the monitoring devices is actually used, and how the final flux and various backgrounds are parametrized.

§3.1 WBB Parametrization

At every momentum setting, some beam time was spent on accumulating data with a slit in the secondary beam closed. The slit is prior to magnets D4 and D5 (fig.1) and consequently the only neutrinos that can then reach Lab E are those that arise from large angle hadron decays or from decays of hadrons themselves at large angles. This background is thus primarily a low energy neutrino source and is known as the wide band background. Since the background is negligible except at low energies, an easy way to parametrize it is simply to count the number of events as a function of energy and radius at Lab E, and use the neutrino cross-section⁽⁸⁾ to obtain the flux. Any systematic errors introduced by this technique are bound to be small (< ~ 1%), in any case much smaller than the statistical error.

We assume that the background uniformly illuminates the detector at Lab E, and that the background is the same for all negative energy settings. Since the beam dumping depends on proton fraction, the background is estimated separately for positive settings but all the negative energy settings are lumped together. Also, since bare target beam fluxes go through a peak⁽¹²⁾ at a low energy (approx. 15 GeV in our case), a form for the flux that peaks at a low energy is assumed. We use the form

$$f(E) = \begin{cases} (1 - e^{-E/E_0}) & E \leq b \\ (1 - e^{-E/E_0})e^{-(E-b)/c} & E \geq b \end{cases} \quad (3.1)$$

The number of neutrino events in the energy range $[E, E + dE]$, $N(E)dE$, is given by

$$N(E)dE = k f(E) dE A n d \sigma(E) \quad (3.2)$$

where,

- A = the area in which events are counted
- nd = the number of nucleons per unit area of the target
- $\sigma(E)$ = the assumed neutrino (or antineutrino) cross-section
- k = the overall normalization (varies with energy setting)

Thus, integrating over energy for a given energy setting,

$$\begin{aligned}
 N &= \int N(E)dE \\
 &= k \left\{ \int f(E)\sigma(E)dE \right\} 5361.8 \times 6.0221 \times 10^{23} \times 10^{-38} \times (\pi 50^2)
 \end{aligned}
 \tag{3.3}$$

where

$$\sigma(E) = \begin{cases} 0.669E (\nu) \\ 0.340E (\bar{\nu}) \end{cases} \quad E \text{ in GeV.}$$

5361.8 is the target density for the fiducial volume used in gm/cm^2 . The fiducial volume is cylindrical with a radius of 50 in . The above equation can now be solved for k , giving

$$k = \frac{N}{\int f(E)\sigma(E)dE} 3.9432 \times 10^6
 \tag{3.4}$$

Hence, we first find E_0 , b and c by fitting the energy distribution of wide band background events and then evaluate k . k must be normalized to the number of protons on target so that this parameter can be used for real open slit data correction. The final values for k are then normalized to 10^9 secondary beam particles. The constants k , E_0 , b and c are tabulated below.

$E_{SET}(\text{GeV})$	k	E_0	b	c
-250	74.72	17.47	12.96	12.63
-200	26.98	17.47	12.96	12.63
-165	18.88	17.47	12.96	12.63
-140	13.68	17.47	12.96	12.63
-120	11.48	17.47	12.96	12.63
+120	4.961	1.18	7.36	21.01
+140	3.668	1.20	8.15	14.68
+165	2.502	0.89	8.07	21.81
+200	2.722	1.78	9.87	19.26
+250	1.603	1.32	7.50	22.97

Table 3.1. Wide band background constants.

§3.2 Beam Centering and Other Cuts

During the E616 run, a constant effort was made to ensure that the beam centre coincided with the centre of the apparatus. The strictest off-line cut was a requirement that the fractional difference between the two split plates in the manhole ion chamber not exceed 0.1 for open slit data. This corresponds to a 1.2 in deviation from the nominal centre at Lab E. Pulses of very low intensity were also thrown out. If either the expansion port or the manhole ion chamber disagreed with the rest of the flux monitors for a run, that run was discarded. The digitizers for the ion chambers were calibrated pulse by pulse with a fixed current being fed in for 3 different lengths of time. The calibration constant and pedestal used were derived from a running average using all previous pulses, most recent pulses being weighted the most. Finally, the calibration corrected sum of ion chamber response for each run was written out on to a file for analysis use.

The spark chambers in Lab E had a recovery time in tens of milliseconds, during which the apparatus was 'dead' for any possible additional events. The flux was measured for the duration of the 'live' periods by sending a pulse on a fast cable to the monitor electronics. Checks have been made on this procedure e.g., it was checked that the trigger rates during livetime and deadtime were equal.

§3.3 The Beam Monte Carlo

All the information extracted from the monitors was used to generate flux distributions at Lab E. We first use a program to generate rays of pions and kaons before the decay pipe using a production model⁽⁸⁾ at the target. Another program then 'decays' these rays using the measured particle fractions, angular dispersion and beam centre. The beam centre is measured by averaging the position of high energy pions at Lab E (since they are wholly contained). After producing all two and three body decays using the beam kinematics described in appendix A, distributions at Lab E are binned in 5 in radial bins around the beam centre. Calculated in each bin are the total flux in the bin, the error on the flux, the mean neutrino energy and its error, separately for pions and kaons. Figure 3.1 shows the resulting flux distributions at Lab E for 1000,000 secondaries in the decay pipe.

§3.4 Flux Parametrization

To use the fluxes for analysis, it is necessary to have a fast function that returns the flux in a specified energy interval at a given radius at Lab E. Since the radial bins used are small (5 in), the exact form of fluxes within a bin is unimportant. A form $a - br^2$ was used for the flux distribution and $E_0/(1 + b^2r^2)$ for the energy distribution. The total flux within a bin and the average energy were normalized to the beam Monte Carlo output mentioned in the previous section. Two checks on the entire procedure were made. Firstly, the flux thus generated was combined with finer binned higher statistics output from the beam Monte Carlo

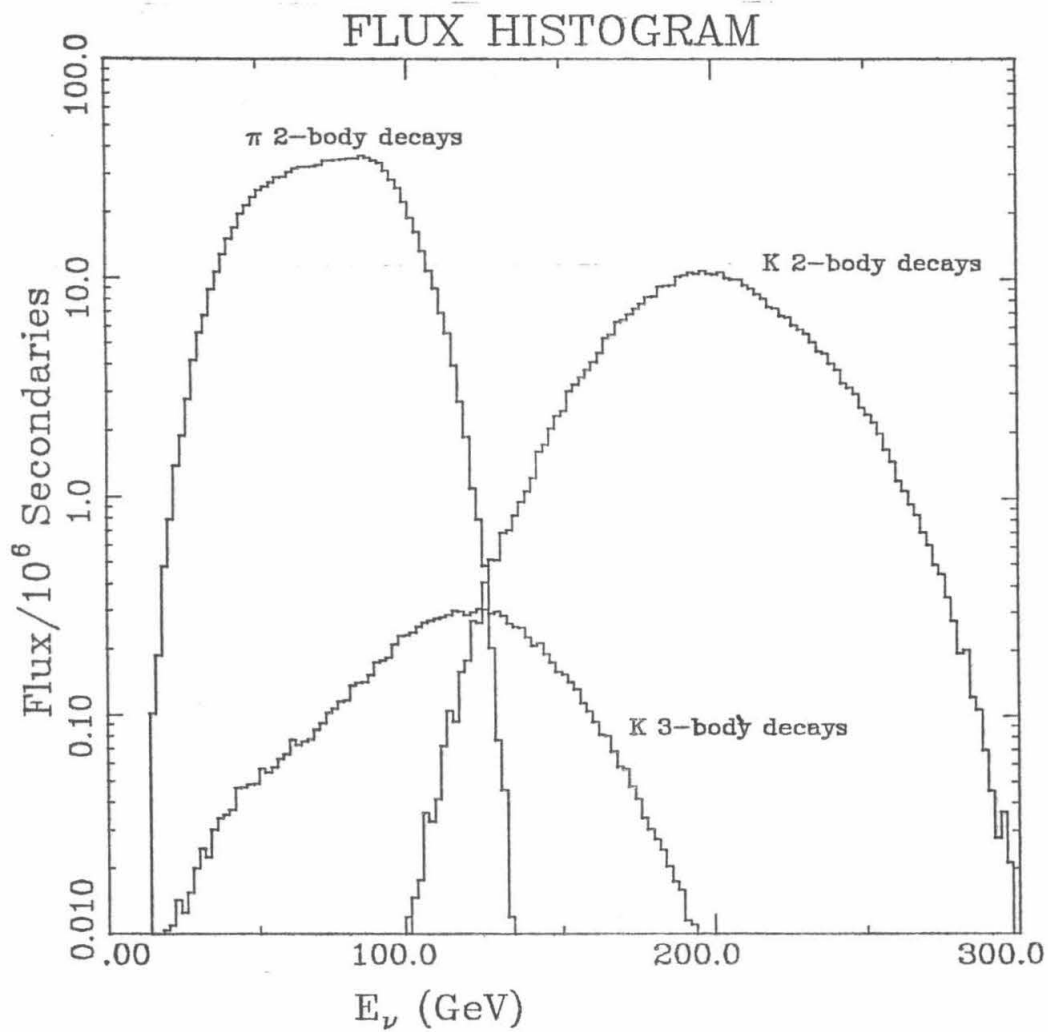


Figure 3.1. Flux distribution for 1000,000 secondaries at 250 GeV

at one energy setting. Also, the entire structure function analysis was done with the latter. No significant differences were found.

The Lab E Detector

§4.1 Requirements

1.1 km downstream of the decay pipe is a 1000 metric ton detector, roughly 60% of which serves as the target for the neutrinos. Any neutrino detector must necessarily be massive, given the small cross section of the neutrino-nucleon interaction. The neutrino can only interact with quarks in the nucleon through the W^\pm or Z^0 as shown in figure 1.1. Only the charged current interactions are studied in this thesis, and thus there is always a muon in the final state. The detector must therefore be capable of measuring both the hadron shower energy and the momentum of the muon. Therefore the target steel is part of a calorimeter, with scintillation counters sandwiched between steel plates. To measure the momentum of the muons there is a toroid magnet spectrometer downstream of the target equipped with spark chambers. The vast majority of muons have sufficient energy to penetrate the entire spectrometer. The angle of the muon at the interaction vertex is measured by spark chambers in the target. The calorimeter counters double as trigger counters with the system of triggering designed to accommodate almost all charged and neutral current events. The enormous quantities of information produced in every event necessitate an on-line data acquisition system that writes all the data onto magnetic tape.

§4.2 Layout, Fiducial Volume and Alignment

A schematic diagram of Lab E appears in fig. 4.1. The target and toroid sections are clearly separated. The target consists of six carts on rollers. Each contains 14 counters and 6 spark chambers. The mean separation between counters is 8.16 in and that between chambers 18.79 in. Counters were separated by two steel plates (2.01 in \times 10 ft \times 10 ft) and chambers by four. The toroidal magnet consists of 3 toroids. Each of these three is further divided into two half-toroids which have a set of chambers covering their downstream ends. Each half-toroid

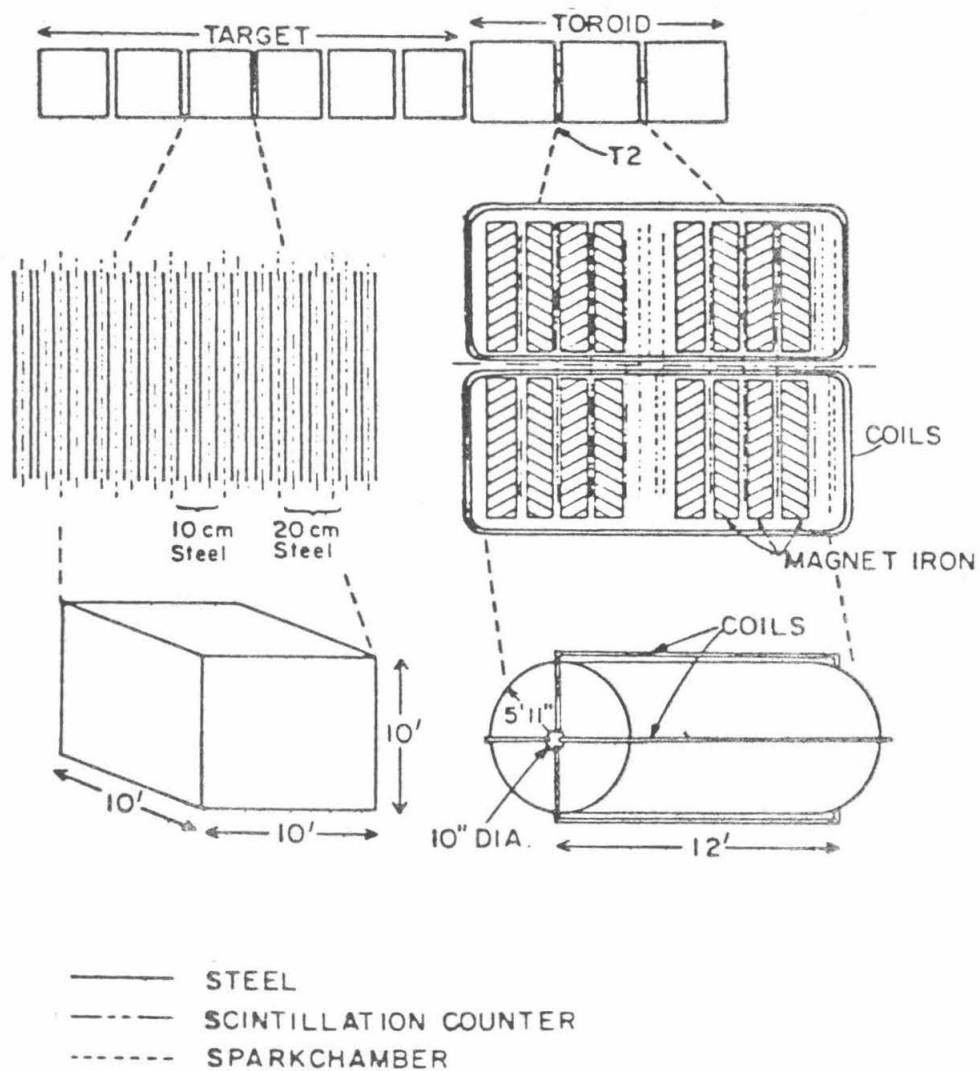


Figure 4.1. The Lab E detector

is itself made of 4 segments equipped with a counter each. Coils go in close to the axis of the toroid and generate a toroidal field averaging approximately 17kG.

For reasons appearing below, the fiducial volume is restricted to the region between the 3rd and the 63rd counters (counting downstream). Meticulous counting of all intervening matter leads to a target thickness of 5361.8 gm/cm^2 . This includes the steel plates, counters (6.5%) and chambers (0.8%).

For accurate physics analysis the longitudinal and transverse positions of the counters and chambers must be well known. Alignment is first done optically, using a theodolite which leads to measurements good to .01 in. This is good enough for the z -positions of the chambers (the Lab E coordinate system has z increasing downstream, y increasing upwards). Translating the transverse position of a chamber as measured from outside into the position of a spark inside involves uncertainty much larger than the intrinsic resolution of a chamber ($\sim 1/2$ mm). The sparks themselves must be used for chamber alignment. This is done by utilizing muons produced upstream of Lab E and going right through it as reference straight lines.

§4.3 Spark Chambers

There were two sizes of spark chambers in Lab E: 10 ft \times 10 ft chambers in the target and 5 ft \times 10 ft chambers in the toroid carts and in the gaps between toroids. Two 5 ft \times 10 ft chambers with a slight overlap made up a single spark plane in the toroids. The chambers had wires spaced a little less than 1 mm apart in both transverse directions. Chambers were pulsed on a trigger with a voltage of ~ 6.5 kV. Sparks occurred where ionization had been produced in the chamber gas and currents in the nearest wires were caused. These currents in turn caused an acoustic pulse in the magnetostrictive wire laid perpendicular to the wires (see fig. 4.2). At the time the chamber is pulsed, two fiducial pulses are generated in each wire to serve as reference marks. The time taken by an acoustic pulse travelling at $\sim 5 \text{ mm}/\mu\text{s}$ with reference to the fiducial pulses was measured by a 20MHz clock. The pulses have a peak at the spark position and were differentiated to improve centre finding. Up to 16 sparks per chamber per direction could be measured in this way.

The gas circulated through the chambers was about 89% Ne, 10% He and 1% $\text{C}_2\text{H}_5\text{OH}$. Purity of the gas was maintained at all times by a purifier that removed contaminants (mainly N_2 and O_2) by condensing them out of the system using liquid nitrogen temperatures.

While the dead time of Lab E depended in part on the data taking of the computer ($\sim 20 \text{ ms}$), it was determined mainly by the spark chambers. The 5 ft \times 10 ft chambers for example, had a HV recharge time of $\sim 6 \text{ ms}$. More importantly, clearing fields were applied to all chambers to clear ions after a spark discharge. The DC field on the target chambers was 90V, the toroid chambers used 30V. In addition a $\sim 600 \text{ V}$ pulse clearing field of $\sim 10 \text{ msec}$ duration was applied. The memory time due to these fields was reduced to $\sim 30 \text{ ms}$.

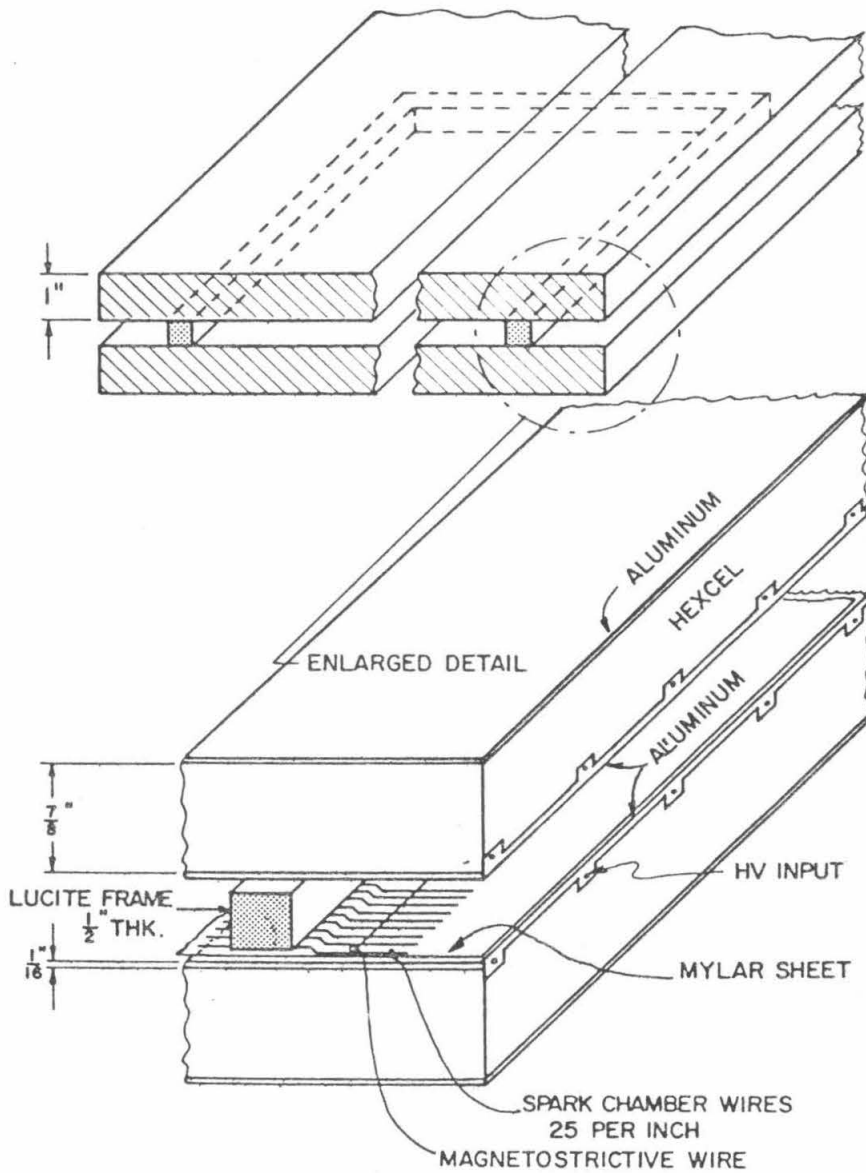


Figure 4.2. A spark chamber

§4.4 Scintillation Counters

As with spark chambers, the counters come in two kinds: liquid scintillation counters for the target and acrylic scintillation counters for the toroids. The target counters are 10 ft \times 10 ft \times 1 in in size. Mixed with the liquid scintillator is wavelength shifter which converts the UV light produced into blue light. From each corner to the middle of the two corresponding sides are shifter bars (see fig. 4.3) which serve to 'shift' the wavelength of light further to green and to collect the light for detection by a phototube at the corner. Wavelength shifter is necessary to reduce attenuation. There is an air gap between the bars and the counter to increase the total internal reflection of light on its way to the phototube. The toroid counters have the more complex arrangement with a total of 10 phototubes and 14 shifter bars per plane. As explained in chapter 5, the toroid counters were not used for hadron energy measurements and we will therefore concentrate on the target counters.

The output from the phototubes for a minimum ionizing particle is a function of several variables. It depends on where through the counter the particle went, which counter it went through and when during the 8-month run this happened. Variation with real time over the course of the experiment was essentially a deterioration in counter gain of $\sim 2.5\%$ as measured by pulse heights from muons. Counter to counter gain variations were removed by requiring the mean hadron energy for events to be independent of counter location. To correct for an imbalance in the gains of the four phototubes for each counter, light from spark gaps was carried to the centre of each counter by light fibres. Phototube voltages could thus be adjusted periodically to get equal gains for all the tubes.

By far the most important effect to account for is the variation of output with position. The important physical effects are attenuation of light in the counter, transmission across the air gap and attenuation in the shifter bar. The transmission across the gap is a function of two angles: θ , with respect to the plane of the counter and ϕ , from the normal to the bar (see fig. 4.4). Because of multiple internal reflections, one can integrate over θ to get

$$T(\phi) = \int_{\theta} T(\phi, \theta) d\theta,$$

an 'averaged' transmission coefficient for every ϕ . Now one considers all possible light paths into a given shifter bar. For the subset of paths between AD and AB for example, the path length for a given path characterized by an angle ϕ is $AC/\cos\phi$. One thus divides up all possibilities into distinct groups of ϕ allowed by lack of total internal reflection. Reflected light paths such as AED are accounted for by extending the shifter bar BG to GB'. In each segment an average $\cos\phi$ is calculated from tables of $\int_0^{\phi} T(\phi) d\phi$ and $\int_0^{\phi} \cos\phi T(\phi) d\phi$. A factor $e^{-AC/\langle\cos\phi\rangle\lambda_x}$ and a similar one for λ_y combine to give

$$\exp(-((x_i - x_0)^2/\lambda_x^2 \langle\cos\phi_{ix}\rangle^2 + (y_i - y_0)^2/\lambda_y^2 \langle\cos\phi_{iy}\rangle^2)^{1/2})$$

for the i^{th} segment. An additional exponential $\exp(-r_i/\lambda_{bar})$ is inserted for attenuation in the bar. λ_{bar} turns out to be large and the maps are insensitive to it, so it is fixed at a mean nominal value of 115 in. λ_x and λ_y are parameters to be determined experimentally for each

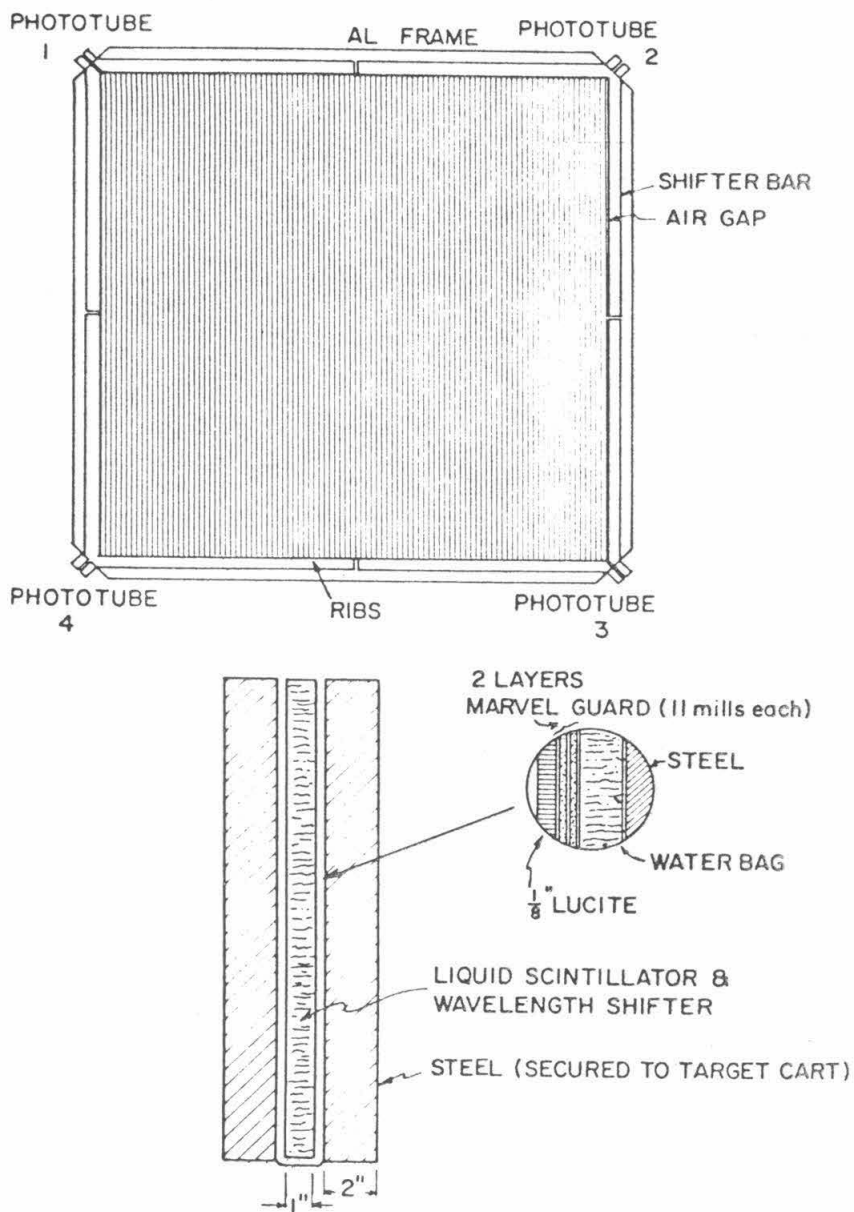


Figure 4.9. A target scintillation counter

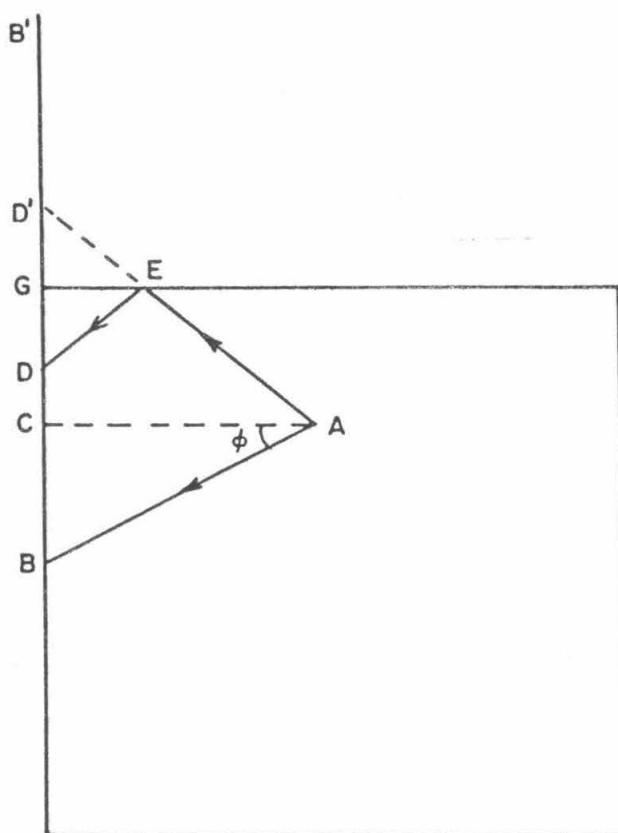


Figure 4.4. Target counter light paths

counter, as are x_0 and y_0 . Almost all x_0, y_0 are less than 3 in from the centre of the counter and $\lambda_x, \lambda_y \approx 70$ in. Fits to the physical model were done using hadron showers, their mean position determined by the spark chambers; χ^2 minimization is used.

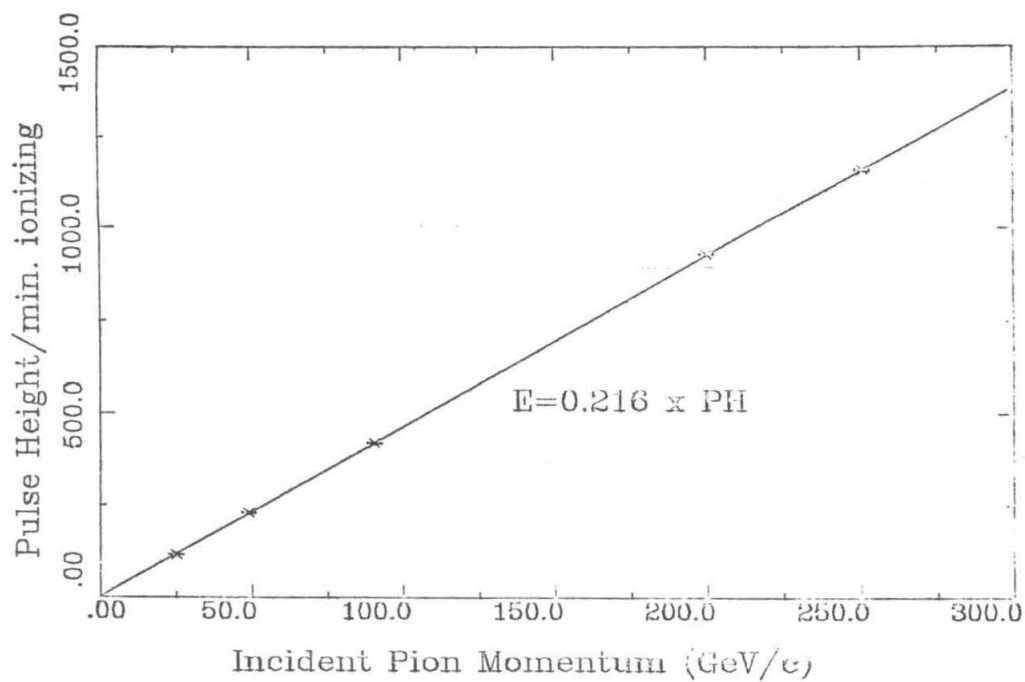


Figure 4.5. Calibration: E_h vs. pulse height sum

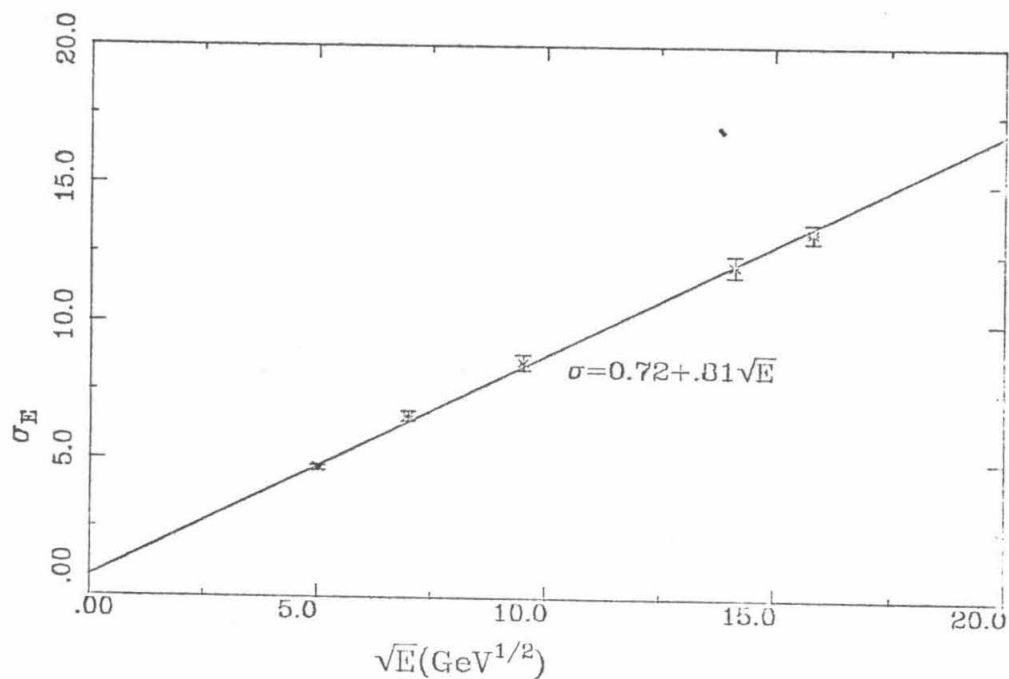


Figure 4.6. Calibration: σ_{E_h} vs. $\sqrt{E_h}$

§4.5 E_{HAD} Calibration

It is possible to move the target in Lab E so that another beam, the N5 hadron beam, goes through it. We ran a beam of incident pions through at 5 different energy settings: 25GeV/c, 50GeV/c, 90GeV/c, 200GeV/c and 250GeV/c. Means and sigmas for the hadron energy were determined at each energy setting. The best fit gave

$$E_h = (0.2157 \pm 0.0006) GeV \times (\text{pulse height in shower in terms of min. ionizing})$$

$$\text{and } \sigma_{E_h} = (0.72 \pm 0.20) + (0.81 \pm 0.03) \sqrt{E_h}$$

(see figs. 4.5 and 4.6).

§4.6 Electronics

The output of every counter is used for two purposes: triggering and shower energy measurement. To cover the whole range of energies possible, ADCs of different ranges were used. The output of each tube went to a "low" ADC, the sum of the 4 target tubes in a counter to a "high", and a combination of various tubes to a "superlow". The highs saturated very fast and are used for minimum ionizing muons; the lows for pulse height measurements. If a low saturated, the pulse height for that tube could be extracted using the superlows (see fig. 4.7).

§4.7 Triggers

The apparatus is designed to trigger on charged current events, neutral current events and straight throughs. Neutral currents do not concern us. The straight throughs are triggered by muons that enter Lab E, fire the wall of veto counters, T2 and T3 (see fig. 4.1). The veto may at times fail; a fiducial cut at 80 counters eliminates such spurious events.

The triggers that are most relevant are the two charged current triggers - trig.1 (muon trigger) and trig.3 (penetration trigger). The logic for these events is shown in figs. 4.8 and 4.9. Essentially, the muon trigger is meant for those events in which the muon is produced at a small angle such that the muon passes through enough of the toroid for its momentum to be measurable. The penetration trigger tries to cover the rest of the charged current events while maintaining a significant amount of overlap with the muon trigger. It requires the muon to penetrate at least 16 counters and has a modest energy requirement of 4 GeV to eliminate cosmic ray muons. The muon trigger requires that the muon originate in the target and fire either T2 or T3. The two triggers use independent logic and independent counters, thus allowing for constant monitoring of efficiencies in the overlap region.

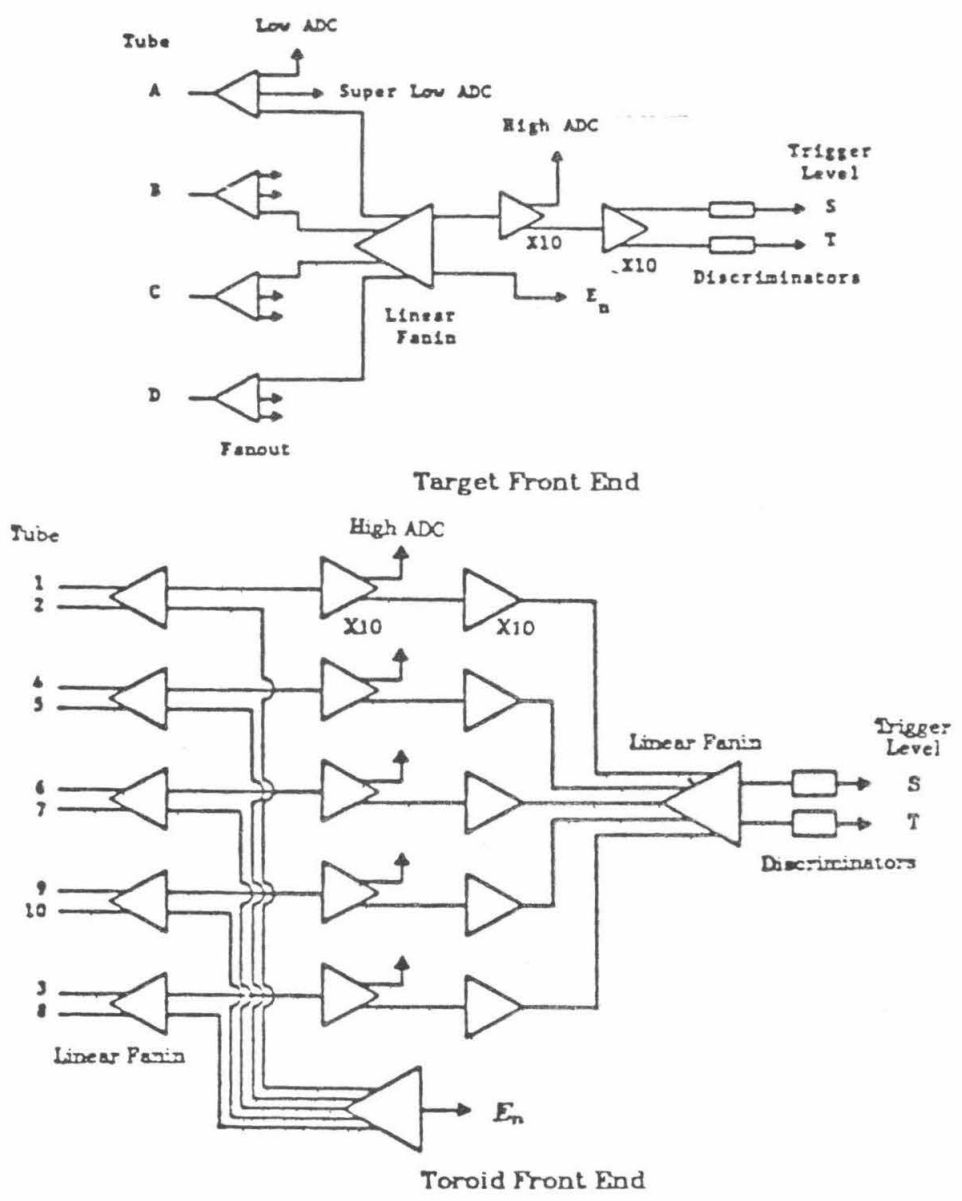


Figure 4.7. Target and toroid front end electronics

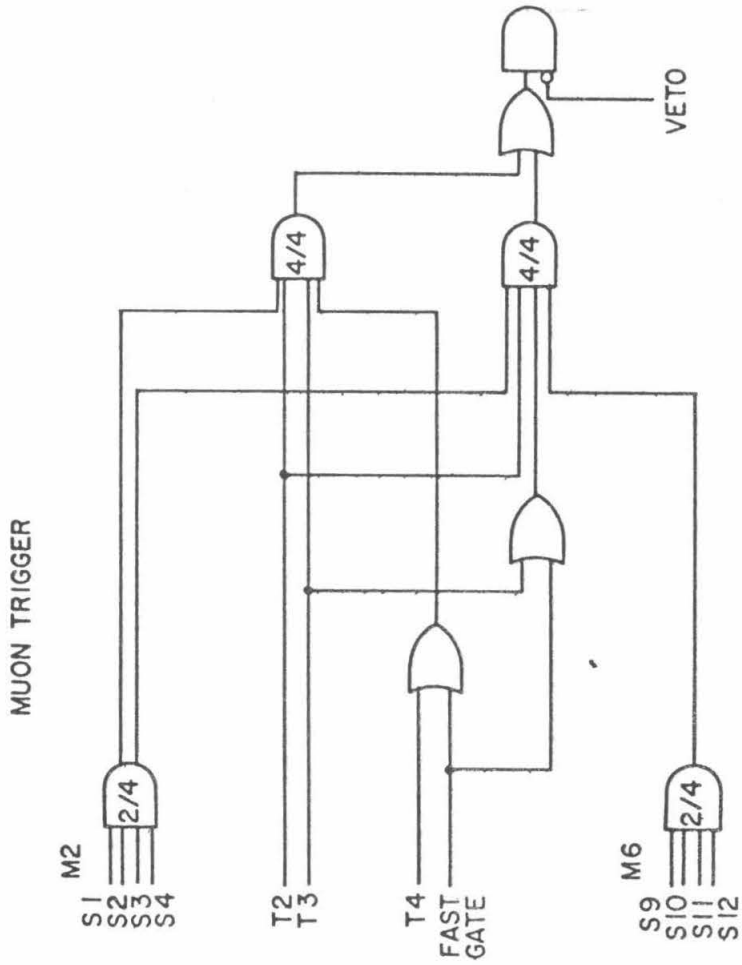


Figure 4.8. Muon trigger logic

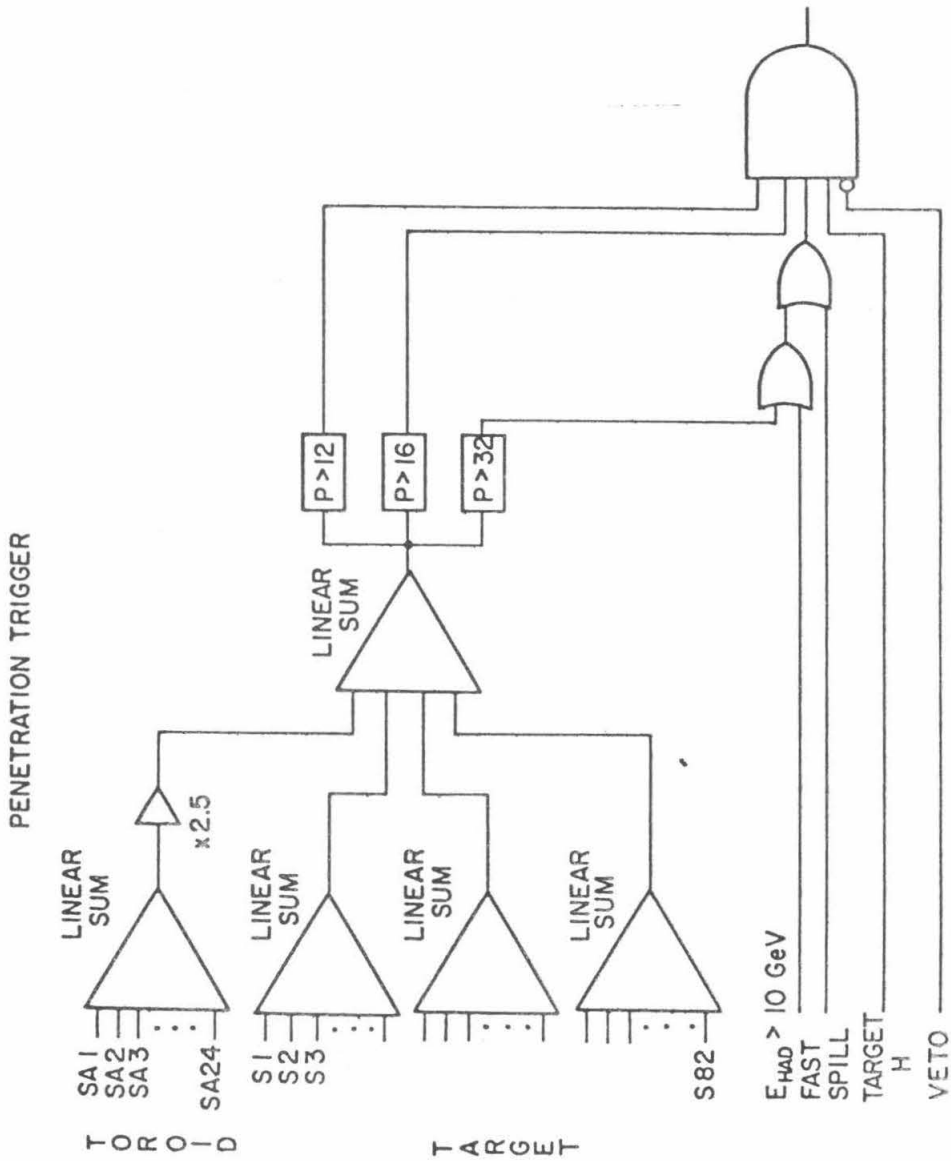


Figure 4.9. Penetration trigger logic

Event Analysis

The kinematics for a charged current event are described in detail in Appendix B. From that discussion it is clear that there are three independent variables which can be measured; they are the energy of the hadron shower, the energy of the muon at the event vertex and the angle the muon makes with the incident neutrino direction. It is possible to measure the mean angle of the hadron shower instead of the muon angle; for reasons cited below this was not attempted.

Shown in fig. 5.1 is a typical muon trigger event. To analyze this event one must identify the first and last counter where the hadron shower is detected, recognize the muon track beyond the shower and track it through the magnetized toroids. To get the muon angle at the vertex, the track must be followed backwards through the shower using a multiple scattering matrix technique described below.

§5.1 E_μ

The software for finding the muon momentum is by far the most complicated part of the analysis of this experiment. A crude vertex position is determined by a routine that picks up most of the sparks near the vertex and does a simple linear fit. Next, sparks from both wands on all the chambers are decoded and converted into position measurements. A least squares fit is then done using chambers in the target with only one spark. Now that a reasonable vertex position is known, we search for tracks by looking in angular bins away from the vertex for a cluster of sparks. Sparks are thus assigned to probable track candidates. Bad sparks are then eliminated if they lie outside a window determined from the spark scatter of a least squares fit. The longest track thus found is used to obtain a better vertex position and the whole procedure is then repeated. At this point bad sparks are removed and then an attempt is made to correlate tracks in the x and y views, if there are more than one in any, by correlating chamber hits. By now the track in the target is well established and only the problems of recognition in the toroid and momentum determination remain.

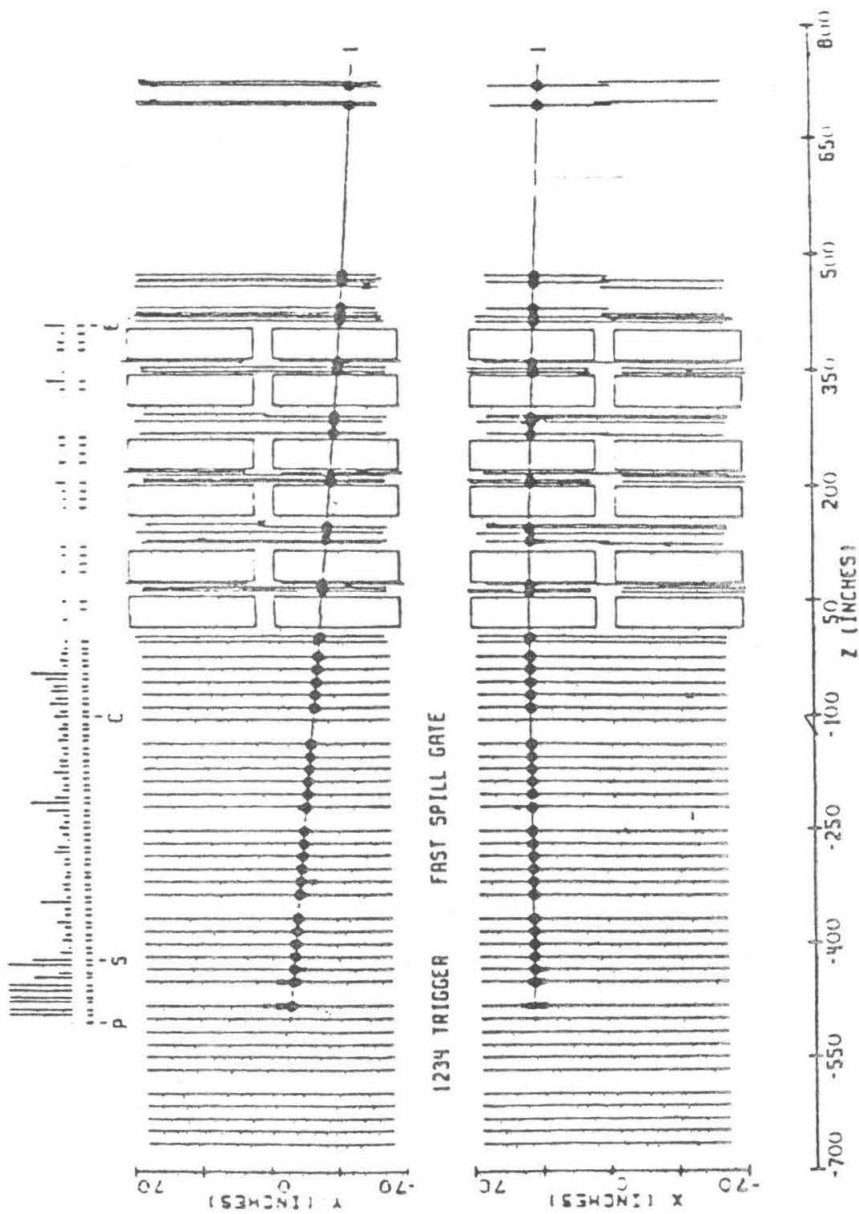


Figure 5.1. A muon trigger event.

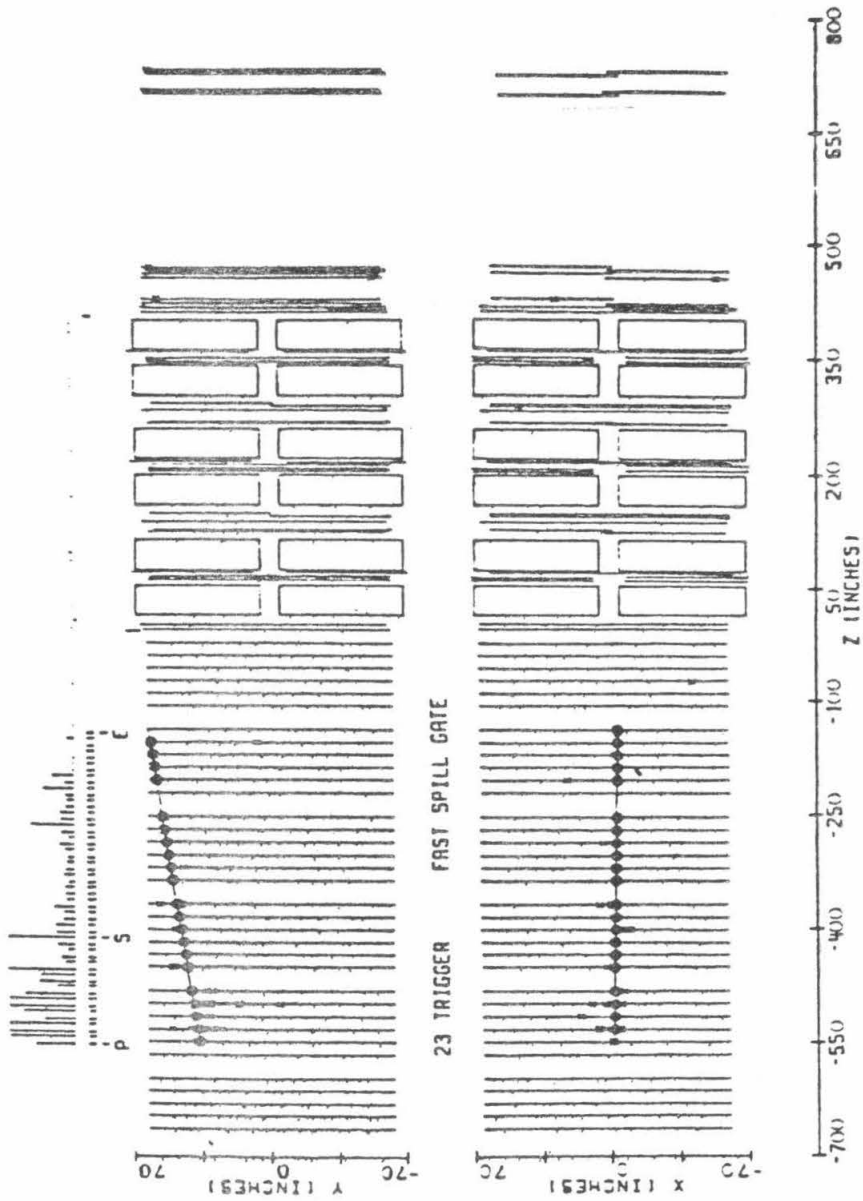


Figure 5.2. A penetration trigger event.

Sparks are picked up in the toroid by trying to follow the principal target track into the toroid. Of course, this is impossible unless the vector momentum \mathbf{p} is known. Neglecting multiple scattering and energy loss and assuming small angles with the beam direction it can be shown however that

$$r^2 \frac{d\phi}{dz} = \text{constant}, \quad (5.1)$$

where we use cylindrical polar coordinates around the beam direction. This follows from the toroidal nature of the magnetic field, $\mathbf{B} = B(r)\hat{\phi}$ and the equation of motion. Actually the iron in the magnet is fairly saturated, so $B(r)$ is a weak function of r ; this does not affect the result (5.1) above in any significant way.

Using sparks thus found a preliminary estimate of momentum may be obtained. This momentum is used to treat errors due to multiple scattering correctly and a still better estimate of the momentum is obtained. It is now time for the final fit.

Three major processes affect the muon as it traverses the apparatus. Energy is lost due to the usual dE/dx losses at the rate, very roughly, of about 11.6 MeV/cm of steel. It is straightforward to account for this effect and the action of the magnetic field. At the same time the particle undergoes multiple scatterings from nuclei leading to a small, random, uncalculable contribution to its path. As is common in all such random walk problems⁽²⁰⁾ the most probable path remains the one without the scattering but the root mean square deviation from it is proportional to the square root of time. Consider the element shown in fig.5.3. It is possible to show⁽²¹⁾, for small angles, that $\langle \theta^2 \rangle \sim L/|p|^2$; in fact, for the projection on to a plane,

$$\sqrt{\langle \theta^2 \rangle} \approx \frac{.015}{|p|} \sqrt{\frac{L}{L_{RAD}}} = \sigma_0 \quad (\text{say}) \quad (5.2)$$

where p is the muon momentum and L_{RAD} , the radiation length in steel (=1.76cm). Also,

$$\langle \theta \delta \rangle = \frac{L}{2} \sigma_0^2 \quad (5.3)$$

$$\langle \theta d \rangle = 0 \quad (5.4)$$

$$\langle \delta^2 \rangle = \frac{L^2}{3} \sigma_0^2 \quad (5.5)$$

$$\text{and} \quad \langle d^2 \rangle = \frac{L^2}{12} \sigma_0^2 \quad (5.6)$$

Thus, to parametrize multiple scattering in any one view, two variables such as θ and d are needed. It would seem that given two planes of perfect spark chambers before and after a 'scattering centre' it would be possible to determine these two variables exactly in both views and thus efficiently parametrize the track. This is true but for the magnetic field. We consider the entire target to be divided into 12 scattering centres (6 in the cart closest to the toroid, 2 in the next, 1 each in the rest) and each half-toroid a scattering centre as well.

Let s_x be the slope in the x-view, x_0 the intercept at z_0 , z_i the position of the i^{th} scattering centre, p_i the multiple scattering momentum kick, q_i the momentum kick due to the

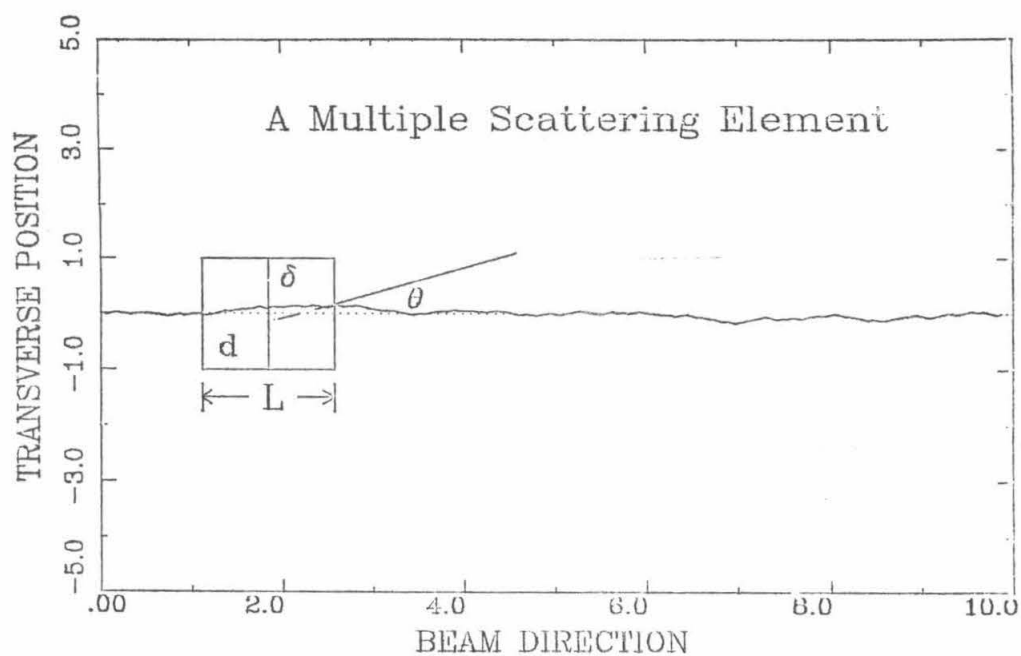


Figure 5.3. A multiple scattering element.

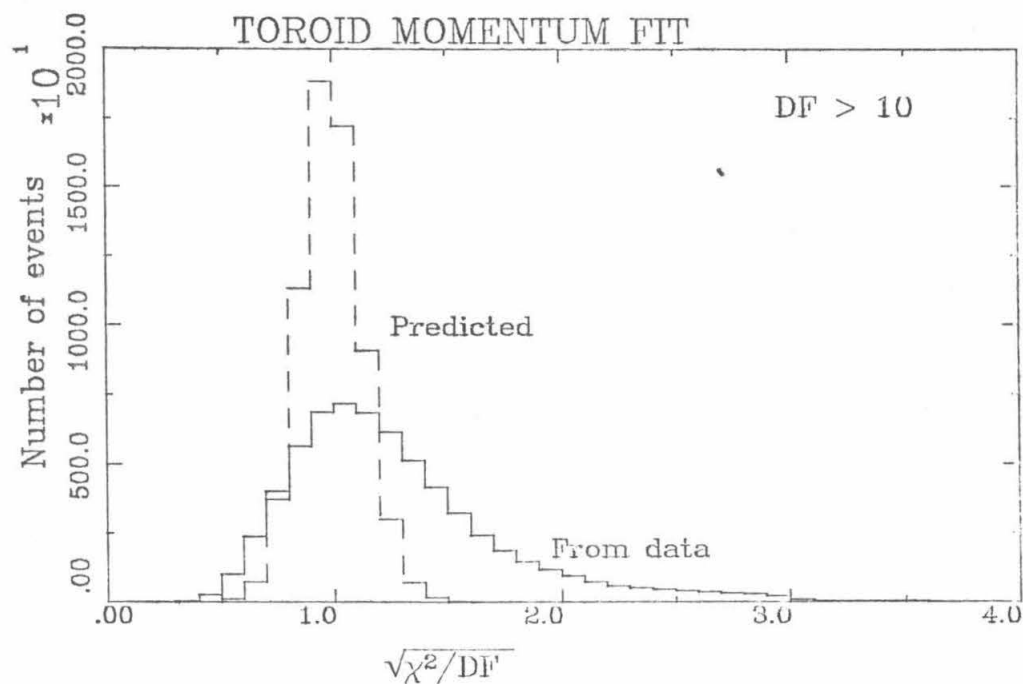


Figure 5.4. χ^2 in the toroids.

magnetic field and x_i the displacement (either d or δ above). Then if p is the momentum of the muon,

$$x_i = x_0 + s_x(z_i - z_0) + \sum_j (z_i - z_j) \frac{p_i}{|p|} L_{ij} + \sum_k x_k L_{ik} + \sum_l (z_i - z_l) \frac{p_l}{|p|} L_{il} \quad (5.7)$$

$$\begin{aligned} L_{ij} &= 0 & i < j, \\ &= 1 & i \geq j. \end{aligned}$$

The unknown parameters are $|p|$, x_0 , s_x , p_i and x_k . The p_i are known almost exactly if we know the path in the magnets well. The problem is a linear least squares one except for $|p|$; we use an old guess for $1/|p|$ and solve that part iteratively⁽²²⁾. To form the error matrix $\langle x_i x_j \rangle$ we use the expressions (5.2) through (5.6) above. The technique works very well, at least to trace the muon path, i.e., eliminate bad sparks, obtain the p_i and x_i and get a good estimate of the momentum. As $1/|p|$ was varied to minimize χ^2 , the other parameters were varied as well. This led to a small bias in the momentum which was corrected by an unbiased routine that merely fit slopes, intercepts and momentum. Appendix D describes some of the mathematical machinery of multiple scattering fits.

A χ^2 distribution that results is shown in fig.5.4. This distribution is for all the events that pass our structure function extraction cuts (about 68000). While the peak is at 1. as it should, the distribution has a long tail on the high side which arises partly from a weak dependence of the mean χ^2 on the number of degrees of freedom and mainly from a few bad sparks.

The deflection due to a uniform magnetic field B (kG) after the muon traverses a distance d (cm) is given by

$$\theta = \frac{0.3Bd}{p} \quad (5.8)$$

where the momentum p is in MeV/c.

$$(5.8) \text{ implies } \frac{\Delta p}{p} = \frac{-\Delta\theta}{\theta} \quad (5.9)$$

Combining (5.9), (5.8) and (5.2) gives⁽⁴³⁾

$$\frac{\Delta p}{p} = \frac{50}{B\sqrt{d}L_{RAD}} \approx 9\% \quad \text{for Lab E.} \quad (5.10)$$

Spark chamber efficiencies, spark position resolution and non-uniformities in B actually make $\Delta p/p$ closer to 12%.

Some small fraction of muons do not go through the magnet but range out due to energy loss. Their momentum is determined from their range to about 0.4 GeV, which is much

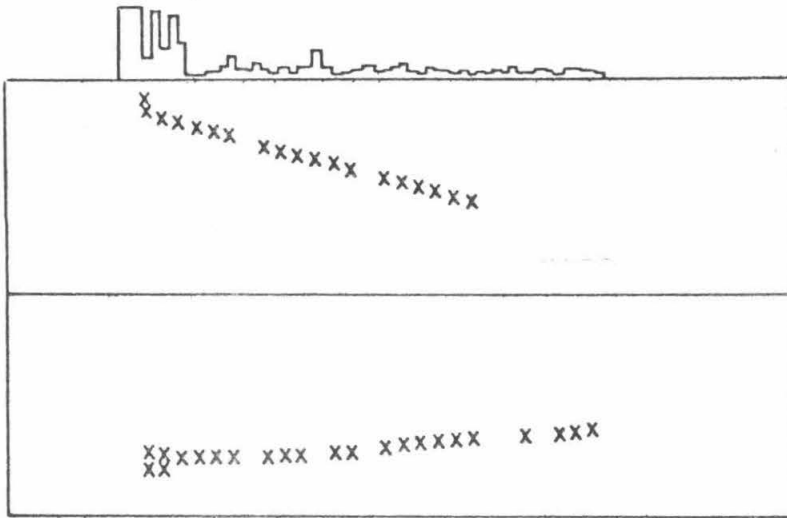


Figure 5.5

A range-out event. Shown are the sparks in two views and the counter pulse heights. The target ends at the right edge of the views. Notice the absence of counter pulse heights at the downstream end.

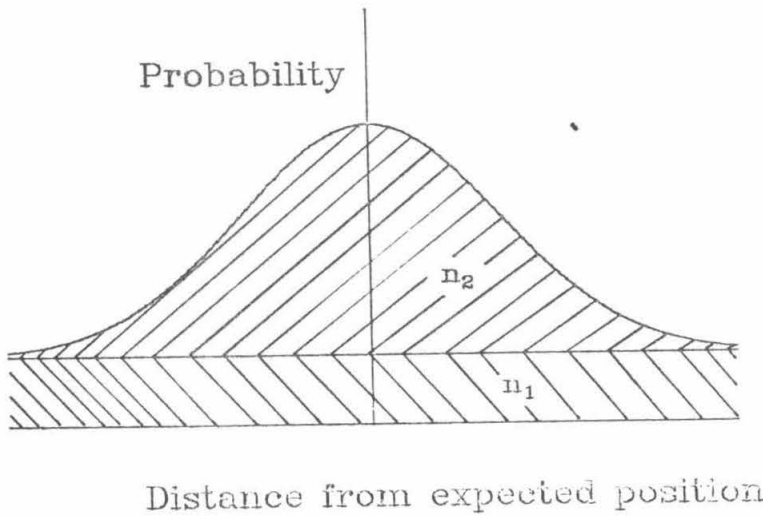


Figure 5.6

Spark distribution near vertex.

better than 12%. These muons are easily identifiable as their tracks stop in the apparatus (chambers that should have sparks do not) and a string of counters with minimum ionizing pulse heights comes to an end at the same spot. A sample 'range-out' event is shown in figure 5.5.

The muons may also suffer small-angle collisions in which they lose significant amounts of energy due to deep inelastic scattering, high energy δ -rays or bremsstrahlung before their momentum is measured in the toroids. Using an algorithm based on the observed distribution of energy loss by the muons in the counters, any set of contiguous counters with an excessive deposition of energy is identified and that energy is added to the muon energy. Effects due to such losses within the shower and hence indistinguishable from it are removed by a Monte Carlo simulation of the effect. Listed in tables 5.1 and 5.2 below is the magnitude of such losses in the form of the *cumulative* probability of energy loss for a given energy muon.

Loss	$0 < E_\mu < 20$	$20 < E_\mu < 40$	$40 < E_\mu < 60$	$60 < E_\mu < 80$	$80 < E_\mu < 100$	$100 < E_\mu < 120$
Range						
(GeV)						
0-2	9.172	27.359	39.270	49.552	55.218	62.789
2-4	4.855	18.100	29.374	38.575	43.072	50.442
4-6	0.875	6.995	14.698	22.377	25.455	28.152
6-8	0.159	3.047	8.631	15.004	18.005	18.351
8-10	0.020	1.202	5.299	11.306	13.775	12.635
10-12	0.000	0.468	3.266	8.333	10.283	9.848
12-14	0.000	0.203	1.893	6.367	8.537	7.879
14-16	0.000	0.070	0.963	4.915	7.140	6.582
16-18	0.000	0.049	0.541	3.581	5.821	5.573
18-20	0.000	0.042	0.260	2.411	4.812	4.804
20-22	0.000	0.021	0.184	1.779	4.346	4.083
22-24	0.000	0.000	0.119	1.147	3.686	3.363
24-26	0.000	0.000	0.065	0.585	3.027	2.930
26-28	0.000	0.000	0.065	0.351	2.328	2.498
28-30	0.000	0.000	0.065	0.164	1.863	2.306
30-32	0.000	0.000	0.043	0.140	1.203	2.210
32-34	0.000	0.000	0.022	0.047	0.621	1.922
34-36	0.000	0.000	0.022	0.023	0.427	1.681
36-38	0.000	0.000	0.022	0.023	0.116	1.537
38-40	0.000	0.000	0.022	0.023	0.116	1.153
40-42	0.000	0.000	0.022	0.023	0.039	0.865
42-44	0.000	0.000	0.011	0.023	0.039	0.769
44-46	0.000	0.000	0.011	0.023	0.039	0.528
46-48	0.000	0.000	0.000	0.023	0.000	0.240
48-50	0.000	0.000	0.000	0.023	0.000	0.096
50-52	0.000	0.000	0.000	0.023	0.000	0.048
52-54	0.000	0.000	0.000	0.023	0.000	0.048
54-56	0.000	0.000	0.000	0.023	0.000	0.000
56-58	0.000	0.000	0.000	0.023	0.000	0.000
58-60	0.000	0.000	0.000	0.023	0.000	0.000

Table 5.1

1000 times the cumulative energy loss probability per metre of steel: Part 1.

Loss	$120 < E_{\mu} < 140$	$140 < E_{\mu} < 160$	$160 < E_{\mu} < 180$	$180 < E_{\mu} < 200$	$200 < E_{\mu} < 220$	$220 < E_{\mu} < 240$
Range						
(GeV)						
0-2	70.963	77.594	81.518	87.047	91.010	85.652
2-4	58.117	65.118	68.428	77.491	79.023	75.919
4-6	35.198	41.460	48.081	54.223	58.158	58.399
6-8	23.767	27.691	35.510	39.888	39.956	52.559
8-10	16.411	20.235	27.475	28.670	33.296	43.799
10-12	12.280	16.356	22.550	21.814	25.749	39.906
12-14	8.941	13.693	18.273	18.282	21.754	35.040
14-16	7.074	10.726	15.163	15.789	19.534	31.146
16-18	6.225	9.357	13.219	14.127	17.758	29.200
18-20	5.150	8.292	10.886	12.673	16.870	23.360
20-22	4.131	7.227	9.850	11.011	15.094	22.386
22-24	3.395	5.782	9.202	10.180	14.206	19.466
24-26	2.660	5.097	8.554	9.141	13.762	18.493
26-28	2.207	4.640	7.776	8.310	12.431	16.546
28-30	2.037	4.032	6.869	7.271	11.543	14.600
30-32	1.754	3.880	6.480	6.440	10.655	12.653
32-34	1.471	3.652	5.702	5.402	9.767	12.653
34-36	1.245	3.119	4.795	4.986	9.767	10.707
36-38	1.075	2.663	3.629	4.363	9.323	9.733
38-40	0.905	1.978	3.240	3.947	8.879	7.787
40-42	0.792	1.674	2.722	3.740	8.879	5.840
42-44	0.679	1.598	2.333	3.324	7.103	4.867
44-46	0.679	1.521	1.944	2.285	6.215	3.893
46-48	0.566	1.217	1.814	1.870	6.215	2.920
48-50	0.453	1.141	1.685	1.662	4.883	1.947
50-52	0.340	0.989	1.555	1.454	4.440	1.947
52-54	0.283	0.989	1.296	1.247	4.440	0.973
54-56	0.113	0.761	0.778	1.039	3.996	0.973
56-58	0.000	0.456	0.778	0.623	2.664	0.973
58-60	0.000	0.304	0.259	0.208	1.332	0.000

Table 5.2

1000 times the cumulative energy loss probability per metre of steel: Part 2.

§5.2 θ_μ

The initial track finding and fitting in the target is described in the previous section, here we shall concentrate on extrapolation of the muon track upstream into the shower. 95% of the shower is typically contained in 70 to 100 cm of steel which means between 3 and 7 spark chambers. In order to extrapolate upstream into the shower, we first choose a best spark in each view and each chamber on the basis of closeness to the track. Sparks with bad second differences (kink in track at spark) are then thrown out, the window being twice the expected scatter from zero of the second difference. A regular multiple scattering fit is then done, again using (5.2) through (5.6) to obtain the error matrix. The procedure is considerably simpler than the toroid case because the momentum is now known and there is no magnetic field. The $z = 0$ plane is first taken to be the downstream-most chamber in the shower. Solving the χ^2 problem gives an expected position for the muon spark there in both views with an error, say σ_0 . Let the spark chamber resolution be s . Then the closest spark is picked up within a radius 2.8σ from the expected position, where $\sigma = \sqrt{\sigma_0^2 + s^2}$, the sigma for the probability of a real spark occurring in the neighbourhood of the predicted position. This procedure is repeated with $z = 0$ being the next upstream chamber and so on until the 'vertex' chamber is reached, if $E_{had} < 25$ GeV. If $25 \text{ GeV} < E_{had} < 100$ GeV we only go down to the 'vertex+1' chamber and if $100 \text{ GeV} < E_{had} < 200$ GeV only to 'vertex+2'. This energy dependent selection of chambers is due to the increase of background hadron sparks with hadron energy.

How did we arrive at the above criterion? Assume, for the sake of simplicity, that there is a uniform background of n_0 sparks per unit area due to the hadron shower. Then the distribution of sparks around the expected position will look like that in fig. 5.6. The probability of picking up a good spark is, approximately, the upper shaded area (n_2) and that of picking up a bad spark n_1 . n_1 can be determined by looking at large distances from zero. n_2 will not be one because of the 2.8σ cut and also because of spark chamber inefficiency. In table 5.3 we list n_1 and n_2 for different E_{had} ranges and at different distances from the vertex. The dotted line indicates that a cut was made when n_2/n_1 was less than 2. The multiple scattering fit also predicts the error on the space angle θ_μ . Clearly this should be proportional to $1/p$, and there may be a slight worsening of the error with an increase of E_{had} due to the higher probability of mistaking a hadron shower spark for a muon spark. Tabulated in table 5.4 are the coefficients a and b for a linear fit in different E_{had} ranges:

$$\sigma_\theta = a + \frac{b}{p} \quad (5.11)$$

a is indistinguishable from zero. As a rough summary, $\Delta\theta \approx 100/p_\mu$ mrad-GeV/c.

EHAD	Quantity	VTX	VTX+1	VTX+2	VTX+3	VTX+4	VTX+5	VTX+6	VTX+7
$0 < E_h < 10$	n_1/n	0.056	0.034	0.045	0.027				
	n_2/n	0.674	0.797	0.760	0.806	1.000			
$10 < E_h < 25$	n_1/n	0.119	0.061	0.047	0.046	0.026	0.000	0.081	0.000
	n_2/n	0.492	0.691	0.733	0.701	0.869	1.000	0.419	1.000
$25 < E_h < 50$	n_1/n	0.172	0.092	0.066	0.044	0.034	0.044	0.000	0.033
	n_2/n	0.261	0.558	0.654	0.676	0.742	0.725	1.000	0.867
$50 < E_h < 100$	n_1/n	0.159	0.125	0.075	0.056	0.056	0.049	0.026	0.014
	n_2/n	0.185	0.480	0.598	0.719	0.672	0.651	0.869	0.903
$100 < E_h < 200$	n_1/n	0.137	0.130	0.092	0.053	0.050	0.041	0.022	0.000
	n_2/n	0.127	0.206	0.513	0.664	0.728	0.813	0.887	1.000

Table 5.3. n_1 and n_2 in planes away from vertex. See fig. 5.6.

E_{HAD} Range (GeV)	a (mrad)	b (mrad-GeV/c)
$0 < E_h < 10$ GeV	.162	84.35
$10 < E_h < 25$ GeV	.257	80.25
$25 < E_h < 50$ GeV	.171	105.38
$50 < E_h < 100$ GeV	.171	106.23
$100 < E_h < 200$ GeV	.126	129.22
$200 < E_h < 400$ GeV	-.031	156.10

Table 5.4. Angular resolution fit parameters. See eqn. 5.11.

§5.3 E_{had}

A description of the counters and hadron energy calibration has been given in the previous chapter. Here we shall describe how the shower limits are located and how E_{had} is obtained. A software bit is set for all target counters if at least 2 out of the following 3 conditions are satisfied:

- (i) The hardware bit is on and the pulse height is > 3 times minimum ionizing.
- (ii) The pulse height is $>$ threshold.
- (iii) The 'high' pulse height is $>$ threshold.

Then we sweep all the counters starting from the downstream-most. Whenever the software bit is turned 'on' a new possible event is logged. When the bit turns 'off' in this sweeping process, the event is taken as beginning just before that particular counter if none of 3 counters upstream also have bits set. The first counter to fire in an event is designated 'PLACE', and the last, 'CEXIT'. If $(\text{CEXIT}-\text{PLACE}+1) \leq 5$, we define CEXIT to be also 'SHEND', the last counter to see shower particles. If not, another sweep is made from $(\text{PLACE}-1)$ to CEXIT. If the sweep ends at the second counter upstream of the toroids, SHEND is set to 2. Otherwise, if 3 successive downstream counters have pulse heights less than 4 times minimum ionizing (and 3 even further downstream have an average pulse height < 4 min. ionizing), that counter is labeled SHEND. The shower thus lies between PLACE and SHEND, the muon continues to CEXIT (see fig.5.1). The hadron energy is obtained by summing up the pulse heights in the shower, subtracting the contribution of the muon and multiplying by the calibration constant described in the previous chapter. As mentioned there,

$$\Delta E_{had} = .72 + .81\sqrt{E_{had}}.$$

The question has been asked "Do we miss any hadron energy in the longitudinal direction?" This can happen if SHEND is one or two counters too close to PLACE. The mean energy is computed (in terms of minimum ionizing) in different E_{had} bins in the 6 counters downstream of SHEND and compared with that in 6 counters even further downstream. Only about $(0.16 \pm .03)$ GeV is being lost and is corrected for. Another worry regarding E_{had} is the possibility that fluctuations due to π^0 decays in the shower might increase the error, ΔE_{had} . A method has been suggested⁽²³⁾ which involves using $E'_i = E_i(1 - c'_i E_i)$ as the response of the i^{th} counter instead of E_i . c'_i is defined by

$$c'_i = \frac{c}{\sqrt{\sum_i E_i \text{ (in min. ionizing)}}}. \quad (5.12)$$

Shown in figure 5.7 is $\Delta E_{had}/E_{had}$ for different values of c for 90 and 250 GeV/c hadron beams used for our hadron energy calibration. Clearly the preferred value is $c = 0$, i.e., we see no such improvement. This may be due to the coarseness of sampling (10cm Fe) being enough to average over electromagnetic fluctuations.

§5.4 Vertex, θ_h , Acceptance, etc.

Some miscellaneous aspects of analysis will be covered in this section. The z-position of the vertex is simply taken to be midway between the first counter of the event and the previous one. We considered the possibility that back scattering faked a more upstream z-position. An algorithm based on typical shower behaviour was employed to improve the vertex z position; it failed to show any significant change in cross-sections ($+0.2\%$ for pions, -0.7% for kaons; 3000 pions, 1900 kaons). The transverse position of the vertex is determined well by the shower probing algorithm - the error in the position is about 0.1 in in each view.

Studies were also made of the possibilities of using θ_h instead of θ_μ and recovering p_μ from multiple scattering in the target. The best achievable value for $\Delta\theta_h$ turns out to be

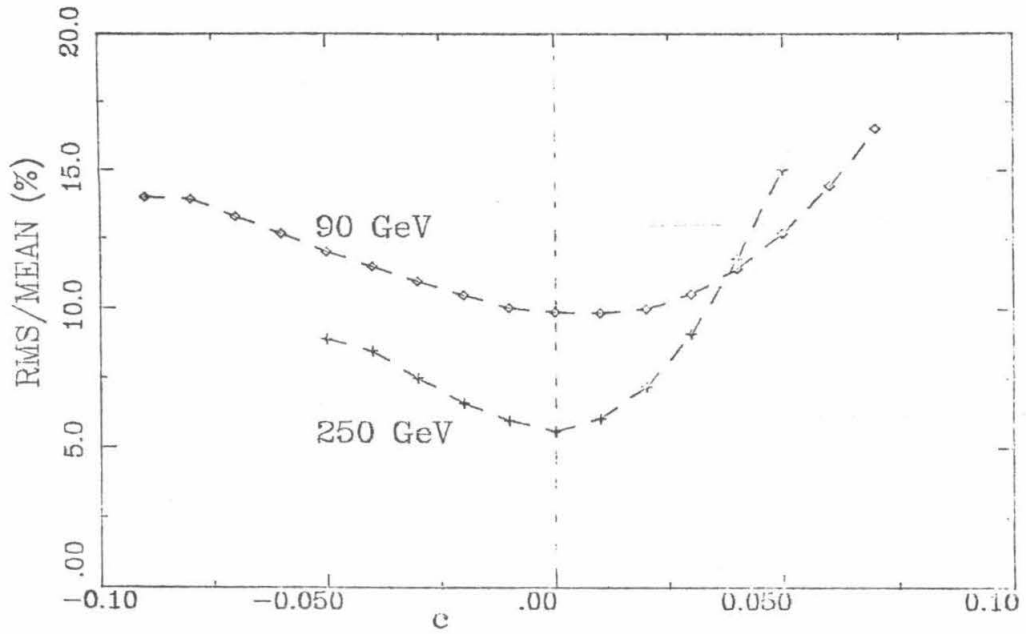


Figure 5.7. $\Delta E_h/E_h$ vs. c (see text; eqn. 5.12)

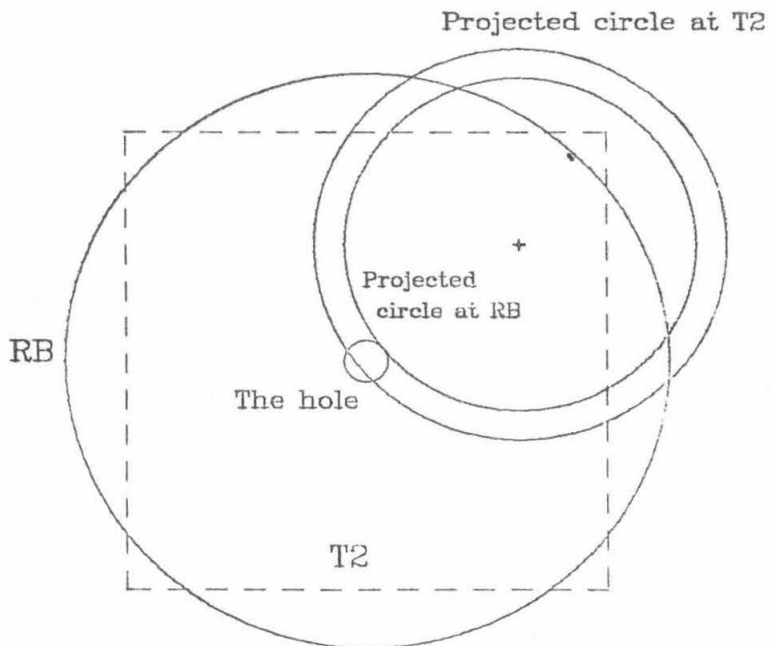


Figure 5.8. Geometric acceptance problem.

50mrad, at the highest E_{had} . This corresponds to a low θ_h region which means very large $\Delta\theta_h/\theta_h$, ruling out the possibility of using θ_h . p_μ may be obtained from multiple scattering, in fact this method works well if the true p_μ is less than about 40 GeV. However, momenta larger than 40 GeV are estimated to be smaller than they really are, making such a technique highly unreliable.

An interesting quantity to measure is the resolution of the target spark chambers. At higher momenta, this is as significant as multiple scattering. Using the χ^2 from the upstreamward extrapolation of the muon track into the hadron shower we find that for muon momenta above 40 GeV/c the χ^2/DF is 1 if the resolution is set to 0.53 mm. This value is also confirmed by comparing predicted and observed spark positions while extrapolating upstream into the shower.

A very important quantity is the geometric acceptance of the detector. For charged current structure function analysis only muon trigger events were used. Penetration triggers were used to complete the set by adding candidate muon triggers that never made it to T2 (see fig.4.1) because of ranging out. Consider the straight line projection of the muon track into the toroids. Since the magnet is focussing, any muon will tend to be 'accepted' if this projection is 'accepted'. Our 'software trigger' then accepts only those events for which the muon projection is within a 110 in -side apparatus-centred square at T2, a 69 in -radius apparatus-centred circle at the front-face of the magnet (TF; see fig.4.1) and spends less than 30% of its time in the magnet hole. Since we pick up all rangeouts, the acceptance depends only on the muon angle θ_μ and the vertex position. As described later, a cut is applied and only events with $\theta_\mu < .2$ are used. The geometric acceptance is calculated as the fraction of times an event with a given θ_μ, v_x, v_y would be accepted if v_z and ϕ_μ took on all possible values with equal probability. (v_x, v_y, v_z) is the vertex position. v_z can take on all values between the z-limits of the fiducial volume; ϕ_μ can take on all values on $[0, 2\pi]$. The problem, as illustrated in figure 5.8, reduces to the intersection of a circle with a circle (at TF), a circle with a square (at T2) and a cone with a cylinder.

Extraction of Structure Functions

§6.1 An Overview of the Physics

Let us take a look at the result of Appendix C which is reproduced here for convenience:

$$\frac{d^2\sigma^{\nu,\bar{\nu}}}{dx dy} = \frac{G^2 m_p E_\nu}{\pi(1 + Q^2/m_W^2)^2} \left\{ \left(1 - y + \frac{y^2}{2} \cdot \frac{(1+2m^2x^2/Q^2)}{(1+R)} \right) F_2 \pm \frac{(1-(1-y)^2)}{2} xF_3 \right. \\ \left. \pm (1-2f) \left(\frac{1}{(1-y)^2} \right) (u_\nu^p - d_\nu^p) + (1 - (1-y)^2) s^N \right. \\ \left. + R_{\nu,\bar{\nu}}(x, Q^2, E) + C_{\nu,\bar{\nu}}(x, Q^2, E, m_c) \right\} \quad (6.1)$$

It would be best if all the structure functions $u_\nu^p, d_\nu^p, \bar{u}^p, \bar{d}^p, \bar{s}^p$, and k^p could be independently and accurately measured as functions of x and Q^2 . From (6.1) it is clear though that only certain combinations of these are measurable. The three main functions of interest are

$$\begin{aligned} 2xF_1 &= q + \bar{q} \\ xF_3 &= q - \bar{q} \\ \text{and } F_2 &= q + \bar{q} + 2k, \end{aligned} \quad (6.2)$$

or, equivalently, xF_3 , F_2 , and R (defined by $F_2 = 2xF_1(1+R)/(1+4m^2x^2/Q^2)$). The neutrino and antineutrino differential cross-sections provide two independent measurements, yielding F_2 and xF_3 with an assumption about R , which, as we shall see, is expected to be small. The nature of the term containing F_2 and R clearly indicates the necessity of using y -dependences in extracting R .

Partly to get a 'feel' for the structure functions and the problems associated with their extraction, a brief description is presented here; excellent references⁽²⁵⁻²⁹⁾ may be found

elsewhere. At the very outset it should be noticed that xF_3 is the 'valence' quark distribution while F_2 is the 'total' quark distribution. Clearly, if quarks were all a proton contained, then $\int_0^1 F_2 dx$ would be 1. This means that σ^ν should be $G^2 s/2\pi$ implying

$$\frac{\sigma^\nu}{E} = \frac{G^2 m_p}{\pi} = 1.58 \times 10^{-38} \text{ cm}^2/\text{GeV}. \quad (6.3)$$

The measured value is closer to $0.67 \times 10^{-38} \text{ cm}^2/\text{GeV}$ ⁽³⁰⁾, indicating that a little over half the nucleon momentum is carried by objects other than quarks. Current wisdom has it that these are gluons, carriers of the strong 'colour' force. Present understanding and calculational abilities prevent us from predicting the structure functions as functions of x and Q^2 . However, there are many clues. At the high Q^2 values in this experiment the distance and time scales of the neutrino-quark interaction are small enough to justify the 'quasi-free' nature of quarks assumed by the parton model. Consequently quark distributions appear to 'scale', i.e., depend on x alone.

Since xF_3 is x times the valence quark probability density, we expect $\int_0^1 xF_3/x dx$ to be 3. The $1/x$ forces xF_3 to go to zero as $x \rightarrow 0$. In fact, valence quark contributions are expected to be nondiffractive in Regge theory, which predicts that Regge exchanges with $\alpha \approx 1/2$ will dominate, giving⁽²⁹⁾ $xF_3 \sim \sqrt{x}$ as $x \rightarrow 0$. The sea arises from virtual pair production by gluons, and is consequently confined to low x . Quark counting rules⁽²⁹⁾ and comparison with the electromagnetic form factor in turn indicate⁽²⁶⁾ that $F_2(x) \sim (1-x)^3$ as $x \rightarrow 1$. Shown in figure 6.1 are the functions xF_3 , F_2 and \bar{q} that satisfy these predictions.

QCD suggests that quarks bremsstrahlung to give gluons and gluons in turn produce more gluons or $q\bar{q}$ pairs (fig. 1.2). These processes are more and more visible as one goes to higher Q^2 . This means that the valence quarks should lose momentum, which appears in the form of extra sea quarks (mostly) and gluons (small increase). All 3 distributions (valence, sea, gluons) should have lower mean x values. In particular, the sea should see an increase at low x . These QCD deviations from the parton model are illustrated in fig. 1.3. One of the objectives of this experiment is to measure such scaling violations and compare the results with QCD. In the limit of very large Q^2 (not reached by this experiment), only sea quarks are significant, and σ^ν and $\sigma^{\bar{\nu}}$ are equal. In the energy range of E616 however (30 \rightarrow 240 GeV), we only expect a slow fall in the neutrino cross-section slope and a slow rise in that from antineutrinos. The onset of charm production tends to reverse any fall with Q^2 .

§6.2 Total Cross Sections

As an illustrative example, let us calculate the total cross section of neutrinos and antineutrinos *assuming* that the slope with energy is constant. The detailed references are, of course, (8) and (30). This section is meant as an introduction to the problem of extracting structure functions by way of the conceptually simpler problem of obtaining a cross-section. An explanation of the mechanics of event counting for cross-sections is included in appendix E.

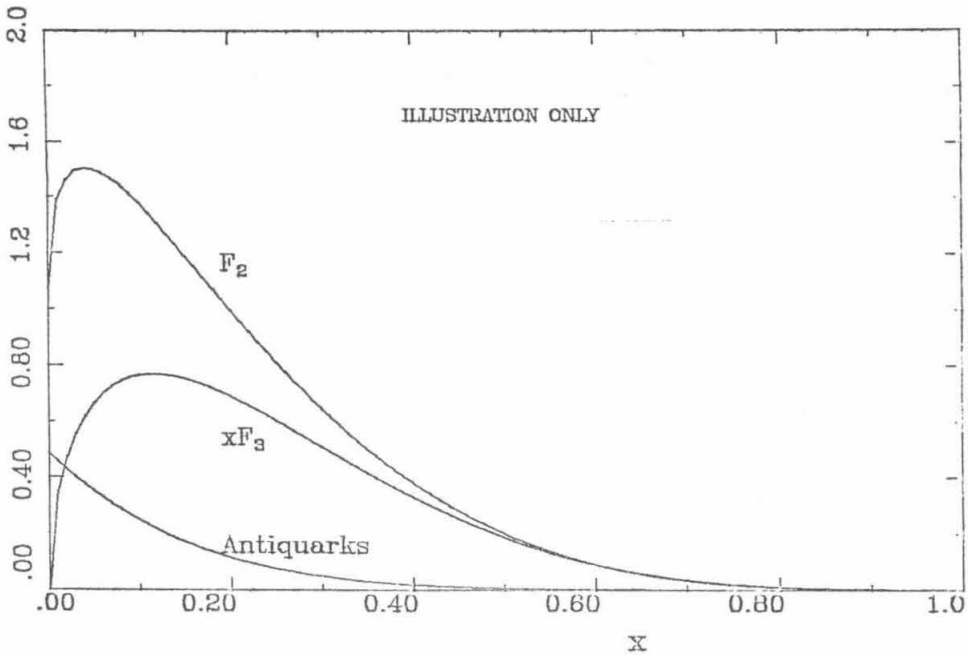


Figure 6.1. F_2 , xF_3 and \bar{q} at fixed Q^2 .

The event sample is restricted to lie in the fiducial volume defined between PLACE=20 (see §6.5) and PLACE=80 (§4.7), which implies a target density of 5361.8 gm/cm^2 . Neutrinos from pion decays are only accepted in a beam-centred circle of 30 in radius at Lab E, while neutrinos from kaon decays are accepted in a beam-centred square with a 100 in side. This is necessary since fluxes are not well understood at large radii for neutrinos from pion decays (Chapter 3; Appendix A). Only those spills in which the beam centre was within a 2.4 in sided box around the centre of Lab E are accepted. Also, if either the expansion port ion chamber or the manhole ion chamber disagreed with the rest of the flux monitors for any run, that run was discarded.

It is useful to separate the neutrinos from pion and kaon decays because they have very different energies. Since the penetration trigger penetration requirement is 16 counters, the apparatus is fully efficient (after geometric inefficiency is corrected for) out to about 600 mrad. We thus safely make a cut at 370 mrad, the outer events being corrected for by a Monte Carlo as described below. The 'software' triggers used can therefore be summarized as follows:

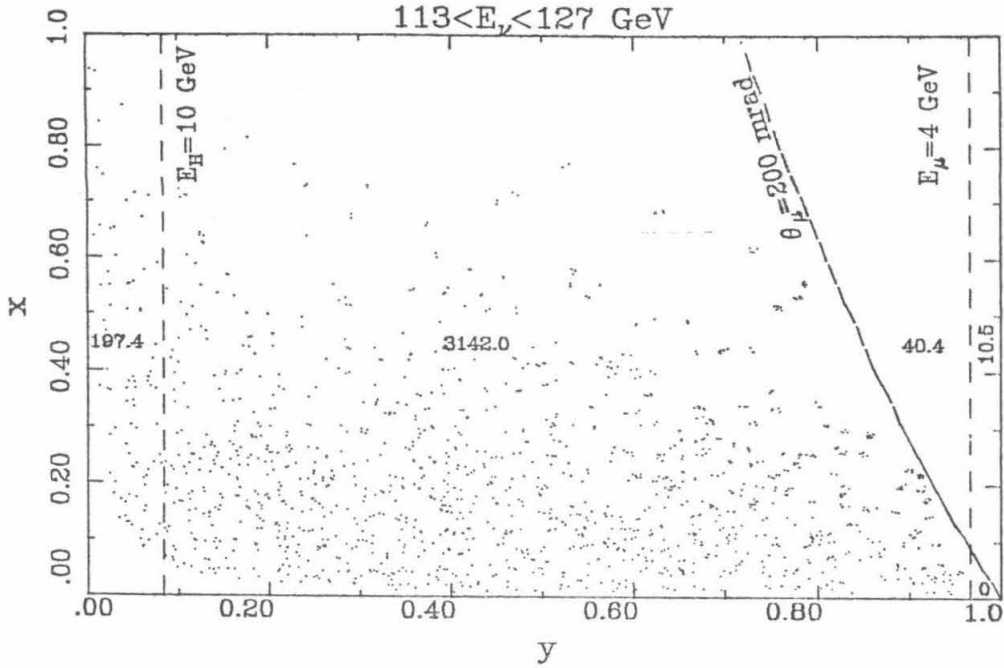


Figure 6.2. Effect of kinematic cuts around $E_\nu = 120 \text{ GeV}$.

Muon trigger(S1)

Penetration trigger(S3)

Hardware trigger 1

Hardware trigger 3

$\theta_\mu < 100 \text{ mrad}$

$\theta_\mu < 370 \text{ mrad}$

$E_\mu > 10 \text{ GeV}$

$E_h > 10 \text{ GeV}$

if $R_{\text{vertex}} < 5 \text{ in}$ then $\theta_\mu > 7.1 \text{ mrad}$

$E_\mu > 2.9 \text{ GeV}$

(6.4)

Clearly the S3 cuts are less restrictive and therefore define the kinematic boundaries as depicted in figure 6.2. The angle beyond which the muon trigger efficiency cannot be geometrically recovered is the angle a line from the apparatus centre at $z = -167 \text{ in}$ (closest event to the toroids) to a corner of T2 (55 in square, $z = 142.5 \text{ in}$) makes with the apparatus axis; this is 251 mrad. As described in appendix E, we can establish categories of events, containing either muon or penetration triggers, and thereby obtain the total number of 'pion' and 'kaon' events.

Assuming that the neutrino cross section is $\sigma_\nu(E) = kE \times 10^{-38} \text{ cm}^2$, where E is in GeV, we can use our knowledge of the neutrino flux (f_π, f_k ; chapter 3) to predict the number of 'kaon' and 'pion' events, e.g.,

$$N_{\nu(\pi)} = \int_0^\infty \sigma_\nu(E) f_\pi(E) \cdot \text{Area} \cdot \text{Target density} \cdot \text{Avogadro's no.} \cdot dE \quad (6.5)$$

Comparison with the experimental value gives k .

A high statistics Monte Carlo generation of events is used to correct for smearing and unsampled regions which are the regions excluded in (6.4). Our final result, obtained after properly averaging over various energy regions to handle systematic errors correctly is⁽³⁰⁾

$$\begin{aligned} \sigma_\nu/E &= (.669 \pm .003 \pm .024) \times 10^{-38} \text{ cm}^2/\text{GeV} \\ \text{and } \sigma_{\bar{\nu}}/E &= (.340 \pm .003 \pm .020) \times 10^{-38} \text{ cm}^2/\text{GeV} \end{aligned} \quad (6.6)$$

Note that the dominant error is systematic, resulting from flux level and particle fraction uncertainties. The slopes as a function of energy are plotted in fig. 6.13. While both slopes are consistent with being flat, there is a slight tendency, at high energies, for the neutrino slope to rise and for the antineutrino slope to fall. This affects the Q^2 behaviour of the structure functions, especially that of xF_3 , which is related to the difference of the neutrino and antineutrino differential cross-sections.

Extraction of structure functions involves an increase in the dimensionality of the problem, since events must now be binned in x and Q^2 as well. We can therefore use only muon trigger events for which a muon energy is known. In the next few sections the structure function extraction procedure is described, with its cuts and corrections, and is followed by a discussion of systematic errors.

§6.3 Cuts, Resolutions and Binning:

From the cross-section discussion it is already clear that cuts must be made; the cuts made for the structure function analysis are listed below.

<u>Fiducial Cuts</u>	<u>Kinematic cuts</u>
1) $20 \leq \text{PLACE} \leq 80$	1) $\theta_\mu < 200 \text{ mrad}$
2) Beam radius ≤ 30 in for neutrinos from π decays	2) $E_h > 10 \text{ GeV}$
3) Beam position within a 100 in square for neutrinos from K decays.	3) $E_\mu > 4 \text{ GeV}$

(6.7)

The beam position requirements in the fiducial cuts reflect the limits beyond which only flux tails exist which are not well understood. PLACE cannot be greater than 80 (i.e., 81 or 82) because one might then be including straight through muons. If PLACE < 20 , there are too few position measurements before the toroids and after the hadron shower for track finding to be fully reliable (see (iv) in §6.5).

As pointed out in the previous section, beyond $\theta_\mu = 251 \text{ mrad}$, the muon trigger efficiency falls irrecoverably and we thus make a conservative cut of 200 mrad. Below $E_h =$

25 GeV there are no calibration data and therefore the calibration curve is extrapolated only down to $E_h = 10 \text{ GeV}$. A minimum E_μ requirement of 4 GeV is ample for the muon to penetrate the longest shower and be identified.

Not mentioned above are the cuts which remove 'stray events' such as those with no track found (very few; see track finding efficiency below). Also eliminated are events with track fitting failures and track fitting χ^2/df greater than 9. The correction for this is also described below. Of course, only muon trigger events are used. Penetration trigger events which satisfy the 'software trigger 1' requirements (radius at magnet front face < 69 in, position at T2 within a 110 in -sided square and less than 30% of time spent by muon track when projected from vertex into toroid) and do not fire the muon trigger are presumed to be range-outs and are picked up and classified as muon triggers. Table 6.1 illustrates the effects of all the cuts as they reduce the raw number of events for each energy setting.

Cut	-250	-200	-165	-140	-120	120	140	165	200	250
Raw evts, PLACE ≥ 20	4241	4507	4374	3972	2857	16241	20235	31785	38224	45822
Event Gate	4156	4441	4324	3950	2830	16000	19200	31330	37565	43854
Muon trigger	3541	3821	3706	3344	2324	11487	13926	23806	29413	35697
Good trg 1	3211	3443	3332	3002	2071	10043	12279	21237	26340	32287
Good fit	3211	3437	3331	3000	2060	10033	12230	21091	26220	32182
$\chi_{tor}^2 < 9$	3210	3426	3329	2999	2040	9979	12120	20749	25910	31932
$\chi_{tar}^2 < 9$	3208	3425	3328	2999	2040	9955	12096	20699	25846	31836
$\theta \leq .2$	3197	3418	3322	2996	2032	9862	11986	20525	25625	31578
$\theta > .0071$ if $r_v < 5''$	3195	3417	3322	2996	2032	9860	11984	20524	25618	31566
$E_{had} \geq 10 \text{ GeV}$	1989	2034	1870	1519	889	5513	7565	14192	18810	24440
$E_\mu \geq 4 \text{ GeV}$	1875	1957	1810	1476	858	5456	7500	14067	18680	24232
$r_b \leq 30''$ if from π	1610	1690	1517	1193	653	4322	6289	12534	17090	22587
In $100''$ square if from K	1576	1642	1482	1162	631	4157	6063	12054	16426	21756
$0 \leq x \leq 1$	1573	1638	1481	1160	631	4146	6048	12024	16374	21685
$1 \text{ GeV}^2 \leq Q^2 \leq 251.2 \text{ GeV}^2$	1468	1531	1365	1065	556	3881	5711	11499	15790	21009

Table 6.1. Effect of structure function cuts

From the expressions

$$Q^2 \approx 4E_\mu E_\nu \sin^2 \frac{\theta_\mu}{2} \quad (6.8)$$

$$\text{and } x = \frac{Q^2}{2m_p E_h} = \frac{2E_\mu E_\nu}{m_p E_h} \sin^2 \frac{\theta_\mu}{2} \quad (6.9)$$

it is easy to calculate the resolutions in x and $\log_{10} Q^2$, given those in E_μ, E_h and θ_μ (see chapter 5).

The x -resolution worsens with increasing x but improves with increasing Q^2 . Listed in table 6.3 are the x and $\log_{10} Q^2$ resolutions for a fixed neutrino energy of 120 GeV. Clearly,

at low x ($x \sim .015$) the x resolution can be as good as 0.005 which helps the determination of the low- x behaviour of xF_3 tremendously. Table 6.2 clearly shows that the low- x resolutions are dominated by the θ_μ resolution and the high- x ones by E_μ (except at lower Q^2 where the effect of the E_{had} resolution eclipses that of the E_μ resolution).

The binning scheme could be adapted to the resolutions, but it was thought best to use the binning shown in table 6.7 to facilitate easy comparison with CDHS who use the same binning except for their $\log_{10} Q^2$ bins, which are twice as fine. For the low- x behaviour of xF_3 , finer binning is used.

		x	% from	% from	% from	$\log_{10} Q^2$	% from	% from	% from
		resol.	E_μ	E_{had}	θ_μ	resol.	E_μ	E_{had}	θ_μ
$x=.015$	$Q^2=2.51$.006	21.82	1.16	77.02	.164	21.23	3.84	74.93
$x=.045$	$Q^2=3.98$.011	61.09	10.43	28.47	.103	64.95	4.79	30.26
$x=.080$	$Q^2=6.31$.019	68.13	14.28	17.59	.098	75.67	4.77	19.56
$x=.150$	$Q^2=15.85$.031	78.34	9.77	11.88	.089	80.07	7.98	11.94
$x=.250$	$Q^2=15.85$.060	72.83	21.06	6.12	.095	88.40	4.13	7.48
$x=.350$	$Q^2=25.12$.080	76.86	18.59	4.55	.093	89.90	4.87	5.23
$x=.450$	$Q^2=39.81$.095	82.06	14.12	3.81	.088	89.39	6.45	4.16
$x=.550$	$Q^2=39.81$.125	78.35	18.70	2.95	.091	91.45	5.12	3.43
$x=.650$	$Q^2=63.10$.132	85.06	12.11	2.82	.085	89.70	7.33	2.97
$x=.850$	$Q^2=63.10$.190	79.90	18.16	1.94	.089	92.71	5.02	2.27

Table 6.2. Resolutions in typical bins and where they come from ($E_\nu=120$ GeV).

x-resolution										
	x=.015	x=.045	x=.080	x=.150	x=.250	x=.350	x=.450	x=.550	x=.650	x=.850
$Q^2=1.26$.005	.016	.033	.075	.152	.245	.351	.468	.596	.883
$Q^2=2.00$.004	.014	.028	.063	.125	.199	.284	.379	.481	.709
$Q^2=3.16$.007	.012	.024	.053	.104	.164	.233	.309	.391	.574
$Q^2=5.01$	-	.010	.021	.045	.088	.137	.193	.254	.321	.468
$Q^2=7.94$	-	.010	.018	.039	.075	.116	.162	.213	.267	.386
$Q^2=12.59$	-	-	.015	.034	.065	.100	.139	.181	.225	.324
$Q^2=19.95$	-	-	-	.028	.056	.087	.120	.155	.193	.274
$Q^2=31.62$	-	-	-	.028	.047	.074	.103	.134	.167	.237
$Q^2=50.12$	-	-	-	-	.040	.061	.087	.115	.144	.205
$Q^2=79.43$	-	-	-	-	-	-	.070	.094	.120	.175
$Q^2=125.89$	-	-	-	-	-	-	-	-	.094	.142
$Q^2=199.53$	-	-	-	-	-	-	-	-	-	-
$\log_{10} Q^2$ -resolution										
	x=.015	x=.045	x=.080	x=.150	x=.250	x=.350	x=.450	x=.550	x=.650	x=.850
$Q^2=1.26$.131	.128	.129	.130	.130	.129	.130	.130	.129	.130
$Q^2=2.00$.124	.118	.118	.120	.120	.120	.120	.121	.121	.120
$Q^2=3.16$.203	.107	.111	.113	.114	.114	.114	.115	.115	.115
$Q^2=5.01$	-	.099	.102	.106	.108	.109	.110	.110	.110	.110
$Q^2=7.94$	-	.097	.094	.099	.102	.105	.106	.106	.107	.108
$Q^2=12.59$	-	-	.086	.093	.097	.100	.102	.103	.103	.105
$Q^2=19.95$	-	-	-	.084	.092	.097	.099	.098	.101	.103
$Q^2=31.62$	-	-	-	.090	.082	.088	.092	.096	.096	.099
$Q^2=50.12$	-	-	-	-	.076	.079	.083	.086	.089	.093
$Q^2=79.43$	-	-	-	-	-	-	.074	.078	.081	.086
$Q^2=125.89$	-	-	-	-	-	-	-	-	.070	.075
$Q^2=199.53$	-	-	-	-	-	-	-	-	-	-

Table 6.3. x and Q^2 resolutions at $E_\nu=120$ GeV.

§6.4 Method of Extraction

The equation to be solved is (6.1). Assuming that all correction terms are calculable, there are three unknowns in any small x and Q^2 bin (integrating over energy), which may be F_2 , $2xF_1$ and xF_3 . With only 2 equations, one of the unknowns must be fixed beforehand. The similarity of the term containing F_2 in both the equations demands that xF_3 not be fixed; it must be F_2 or R . F_2 being the most interesting quantity and R being small (~ 0.1), we chose to fix R while analyzing the data. The values chosen were

$$R = 0., 0.1 \text{ and } \frac{.73(1-x)^{3.68}}{\ln(Q^2/.24^2)} \quad (6.10)$$

the last of which derives from calculations based on our results for the QCD evolution of $F_2(x, Q^2)$.

The number of events in a given x and $\log_{10} Q^2$ bin is given by

$$N_{\nu, \bar{\nu}} = \iiint \iiint 2.303 \frac{G^2 m_p E_\nu}{\pi(1+Q^2/m_W^2)^2} \cdot y \cdot \phi_{\nu, \bar{\nu}}(v_x, v_y, E) dE \cdot A(v_x, v_y, \theta_\mu) dv_x dv_y dx d \log_{10} Q^2 \\ \times [\text{y-dependent form as in (6.1)}] \quad (6.11)$$

$A(v_x, v_y, \theta_\mu)$ is the acceptance and $\phi_{\nu, \bar{\nu}}(v_x, v_y, E) dv_x dv_y dE$ the flux of neutrinos or antineutrinos in a small area $dv_x dv_y$ and a small energy interval $[E, E + dE)$. v_x and v_y are the transverse coordinates of an event. The acceptance $A(v_x, v_y, \theta_\mu)$ is integrated over all v_x values within the fiducial volume and hence is not a function of v_x . We now assume that F_2 and $x F_3$ are linear in the bins used (see section on corrections below). Then, using the value at the bin centre as a fixed unknown, the neutrino and antineutrino equations may be integrated to give 2 simultaneous equations in 2 unknowns which are then easily solved.

If F_2 and $x F_3$ be the (constant) unknowns in a given bin, then the expected number of events is

$$\left. \begin{aligned} N_\nu &= aF_2 + b x F_3 + c \\ N_{\bar{\nu}} &= \bar{a}F_2 + \bar{b} x F_3 + \bar{c} \end{aligned} \right\} \quad (6.12)$$

where the 6 constants $a, b, c, \bar{a}, \bar{b}$ and \bar{c} are known from the integral 6.11. The likelihood \mathcal{L} of seeing N_ν neutrino and $N_{\bar{\nu}}$ antineutrino events in the bin is then simply the product of two Poissons with the expected values of N_ν and $N_{\bar{\nu}}$ as the means:

$$\mathcal{L} = \frac{e^{-(aF_2 + b x F_3 + c)} (aF_2 + b x F_3 + c)^{N_\nu}}{N_\nu!} \frac{e^{-(\bar{a}F_2 + \bar{b} x F_3 + \bar{c})} (\bar{a}F_2 + \bar{b} x F_3 + \bar{c})^{N_{\bar{\nu}}}}{N_{\bar{\nu}}!} \quad (6.13)$$

Maximizing \mathcal{L} or, equivalently, minimizing $-\ln \mathcal{L}$ gives

$$\left. \begin{aligned} a - \frac{a N_\nu}{aF_2 + b x F_3 + c} + \bar{a} - \frac{\bar{a} N_{\bar{\nu}}}{\bar{a}F_2 + \bar{b} x F_3 + \bar{c}} &= 0 \\ \text{and, } b - \frac{b N_\nu}{aF_2 + b x F_3 + c} + \bar{b} - \frac{\bar{b} N_{\bar{\nu}}}{\bar{a}F_2 + \bar{b} x F_3 + \bar{c}} &= 0 \end{aligned} \right\} \quad (6.14)$$

It is obvious that (6.12) is indeed a solution of (6.14). To speed up the integration, the product $A(v_x, v_y, \theta_\mu) \phi_{\nu, \bar{\nu}}(v_x, v_y, E) dE dv_x dv_y$ is evaluated first after integrating over ϕ_μ and is stored in tabulated form as a function of E, θ_μ , and r . This reduces the problem to a 4-dimensional integral of which at least one integration, over r_{beam} , is easily performed without including the y-dependent terms. The kinematic cuts described earlier are applied during the integration, thereby restricting it to allowed regions only.

Another technique is used by D.B. MacFarlane as described in his thesis⁽¹⁰⁾. That technique eliminates two integrals by utilizing the fact that it is also possible to take $A(v_x, v_y, \theta_\mu)$ to the left-hand side of (6.11) before the integrations (i.e., in the differential expression) and sum up weights (1/acceptance) instead of 1 for each event. It is easily checked that this leads to a larger fractional error for the left hand side of (6.11); the fractional error increases from $1/\sqrt{N}$ to

$$\frac{\sigma(\sum W_i)}{\sum W_i} = \frac{1}{\sqrt{N}} \left(1 + \frac{\sigma^2}{\omega^2} \right) \quad (6.15)$$

where ω and σ are the mean and standard deviation respectively of the weights of the N events in the bin. A large dispersion of weights in a bin will therefore lead to a larger error on the extracted structure functions. However, since we keep $A(v_x, v_y, \theta_\mu)$ on the right hand side of (6.11) a 5-dimensional integral has to be performed as opposed to a 3-dimensional one otherwise. We effectively reduce the integration to a 4-dimensional one (see above) and with the help of some programming short cuts find that the integration takes less than 50% longer than the other technique.

Apart from the completely independent computer implementations, other differences also exist between the two methods. We choose to parametrize the flux as a function of energy and radius at Lab E, instead of binning it in an energy histogram. This allows greater flexibility and ease of use. We also choose to make all the corrections in an additive fashion as opposed to multiplicatively in the other technique. It has been verified that none of these differences is quantitatively significant.

§6.5 Corrections

Several corrections, most of them tiny, must be made before structure functions can be extracted. These fall into two kinds: those that arise from experimental inefficiencies and those that are either theoretically motivated or require prior knowledge of the structure functions; the former are described first.

i. Veto deadtime correction

An unbiased loss of events occurs because some of the flux is vetoed by the veto wall. The magnitude of the effect is small ($\leq 2\%$) and is tabulated in table 6.4.

ii. χ^2 -failures

There are two fits to the track: one in the toroids for momentum finding, and one in the target for the muon angle. In either case it was felt that events with a bad $\chi^2/d.f.$ would lead to worse resolutions, hence only events with $\chi^2/d.f. < 9$ were accepted. The effect of this cut is $\sim 1\%$ after kinematic cuts, as evidenced in table 6.4. A setting by setting correction is computed by making all possible cuts in a 30 in beam centred radius including the E_μ cut for events with a good χ^2 .

Energy Setting (GeV)	Veto Deadtime correction	$\chi^2 > 9$ correction
-250	1.016	1.0025
-200	1.004	1.0080
-165	1.006	1.0014
-140	1.016	1.0009
-120	1.020	1.0250
120	1.012	1.0059
140	1.010	1.0123
165	1.009	1.0265
200	1.011	1.0169
250	1.014	1.0072

Table 6.4. Corrections (i) and (ii) described in the text.

iii. Trigger inefficiencies

One may ask whether the muon trigger is really 100% efficient. A way to determine this is to examine small- θ_μ events for which both the muon trigger and the penetration trigger should be 100% efficient. Such an analysis has been performed for fast-spill events⁽⁴²⁾ with no significant difference from 100% detected.

We have also investigated the θ_μ behaviour of the muon trigger efficiency and the E_{had} behaviour of the penetration trigger efficiency. After geometric efficiency corrections both are equal to unity in the expected regions. Beyond $\theta_\mu = 251 mrad$ the muon trigger efficiency shows a fall off. The penetration trigger efficiency is only relevant for the purposes of picking up rangeouts and reaches one well before the hadron energy cut of 10 GeV. These dependences are shown in fig 6.11.

iv. Track finding efficiency

The track-finding efficiency is virtually 100%. This was directly checked by asking how many muon triggers underwent successful track finding. The result if plotted as a function of PLACE is flat at 100% except for PLACE < 14 where it rapidly begins to fall to zero. We impose a cut to eliminate PLACE < 20 and hence there is no correction to be made.

v. Wide band background

This correction is made by including the wide band flux correctly scaled to the number of open slit protons and has already been discussed in chapter 3.

vi. Cosmic rays

When the structure function analysis cuts are applied to events in the cosmic ray gates, only 2 events (one at +200 GeV/c, one at +250 GeV/c) make it through. Allowing for a slow spill livetime ratio of 3.7, this number translates into 7.4 events out of $\sim 30,000$ slow spill events. This is an extremely small fraction and hence the cosmic ray background will be ignored.

vii. Flat cross-section correction

Due to experimental uncertainties the slope of the cross-section measurements with energy is not a smooth curve (references 8,30; figure 6.13). QCD scaling violations, charm production etc. make this curve not flat. Figure 6.14 shows a prediction from QCD using a Buras-Gaemers⁽⁴¹⁾ kind of fit ($\Lambda = 0.1 \text{ GeV}$) and charm production assuming $m_C = 1.5 \text{ GeV}/c^2$. Since neither Λ nor m_C is really well known, our assumption to force the cross-section slope to be flat is adequate. This serves to remove experimental fluctuations.

There are many ways of applying this correction. The most obvious is to use, at each energy, a multiplicative factor that changes figure 6.13 to a horizontal flat line. Another way is to separately alter the pion and kaon flux at each energy setting so that the pion and kaon decay neutrino cross-section is the same at all energy settings.

A third technique, the one we used, involves adjusting the relative flux levels of each momentum setting so that the structure functions integrated over the measured x and Q^2 range of that setting agree with the averaged structure functions in that range. A $\sim 0.5\%$ correction was then applied for consistency with the cross-section measurement. The constants we multiplied the fluxes with are listed below. Presumably they remove errors in particle fractions i.e., the fluctuations in the cross-section slope measurement are mainly due to errors in particle fractions and partly due to inaccuracies in flux measurements (we find that the rms for the adjustment constants is roughly equal to the expected errors on particle fractions). Our technique would be the same as assuming a QCD cross-section slope if all the fractions in fig. 6.14 were 100%, since the model is an approximation to QCD. Since the total cross-section is insensitive to R , we do not expect the uncertainty in R to affect the adjustment constants.

	250 GeV	200 GeV	165 GeV	140 GeV	120 GeV
- Pions	.963 \pm .034	.964 \pm .034	1.043 \pm .039	1.126 \pm .055	1.004 \pm .064
+ Pions	.964 \pm .014	.973 \pm .015	.947 \pm .016	.938 \pm .022	.967 \pm .026
- Kaons	.901 \pm .050	.896 \pm .047	.964 \pm .051	1.071 \pm .065	.970 \pm .081
+ Kaons	1.112 \pm .012	1.042 \pm .014	1.028 \pm .016	.986 \pm .023	.993 \pm .030

Table 6.5

Flux adjustment constants - they flatten the cross-section in regions where structure functions are measured.

All the following corrections require prior knowledge of the structure functions. For this reason we iterate. Starting from an approximate set of structure functions, corrections can be calculated, made and then the newly obtained set of structure functions used to repeat the process. Experience has shown that one iteration is enough. The structure functions used for corrections are really fits, and we used two different models (see appendix F).

For the purpose of smearing corrections and external radiative corrections, the empiri-

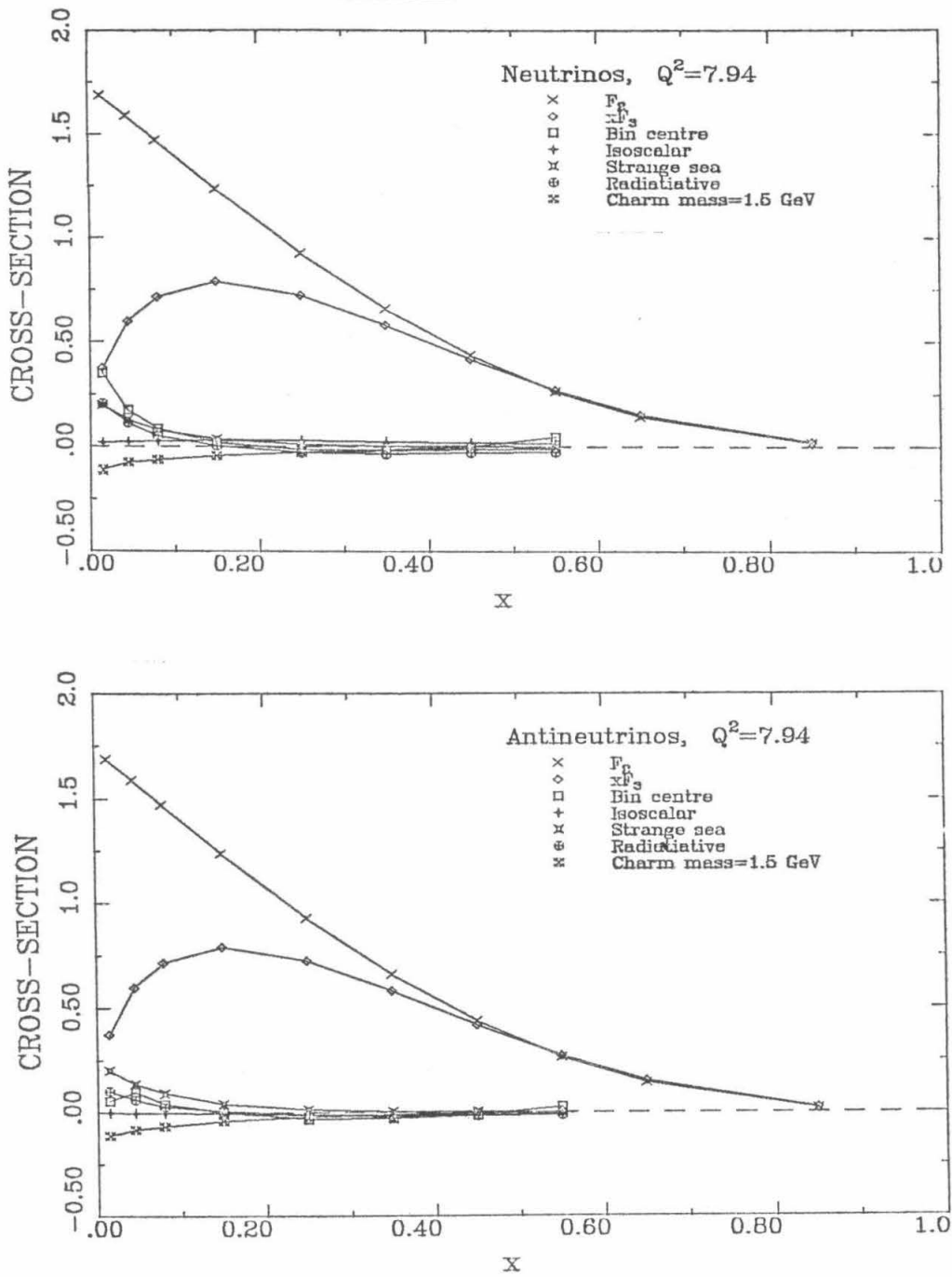


Figure 6.9

Magnitude of various corrections for neutrino and antineutrino differential cross-sections.

cal model forms the kernel of a Monte Carlo which generates events. The generated variables E_μ, E_h and θ_μ are then smeared using the resolutions described in section 6.3. This Monte Carlo is very fast and ample events at each energy can be quickly generated.

Figure 6.3 illustrates the following physics corrections in the form of their contributions to the neutrino and anti-neutrino cross-sections. Clearly F_2 and xF_3 dominate at all but the lowest x values where the strange sea, radiative and other corrections begin to get large as $x \rightarrow 0$.

viii. Smearing corrections

Ideally, an integral in an x and Q^2 bin over x, Q^2 and E , say

$$\iiint f(x, Q^2, E) dx dQ^2 dE \quad (6.16)$$

can be transformed into an integral over E_μ, E_h and θ_μ as

$$\iiint f(x, Q^2, E) J(x, Q^2, E; E_\mu, E_h, \theta_\mu) dE_\mu dE_h d\theta_\mu, \text{ where } J \text{ is the Jacobian} \quad (6.17)$$

(Two other integrations that are performed over v_x and v_y , the transverse event coordinates, are understood here). It is now easy to include the effect of non-zero resolutions. If the probability that a given variable, say q , truly lies in $[q, q + dq)$ when the measured value is q' is $R_q(q'; q) dq$, then the above integrals should change to

$$\iiint \iiint \int dE'_\mu dE'_h d\theta'_\mu dE_\mu dE_h d\theta_\mu f(x, Q^2, E) J(x, Q^2, E; E_\mu, E_h, \theta_\mu) R_{E_\mu}(E_\mu; E'_\mu) R_{E_h}(E_h; E'_h) R_{\theta_\mu}(\theta_\mu; \theta'_\mu) \quad (6.18)$$

where the integrals over E'_μ, E'_h and θ'_μ are over all space. Given the complexity of $f(x, Q^2, E)$, the problem of evaluating these 8-dimensional integrals with the available CP time was insuperable. We settled for the alternative technique of generating much higher statistics than the data using the Monte Carlo described above, and using the ratio of unsmeared to smeared events in every bin to multiply the number of data events in each bin. If n_i be the number of events initially in a bin, with n_i^e entering due to smearing and n_i^l leaving, the number of events after smearing in the bin will be

$$n_i^f = n_i + n_i^e - n_i^l \quad (6.19)$$

The smearing correction is then defined by

$$f_i = \frac{n_i^f}{n_i} = 1 - \frac{n_i^l}{n_i} + \frac{n_i^e}{n_i} \quad (6.20)$$

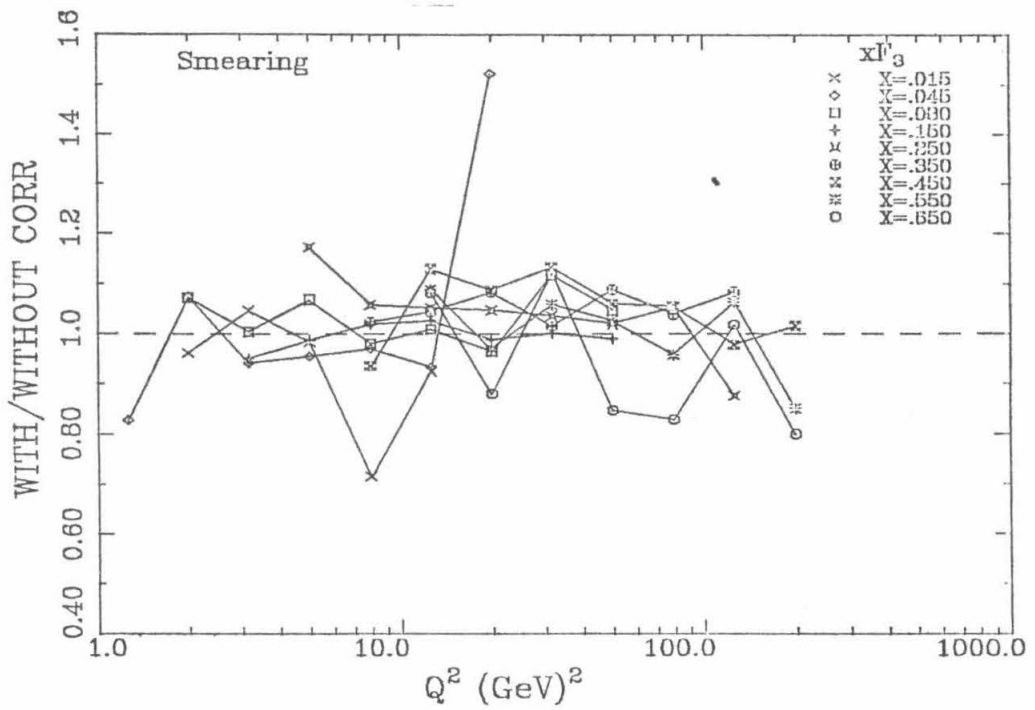
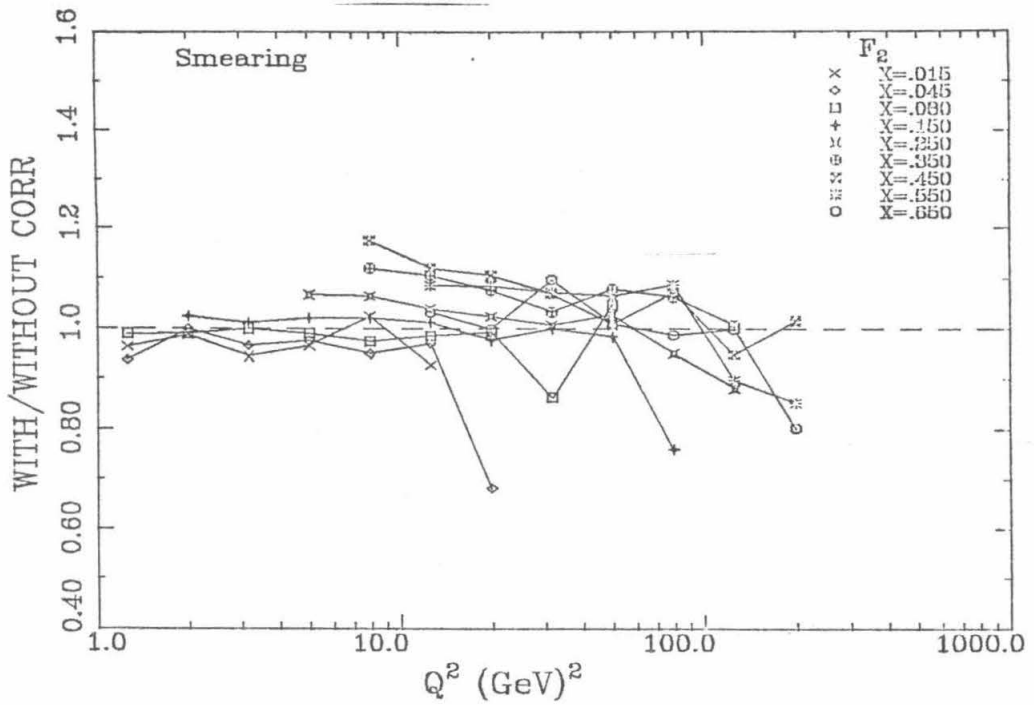


Figure 6.4. Magnitude of Smearing corrections.

n_i^e is independent of n_i and n_i^l . However, n_i is binomially split up into events that remain in the i^{th} bin and those that leave the bin. Thus the error on n_i^l/n_i is the error on an efficiency, giving

$$(\Delta f_i)^2 = \frac{(n_i^l/n_i)(1 - (n_i^l/n_i))}{n_i} + \frac{n_i^e}{n_i^2} + \frac{n_i^{e2}}{n_i^3} \quad (6.21)$$

By generating a large number of events this error is kept at a fraction of the statistical error but is nevertheless propagated into the statistical error on the structure functions. Kinematic, fiducial and acceptance cuts applied during the calculation of smearing corrections are identical to those used on the data. Corrections for large muon energy depositions within the hadron shower are simultaneously made by randomly simulating such processes utilizing the data collected outside the shower (see end of §5.1).

ix. Bin centre corrections

Within every x and Q^2 bin, the flux is not necessarily uniform, and the structure functions are not linear either. Further, parts of the bin may lie outside the kinematically allowed region after cuts. Therefore, the evaluated value of a structure function is only guaranteed to be the value somewhere in the bin. To obtain a value at the bin centre, say F_{20} for F_2 , we must calculate the above effects using a fit. The integral within a bin,

$$\begin{aligned} I &= \int dV \{ \dots \} F_2 \\ &= \int dV \{ \dots \} \left\{ F_{20} + \frac{\partial F_2}{\partial x} \Big|_0 (x - x_0) + \frac{\partial F_2}{\partial \log_{10} Q^2} \Big|_0 (\log_{10} Q^2 - \log_{10} Q_0^2) \right. \\ &\quad + \frac{1}{2} \left(\frac{\partial^2 F_2}{\partial x^2} \Big|_0 (x - x_0)^2 + \frac{\partial^2 F_2}{\partial x \partial \log_{10} Q^2} \Big|_0 (x - x_0)(\log_{10} Q^2 - \log_{10} Q_0^2) \right. \\ &\quad \left. \left. + \frac{\partial^2 F_2}{\partial (\log_{10} Q^2)^2} \Big|_0 (\log_{10} Q^2 - \log_{10} Q_0^2)^2 \right) + \dots \right\} \end{aligned} \quad (6.22)$$

The subscript zero refers to the bin centre. The derivatives are evaluated using the fit; the integrals of $(x - x_0)$, $(\log_{10} Q^2 - \log_{10} Q_0^2)$, $(x - x_0)^2$, $(x - x_0)(\log_{10} Q^2 - \log_{10} Q_0^2)$ and $(\log_{10} Q^2 - \log_{10} Q_0^2)^2$ are evaluated using the correct flux and kinematic cuts. Thus we find $I_0 = \int dV \{ \dots \} F_{20}$, where F_{20} is the unknown to be determined. As shown in figure 6.5, bin centre corrections are usually small, except in edge bins where cuts imply larger corrections.

x. Isoscalar correction

Easily the most straightforward of corrections, this one is also small ($\leq 5\%$). It is the $\pm(1 - 2f)(\frac{1}{1-y})^2(u_v^p - d_v^p)$ term in (6.1). Clearly it goes to zero if $f = 1/2$ ($\langle Z \rangle = \langle A \rangle / 2$) or if $u_v^p = d_v^p$. For our target, f is close to $1/2$ ($f=0.466$). The models we use for corrections are explained in appendix F, where the difference between u_v^p and d_v^p is described. The correction is plotted in figure 6.6.

xi. Radiative corrections

There are electromagnetic corrections to the basic weak interaction charged current process.

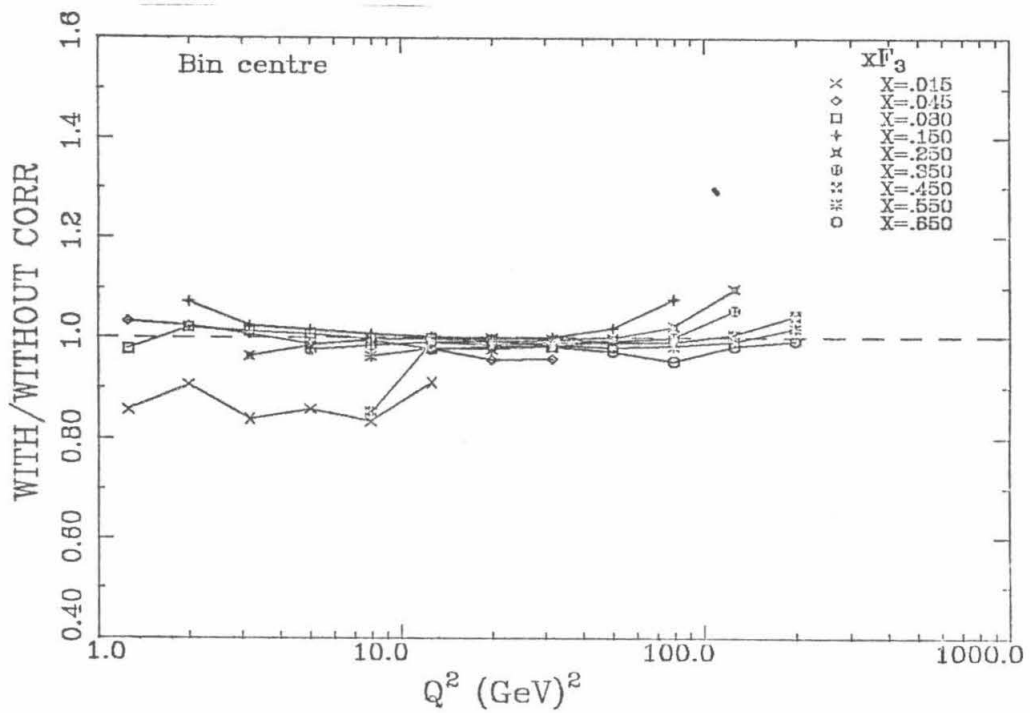
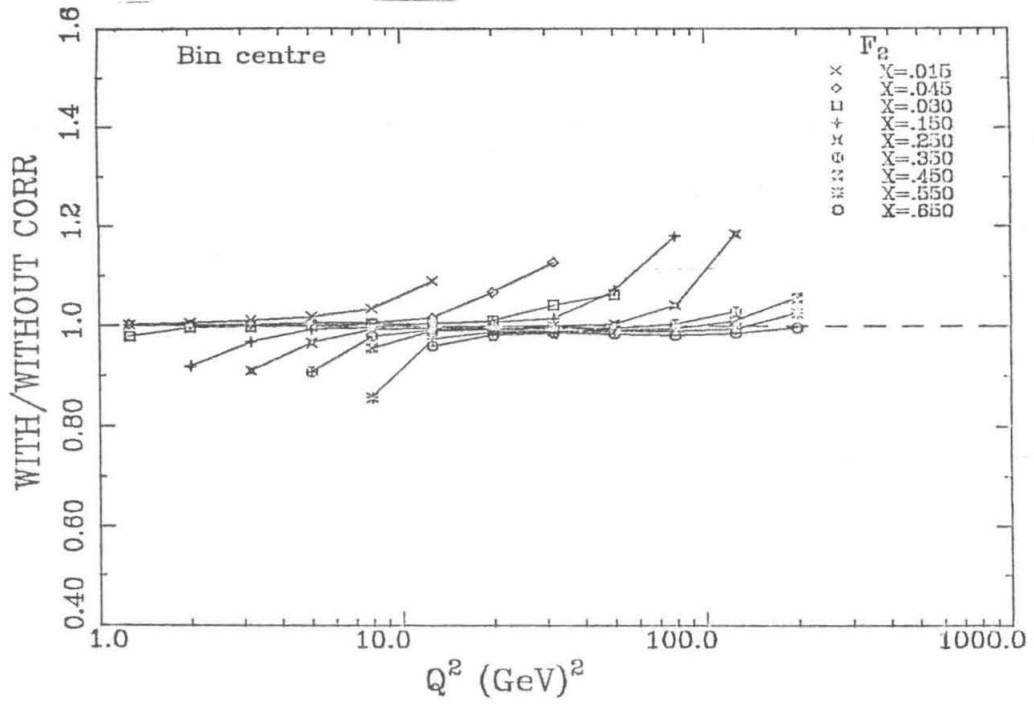


Figure 6.5. Magnitude of bin centre corrections.

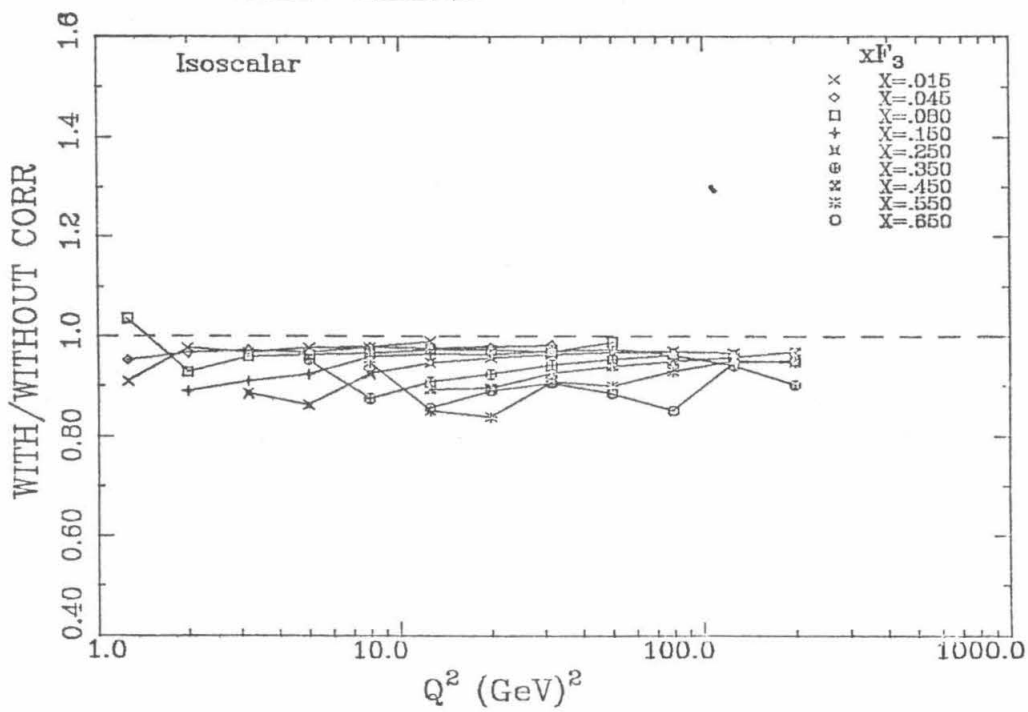
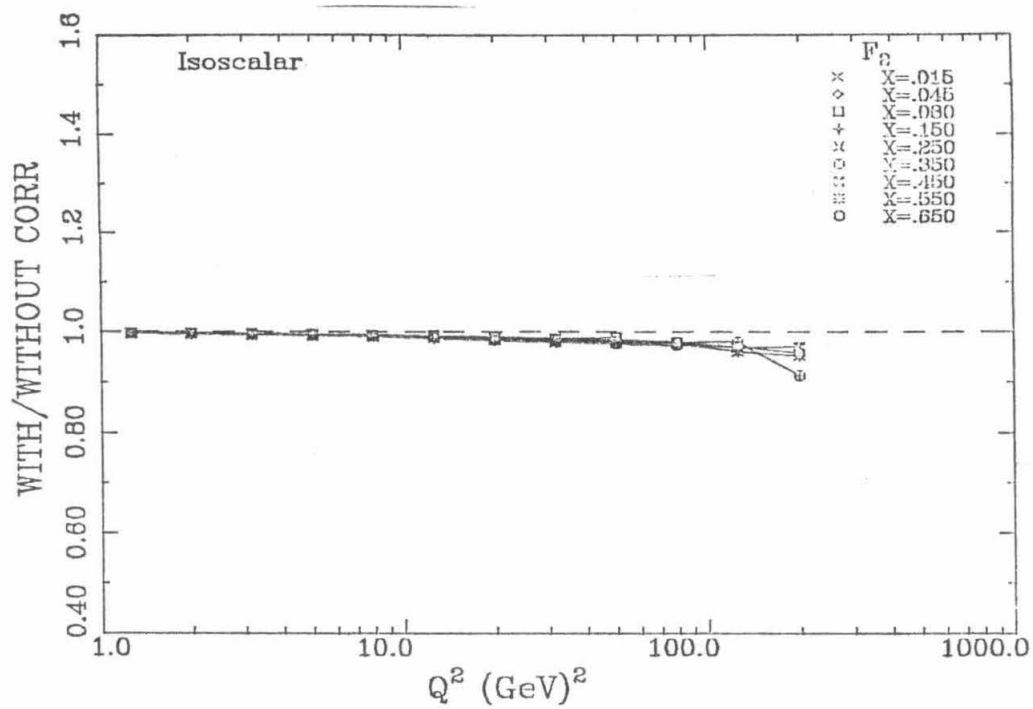


Figure 6.6. Magnitude of the isoscalar correction.

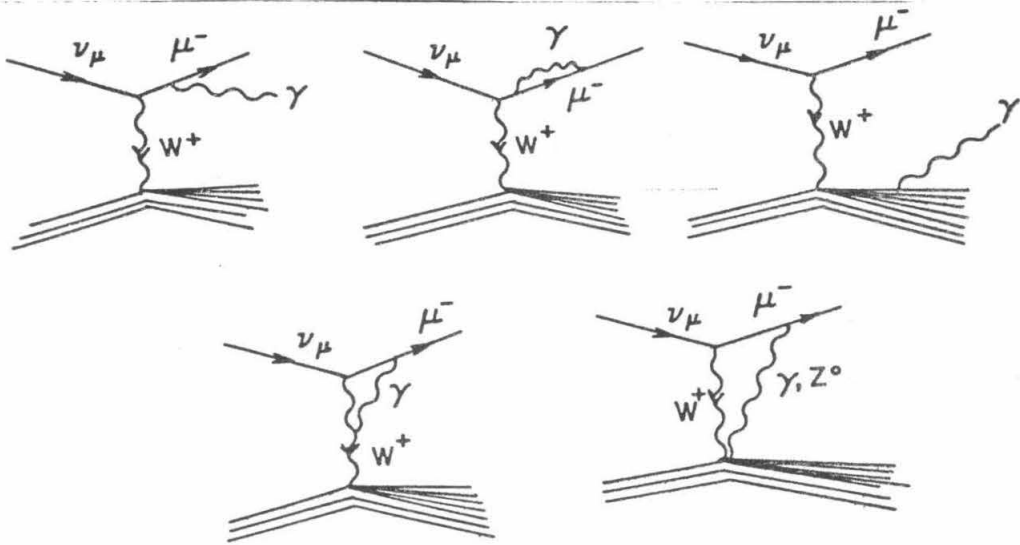


Figure 6.7. Diagrams for radiative corrections.

These involve photon bremsstrahlung from the muon and hadron legs of the diagram, self-energy terms and interference terms which could include the W -boson. Some of these diagrams are shown in figure 6.7.

Radiative corrections are most important for the lightest particles (here muons), since they tend to go like $\ln Q^2/m^2$. Of course a rigorous discussion^(32,33) must include all diagrams and calculational results must be gauge-invariant. Unknown quark masses and unknown details of the hadron leg are potential problems. However, as de Rújula et al.⁽³³⁾ show, most of the corrections are quark-mass independent. They show that to leading log order calculations may be performed because the lepton leg factorizes. The observed cross-section σ_{obs} , can be written in terms of the 'bare' cross-section σ_B , as

$$\sigma_{obs} = \sigma_B + \frac{\alpha}{2\pi} \ln \frac{Q^2}{m_\mu^2} F(\sigma_B) + \frac{\alpha}{2\pi} \ln \frac{Q^2}{M^2} H + \frac{\alpha}{2\pi} G \quad (6.23)$$

The lepton 'log', hadron 'log' and remaining terms are clearly separated. G is small, and even H may be neglected. $F(\sigma_B)$ is a calculable function.

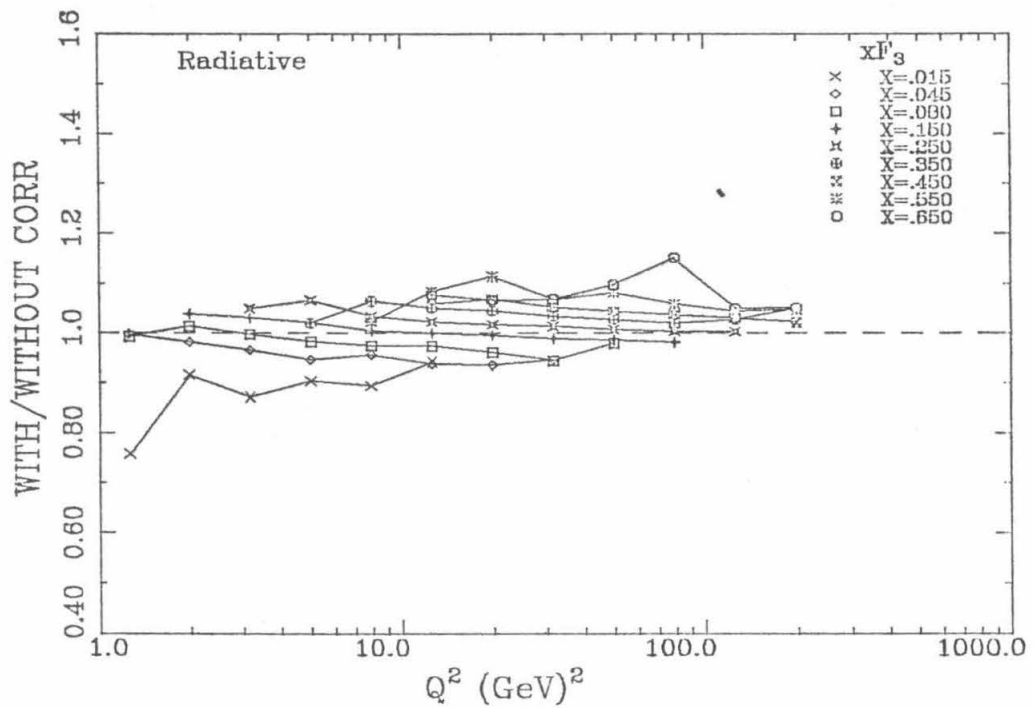
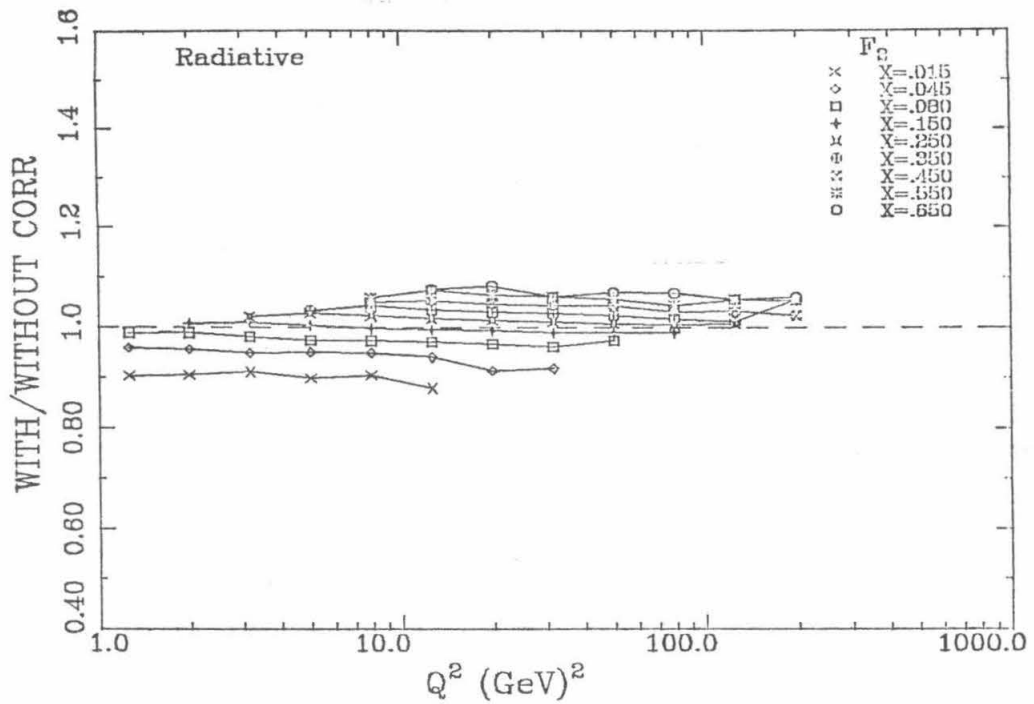


Figure 6.8. Magnitude of radiative corrections.

The end result is

$$\frac{d\sigma_{obs}}{dx dy} = \frac{d\sigma_B}{dx dy} + \frac{\alpha}{2\pi} \ln \frac{s(1-y+xy)^2}{m_\mu^2} \times \int_0^1 dz \frac{1+z^2}{1-z} \left\{ \frac{y\theta(z-z_{min})}{z(y+z-1)} \left[\frac{d\sigma_B}{dx dy} \Big|_{\substack{x=\bar{x} \\ y=\bar{y}}} \right] - \frac{d\sigma_B}{dx dy} \right\} + O\left(\frac{\alpha}{2\pi}\right) \quad (6.24)$$

$$\text{Here,} \quad \bar{x} = \frac{xy}{z+y-1} \\ \bar{y} = \frac{z+y-1}{z} \quad (6.25)$$

Radiative corrections are large ($\sim 10\%$) at very low and very high x , also at very low y . They are plotted in figure 6.8. Note that our $E_{had} > 10 \text{ GeV}$ cut effectively excludes the very low y region.

xii. Strange sea correction

This is the $(1 - (1-y)^2)s^N$ term in (6.1) above. The y -dependence is exactly the same as for xF_3 , but the sign remains positive even for antineutrinos. Hence this correction has virtually no effect on xF_3 . Assuming that s^N is some fraction of \bar{q} , which can be iteratively well extracted, the only uncertainty is in the fraction. Dimuon data^(34,35) suggest that s^N must be half of \bar{u} or \bar{d} , a value which we used. This correction is obviously significant only at low x , since $\bar{q} \sim (1-x)^{6.5}$. It is shown in figure 6.9.

xiii. Charm-mass correction

A correction arises due to the heavy mass of the charm quark. Because of its mass, charm is not produced at low energies and production sets in as described in reference 24. Parton model kinematics prescribes a change from the variable x to $\xi = x + m_c^2/2m_p E_h$. Whenever a light quark changes into a heavy one, the differential cross-section remains the same if $Q^2 \gg m_p^2$, except for the replacement everywhere of Q^2 by $Q^2 + m_H^2$, where m_H is the mass of the heavy quark. Also, the structure function scales in ξ , where $\xi = x + m_H^2/2m_p E y$ is now the fraction of the nucleon momentum carried by the struck quark. These changes are included in the differential cross-section expression of appendix 3. The resulting effect is depicted in figure 6.10.

xiv. Fermi motion correction

If nucleons are bound in the nucleus, but freely move within it, and they resemble a Fermi gas, we can calculate^(36,37) the effect of this motion on structure functions and total cross-sections. For example, for an average momentum $\langle p^2 \rangle = (250 \text{ MeV})^2$, a number close to that for nucleons in iron nuclei, it is easy to show that s can increase by $\sim 3\%$. Detailed calculations⁽³⁷⁾ assume a flat Fermi-gas-like momentum distribution from zero to the limit, say K_F , and then a tail that falls off as $1/p^4$. Corrections to both F_2 and xF_3 have thus been calculated. However the assumption of free nucleon motion is not valid for iron nuclei. Deuterons have a much smaller binding energy (\sim

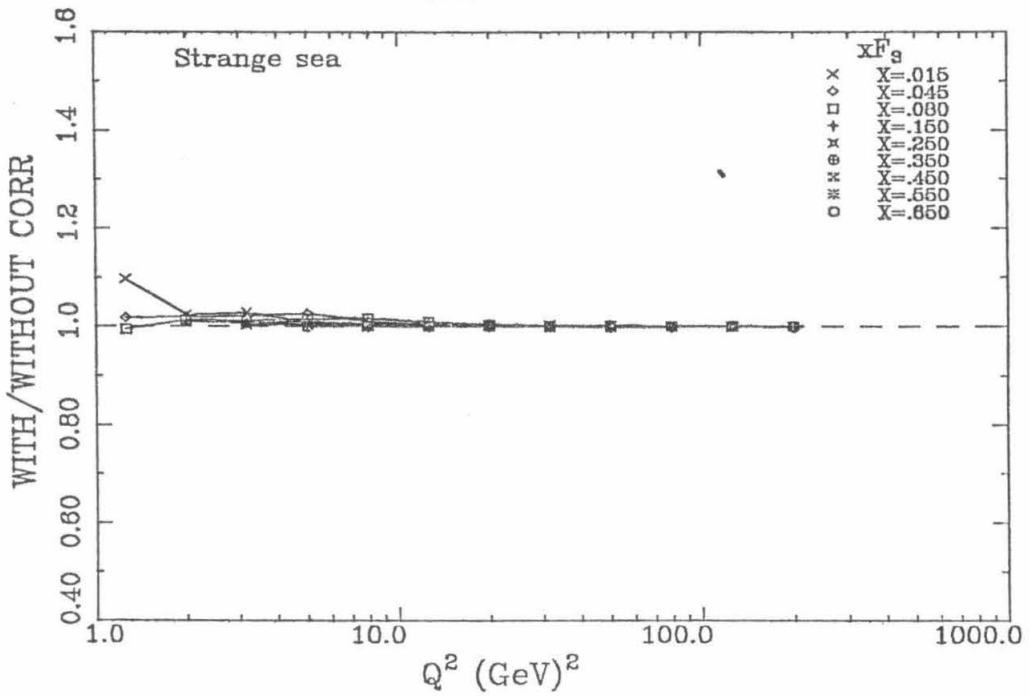
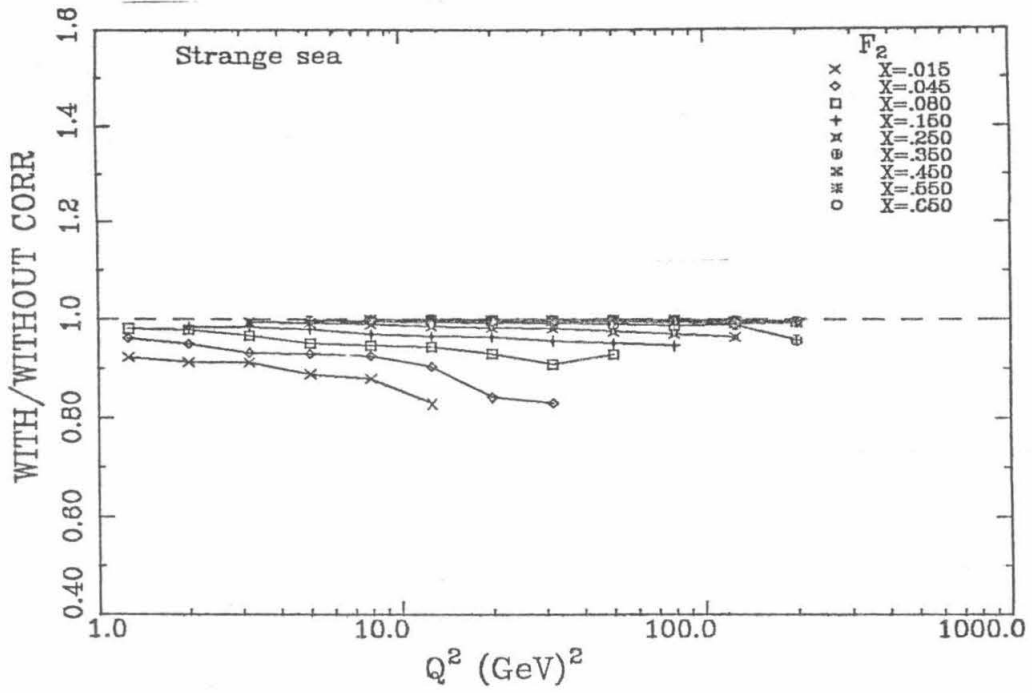


Figure 6.9. Magnitude of the strange sea correction.

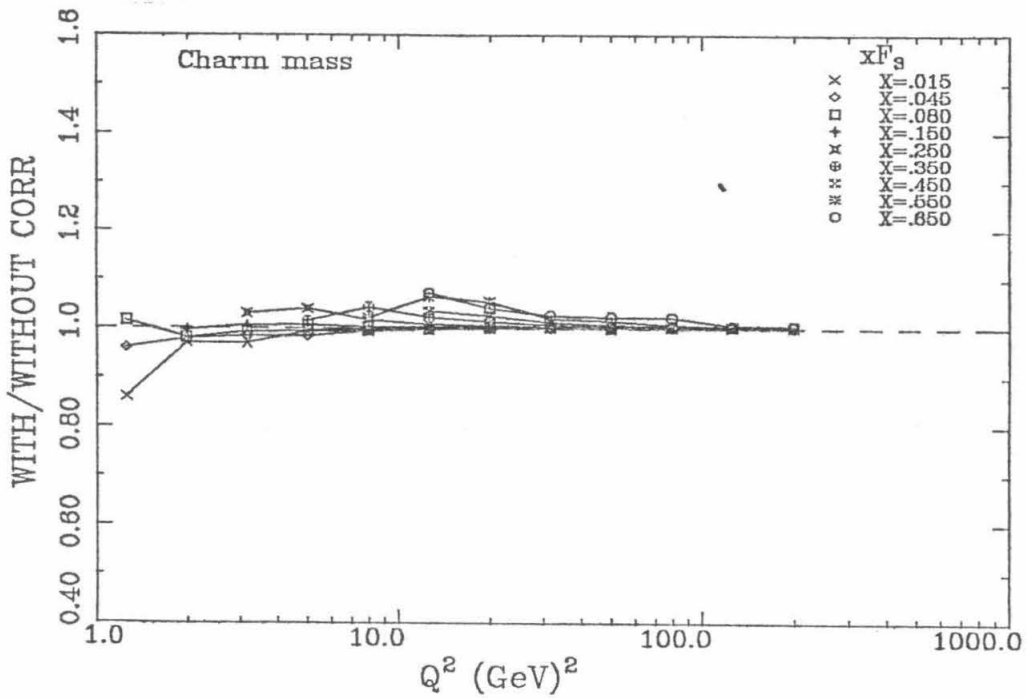
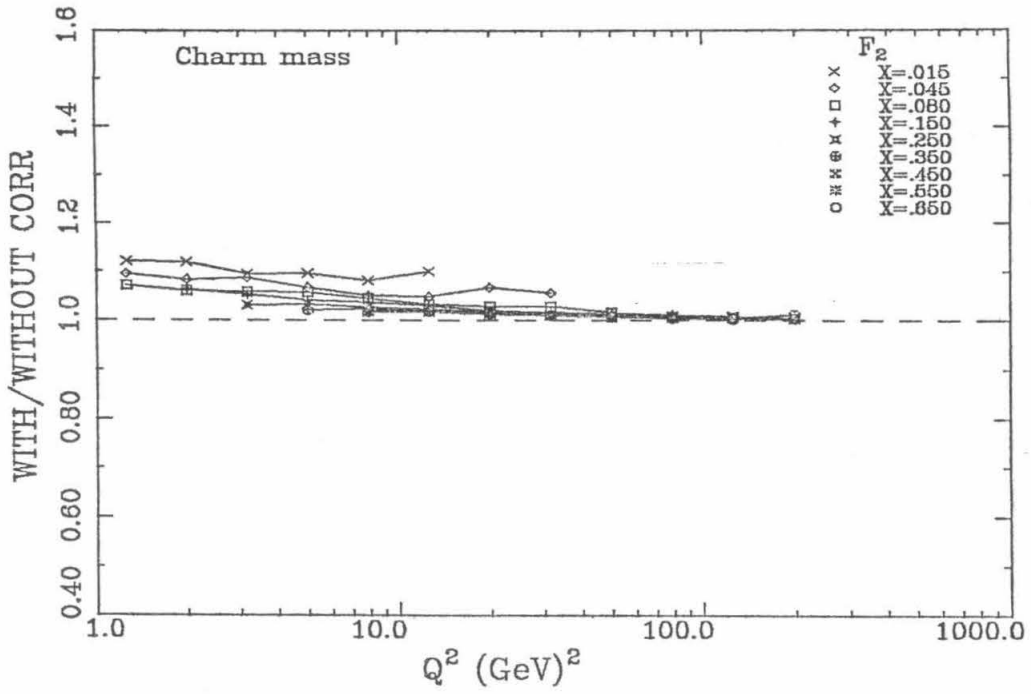


Figure 6.10. Magnitude of the charm mass correction.

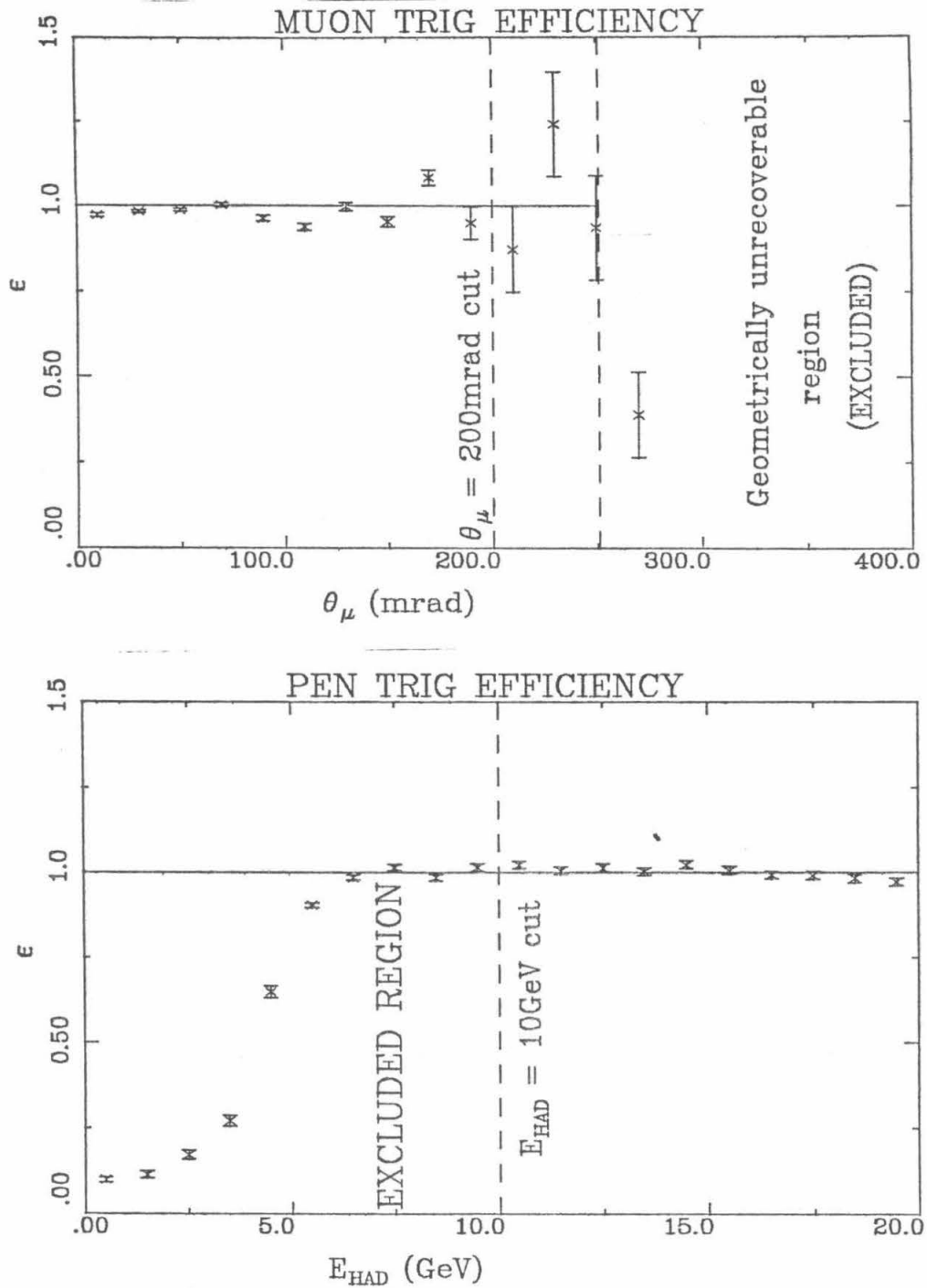


Figure 6.11

Efficiency of the muon trigger as a function of the muon angle and of the penetration trigger as a function of E_{had} .

2.5 MeV/nucleon as opposed to ~ 8.7 MeV/nucleon in Fe) and the nucleons in them are expected to be closer to being free. Data from EMC and the SLAC-MIT experiments show that the ratio of cross-sections for iron and deuterium is markedly different from predictions (fig. 6.12, refs. 38,39). Aluminum data show virtually the same x dependence as iron data. Experiments have recently been performed⁽⁸⁰⁾ to study the A -dependence of lepton-nucleon cross-sections and better theoretical understanding should result. For our purposes we shall be satisfied with the observation that the Q^2 dependence in both cases is minimal (fairly flat in Q^2) and therefore should not affect QCD studies. At this point in time it does not seem wise therefore, to make Fermi motion corrections and we have not made them.

§6.6 Systematic Errors

Estimation of systematic errors is limited by two important factors. One is the usual obstacle that systematic errors are only estimated for effects not completely understood. The other is the tendency of the statistical errors to creep into the systematic errors if the data are used for their estimation. We try to guard against the latter as far as is possible. Some of the topics listed below are not necessarily 'errors', but are included as this is a convenient place to group them with the rest. The numbers in tables H.6 and H.7 (appendix H) are the errors in individual x and Q^2 bins with no attempt to remove correlations i.e., they are the 'diagonal terms'.

i. E_{had} shift

From the hadron beam data used for E_{had} calibration we estimate a 0.41% possible error on E_{had} . Along with a 0.25% error that could come from map corrections, a total error of 0.5% is estimated. Comparisons of the predicted neutrino energy as a function of radius at Lab E with the measured energy in y -bins indicates that the systematic error on both E_{had} and E_μ is less than or equal to 1% .

This 1% is propagated into the structure functions by evaluating them with and without a 1% shift in E_{had} in the integrations. Instead of using the data for the number of neutrinos in a bin we use an integration of the 'Buras-Gaemers' model to predict these numbers, thereby eliminating the possibility of statistics dominating the result. We shall call this the 'unlimited statistics' technique for future reference. As can be seen in tables H.6 and H.7, this error is extremely small except at the highest x -values where it still is negligible compared to the statistical error.

ii. E_μ shift

The magnetic field in our toroids was measured at 3 different radii (10 in , 30 in , 50 in) with a Hall probe. We obtained $\int \mathbf{B} \cdot d\mathbf{l}$ using these data as input points and a computer program and estimate the uncertainty to be around 1% . Another experiment (E595)^(78,79) used the same toroids for muon momentum measurement. They had a muon beam (with momentum known from bending magnets) go through the toroids and the mean ratio of the two momentum measurements at different momentum settings (between 100 and 278 GeV/c) was different from 1 by $(0.7 \pm 0.6)\%$. Taken together with the estimate in (i)

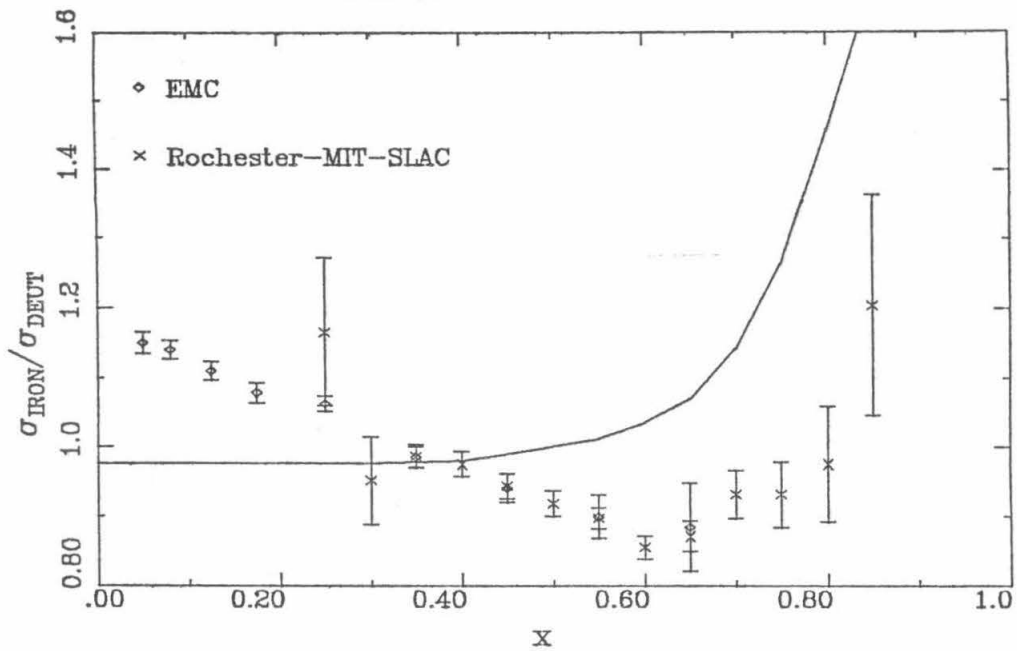


Figure 6.12

Confrontation of Fermi-motion calculations with experiment.

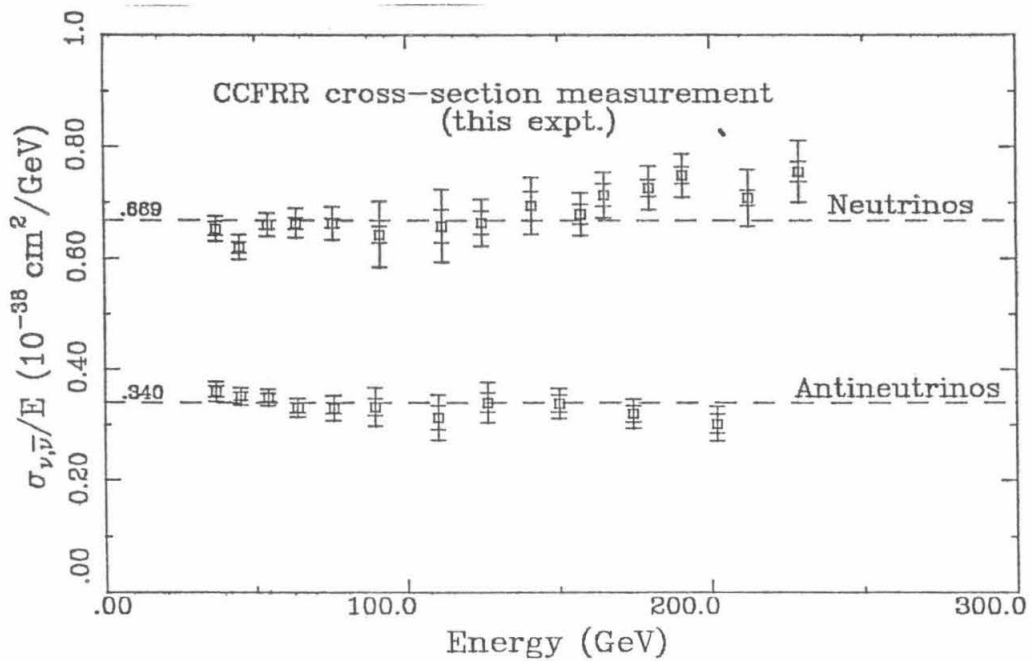


Figure 6.13

E616 cross-section slope as a function of energy.

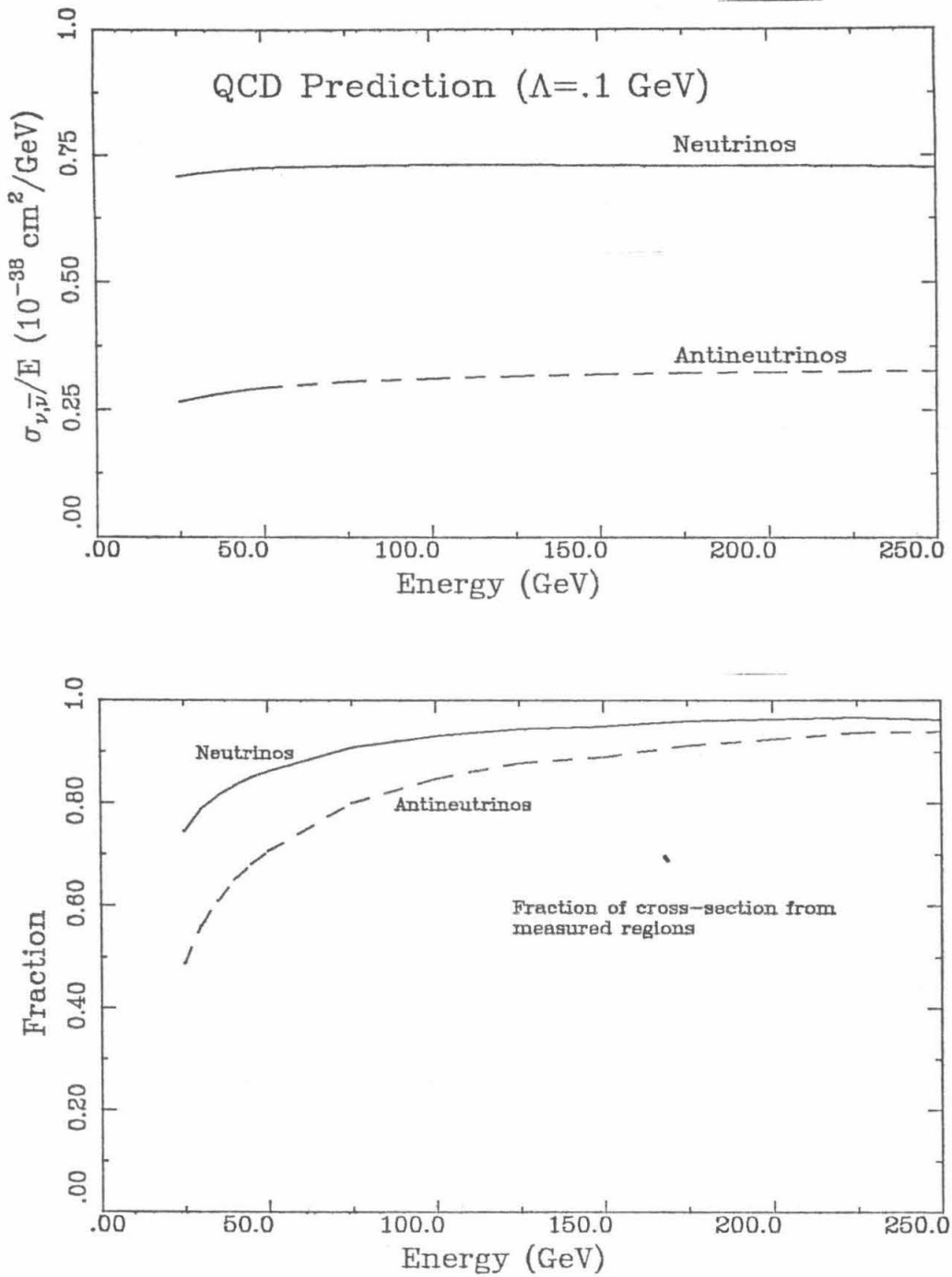


Figure 6.14

A QCD prediction ($\Lambda = 0.1 \text{ GeV}$) for the cross-section slope; fraction of the prediction that comes from regions measured by this experiment.

above, we conclude that there is possibly a 1% error on E_μ and study its effect as for E_{had} above (i.e., using 'unlimited statistics'). Again, the error is very small and gets larger at high x where it is still smaller than the statistical error.

Notice that a simple Taylor expansion of the structure functions may also be performed to obtain this and the previous error (x and Q^2 are expanded in E_μ , enabling an expansion of the structure functions in E_μ). We have checked that both procedures lead to the same values for the errors.

iii. Uncertainty in R

There is no accurate measurement of R in our Q^2 -range spanning all x . Hence we have extracted structure functions using three different values of R (see §6.5) and we take the standard deviation of the three values obtained in every bin as a measure of the error. Of course, such an estimate is subject to statistical fluctuations and yet the effect is small except at low x for F_2 as expected (see tables in appendix H). The structure functions for $R = R_{QCD}$ and $R = 0.1$ are listed in table 6.7 and G.1 respectively.

iv. Extraction technique

As mentioned in §6.4, structure functions have been extracted using two different techniques and with completely independent software. We find that the resulting integrals of F_2 and xF_3 differ by 2% and 0.3% respectively. If the difference between the two techniques weighted with statistics is plotted for all the available points, we find a mean shift of 0.8% for F_2 and 0.7% for xF_3 with standard deviations of 2.1% and 5.6% respectively. Monte Carlo studies indicate an even smaller difference: about 0.5% for the difference in the integrals of F_2 and xF_3 . Clearly, statistics plays a limiting role here. It is emphasized that in all results we use a set of structure functions that is an average of the results of the two techniques.

v. Model dependence

The dependence of the extracted structure functions on the two models used for iterating the correction terms is found to be insignificant as evidenced in tables H.6 and H.7.

vi. SU(3) symmetry of the strange sea

Analysis of our dimuon data⁽³⁵⁾ indicates that the error on the 1/2 SU(3) assumption about the strange fraction of the sea is about 35% ($\lambda_s = .50_{-0.18}^{+0.18}$). CDHS quote a smaller error⁽³⁴⁾ i.e., $\lambda_s = .52 \pm .09$. Using our value and 'unlimited statistics' we find the errors on F_2 and xF_3 (tables H.6 and H.7). Because of the similar y -dependence of the strange sea correction term and the xF_3 term we don't expect a sizeable error on xF_3 . Even for F_2 it is significant only at low x where it is less than 2%.

vii. Smearing corrections

High statistics were used to calculate these corrections making them free of statistical errors. Errors on the resolutions of E_{had} , E_μ and θ_μ and on the parameters contributed even less to the errors as was verified by changing them by one standard deviation. Therefore, no error is assumed from this source.

viii. Angular dispersion of the beam

The uncertainty in the angular dispersion of the secondary beam is discussed in the

appendix to reference 8. There it is pointed out that no obvious correlation exists among the angular dispersion errors at different momentum settings. However it appears that, in the y -view at least, the measured angular dispersion is uniformly higher than the dispersion calculated by a Monte Carlo. Since this difference was used to estimate the error, we calculate the effect of the angular dispersion in two ways: assuming perfect correlation between all dispersions and assuming no correlations between them.

The perfect correlation case is easy: we perform the integrals necessary for structure function extraction and use 'unlimited statistics' with and without all the dispersions off by one standard deviation in the same direction. The uncorrelated case is handled by randomly throwing an angular dispersion at each energy setting using a Gaussian distribution with the known mean and standard deviation and then evaluating the integrals. This procedure was repeated 26 times and the standard deviation of the resulting structure functions in each bin was taken to be the error. The two assumptions about the correlations bracket the error from this source; in summary we find that it is less than 2% and always much smaller than the statistical error.

ix. Flux level uncertainties

Both correlated and uncorrelated uncertainties in the flux levels of neutrinos and antineutrinos contribute to systematic uncertainties in the values of F_2 and xF_3 . The correlated parts of the errors directly translate into errors on F_2 and xF_3 of the same magnitude. The error on F_2 due to the uncorrelated errors on the ν and $\bar{\nu}$ flux levels lies between the two (since F_2 is related to the sum of the differential cross-sections). However, the same is obviously not true of xF_3 . As can be seen in table H.7, for $x = 0.15$ and $x = 0.25$ this error is roughly equal to the statistical error and therefore must be heeded in any higher statistics experiment.

ν			$\bar{\nu}$	
Correlated	Uncorrelated		Correlated	Uncorrelated
1.5%		Ion ch. calib.	1.5%	
2.0%		Connection to ion ch. calib. run	2.0%	
		+ to - changeover		3%
	1%	Ion ch. temperature		1%
	1%	Proton fraction		
1%		E_ν error	1%	
0.5%		Veto deadtime	0.5%	
2.3%		Lab E livetime	0.7%	
0.5%		χ^2 losses	0.5%	

Table 6.6. Sources of systematic errors on fluxes

Most sources of flux level uncertainties are described in reference 8. We list in table 6.6 all the errors assumed. The error due to temperature comes from the variation in

the temperature of the Čerenkov counter (which is close to the ion chamber) during the running period. For the positive momentum settings, protons were a major fraction in the flux and the uncertainty in the proton fraction is added as a source of error. We have added a 0.5% error on the events lost due to a bad χ^2 ($\chi^2/DF > 9$) in the fluxes, as this is the most convenient place to include this error. Similarly, a 1% systematic error on E_ν is also added here. The error on the Lab E livetime comes from a comparison of the live muon trigger rate at Lab E and the livetime proton fraction in the BCT.

In summary, the overall error on the neutrino flux level is 3.9% , that on the antineutrino flux level is 4.3% and the correlation coefficient is 0.57. The uncertainties on the structure functions were calculated using the same technique as for the E_{had} error, i.e., using simulated 'unlimited statistics'.

x. Flat cross-section correction

As described in §6.5, we correct for particle fraction errors using the constraint that the structure functions from different energy settings be the same. As for the uncorrelated angular dispersions we randomly throw the flux adjustment factors and use simulated unlimited statistics to estimate the errors shown in tables H.6 and H.7. These are, again, much smaller than the statistical errors. In a higher statistics experiment with precisely measured particle fractions, presumably there will be no need for such a correction.

§6.7 Results and Comparisons

The final results for $R=R_{QCD}$ are displayed in figures 6.15 and 6.16 and in table 6.7. Appendix G contains the $R = 0.1$ results. In both cases as well as in all the analysis we use the average of the results from the two extraction techniques. The statistical errors on the structure functions are, of course, easily estimated from (6.12). We eliminate bins with a statistical error greater than 50% . Not unexpectedly, most of these bins are also the ones with larger systematic errors. As is clear from the previous section, the magnitude of the various systematic errors is not the major limitation for us – it is the statistical errors.

x	Q^2	F_2	ΔF_2	$x F_3$	$\Delta x F_3$
.015	1.259	1.28722	.05054	.16496	.05778
	1.995	1.34295	.05850	.36558	.05555
	3.162	1.53678	.08391	.30329	.07627
	5.012	1.40248	.11610	.43061	.10614
	7.943	1.58422	.26887	-	-
.045	1.259	1.13355	.05026	.44017	.14347
	1.995	1.35851	.04696	.61983	.08875
	3.162	1.36325	.04445	.60818	.06233
	5.012	1.54465	.05858	.50844	.07176
	7.943	1.66153	.08052	.69292	.09354
	12.589	1.53078	.11347	.64604	.11634
19.953	1.07091	.19650	.63074	.18162	
.080	1.259	1.24351	.12804	-	-
	1.995	1.44496	.05454	.61452	.18234
	3.162	1.48738	.04635	.76930	.10337
	5.012	1.46410	.04393	.66560	.06999
	7.943	1.54460	.05137	.65504	.06895
	12.589	1.59056	.06787	.78069	.08524
	19.953	1.57623	.08978	.77118	.09767
31.623	1.22757	.16582	.66213	.16162	
.150	1.995	1.18261	.10895	-	-
	3.162	1.18013	.03634	.73186	.13484
	5.012	1.28000	.02828	.68901	.07346
	7.943	1.23488	.02545	.87850	.04599
	12.589	1.23209	.02815	.85483	.04166
	19.953	1.29159	.03614	.79031	.04853
	31.623	1.26979	.04625	.84719	.05516
	50.119	1.16089	.07534	.79934	.07985
79.433	0.88873	.25122	.70402	.23871	
.250	3.162	1.86830	.72375	-	-
	5.012	1.02552	.03873	.62307	.16119
	7.943	0.98540	.02647	.79386	.07627
	12.589	0.93337	.02412	.79652	.04805
	19.953	0.92345	.02640	.76972	.04247
	31.623	0.95203	.03339	.79887	.04974
	50.119	0.83999	.03383	.74736	.04232
	79.433	0.74729	.05295	.65042	.05688
	125.893	0.56844	.27936	-	-

x	Q^2	F_2	ΔF_2	xF_3	ΔxF_3
.350	5.012	0.88210	.18935	-	-
	7.943	0.67603	.02730	.58361	.10834
	12.589	0.64851	.02250	.55283	.05959
	19.953	0.63772	.02381	.46873	.04743
	31.623	0.62709	.02743	.51247	.04784
	50.119	0.58736	.02812	.56287	.04116
	79.433	0.59725	.03720	.50031	.04531
	125.893	0.68446	.07624	.26579	.08257
.450	7.943	0.49786	.04114	-	-
	12.589	0.41907	.01975	.45220	.06766
	19.953	0.39458	.01866	.30636	.04320
	31.623	0.38217	.02039	.31889	.03833
	50.119	0.34730	.02115	.33956	.03577
	79.433	0.37452	.02649	.31687	.03652
	125.893	0.27919	.02780	.30267	.03180
	199.526	0.28974	.13247	.30152	.13921
.550	12.589	0.24078	.01712	.21779	.07091
	19.953	0.23066	.01550	.16832	.04358
	31.623	0.20599	.01434	.20865	.02944
	50.119	0.19837	.01807	.17112	.03260
	79.433	0.19854	.02046	.16888	.03086
	125.893	0.14983	.01905	.16956	.02377
	199.526	0.11988	.04019	.12987	.04402
.650	12.589	0.14994	.01762	.16284	.07990
	19.953	0.12042	.01044	.17144	.03326
	31.623	0.13803	.01507	.12170	.03943
	50.119	0.11095	.01453	.07206	.03036
	79.433	0.09837	.01613	.05842	.02795
	125.893	0.09249	.01350	.09891	.01817
	199.526	0.06768	.02048	.07645	.02343

Table 6.7. F_2 and xF_3 with statistical errors for $R=R_{QCD}$

We shall defer the comparison of F_2 from different experiments until its natural place among the tests of the quark parton model (§7.4). Comparison of the integrals of F_2 and xF_3 with the total neutrino and antineutrino cross-sections is complicated by the fact that the former covers only a subset of the region in x and Q^2 covered by the latter. The total cross-section results include events out to larger angles and smaller hadron energies (§6.2 and appendix E). For this reason, we cannot make an exact comparison. Approximately, however, the results of the $R=0$ and $R=0.1$ extractions can be used with the relation between the total cross-section slopes and the structure function integrals. In the scaling approximation and

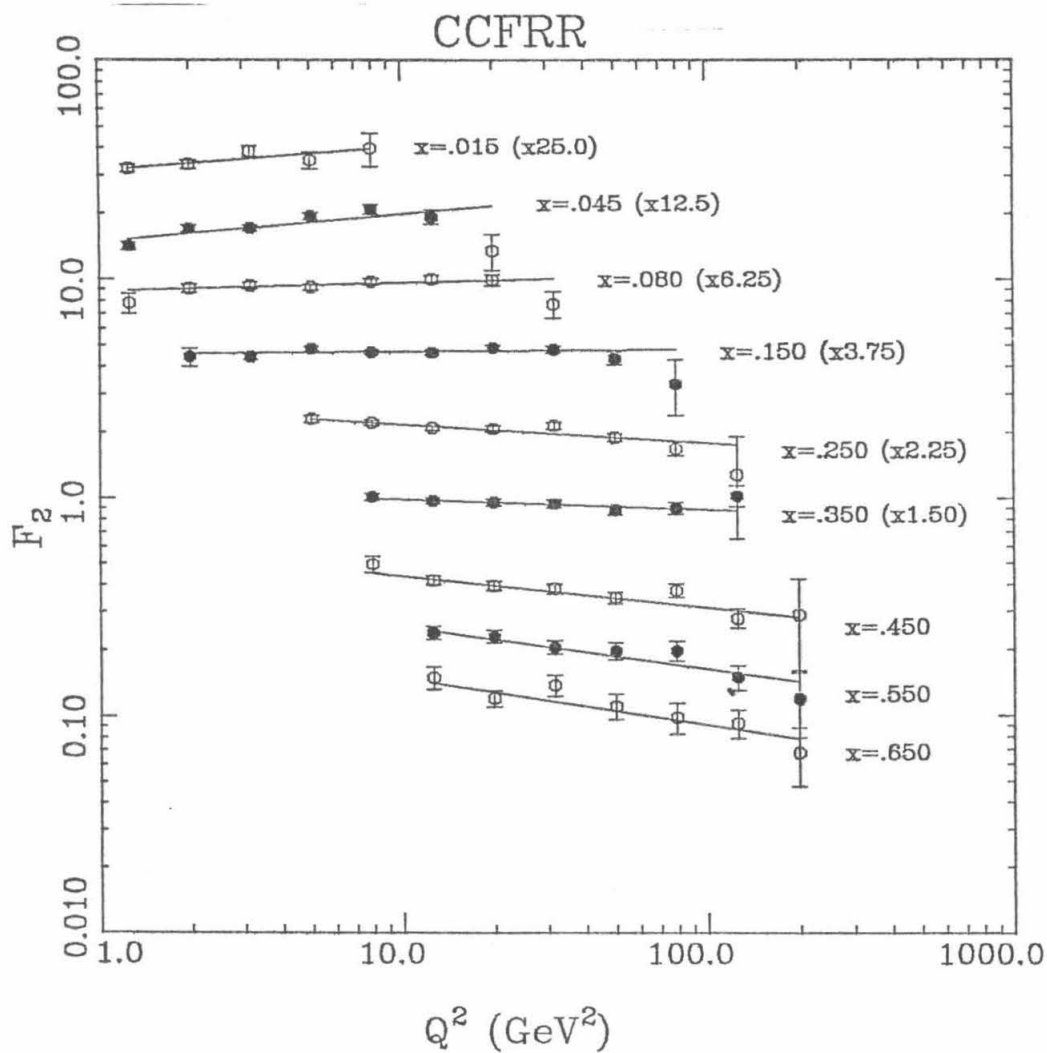


Figure 6.15. The structure function $F_2(x, Q^2)$ for $R=R_{QCD}$

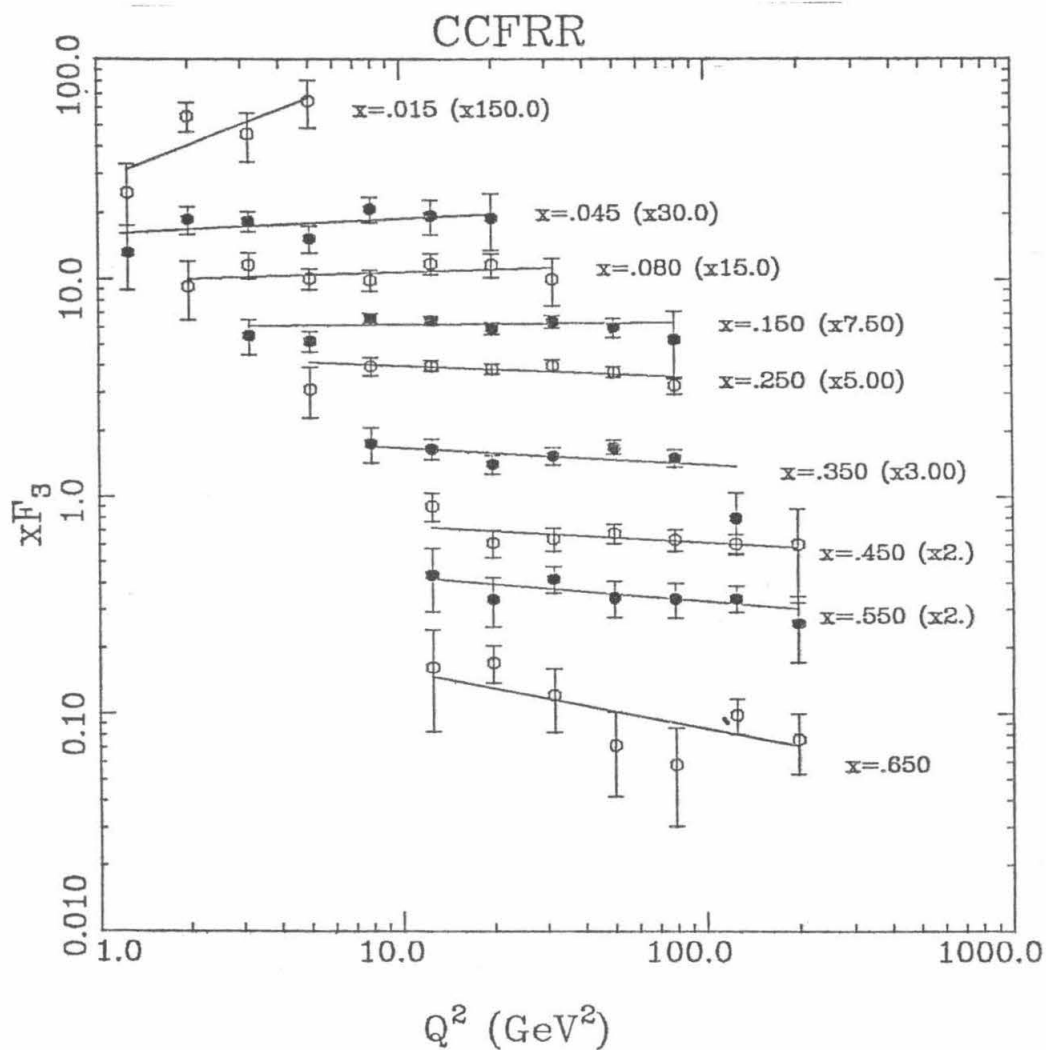


Figure 6.16. The structure function $x F_3(x, Q^2)$ for $R=R_{QCD}$

neglecting the effects of a non-zero charm quark mass,

$$\begin{aligned}\frac{\sigma^\nu + \sigma^{\bar{\nu}}}{E} &= \frac{4}{3} \frac{G^2 m_p}{\pi} c' \int_0^1 F_2 dx \\ \frac{\sigma^\nu - \sigma^{\bar{\nu}}}{E} &= \frac{2}{3} \frac{G^2 m_p}{\pi} \int_0^1 x F_3 dx\end{aligned}\tag{6.26}$$

where,

$$c' = \left(1 + \frac{3}{4}R + \frac{1}{2} \frac{\int (s + \bar{s}) dx}{\int (q + \bar{q}) dx} \right) / (1 + R)\tag{6.27}$$

These approximate relations serve as a useful check on the internal consistency of data sets. For $R=0.1$ and $\int (s + \bar{s}) dx / \int (q + \bar{q}) dx = .05$, $c' = 1$. This corresponds to the assumption of a 1/2 SU(3) symmetric sea. In table 6.8 we make a comparison of the various available high statistics data sets. Different experiments make different assumptions about R as listed. To facilitate comparisons we have homogenized the data sets by making appropriate corrections (very small) in each case to obtain data with the following uniform assumptions in all cases:

- (i) A 1/2 SU(3) symmetric strange sea.
- (ii) A mass of 80 GeV/c² for the W boson.
- (iii) Complete coverage of the $0 < x < 1$ region.
- (iv) A zero mass for the charmed quark.

All the data sets seem internally consistent, within errors, except for the CDHS data set where the integrals of the structure functions, especially the integral of F_2 , are not compatible with the prediction from the cross-sections.

With this in mind, we now compare the $x F_3$ results for the different data sets. As is clear from table 6.8, there are differences in the overall levels of $x F_3$ from the four experiments, with our data and the HPWF data having the largest integrals followed by CHARM (12.3%) lower and then CDHS (16.3% lower). The CHARM level difference is covered by systematic errors, and the CDHS difference is 1.4σ away from zero, still plausible. If we take the prediction for $\int x F_3$ from the cross-sections as the best measure of $\int x F_3$, then all the experiments are consistent with each other within errors.

	CCFRR	CCFRR	CDHS	CHARM	HPWF
σ_ν/E	.669±.024	.669±.024	.62±.022	.604±.032	.63±.02
$\sigma_{\bar{\nu}}/E$.340±.020	.340±.020	.30±.013	.301±.018	.30±.01
R	0.	0.1	0.1	0.	0.
$\int F_2$ predicted from cross-sections	.466±.015	.478±.015	.436±.012	.418±.017	.430±.010
$\int xF_3$ predicted from cross-sections	.312±.030	.312±.030	.303±.024	.287±.035	.313±.021
$\int F_2$ from data (statistical errors only)	.474±.003	.482±.003	.402±.002	.412±.006	.458±.003
$\int xF_3$ from data (statistical errors only)	.328±.005	.326±.005	.273±.003	.285±.012	.322±.005

Table 6.8. Comparison of integrals of data sets

Apart from level differences, we can compare the x and Q^2 behaviour of xF_3 . First we make linear fits in $\log Q^2$ to data in a given x bin (since scaling violations are expected to depend on $\log Q^2$).

$$xF_3(x, Q^2) = a + b \log_{10} \left(\frac{Q^2}{10 \text{ GeV}^2} \right) \quad (6.28)$$

10 GeV^2 is chosen as it is roughly the central point in $\log Q^2$ for the data. To make the comparison of the x -behaviour of the structure functions, we then fit a form to our xF_3 data at $Q^2 = 10 \text{ GeV}^2$:

$$xF_3(x, Q^2 = 10 \text{ GeV}^2) = Ax^\alpha(1-x)^\beta \quad (6.29)$$

The resulting fit parameters are

$$\begin{aligned} A &= 3.49 \pm .61 \\ \alpha &= .511 \pm .069 \\ \beta &= 2.96 \pm .24 \end{aligned} \quad (6.30)$$

with a $\chi^2/DF = 1.05$.

We then divide the values of xF_3 at a given x for a given data set by the value of this fit at that x . The resulting ratios are plotted in fig. 6.17. Systematic errors are not included on the points since we are ignoring overall level differences; they are shown at the right with the dashed lines indicating the ratios expected from the integrals of xF_3 averaged over Q^2 . Clearly, the HPWF data show a marked rise with x . Although this is in the right direction expected from the EMC effect⁽³⁸⁾ (since HPWF have a mixture of iron and scintillator as a target) we do not expect that effect to be quite as large as the observed variation. However, no definite quantitative statement can be made until the EMC effect has been studied in materials other than deuterium, aluminum and iron, the only substances for which data are presently available.

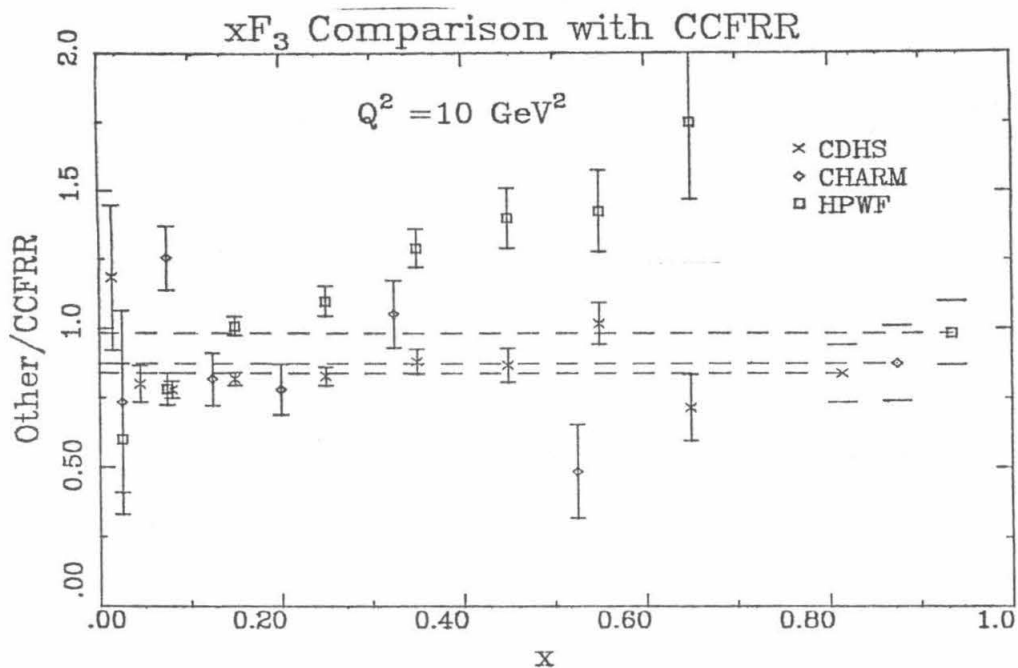


Figure 6.17

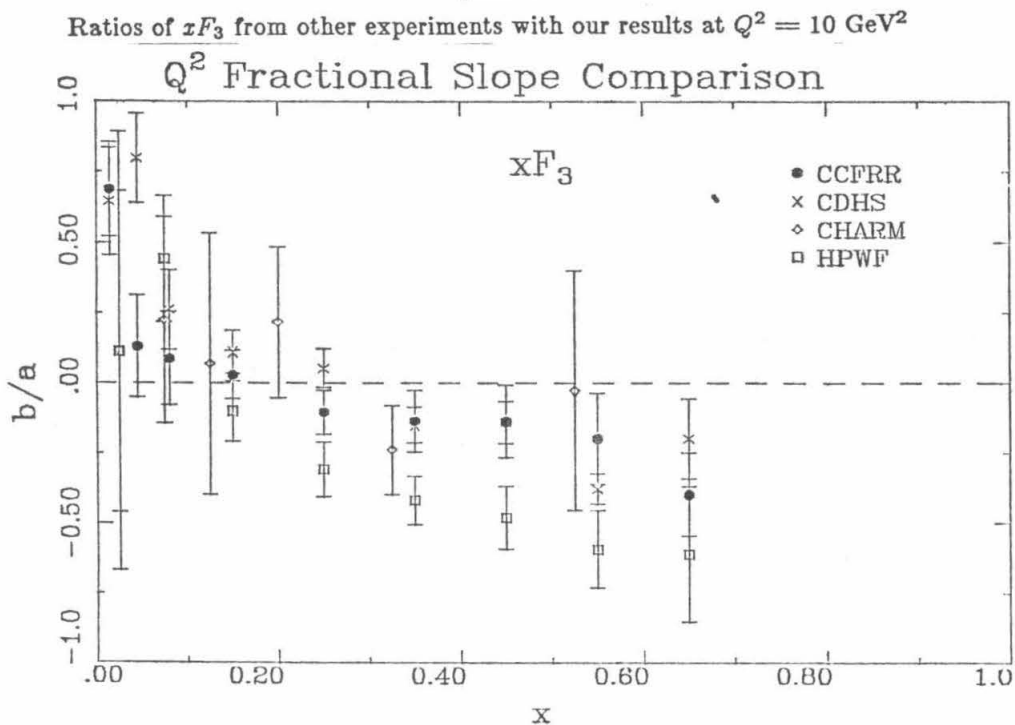


Figure 6.18

Fractional slopes w.r.t. $\log_{10} Q^2$ of xF_3 from various experiments.

The CHARM ratios suffer from poor statistics and are consistent with being flat. The CDHS data show a slight rise with x , but not as marked as in the F_2 case (§7.4). The ratios at high x , of course, track those of F_2 . We conclude that there is a rise in the ratio as x increases but keeping in mind the additional systematic errors not associated with level differences, the rise appears to be smaller than for F_2 .

The fractional slope (b/a – eqn. 6.28) of xF_3 in various bins is shown in figure 6.18. Again, the errors displayed are only statistical and again the errors on the CHARM data are too large to warrant any firm conclusions about that data set. Clearly, the HPWF data exhibit the largest scaling violation. That data set spans a range with slightly lower Q^2 values ($.7 \text{ GeV}^2 < Q^2 < 125 \text{ GeV}^2$), where non-perturbative effects are expected to be larger, but this does not seem enough to explain the observed magnitude, especially at high x where Q^2 values are higher. The CCFRR and CDHS data sets both show a smaller Q^2 dependence and are clearly consistent with each other, except at $x = .045$, with CDHS showing a slightly larger scaling violation. A more rigorous QCD analysis of the scaling violations in our data are presented in §7.5.

More graphic displays of the differences between the data sets are shown in figures 6.19, 6.20 and 6.21. In these plots, the dashed lines are the fits to our data and the solid lines are these same fits with the overall level adjusted so as to best fit the data set displayed. Thus the difference in levels of the two lines indicates the degree of x -dependent differences and the goodness of fit of the solid line indicates the level of agreement between the Q^2 behaviours. There are insufficient data from the CHARM group at all their x values. The observations above about CDHS and HPWF remain the same. We conclude that xF_3 from the CDHS group is in agreement with our values for xF_3 , but it will be interesting to see if this holds true when higher statistics data are available.

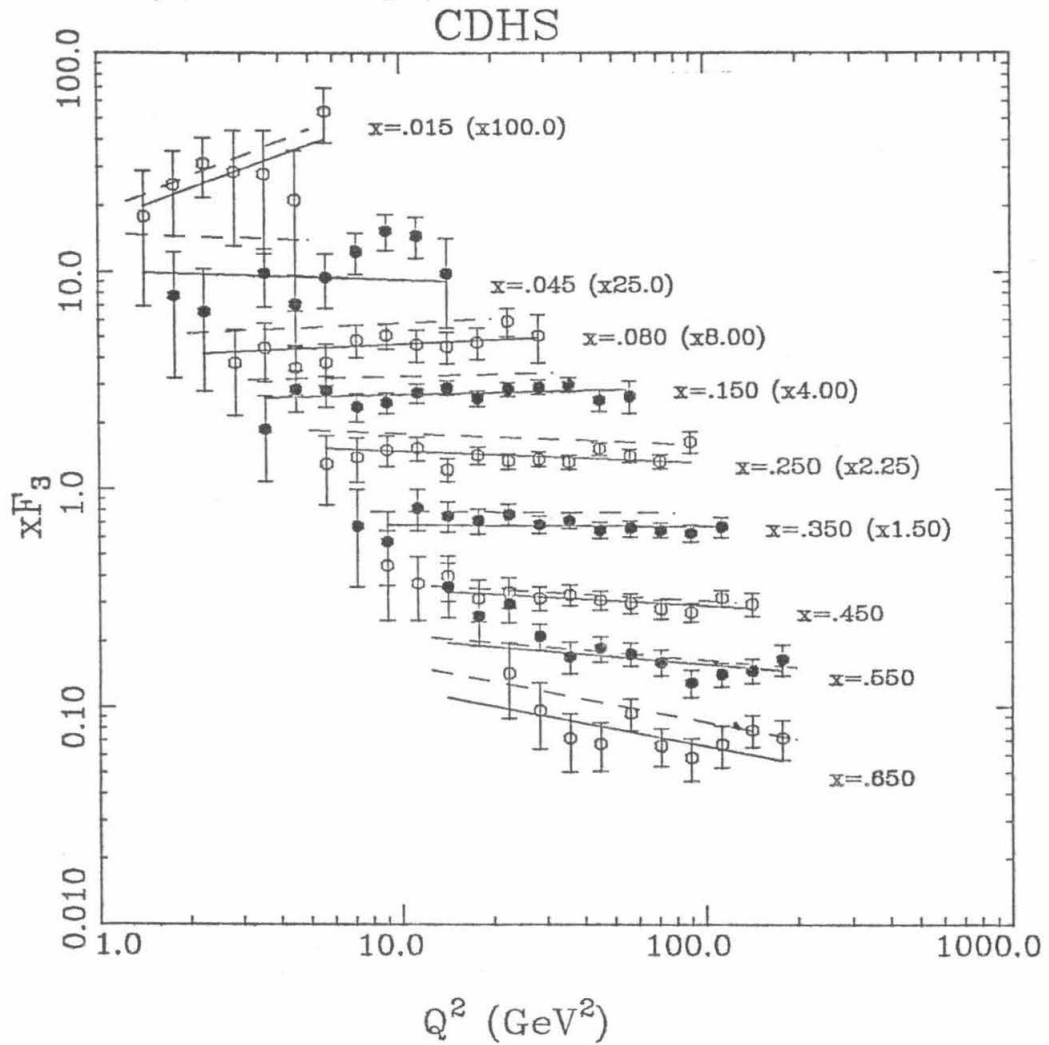


Figure 6.19

$x F_3$ from the CDHS group with fits to our data (dashed lines) and the same fits adjusted to the level of the CDHS data (solid lines) in our Q^2 range.

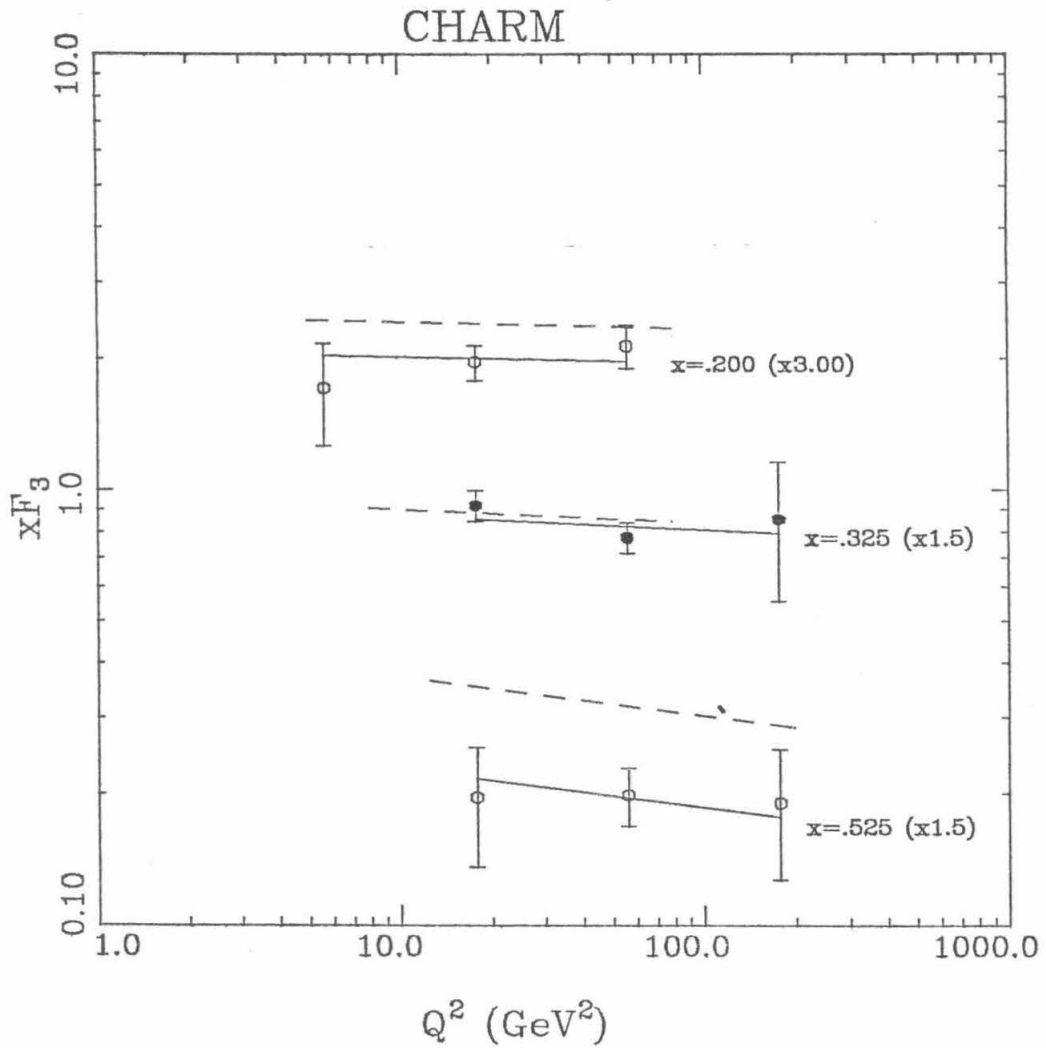


Figure 6.20

xF_3 from the CHARM group with fits to our data (dashed lines) and the same fits adjusted to the level of the CHARM data (solid lines) in our Q^2 range.

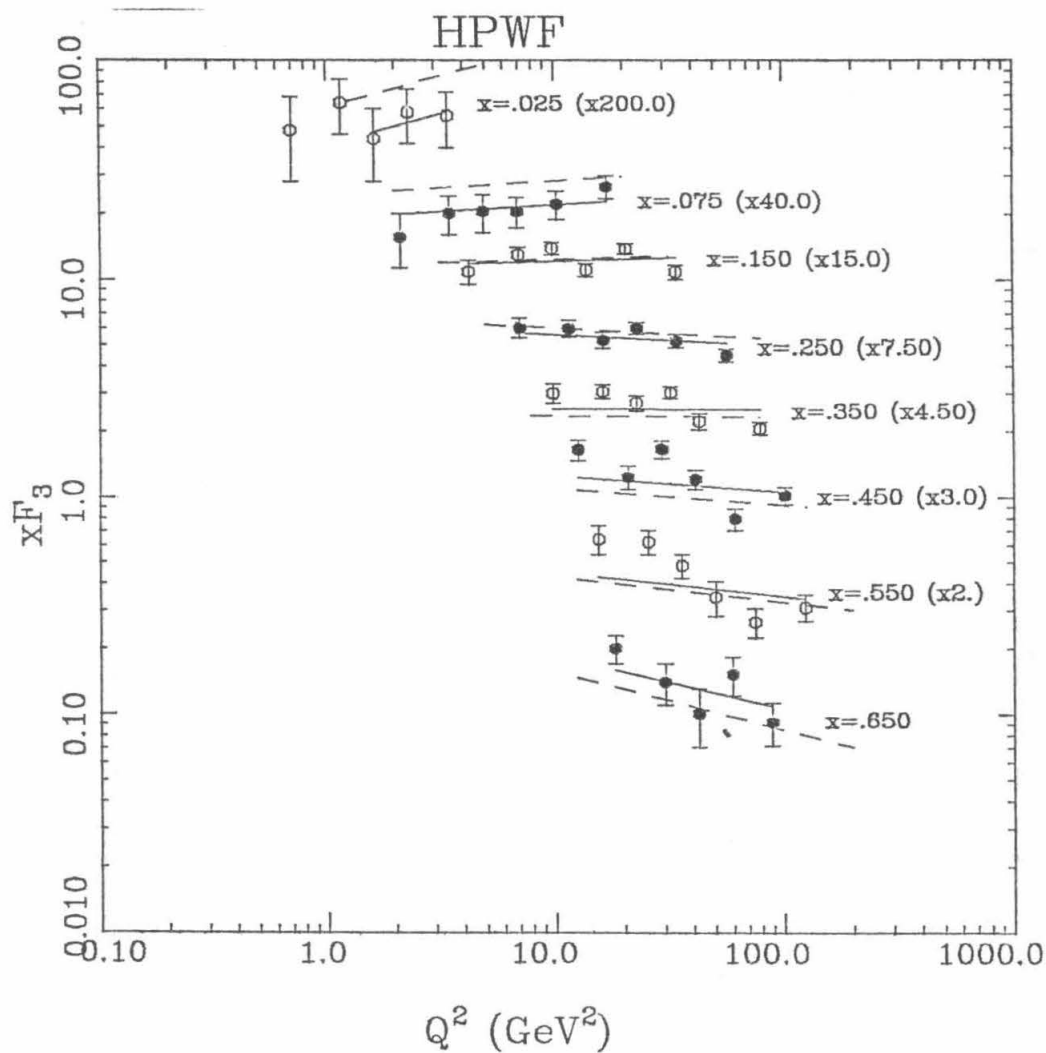


Figure 6.21

$x F_3$ from the HPWF group with fits to our data (dashed lines) and the same fits adjusted to the level of the HPWF data (solid lines) in our Q^2 range.

Physics Analysis and Conclusions

In the first three sections of this chapter we present a brief theoretical outline of the physics of charged current neutrino interactions. Comparisons of the data with theory begin with §7.4.

§7.1 Weak Interactions

In 1934 Fermi proposed^(48,49) a current-current interaction theory of weak interactions which together with universality, explained a whole range of weak processes. In this theory the weak interactions occurred at a point, with one current interacting with the other directly, and not through a mediating quantum.

Later, a couple of modifications had to be made. The intermediate vector bosons were introduced to mediate the current-current interaction. Since they were not observed in decays and high-energy neutrino interactions, they were assigned a high mass, ≥ 5 GeV. Recent neutrino scattering experiments pushed this limit up to ~ 30 GeV. The massive nature of these bosons implies a short-distance weak interaction, as opposed to QED. The prediction and discovery of parity violation^(50,51) further changed the theory. Only left-handed neutrinos and right-handed antineutrinos were allowed, and leptonic weak currents could only have a V-A nature. Subsequently, universality was extended to the non-leptonic (quark) weak currents by Cabibbo.⁽⁵²⁾ The weak charged current changed u -quarks into a state that is a mixture of d -quarks and s -quarks:

$$\begin{aligned}d_c &= d \cos \theta_c + s \sin \theta_c \\s_c &= -d \sin \theta_c + s \cos \theta_c\end{aligned}$$

This extension seemed to imply the presence of weak neutral currents, but the experimental absence of strangeness-changing neutral currents discouraged much progress. By this time Glashow⁽⁵³⁾ (1961), and then Weinberg⁽⁵⁴⁾ (1967) and Salam⁽⁵⁵⁾ (1968) had proposed a model of weak interactions. Glashow, Iliopoulos and Maiani⁽⁵⁶⁾ proposed a mechanism in 1970 which

completed the s_c doublet by adding a fourth-quark, called "charm". This also explained the very small $K_L^0 \rightarrow \mu^+ \mu^-$ decay rate, expected to be of the same order as $K^+ \rightarrow \mu^+ \nu_\mu$. In fact this was used to predict m_c to be between 1 and 3 GeV.

The Fermi theory involving point interactions could not handle higher-order corrections to processes like $\nu_\mu e^- \rightarrow \nu_\mu e^-$: in every order infinities appear and we need an infinite number of parameters to correct for them. For this reason the Fermi theory is non-renormalizable and in spite of its dimensionless coupling constant, so is the intermediate vector boson model. In 1971 't Hooft⁽⁵⁷⁾ showed that gauge theories with massive fields introduced by spontaneous symmetry breaking, as in the standard model, were renormalizable. In the early 1970s neutral currents were discovered in high energy neutrino scattering experiments (1973, 1974) and by November 1974 the charmed quark had been inferred to exist. Hence by this time the standard model had been accepted. Today we believe that the W^\pm and Z^0 have been observed^(45,46) leaving only the Higgs scalar to complete the triumph of the GSW theory.

In this now accepted theory, the charged current couplings are still strictly V-A:

$$J_\mu^{CC} = \sum_{l=\{e,\mu,\tau\}} \bar{\nu}_l \gamma_\mu \frac{(1-\gamma_5)}{2} l + \bar{U}_i \gamma_\mu \frac{(1-\gamma_5)}{2} M_{ij} L_j \quad (7.1)$$

$$U = (u, c, t) \quad (7.2)$$

$$L = (d, s, b) \quad (7.3)$$

and M_{ij} connects them (the Kobayashi-Maskawa⁽⁵⁸⁾ matrix). For example the familiar Cabibbo mixing angle is now

$$M_{ud} = \cos \theta_1 = \cos \theta_C \quad (7.4)$$

$$\text{Experimentally, } \cos \theta_C = 0.9737 \pm 0.0025^{(47)}. \quad (7.5)$$

The neutral current couplings are no longer strictly V-A, they are in general some linear combination of V and A which depends on $\sin^2 \theta_W$, where θ_W is the Glashow-Weinberg angle.

$$\sin^2 \theta_W \approx 0.23 \quad (7.6)$$

The standard model is based on the observation that only left-handed components of charged current lepton wavefunctions interact as weak charged currents, their right-handed counterparts do not. Of course, only left-handed neutrinos exist. This suggests consideration of the left-handed lepton and its neutrino as a doublet under some symmetry and the right-handed lepton as a singlet. In the quark sector, the left handed components of $+2/3$ quarks and their K-M rotated $-1/3$ counterparts form weak doublets, the right-handed parts all falling into singlets.

This symmetry leads to a SU(2) gauge invariance and associated is a weak isospin. For example, the neutrino has $I_3^{wk} = +1/2$ and the left handed lepton has $I_3^{wk} = -1/2$. An

SU(2) gauge theory has only 3 gauge fields however, and associating this triplet with W^\pm and Z^0 gives the same V-A nature for both charged and neutral currents. Consequently, a weak hypercharge is introduced with a corresponding U(1) group. In order that the W^\pm and Z^0 are massive and the photon remains massless the mechanism of spontaneous symmetry breaking is invoked. In the resulting model, the weak charge g turns out to be related to e by

$$g \sin \theta_W = e \quad (7.7)$$

Also, the masses of the W^\pm and Z^0 come out as

$$m_W = \frac{e}{2 \sin \theta_W} \frac{1}{\sqrt{\sqrt{2} G_F}} \approx 80 \text{ GeV} \quad (7.8)$$

$$\text{and } m_Z = \frac{m_W}{\cos \theta_W} \approx 90 \text{ GeV} \quad (7.9)$$

The m_W along with a propagator term for the W^\pm contribute a factor $1/(1 + Q^2/m_W^2)^2$ that modifies the current-current expression for charged current neutrino scattering. This fact and the V-A nature of charged current interactions are the most important features of the standard model relevant to us.

§7.2 The Parton Model

We now turn from the nature of the interaction vertices to the object being probed viz., the nucleon. Traditionally, the parton model is introduced via charged lepton scattering and we do the same. Consider the scattering diagram in fig. 7.1. The cross-section for this process is given by

$$\frac{d^2 \sigma}{d\Omega dE'} = \frac{E'}{E} |M|^2 \quad (7.10)$$

The matrix element squared is

$$\frac{1}{4} \sum_X \sum_{s_p} \sum_{s'} \sum_s \bar{u}(k' s') \gamma_\mu u(k s) \bar{u}(k s) \gamma_\nu u(k' s') \frac{\alpha^2}{Q^4} \langle p, s_p | J^\mu | X \rangle \langle X | J^\nu | p, s_p \rangle (2\pi)^4 \delta^4(p + q - p') \quad (7.11)$$

This can be separated into a lepton tensor $L_{\mu\nu}$ which is evaluated to be

$$L_{\mu\nu} = 2[k'_\mu k_\nu + k'_\nu k_\mu + \frac{q^2}{2} g_{\mu\nu}] \quad (7.12)$$

and a hadron tensor $W^{\mu\nu}$. Since we do not know the final state X, we use gauge invariance, Lorentz invariance and the symmetry of $L_{\mu\nu}$ to write $W^{\mu\nu}$ in terms of only 2 structure functions,

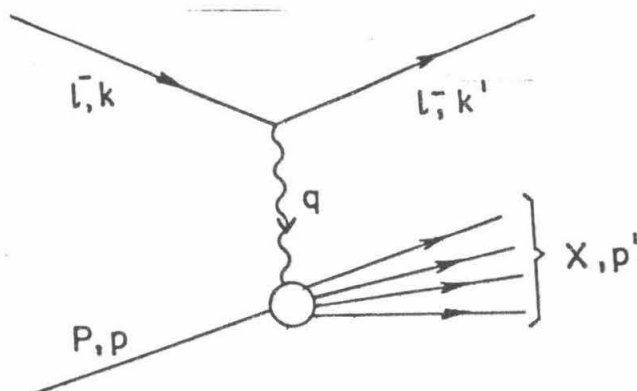


Figure 7.1. Diagram for electron-nucleon scattering.

W_1 and W_2 which are functions of $Q^2 (= -q^2)$ and $\nu (= k_0 - k'_0)$:

$$W^{\mu\nu} = W_1(\nu, q^2) \left(-g^{\mu\nu} + \frac{q^\mu q^\nu}{q^2} \right) + W_2(\nu, q^2) \left\{ \left(p^\mu - \frac{p \cdot q}{q^2} q^\mu \right) \left(p^\nu - \frac{p \cdot q}{q^2} q^\nu \right) \right\} \quad (7.13)$$

This leads finally to

$$\frac{d^2\sigma}{dE' d\Omega} = \frac{\alpha^2}{4E^2 \sin^4(\theta/2)} [2W_1(\nu, Q^2) \sin^2(\theta/2) + W_2(\nu, Q^2) \cos^2(\theta/2)] \quad (7.14)$$

Bjorken argued⁽⁵⁹⁾ that the structure functions W_1 and W_2 are functions of $x = Q^2/2m\nu$ alone in the limit in which $Q^2 \rightarrow \infty$ and $\nu \rightarrow \infty$. This is the celebrated phenomenon of scaling in which the structure functions $F_2 (= \nu W_2)$ and $2xF_1 (= 2mxW_1)$ are functions of x alone and do not depend on Q^2 . Feynman interpreted this⁽³⁾ as evidence that the nucleon is composed of point scatterers, called partons. Scattering of leptons from these partons then imposes an elastic scattering condition, $Q^2 = 2m_q\nu$ where m_q is the mass of the parton.

It is instructive to work out the kinematics of parton scattering. If the parton carries a fraction ξ of the initial nucleon momentum p then

$$(\xi p + q)^2 = m_f^2 \quad (7.15)$$

where m_f is the mass of the final state quark, giving

$$\xi \approx \frac{Q^2 + m_f^2}{2m_p\nu} \quad (7.16)$$

Clearly, ξ is identified with x above (we neglect all masses.)

By now, it has become natural to identify these partons with quarks, the constituents of a nucleon. The parton model of the nucleon assumes that the quarks are confined within the nucleon, but that this confining force acts over a sufficiently long time scale so it doesn't interfere with probe-parton scattering at high Q^2 . The identification of partons as quarks is further established by the discovery that the partons have spin-1/2. The essential advantage of the quark-parton model is that the W_1 and W_2 are no longer specific to this process but are related to the x -distributions of quarks and antiquarks in the nucleon and *all processes* involving nucleons see the same structure functions.

A relevant example is the very similar case of neutrino scattering. Here, the exchanged virtual boson is a W^+ , not a photon. The hadron tensor $W^{\mu\nu}$ now contains 4 more structure functions. Three of these contribute as (m_i^2/m_p^2) and are neglected; the parity violating fourth must be included however. The differential cross-section is

$$\frac{d^2\sigma(\nu,\bar{\nu})}{d\Omega dE'} = \frac{G^2 E'^2}{2\pi^2} \left(\frac{1}{1 + Q^2/m_W^2} \right)^2 \left\{ 2W_1 \sin^2 \frac{\theta}{2} + W_2 \cos^2 \frac{\theta}{2} \mp W_3 \frac{(E + E')}{m_p} \sin^2 \frac{\theta}{2} \right\} \quad (7.17)$$

The charged lepton and neutrino scattering structure functions W_1 , W_2 and W_3 may be abandoned in favour of 3 other variables. One conventional choice is the cross sections for the three virtual boson polarizations (two transverse: $+$, $-$ and one longitudinal: L). In both the charged lepton and the neutrino case one obtains

$$W_1 = k \frac{(\sigma_+ + \sigma_-)}{2} \quad (7.18)$$

$$W_2 = k \frac{Q^2}{Q^2 + \nu^2} \left(\frac{\sigma_+ + \sigma_-}{2} + \sigma_L \right) \quad (7.19)$$

$$W_3 = k \frac{m_p}{\sqrt{\nu^2 + Q^2}} (\sigma_+ - \sigma_-) \quad (7.20)$$

where the constant k is different in the two cases. In the electromagnetic case, $\sigma_+ = \sigma_-$ (parity conservation), and $W_3 = 0$. We define the transverse cross-section as

$$\sigma_T = \frac{\sigma_+ + \sigma_-}{2} \quad (7.21)$$

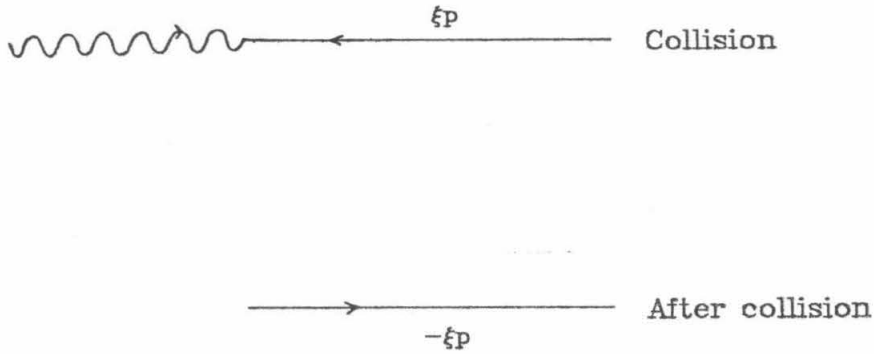


Figure 7.2

Collision of parton and photon in frame in which the 3-momentum of the parton is reversed.

and R by

$$R \equiv \frac{\sigma_L}{\sigma_T} = \frac{W_2}{W_1} \left(1 + \frac{\nu^2}{Q^2} \right) - 1 \quad (7.22)$$

In terms of F_2 and $2xF_1$ defined above ($xF_3 = \nu xW_3$),

$$R = \frac{\sigma_L}{\sigma_T} = \frac{F_2}{2xF_1} \left(\frac{Q^2}{\nu^2} + 1 \right) - 1 = \frac{F_2}{2xF_1} \left(\frac{4m^2x^2}{Q^2} + 1 \right) - 1 \quad (7.23)$$

For $\sigma_L = 0$, this gives $R = 0$. Including transverse momenta of the partons one gets

$$R = \frac{4(m^2x^2 + p_{\perp}^2)}{Q^2 + 2p_{\perp}^2} \quad (7.24)$$

$m^2x^2 + p_{\perp}^2$ may be interpreted as a transverse mass squared $= \mu_{\perp}^2$.

$$R \text{ becomes}^{(63)} \quad \frac{4 \langle \mu_{\perp}^2 \rangle}{\langle Q^2 + 2p_{\perp}^2 \rangle} \quad (7.25)$$

where the average is over the parton density.

We can examine what happens to R given that quarks all have spin 1/2. Both vector and axial vector currents conserve the helicity of massless particles. Now consider a frame in which the boson and parton are collinear and the 3-momentum of the parton is reversed, fig. 7.2.

For the boson to be absorbed, and helicity conserved, only (anti)quarks with spin 1/2 can absorb a transverse boson (helicity $= \pm 1$) and only spin zero quarks can absorb longitudinal bosons (helicity $= 0$). Experimental observations^(60,61,62) support $\sigma_L = 0$, implying spin 1/2 quarks. This can also be expressed as the Callan-Gross relation, which in the limit $4m^2x^2/Q^2 \ll$

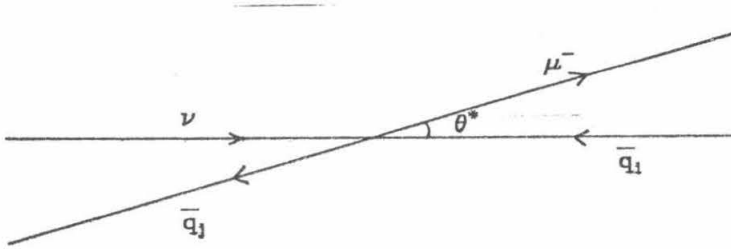


Figure 7.3. Spin considerations in a neutrino-antiquark collision.

1 gives

$$\lim_{4m^2x^2/Q^2 \ll 1} F_2 = 2xF_1 \quad (7.26)$$

The question of R in QCD will be discussed in the next section.

The quark parton model makes additional basic predictions. The y -distributions of the differential cross sections (or angular distributions in the c.m. frame) follow quite naturally in the massless model. From (B.11),

$$y = \sin^2 \frac{\theta^*}{2} \quad (7.27)$$

Consider a neutrino-antiquark collision, as in figure 7.3. The initial state helicity and final state helicity are dictated by the V-A interaction; they are both -1 . The angular distribution is governed by $|d_{11}^1(\theta)|^2 = (1 + \cos \theta^*)^2/4$. Similarly, the helicities for a neutrino quark collision are both zero, and lead to a $|d_{00}^0(\theta)|^2$ or isotropic distribution. Thus,

$$\frac{d\sigma^\nu}{dy} = k[q(x) + (1-y)^2\bar{q}(x)] \quad (7.28)$$

Here, $q(x)$ and $\bar{q}(x)$ are the x distributions of quarks and antiquarks. Actually, a nucleon has both valence quarks and a "sea" of quark-antiquark pairs, and all these come in more than one flavour. These have already been described in the introduction. Here we merely point out that using the y -distributions above, it is possible to proceed as in appendix C and heuristically derive the cross section. It is clear from (C.23) that the total cross section rises linearly with neutrino or antineutrino energy, apart from scaling violations expressed as a weak dependence

of $\int F_2 dx$ and $\int xF_3 dx$ on Q^2 . The x -distributions can, in the quark-parton model, be described as obeying sum rules, for example

$$\int_0^1 F_3(x) dx = 3 \quad \text{the GLS sum rule} \quad (7.29)$$

which merely expresses the fact that there are 3 valence quarks in a nucleon. The identification of xF_3 with the valence quark distribution is clear from (7.20). Other sum rules which are similarly obvious include, for the proton,

$$\int_0^1 (u(x) - \bar{u}(x)) dx = 2 \quad (7.30)$$

$$\int_0^1 (d(x) - \bar{d}(x)) dx = 1 \quad (7.31)$$

$$\int_0^1 (s(x) - \bar{s}(x)) dx = 0 \quad (7.32)$$

Combinations of these give rise to the Gross-Llewellyn-Smith sum rule and the Adler sum rule. One important conclusion can be formed for the comparison of charged and neutral lepton-nucleon scattering. Since charged lepton scattering occurs via a photon, the parton distributions are multiplied by their charge squared, and $F_2^{e.m.}$ should be $F_2^{wk.}$ times the mean square charge in a nucleon:

$$F_2^{e.m.} = \frac{5}{18} F_2^{wk.} \quad (7.33)$$

What can be said about the x shapes of the parton distributions? As x tends to zero, one expects more and more quark-antiquark pairs to be produced, possibly by gluon bremsstrahlung followed by pair creation. Thus the sea dominates at $x \rightarrow 0$, with the bremsstrahlung distribution $dk/E \sim dx/x$ implying a

$$\text{number density} \sim \frac{1}{x} \quad (7.34)$$

and a momentum distribution ~ 1 i.e., approaching $x = 0$ as a constant. This is also explained by associating the sea with diffractive components ($\alpha = 1$; Pomeron exchange) and the valence quarks with non-diffractive components ($\alpha \approx 1/2$; f , A_2 exchanges). We then predict in addition that

$$xF_3 \sim x \cdot \frac{1}{\sqrt{x}} \sim \sqrt{x} \quad \text{as } x \rightarrow 0 \quad (7.35)$$

Quark counting rules⁽²⁹⁾ and form factor arguments^(3,26) suggest that

$$\lim_{x \rightarrow 1} F_2(x) \sim (1-x)^3 \quad (7.36)$$

$$\text{and } \bar{q}(x) \sim (1-x)^n \quad 5 \leq n \leq 7 \quad (7.37)$$

§7.3 Quantum Chromodynamics

It is actually quite surprising that the parton model described in the previous section works so well; after all, it says nothing at all about the strong force between the quarks. The current candidate theory of strong interactions is QCD and as it turns out, deep inelastic scattering is one of the few processes where it makes definite predictions.

There are many pointers to an additional degree of freedom in quarks, colour. If quarks did not possess this degree of freedom, the ratio

$$R_{e^+e^-} \equiv \frac{e^+e^- \rightarrow \text{hadrons}}{e^+e^- \rightarrow \mu^+\mu^-} \quad (7.38)$$

would be a factor of 3 smaller than experimentally observed. Similarly, the rate for $\pi^0 \rightarrow \gamma\gamma$ can be calculated exactly; for no coloured quarks the rate is 1/3 smaller than observed. Baryon spectroscopy breaks down for Δ^{++} (spin 3/2) unless an antisymmetric colour wavefunction is introduced since without it the wavefunction is symmetric under an interchange of any 2 u quarks. Other evidence for 3 colours includes the roughly 20% branching ratio for $\tau^- \rightarrow e^- \bar{\nu}_e \nu_\tau$ and $\tau^- \rightarrow \mu^- \bar{\nu}_\mu \nu_\tau$ as opposed to the $\sim 33\%$ expected without colour.

QCD utilizes this extra degree of freedom and coloured quarks experience a strong force mediated by coloured gluons. Unlike $SU(2)_L$, colour symmetry is exact, even for massive quarks. There are 8 gluons, all massless, and since they are themselves coloured (unlike QED where the photon is neutral), they couple to each other (fig. 1.2). Baryons and mesons are colour singlets.

Evidence for gluons lies in gluon jets in e^+e^- scattering and the fact that quarks carry only about half the momentum of nucleons – the other half is presumably carried by gluons. In QED, the coupling constant α is a function of Q^2 because vacuum polarization contributions modify even lowest order diagrams. $\alpha(Q^2)$ increases extremely slowly with Q^2 from the value α_0 at $Q^2 = 0$, the dominant contributions giving, for $Q^2 \gg m^2$,

$$\alpha(Q^2) = \frac{\alpha_0}{1 - (\alpha_0/3\pi) \ln Q^2/m^2} \quad (7.39)$$

For example, at $Q^2 = 1000 \text{ GeV}^2$, α has changed by only about 1.7%. The denominator in (7.39) becomes zero around $Q^2 \approx 10^{555} \text{ GeV}^2$. In QED we can thus safely do all low energy calculations with a well defined $Q^2 = 0$ limit to start from. In QCD however, $\alpha_S(Q^2)$ gets large as $Q^2 \rightarrow 0$, and one must use the $Q^2 \rightarrow \infty$ region for perturbative theory. That is, QCD is an asymptotically free theory and at low Q^2 confinement of quarks and gluons occurs. The unproven attribute of confinement explains why no free quarks or gluons are seen and asymptotic freedom is the reason for the applicability of QCD to deep inelastic scattering, where Q^2 is presumably high enough. Since we do not have a definite mass-scale in the high Q^2 region to normalize to (unlike QED where $Q^2 = 0$ serves well), an arbitrary mass-scale must be introduced. Normally, this is exchanged for a parameter Λ and the dominant contributions to $\alpha_S(Q^2)$ can be summed up to give

$$\alpha_S(Q^2) = \frac{4\pi}{\beta_0 \ln(Q^2/\Lambda^2)} \quad (7.40)$$

$$\beta_0 = 11 - \frac{2}{3}n_f, \quad n_f \text{ is the number of quark flavours.}$$

Since several excellent reviews of QCD exist⁽⁶⁴⁻⁶⁸⁾, we will not dwell on generalities any further and move on to perturbative QCD and its applications to deep inelastic scattering⁽⁶⁸⁻⁷³⁾.

Given that confinement is yet unproven, the absence of calculations to all orders in deep inelastic scattering and a lack of a clear point in Q^2 beyond which perturbative QCD can be guaranteed to apply, why do we adopt this approach at all? Perhaps the most compelling reason is the closeness of the high Q^2 data to zeroth order QCD (quark-parton model) e.g., $R_{e^+e^-}$ is close to $3\sum e_q^2$ and deep inelastic structure functions very nearly scale. Perturbative QCD also has been successful (albeit to varying degrees) in explaining jet production in e^+e^- collisions and large momentum transfer processes.

Perturbative QCD makes predictions for several high energy processes, but only prescribes their Q^2 dependence. The hope therefore is that parton distributions ($q(x, Q^2)$, $\bar{q}(x, Q^2)$, $G(x, Q^2)$) and their fragmentation functions be measured in a few processes and then be used to predict quantities in others. In other words, another check on the applicability of perturbative theory is the extraction of the same value of $\alpha_S(Q^2)$ from different processes.

Specializing to deep inelastic scattering, the processes involved to first order are shown in figure 7.4. The first process describes the creation of gluons and lower momentum quarks by bremsstrahlung. The second and third are pair creation of gluons (unique to non-Abelian theories) and $q\bar{q}$ pairs. Consider the moments of a general structure function \mathcal{F} :

$$M_n(Q^2) = \int_0^1 dx x^{n-2} \mathcal{F}(x, Q^2), \text{ where} \quad (7.41)$$

\mathcal{F} may be F_2 or xF_3 . In reality, all high energy processes are mixtures of high and low energy subprocesses making it hard to make predictions. In QCD we cannot as yet calculate all the $M_n(Q^2)$, however, wonderfully we are able to separate the high- Q^2 (perturbative) and non-perturbative parts of $M_n(Q^2)$. This property is known as factorization and enables us to write

$$M_n(Q^2) = \sum_i A_n^i(\mu^2) C_n^i\left(\frac{Q^2}{\mu^2}, g^2\right) \quad (7.42)$$

The summation is over all the non-singlet, singlet and gluon pieces. μ is the mass scale at which the theory is renormalized and g^2 is related to α_S by

$$\alpha_S(Q^2) = \frac{g^2}{4\pi}(Q^2) \quad (7.43)$$

In (7.42) the $A_n^i(\mu^2)$ are non-perturbative and must be determined from experiment at some $Q^2 = \mu^2$. The perturbative parts C_n^i can be evaluated explicitly. For example, in the non-singlet case we may write⁽⁶⁹⁾, to order g^2 ,

$$M_n^{NS}(Q^2) = A_n^{NS}(\mu^2) \left[\frac{\bar{g}^2(Q^2)}{\bar{g}^2(\mu^2)} \right]^{d_n^{NS}} \left[1 + \frac{\bar{g}^2(Q^2) - \bar{g}^2(\mu^2)}{16\pi^2} Z_n^{NS} \right] \left[1 + \frac{\bar{g}^2(Q^2)}{16\pi^2} B_n^{NS} \right] \quad (7.44)$$

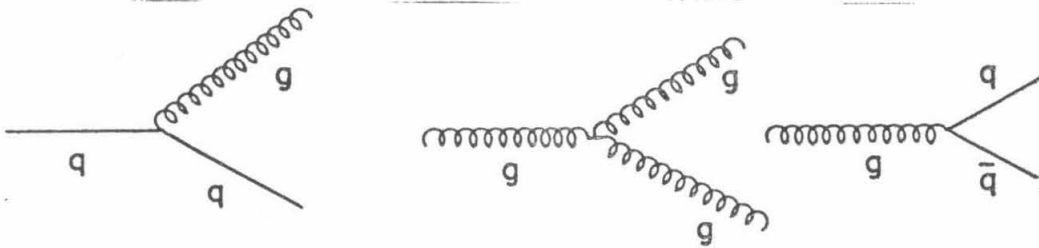


Figure 7.4. First order QCD corrections to deep inelastic scattering.

The coefficients d_n^{NS} , Z_n^{NS} and B_n^{NS} are all calculable and \bar{g} is the effective coupling constant. The term 'singlet' refers to flavour. The sum of all quark distributions is a singlet distribution ($\sum_i (q_i + \bar{q}_i)$); non-singlet structure functions, like xF_3 , involve differences of quark distributions and the singlet contributions cancel.

These predictions can all be restated directly in density space. Before doing that we will mention that in leading order all parton densities are the same as in the naive quark-parton model. The ambiguities of renormalization scheme dependence only develop in next to leading order. There are many schemes in existence. The momentum subtraction scheme *MOM*, minimal subtraction *MS*, and modified minimal subtraction \overline{MS} are the most common; we use \overline{MS} throughout. (*MOM* seeks to minimize third order terms, while \overline{MS} is closest to leading order, with a minimum of corrections.) One reason for using next to leading order calculations is the ambiguity in the leading order expression for $\alpha_S(Q^2)$:

$$\text{In general, } \alpha_S(Q^2) = \frac{4\pi}{\beta_0(\ln Q^2/\Lambda^2 + c)} \quad (7.45)$$

For large Q^2 this becomes

$$\alpha_S(Q^2) = \frac{4\pi}{\beta_0 \ln Q^2/\Lambda^2} \left(1 - \frac{c}{\ln Q^2/\Lambda^2} \right) \quad (7.46)$$

The second order expression in fact is

$$\alpha_S(Q^2) = \frac{4\pi}{\beta_0 \ln Q^2/\Lambda^2 + \frac{\beta_1}{\beta_0} \ln \ln Q^2/\Lambda^2} \quad (7.47)$$

where

$$\beta_1 = 102 - \frac{38}{3}n_f \quad (7.48)$$

The quark distributions at a given x receive contributions from bremsstrahlung of higher x quarks and pair production of $q\bar{q}$ pairs from gluons; gluon distributions from bremsstrahlung and $g \rightarrow gg$ diagrams. Let z denote the fraction of the parent's momentum carried by the resultant object. Then P_{qq} , P_{qg} , P_{gq} and P_{gg} are the probability densities or "splitting functions" of the above processes. Defining $q_i(x, Q^2)$ as the density of a given flavour of quark (or antiquark) and $g(x, Q^2)$ as the gluon density, the leading order evolution equations are simply

$$\frac{dq_i(x, Q^2)}{d \ln Q^2} = \frac{\alpha(Q^2)}{2\pi} \int_x^1 \frac{dy}{y} \left[q_i(y, Q^2) P_{qq}\left(\frac{x}{y}\right) + g(y, Q^2) P_{qg}\left(\frac{x}{y}\right) \right] \quad (7.49)$$

$$\text{and } \frac{dg(x, Q^2)}{d \ln Q^2} = \frac{\alpha(Q^2)}{2\pi} \int_x^1 \frac{dy}{y} \left[\sum_i q_i(y, Q^2) P_{gq}\left(\frac{x}{y}\right) + g(y, Q^2) P_{gg}\left(\frac{x}{y}\right) \right] \quad (7.50)$$

Utilizing the convention

$$A \otimes B = \int_x^1 \frac{dy}{y} A(y) B\left(\frac{x}{y}\right) = B \otimes A \quad (7.51)$$

the above equations (7.49) and (7.50) can be cast in matrix form

$$\frac{d}{d \ln Q^2} \begin{pmatrix} \sum_i q_i(x, Q^2) \\ g(x, Q^2) \end{pmatrix} = \frac{\alpha_S(Q^2)}{2\pi} \begin{pmatrix} \sum_i q_i(x, Q^2) \\ g(x, Q^2) \end{pmatrix} \otimes \begin{pmatrix} P_{qq}(x) & 2n_f P_{qg}(x) \\ P_{gq}(x) & P_{gg}(x) \end{pmatrix} \quad (7.52)$$

The non-singlet equation is not coupled with the gluon density:

$$\frac{d}{d \ln Q^2} q^{NS}(x, Q^2) = \frac{\alpha_S(Q^2)}{2\pi} [q^{NS} \otimes P_{qq}](x, Q^2) \quad (7.53)$$

In leading order,

$$P_{qq}(x) = C_F \left(\frac{1+x^2}{1-x} \right)_+ \quad (7.54)$$

$$P_{qg}(x) = \frac{T}{n_f} (x^2 + (1-x)^2) \quad (7.55)$$

$$P_{gq}(x) = C_F \frac{1+(1-x^2)}{x} \quad (7.56)$$

$$P_{gg}(x) = 2C_A \left[\frac{x}{(1-x)_+} + \frac{1-x}{x} + x(1-x) \right] + 2\pi b\delta(1-x) \quad (7.57)$$

The + definition implies a singularity at $x = 1$ which is removed by integration:

$$\int_0^1 dx g(x)(f(x))_+ = \int_0^1 dx [g(x) - g(1)]f(x) \quad (7.58)$$

$$C_F = \frac{4}{3}, \quad C_A = 3, \quad T = \frac{n_f}{2} \text{ and } b = \frac{11C_A - 4T}{12\pi} \quad (7.59)$$

Interestingly, in the high x region (but not too close to 1 i.e., $1/(1-x) \gg 1$ and $(\alpha_S(Q^2)/\pi) \ln(1/(1-x)) \ll 1$) the valence quark equation is satisfied in the leading log order by a $A(1-x)^B$ form, where⁽⁶⁶⁾

$$B \approx \frac{4}{3\pi b} \ln \frac{\alpha_S(\mu^2)}{\alpha_S(Q^2)} + c \quad (7.60)$$

In the same region, the gluon and sea densities fall by one and two extra powers of $(1-x)$ faster than the non-singlet case.

The ambiguities that arise in going from the leading log approximation to the next-to-leading order can be resolved in several ways. Most commonly, the quark number and momentum sum rules receive no corrections to all orders in $\alpha_S(Q^2)$ and the quark-densities are then process-dependent. We may, for example, use an F_2 which satisfies the Adler sum rule to all orders (this is motivated by the independent derivation of this sum rule from current algebra):

$$\int_0^1 \frac{dx}{x} [F_2^{\nu N}(x, Q^2) - F_2^{\bar{\nu} N}(x, Q^2)] = \text{constant} \quad (7.61)$$

In this definition F_2 is still $q + \bar{q}$, but $x F_3$ is $(q - \bar{q})$ convoluted with an order α addition to a δ -function. Of particular interest to us is the resulting GLS sum rule:

$$\int_0^1 F_3 dx = 3 \left(1 - \frac{\alpha_S(Q^2)}{\pi} \right) \quad (7.62)$$

The most important result of a QCD analysis of our data is then the value of Λ_{LO} and $\Lambda_{\overline{MS}}$, but all the preceding caveats and details should be borne in mind while interpreting these values. If the result agrees with all other experiments exploring the same region of Q^2 we may be past the higher twist and non-perturbative regions. One reason to settle on a value of Λ is the critical dependence of the proton lifetime on Λ in some grand unification models. The mass scale at which the falling $\alpha_S(Q^2)$ meets the weak-electromagnetic $\alpha(Q^2)$ gets larger with decreasing Λ ; since this mass-scale is the propagator mass for decays,

$$\tau_p \sim \Lambda^4 \quad (7.63)$$

Any analysis leading to a value of Λ must correctly include non-perturbative and higher-twist effects. The former arise because of effects like primordial p_\perp (from quark

confinement within a hadron's radius) which contributes $\sim p_{\perp}^2/Q^2$. Such effects are negligible at higher Q^2 . Higher-twist effects from coherent phenomena (diquark scattering, elastic scattering, resonance production etc.) add to (7.42) or (7.44) whole new series down by powers of Q^2 . Higher twist moments are expected to increase with n (greater importance of higher-twist as $x \rightarrow 1$). Consequently, structure functions are sometimes parametrized as

$$F(x, Q^2) \approx F_0(x, Q^2) \left[1 + \frac{a}{Q^2(1-x)} + \frac{b}{Q^4(1-x)^2} + \dots \right] \quad (7.64)$$

In any case, barring new calculational results, these terms are unknown. Some terms have been calculated, in the bag model for example, and have a negative sign leading to speculation that A might increase and not necessarily decrease with the inclusion of these terms.

Finally, we examine QCD predictions regarding R . The longitudinal structure function F_L is, to order α_S ,

$$F_L = \frac{\alpha_S(Q^2)}{2\pi} x^2 \int_x^1 \frac{dy}{y^3} \left\{ \frac{8}{3} F_2(y, Q^2) + 4n_f \left(1 - \frac{x}{y} \right) y G(y, Q^2) \right\} \quad (7.65)$$

Since R is defined by $R = F_L/2xF_1$, R is expected to be small at large x and large at small x (from the integral). Also, apart from the parton model contributions to σ_L , we expect R to fall with Q^2 like $1/\ln Q^2$. Integrating (7.65) over x one gets

$$\overline{F_L} = \frac{\alpha_S(Q^2)}{2\pi} \left\{ \frac{8}{9} \overline{F_2}(Q^2) + \frac{n_f}{3} \overline{G}(Q^2) \right\} \quad (7.66)$$

where the bar indicates an average (or integral) over x . For example, assuming $\overline{F_2} = \overline{G} = 0.5$ (at $Q^2 = 10 \text{ GeV}^2$, say), gives, for $n_f = 4$,

$$R \approx .35\alpha_S \quad , \quad (7.67)$$

§7.4 Tests of the Quark-parton Model

7.4.1 F_2 Comparisons

As mentioned in §7.2, $F_2^{wk.}$ and $F_2^{e.m.}$ are related by the simple relation

$$F_2^{wk.} = \frac{18}{5} F_2^{e.m.} \quad (7.68)$$

Actually, there is a correction term, which comes from the strange sea correction, leading to

$$F_2^{wk.} = \frac{18}{5} F_2^{e.m.} \left/ \left(1 - \frac{3}{5} \frac{s + \bar{s}}{q + \bar{q}} \right) \right. \quad (7.69)$$

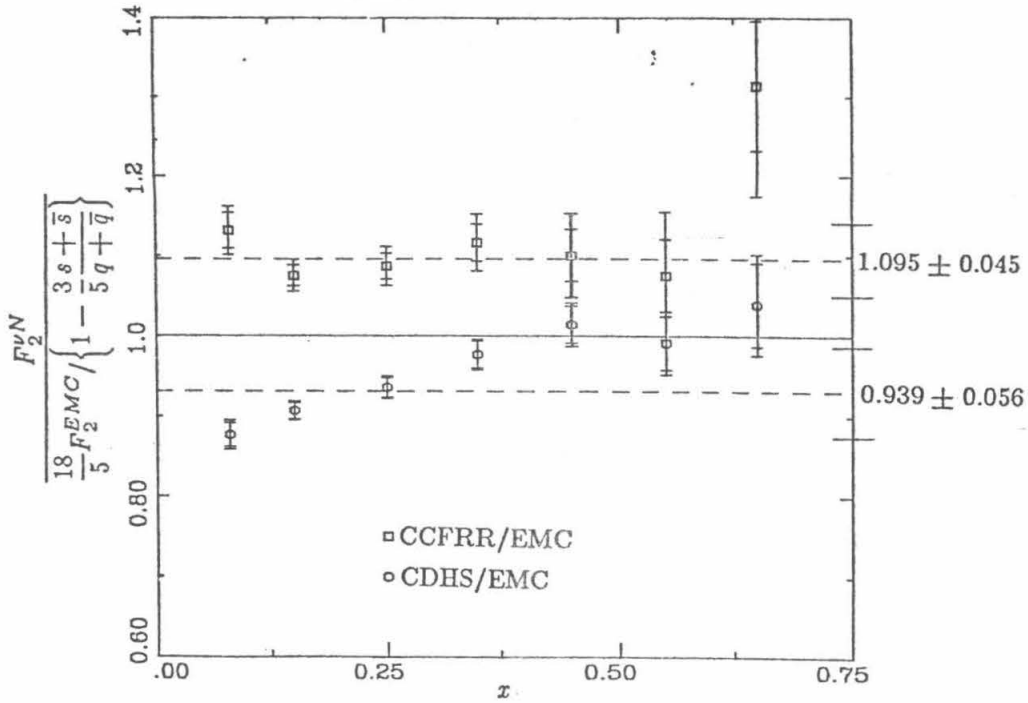


Figure 7.5

F_2 ratios with EMC. The numbers on the right are mean values of the ratios with systematic errors.

We use this to convert EMC data⁽⁸⁶⁾ into a neutrino F_2 and then compare that data set with CDHS data⁽⁸¹⁾ and our data. Again, we shall assume a 1/2 SU(3) sea and make corrections to the CDHS data set to include an 80 GeV W-boson propagator and slow rescaling with $m_c = 1.5$ GeV. Also, as in the $x F_3$ case, we interpolate all data sets linearly in $\log Q^2$ to $Q^2 = 10 \text{ GeV}^2$. Since all three data sets involve an iron target, the comparison is independent of Fermi motion effects. Also, since EMC quote results for $R=0$. and $R=0.2$, we have used $R=0.1$ in all three data sets.

The ratio of our data to those of EMC and similar ratios for CDHS are shown in figure 7.5. On the average our points lie 9.5% higher than EMC but exhibit no x dependence. The combined systematic errors (3% for EMC and 5% for us) come close to explaining the level difference. A recent measurement⁽⁸²⁾ of $F_2^{\nu N}$ indicates that the EMC data may be systematically low by as much as 4.7%. On the other hand, the CDHS ratios are not only 6.1% lower than 1, they also show a striking low- x fall off, i.e., are not explainable by overall level systematics. Note that the strange sea correction can at most be $\sim 12\%$ at $x = 0$, with an error of $\sim 2\%$ using the CDHS value⁽³⁴⁾ for the strange fraction of the sea. The correction gets much smaller as x increases and $q(x)$ dominates $\bar{q}(x)$.

The reader interested in greater details of F_2 comparisons is referred to ref. 10.

7.4.2 The Gross-Llewellyn-Smith Sum Rule

We now examine the integral of $F_3(x)$, which is expected to be 3 in the quark-parton model. QCD predicts, in next to leading order,

$$\int_0^1 F_3(x, Q^2) dx = 3 \left(1 - \frac{\alpha_S(Q^2)}{\pi} \right) \quad (7.62)$$

The obvious thing to do is to sum up $x F_3/x$ times the bin width for all x bins. The problem with this approach is illustrated in fig 7.6. Of the total integral, equal to 3, about 1.5 comes from the region $x < .06$ of which about 0.5 is from $x < .01$. As mentioned before, our good angular resolution enables us to make a meaningful attempt to measure $x F_3$ below $x = .06$. However, as $x F_3$ tends to zero, the statistical errors get large, leading to large errors for $\int_0^1 F_3 dx$. Further, since most of the integral is from low x , it is also from low Q^2 ($Q^2 < 6 GeV^2$), thereby casting doubt on a QCD conclusion.

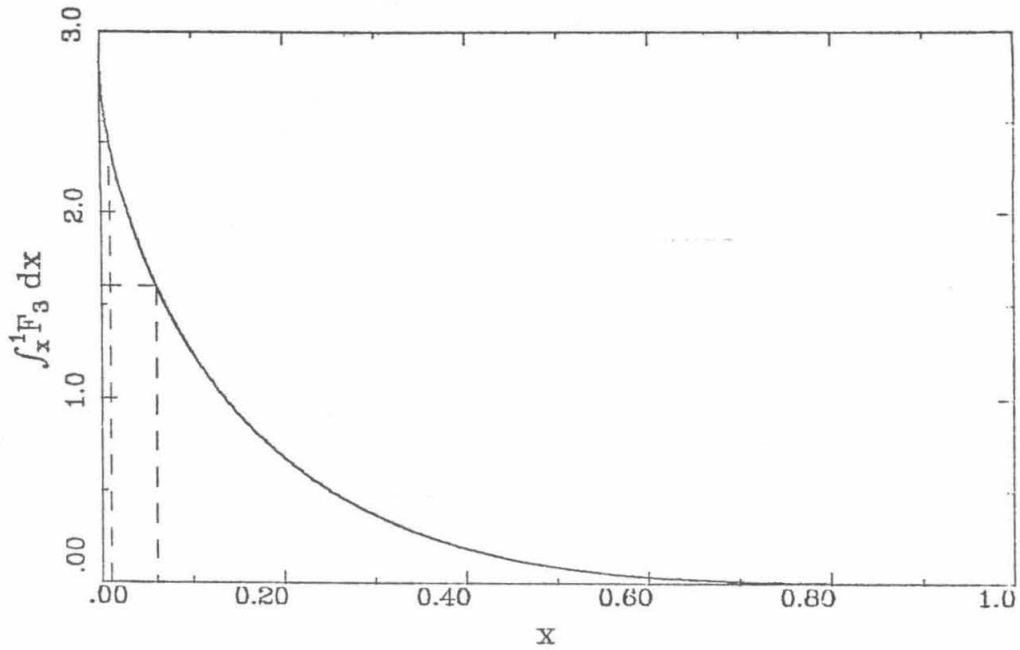


Figure 7.6. $\int_x^1 F_3 dx$ illustrates the concentration at low x .

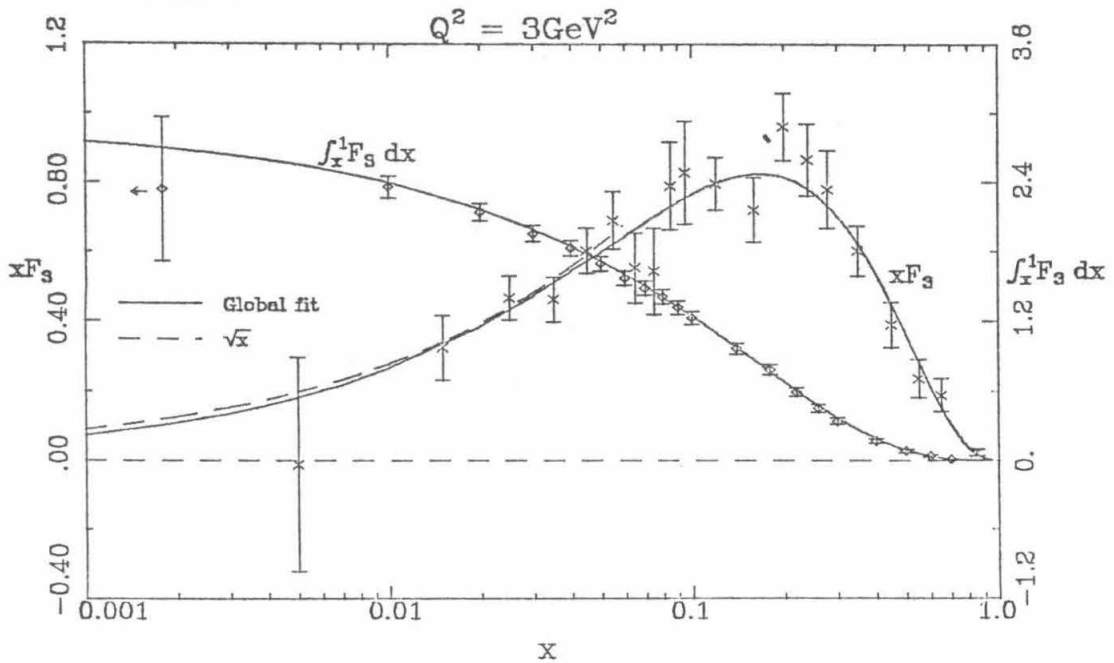


Figure 7.7

xF_3 in fine x bins at $Q^2 = 3 \text{ GeV}^2$ with the fit (7.70). Also shown is $\int_x^1 F_3 dx$ from the fit with points from the simple summation technique superimposed.

x	xF_3	Error	$\int xF_3$	Error	$\int F_3$	Error
.005	-.012	.307	.365	.016	2.339	.623
.015	.324	.092	.365	.016	2.364	.095
.025	.466	.062	.362	.015	2.148	.072
.035	.462	.064	.357	.015	1.961	.068
.045	.603	.066	.353	.015	1.829	.065
.055	.690	.083	.347	.015	1.695	.064
.065	.553	.100	.340	.015	1.570	.062
.075	.544	.123	.334	.015	1.484	.060
.085	.790	.126	.329	.015	1.412	.058
.095	.829	.148	.321	.015	1.319	.056
.120	.796	.075	.313	.015	1.231	.054
.160	.721	.093	.281	.015	.966	.047
.200	.959	.097	.252	.014	.786	.041
.240	.865	.103	.214	.014	.594	.036
.280	.780	.111	.179	.013	.449	.032
.350	.602	.073	.148	.012	.338	.028
.450	.390	.064	.087	.010	.166	.019
.550	.236	.054	.048	.008	.079	.012
.650	.187	.047	.025	.006	.036	.008
.850	.021	.009	.007	.003	.007	.003

Table 7.1

xF_3 interpolated to $Q^2 = 3 \text{ GeV}^2$ in fine x bins; cumulative integrals of xF_3 and F_3 from $x = 1$ to lower limit of each bin obtained by simple summation, with statistical errors.

As shown in table 7.3, we get our best estimate of $\int_0^1 F_3 dx$ around $Q^2 = 3 \text{ GeV}^2$. We therefore make fine bins in x at low x and interpolate our data to $Q^2 = 3 \text{ GeV}^2$ after making linear fits in $\log Q^2$, as usual. As is clear from table 7.1, a simple summation of xF_3/x from $x = 1$ leads to good errors for all except the lowest x bin. There we must use a fit. As mentioned before, a Regge theory prejudice suggests a form $\sim a\sqrt{x}$ for xF_3 as $x \rightarrow 0$. We have tried several forms and feel that it is valid to use all x provided a high- x behaviour term is included. The results of these attempts are displayed in table 7.2. Clearly, including all x with a $(1-x)^\beta$ term, i.e.,

$$xF_3(x) = Ax^\alpha(1-x)^\beta \quad (7.70)$$

does not significantly shift the result. We can therefore state that

$$\int_0^1 F_3 dx = 2.83 \pm .146, \quad Q^2 = 3 \text{ GeV}^2, \quad \text{statistical errors only.} \quad (7.71)$$

Figure 7.7 shows the fit to xF_3 and the resultant $\int_x^1 F_3 dx$ with the values from simple summation superimposed.

Fit limits		Integr limits		A	α	β	$\int_0^1 F_3$	χ^2/DF
0	1	0	1	$3.91 \pm .73$	$.577 \pm .064$	$2.86 \pm .27$	$2.83 \pm .15$	12.2/17
		0	.1				$2.83 \pm .14$	
		0	.02				$2.84 \pm .15$	
0	.06	0	.06	3.55 ± 2.09	$.575 \pm .177$	0	$2.79 \pm .28$	1.58/4
		0	.02				$2.80 \pm .28$	
		0	.01				$2.80 \pm .25$	
0	.06	0	.06	$2.78 \pm .17$	0.5	0	$2.92 \pm .10$	1.76/5
		0	.02				$2.93 \pm .09$	
		0	.01				$2.92 \pm .10$	

Table 7.2

$\int_0^1 F_3$ with statistical errors by making fits of the form (7.70). The regions for the fit and for the integration are specified. The rest of the integral is done by the simple summation technique. Fit parameters without errors indicate that they were fixed. The binning in x is the same as in table 7.1.

Estimating a systematic error for the above number requires knowledge of all correlations between errors. The statistical error indicates that such an effort is not warranted. Instead, we assume that all systematic errors except the 3.2% correlated overall error on the ν and $\bar{\nu}$ fluxes enter in the same way as the statistical errors, i.e., as uncorrelated errors. Weighting the ratio of these errors to the statistical error with $\int F_3$ in every bin, we find the contribution from this source to be 70% of the statistical error. Thus we conclude that at $Q^2 = 3 \text{ GeV}^2$,

$$\int_0^1 F_3 dx = 2.83 \pm .15 \pm .09 \pm .10 \quad (7.72)$$

where the first error is statistical, the second is the correlated level error and the third includes the rest of the systematic errors. At the 1σ level we can say that $\Lambda < 525 \text{ MeV}$.

It is noteworthy that at this time this is the best available value for the GLS rule. The measurement derives mainly from low x , and hence a reasonably high Q^2 implies a high energy experiment. We have such high energy data with high statistics and good angular resolution, which dominates the x -resolution at low x . Other results include that of CDHS who quote⁽⁸⁹⁾ $3.2 \pm .5$, and CHARM⁽⁹²⁾ ($2.66 \pm .41$). These values are from data averaged over Q^2 . ABCLOS report⁽¹⁰⁷⁾ $2.89 \pm .45$ in the range $1 < Q^2 < 10 \text{ GeV}^2$. CDHS use a fit below $x = .005$, CHARM use one below $x = .01$ and ABCLOS use a fit below $\xi = 0.1$, where ξ is the Nachtmann variable (7.77), not too different from x at these x and Q^2 values. Only CHARM do not assume a \sqrt{x} behaviour as $x \rightarrow 0$, but instead fit the power of x , like us. Our values for the power of x at low- x are quite consistent with 0.5 (table 7.2). Also notice that the power of $(1-x)$ at high- x from the global fit is consistent with 3, as expected on theoretical grounds.^(3,26,29)

Q^2 (GeV ²)	$\int_0^1 F_3 dx$
2	$2.63 \pm .142$
3	$2.83 \pm .146$
4	$2.95 \pm .167$
5	$3.03 \pm .180$
6	$3.09 \pm .198$
8	$3.18 \pm .224$
10	$3.27 \pm .265$

Table 7.9

$\int_0^1 F_3$ with statistical errors by making a fit of the form (7.70) in the region $0 < x < 1$. At high Q^2 ($Q^2 > 5 \text{ GeV}^2$) the integral involves large extrapolations in the important low- x regions and therefore becomes unreliable. We emphasize that no meaning should be attached to the Q^2 variation, this table only shows where the minimum error is to be found.

§7.5 QCD Analysis

7.5.1 Leading Order Non-singlet Analysis

The QCD evolution of the non-singlet structure function xF_3 is independent of the largely unknown gluon x -distribution. Also, the extraction of xF_3 's is, as we have seen, independent of R and the strange sea. Therefore, analysis of xF_3 is an excellent and unbiased way to extract the QCD parameter Λ . We therefore proceed to quantify the observed scaling violations of xF_3 (and briefly, of F_2) in the framework of QCD. The literature is replete with articles of interest^(64-77, 83-104). There are several approaches to the problem, including fitting moments of structure functions to QCD expectations and fitting functions known to satisfy QCD moment evolution expressions, at least for some first n moments.

We choose to evolve the structure functions directly using the Altarelli-Parisi⁽⁹²⁾ equations. The procedure used to determine Λ begins with parametrizing the structure functions xF_3 , F_2 and the gluon distribution G at some Q_0^2 :

$$\begin{aligned}
 xF_3(x, Q_0^2) &= a_3 x^{b_3} (1-x)^{c_3} \\
 F_2(x, Q_0^2) &= a_2 (1-x)^{c_2} (1+\gamma_2 x) \\
 G(x, Q_0^2) &= a_G (1-x)^{c_G} (1+\gamma_G x)
 \end{aligned}
 \tag{7.73}$$

Either xF_3 or the coupled pair F_2 and G (or both, simultaneously) are then evolved using the general formalism described in §7.3. Target mass corrections, if to be applied (see below), are made at this point. The resulting structure functions are compared to the measured values, with errors, to form a χ^2 which is then minimized with respect to the parameters at Q_0^2 and Λ .

The leading order evolution equation for xF_3 at fixed x is,

$$\frac{d xF_3(x, Q^2)}{d \ln Q^2} = \frac{\alpha_S}{2\pi} 4 \left[\int_x^1 dz \frac{(1+z^2)}{(1-z)} \left\{ \frac{x}{z} F_3\left(\frac{x}{z}, Q^2\right) - xF_3(x, Q^2) \right\} - xF_3(x, Q^2) \int_0^x dz \frac{(1+z^2)}{(1-z)} \right] \quad (7.74)$$

The prescription of Georgi and Politzer^(24, 104) may be applied to make target mass corrections. In this prescription, the observed xF_3 is reconstructed from an evolved one, say $F(x, Q^2)$, by

$$xF_3(x, Q^2) = \frac{x^2 v^2}{\xi^2} F(\xi, Q^2) + \frac{2m_p^2 x^3 v^3}{Q^2} \int_\xi^1 dy \frac{F(y, Q^2)}{y^2} \quad (7.75)$$

$$\text{where} \quad v = \frac{1}{\sqrt{1 + 4m_p^2 x^2 / Q^2}} \quad (7.76)$$

$$\text{and} \quad \xi = \frac{2x}{1 + \sqrt{1 + 4m_p^2 x^2 / Q^2}} \quad (7.77)$$

is the Nachtmann variable.

However, as pointed out by Devoto et al.⁽⁸³⁾, the expressions for target mass corrections are inconsistent, to order of $1/Q^2$ terms, with the equality of the regular moments of F and the Nachtmann moments of the corrected function. We resolve this problem by restricting our analysis to regions where these effects are small. We cut out the high- x region ($x > .7$) where non-perturbative effects, Fermi motion, bin centre corrections and smearing corrections are large as well as the low Q^2 region ($Q^2 < 5 \text{ GeV}^2$) where non-perturbative effects are large. The Q^2 cut effectively eliminates the low- x region and we therefore also cut out $x < .03$. The change in xF_3 over the resulting Q^2 -range at any given x -value from (7.75) can easily be estimated. In every x -bin, we find it to be less than $\sim 10\%$ of the observed change and less than 3% of the observed change for $x < .5$. We have also verified that the value of α_S changes by $\sim 3\%$ due to the inclusion of ξ -scaling as in (7.75). Therefore, we have decided not to make any target mass corrections in the xF_3 analysis. We also do not apply the GLS rule constraint to the fits since the low- x region is excluded. To further minimize non-perturbative effects,⁽⁹⁸⁾ the low W^2 region ($W^2 < 10 \text{ GeV}^2$) is eliminated ($W^2 = Q^2(1-x)/x + m_p^2$; it is the square of the invariant final state hadronic mass). In all our analysis we have assumed that there are 4 flavours of quarks.

The result of the leading log analysis is

$$\begin{aligned}
 \Lambda_{LO} &= 88_{-78}^{+163} \text{ }_{-70}^{+113} \text{ MeV} \\
 \alpha_S &= .204 \pm .079 \text{ for } Q_0^2 = 12.6 \text{ GeV}^2 \\
 b_3 &= .672 \pm .058 \\
 c_3 &= 3.29 \pm .24 \\
 a_3 &= 4.34 \pm .24 \\
 \chi^2 &= 44.2 \text{ for 45 DF}
 \end{aligned}$$

The χ^2 indicates a good fit. χ^2 is plotted versus Λ and versus α_S in figures 7.8 and 7.9 (the curves labeled $x F_3$). Notice the striking asymmetry of χ^2 around the minimum in fig. 7.8 — this arises due to the nonlinear nature of the Λ dependence of α_S . On the other hand, the χ^2 plot versus α_S is quite symmetric and quadratic since $d x F_3 / d \ln Q^2$ is proportional to α_S (7.74). In recognition of this fact we feel that at low values of Λ it is better to quote statistical and systematic errors on α_S rather than Λ , where α_S is evaluated at $Q^2 = 12.6 \text{ GeV}^2$ (roughly the mid-point of our Q^2 -range). We shall henceforth use the symbol α_S^0 for $\alpha_S(Q^2 = 12.6 \text{ GeV}^2)$. In figures 7.10 — 7.12 we see that the strongest correlation of α_S^0 is a negative correlation with the power of $(1 - x)$ indicating some feedthrough of the x -dependence into the Q^2 evolution.

Despite the absence of $x < .03$ data in the fit, the best fit values above correspond to

$$\int_0^1 F_3 dx = 2.70 \pm .15 \tag{7.78}$$

This value is at $Q^2 = 12.6 \text{ GeV}^2$ and is in good agreement with the value quoted in the previous section for $Q^2 = 3 \text{ GeV}^2$ by a global fit (7.72). The statistical error from the global fit is also 0.15, indicating that adding a Q^2 -dependence parameter Λ does not affect the error on the integral of F_3 , as expected.

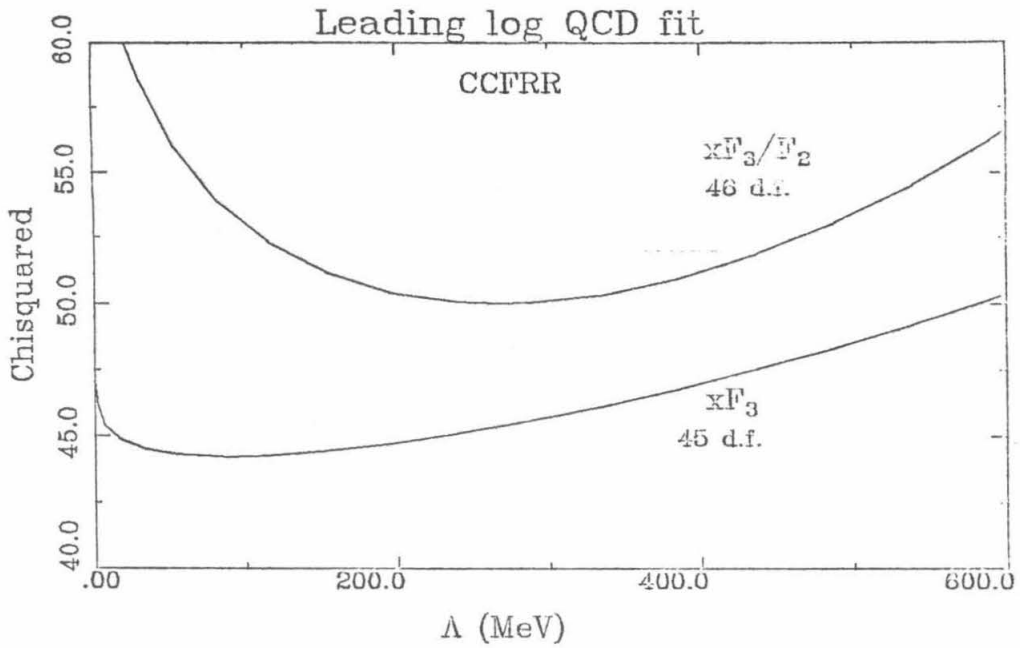


Figure 7.8. χ^2 vs. Λ , leading order.

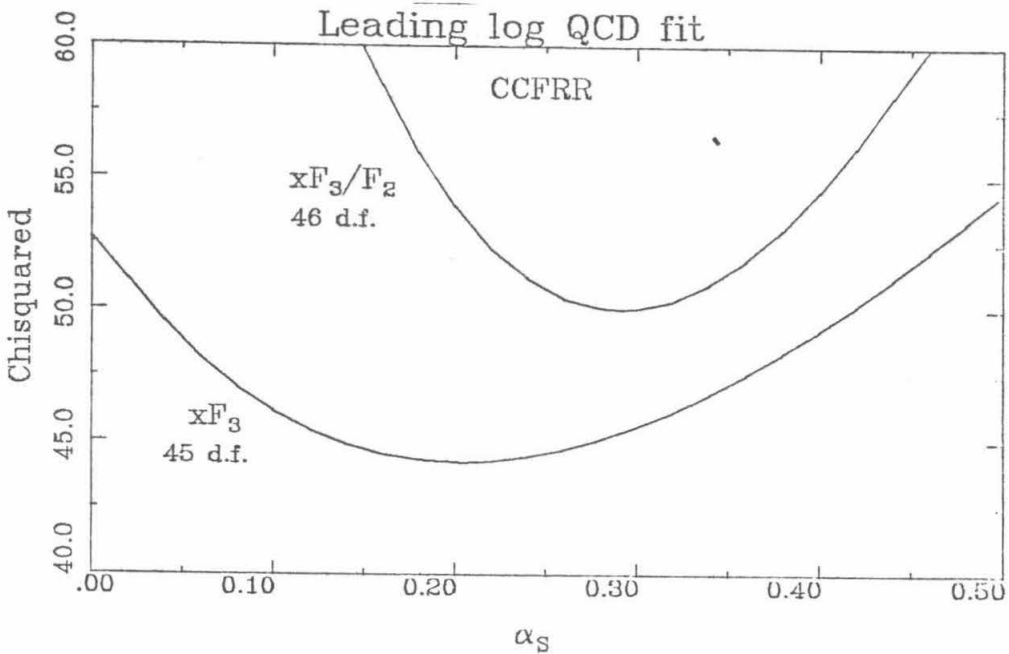


Figure 7.9

χ^2 vs. α_S , leading order. The curves labeled xF_3/F_2 use xF_3 below $x=.4$ and F_2 above.

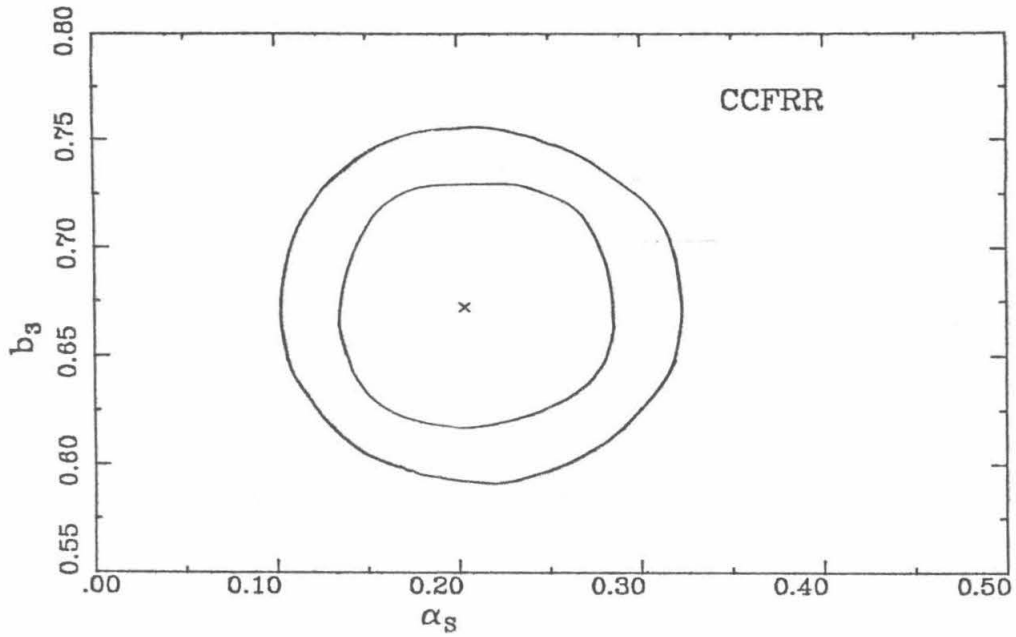


Figure 7.10. Correlation between b_3 and α_S^0 ; $x F_3$, leading order.

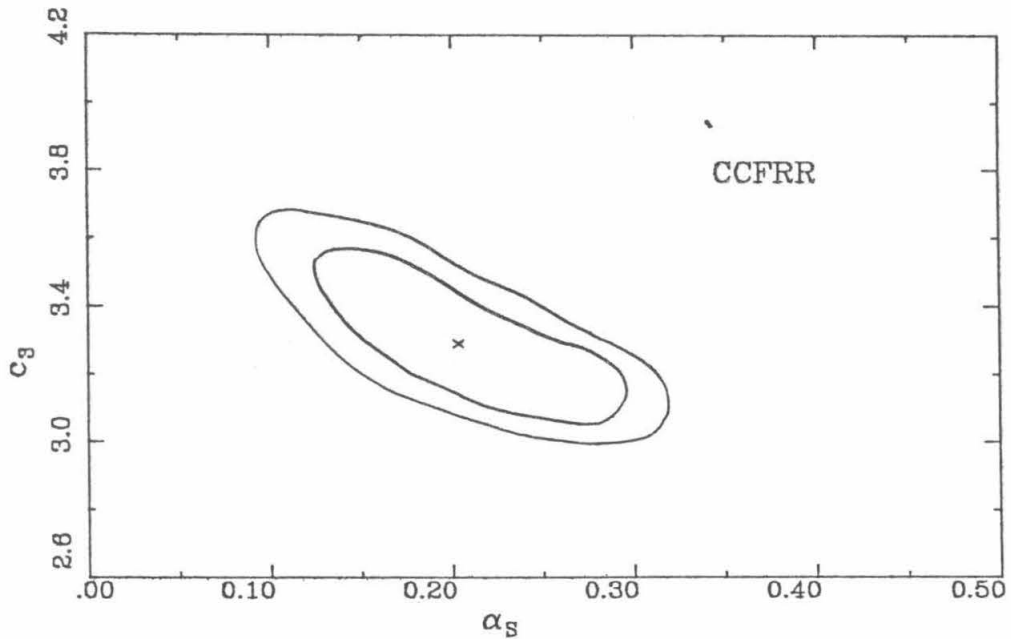


Figure 7.11

Correlation between c_3 and α_S^0 ; $x F_3$, leading order. Displayed in both figures are 1σ and 2σ contours.

Systematic effect	xF_3	xF_3/F_2
	$\Delta\alpha_S^0$	$\Delta\alpha_S^0$
Flux smoothing	.027	.010
Flux level errors	.047	.006
Angular disp.	.018	.024
Angular disp. (uncorr)	.028	.011
Systematic error in E_{had}	.011	.011
Systematic error in E_μ	.014	.009
Different R assumptions	.004	.015
1/2 SU(3) changed to SU(3)	.002	.002
Different models for correction terms in F_2 , xF_3 extraction	.008	.006
$n_f = 4$ changed to $n_f = 3$.001	.003
Inclusion of $(1 + \gamma_x x)$ term	.0003	.002
Change in Q_0^2 (12.6 \rightarrow 5 GeV ²)	.001	.001

Table 7.4

Effect of systematics on α_S^0 and changes in α_S^0 due to other assumptions in leading order.

Systematic errors on α_S^0 are as shown in table 7.4. The sources of error have already been discussed (§6.6); here we only touch upon points pertinent to the QCD analysis. The 'unlimited statistics' technique is extended to QCD by extracting α_S^0 for the 26 data sets and using the standard deviation as an estimate of the error. This applies to the first three errors listed, which are among the largest. Clearly, xF_3 is most sensitive to uncorrelated flux level errors. The two assumptions about beam angular dispersion serve to bracket the error from that source.

Again, the error due to R comes from analyzing data extracted with three different assumptions for its value (6.10). The error is small, as expected, despite the fact that real data (limited statistics) are used. The effect of changing the assumption regarding the strange fraction of the sea is also small, again as expected. The models used for structure function extraction also make little difference.

We have also tried to change certain assumptions regarding the QCD analysis. Changing the assumed number of quark flavours to 3 and changing the value of Q_0^2 (starting point for evolution) have no significant effect. The functional form for xF_3 at Q_0^2 (7.73) was modified to multiplicatively include a $(1 + \gamma_x x)$ term but again the change in α_S^0 is slight. We conclude therefore that the most significant problem in extracting a value for Λ from xF_3 presently is statistics, since the combined systematic error on α_S^0 is .06, as compared to .08 for the statistical error. This corresponds to systematic errors of +113 MeV and -70 MeV on our value for Λ_{LO} . In a high statistics quad-triplet run at the Tevatron, which would cover roughly the same energy range as this experiment, the uncorrelated error on the flux levels may be further reduced by using $d\sigma/dy$ at $y = 0$. Thus the systematic errors can be reduced too

when statistics increases, even for an unnormalized wide-band run.

Following a standard technique⁽⁸³⁾, we have analyzed our data in the same non-singlet framework using F_2 or $2xF_1$ instead of xF_3 in the high- x region. The major justification for this procedure comes from the fact that $\bar{q} = 0$ when $x > .4$. Table 7.5 lists values of F_2 and \bar{q} in x bins and the CDHS values⁽⁸¹⁾ of \bar{q} , which they determined by adding to their narrow-band data another 155,000 $\bar{\nu}$ and 35,000 ν wide-band events with $E_\nu > 20$ GeV. Clearly, above $x = .4$ both data sets imply $\bar{q} = 0$. Notwithstanding the difference in the \bar{q} values from the two experiments at low x , which arise mainly from overall level differences, we can set $\bar{q} = 0$ for $x > .4$. This is because adjusting the values of \bar{q} for the level difference in cross-sections beyond $x = 0.4$ does not change the result $\bar{q} = 0$. The Q^2 range over which the two data sets are averaged for table 7.5 is virtually identical except for $x < .4$, where the CDHS data displayed cover a range about 0.1–0.2 lower in $\log_{10} Q^2$. In the region of interest the errors on the CDHS \bar{q} values are much smaller than our F_2 errors, thereby facilitating the procedure of combining F_2 or $2xF_1$ and xF_3 .

x	F_2	\bar{q}	CDHS \bar{q}
.015	$1.36 \pm .033$	$.477 \pm .023$	$.344 \pm .016$
.045	$1.37 \pm .023$	$.354 \pm .021$	$.321 \pm .013$
.080	$1.49 \pm .022$	$.341 \pm .021$	$.277 \pm .010$
.150	$1.24 \pm .013$	$.159 \pm .012$	$.155 \pm .0058$
.250	$0.93 \pm .012$	$.034 \pm .012$	$.054 \pm .0040$
.350	$0.64 \pm .011$	$.033 \pm .012$	$.013 \pm .0027$
.450	$0.38 \pm .009$	$.0021 \pm .0092$	$.00076 \pm .00197$
.550	$0.20 \pm .007$	$-.00094 \pm .0074$	$-.00128 \pm .00160$
.650	$0.11 \pm .006$	$-.0018 \pm .0061$	—

Table 7.5

Values of F_2 , \bar{q} and the high-statistics CDHS \bar{q} averaged over Q^2 with statistical errors.

The result of combining F_2 for $x > .4$ and xF_3 for $x < .4$ and doing a non-singlet analysis is the following set of values for the parameters:

$$\begin{aligned} \Lambda_{LO} &= 266^{+114}_{-104} \text{ } ^{+85}_{-79} \text{ MeV} \\ \alpha_S &= .291 \pm .047 \text{ for } Q_0^2 = 12.6 \text{ GeV}^2 \\ b_3 &= .635 \pm .049 \\ c_3 &= 2.90 \pm .13 \\ a_3 &= 4.29 \pm .22 \\ \chi^2 &= 50.0 \text{ for } 46 \text{ DF} \end{aligned}$$

One important point is served in doing this analysis. We get an idea of how much the systematics are improved (except those due to R) by a glance at table 7.4 which also lists the

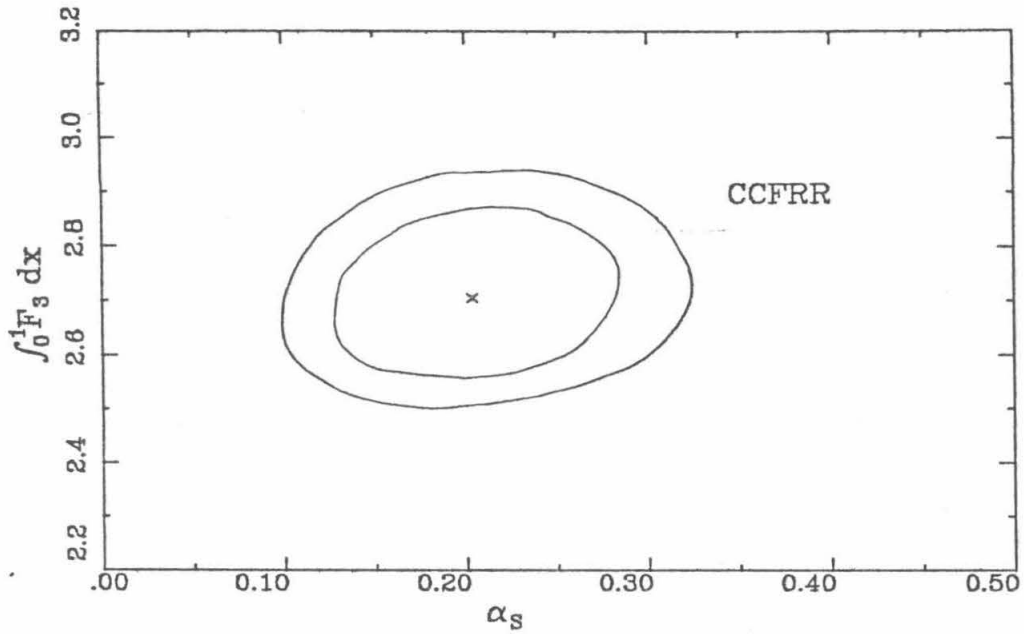


Figure 7.12

Correlation between $\int_0^1 dx F_3$ and $\alpha_S^0; xF_3$, leading order. Displayed are 1σ and 2σ contours.

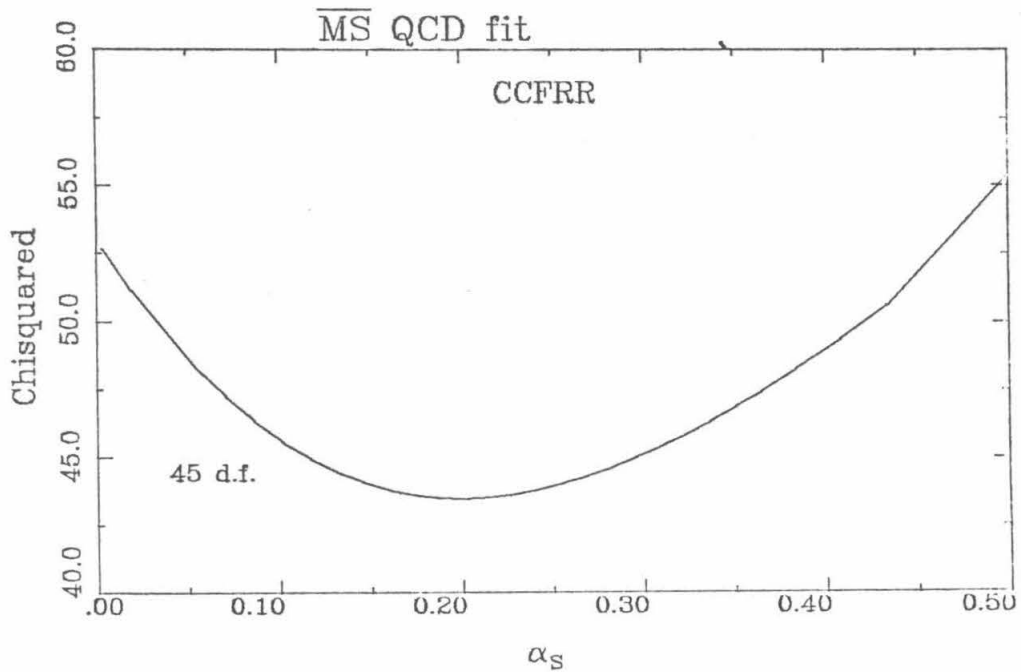


Figure 7.13. χ^2 vs. α_S ; \overline{MS} analysis of xF_3 .

errors from this analysis. As expected, the relative insensitivity of F_2 to the flux smoothing procedure and to the $\sim 4\%$ level fluctuations reduces those errors dramatically. The error on α_S^0 is .035, which translates into errors of +85 MeV and -79 MeV on the value of Λ .

However, in doing such an analysis we are confronted with the uncertainty in R . Since $\bar{q} = 0$ implies $x F_3 = 2x F_1$, we should use

$$2x F_1 = \frac{(1 + 4m_p^2 x^2 / Q^2)}{(1 + R)} F_2 \quad (7.79)$$

instead of F_2 in the high- x region. Fixed values of R and QCD values of R induce minor Q^2 variations, but the $4m_p^2 x^2 / Q^2$ term induces large (up to $\sim 10\%$) variations in $2x F_1$ with respect to F_2 . This changes the value of Λ , or α_S , significantly as seen by the result of a fit with $2x F_1$ used instead of F_2 for $x > .4$ and $R = R_{QCD}$:

$$\begin{aligned} \Lambda_{LO} &= 426_{-113}^{+119} \text{ MeV} \\ \alpha_S &= .355 \pm .046 \text{ for } Q_0^2 = 12.6 \text{ GeV}^2 \\ b_3 &= .627 \pm .047 \\ c_3 &= 2.76 \pm .13 \\ a_3 &= 4.45 \pm .22 \\ \chi^2 &= 51.9 \text{ for } 47 \text{ DF} \end{aligned}$$

Perhaps the wisest approach in attempting to substitute F_2 for $x F_3$ at large x is to wait until data are available in regions where $4m_p^2 x^2 / Q^2 \ll 1$.

7.5.2 \overline{MS} Non-singlet Analysis

We have also done a second order analysis of the $x F_3$ data. We choose to work in the \overline{MS} scheme; the value of Λ in a different scheme can be obtained from the \overline{MS} result. We have used the programs of Duke et al.⁽⁸³⁾ and of Barnett⁽⁸⁴⁾. The latter parametrizes $x F_3$ at Q_0^2 as in the leading order case while using the second order evolution equation, of course. The other approach, that of Duke et al., uses a definition of parton densities that makes them 'universal' i.e., the same densities apply in all processes. In this method, the parton densities are first evolved and then the structure function is constructed from them at any given Q_0^2 . Effectively, this is a two-step procedure. In the Barnett approach the coefficient functions that are convoluted with the parton densities to obtain $x F_3$ in the two-step procedure are absorbed into the $x F_3$ evolution equation (7.80). In order to get the same value for $\Lambda_{\overline{MS}}$ from both procedures, the parametrization of $x F_3$ at Q_0^2 in one case must be different from the parametrization of the parton densities at Q_0^2 in the other, and both must be the true functional forms. Since those forms are unknown, both Barnett and Duke et al. have chosen to parametrize their distributions at Q_0^2 by the *same* functional form, the one in (7.73). Thus, the result is two different $\Lambda_{\overline{MS}}$ values. However, the difference in α_S ($Q^2 = 12.6 \text{ GeV}^2$) is small

in comparison to the statistical error and both values of α_S^0 agree with the leading order result (table 7.6). The xF_3 evolution equation in second order is

$$\begin{aligned} \frac{d x F_3(x, Q^2)}{d \ln Q^2} = \frac{\alpha_S(Q^2)}{2\pi} \left\{ \left(2 + \frac{8}{3} \ln(1-x) \right) x F_3(x, Q^2) \right. \\ \left. + \int_x^1 \frac{4}{3} \frac{((1+z^2) \frac{x}{z} F_3(\frac{x}{z}, Q^2) - 2x F_3(x, Q^2)) dz}{(1-z)} \right. \\ \left. + \frac{\alpha_S(Q^2)}{2\pi} \int_x^1 dz \left(\frac{x}{z} F_3(\frac{x}{z}, Q^2) - x F_3(x, Q^2) \right) W(z) \right. \\ \left. - \frac{\alpha_S(Q^2)}{2\pi} x F_3(x, Q^2) \int_0^x dz W(z) \right\} \end{aligned} \quad (7.80)$$

where, $\alpha_S(Q^2)$ is the second order expression (7.47) and

$$\begin{aligned} W(z) = & -\frac{2\beta_0}{3} \left(\frac{(1+z^2)}{(1-z)} \left(\ln \left(\frac{1-z}{z} \right) - \frac{3}{4} \right) + \left(\frac{9+5z}{4} \right) - (1+z) \right) \\ & + \frac{16}{9} \left(-2(1+z^2) \ln z \frac{\ln(1-z)}{(1-z)} - \left(\frac{3}{1-z} + 2z \right) \ln z - \frac{1}{2}(1+z) \ln^2 z - 5(1-z) \right) \\ & + 2 \left(\frac{(1+z^2)}{(1-z)} (\ln^2 z + \frac{11}{3} \ln z + \frac{67}{9} - \frac{\pi^2}{3}) + 2(1+z) \ln z + \frac{40}{3}(1-z) \right) \\ & + \frac{16}{9} \left(\frac{(1+z^2)}{(1-z)} (-\ln z - \frac{5}{3}) - 2(1-z) \right) \\ & + \frac{4}{9} \left(\frac{1+z^2}{1+z} \int_{1/z}^z dy \left(\frac{-\ln y}{1+y} \right) + (1+z) \ln z + 2(1-z) \right) \end{aligned} \quad (7.81)$$

The χ^2 versus α_S curve for the Duke et al. technique is displayed in figure 7.13. The fit is plotted through the data in figure 7.14. The best fit parameters, it is emphasized, for the two techniques are for xF_3 in the Barnett case and for the universal parton distribution in the other. We do not show the (fractional) systematic errors in the \overline{MS} case which would merely be a duplication of the fractional errors in the leading log case.

Parameter	Leading Order	\overline{MS} Barnett (ref.84)	\overline{MS} Duke et al. (ref. 83)
Λ	88^{+103}_{-78}	120^{+200}_{-108}	193^{+272}_{-158}
$\alpha_S(Q^2 = 12.6 \text{ GeV}^2)$	$.204 \pm .079$	$.176 \pm .062$	$.201 \pm .070$
b_3	$.672 \pm .058$	$.631 \pm .059$	$.664 \pm .058$
c_3	$3.29 \pm .24$	$3.36 \pm .22$	$3.54 \pm .20$
a_3	$4.34 \pm .24$	$5.05 \pm .35$	$5.94 \pm .46$
χ^2/DF	44.2/45	44.0/45	43.5/45

Table 7.6

Best fit parameters resulting from first and second order (\overline{MS}) fits to xF_3 .

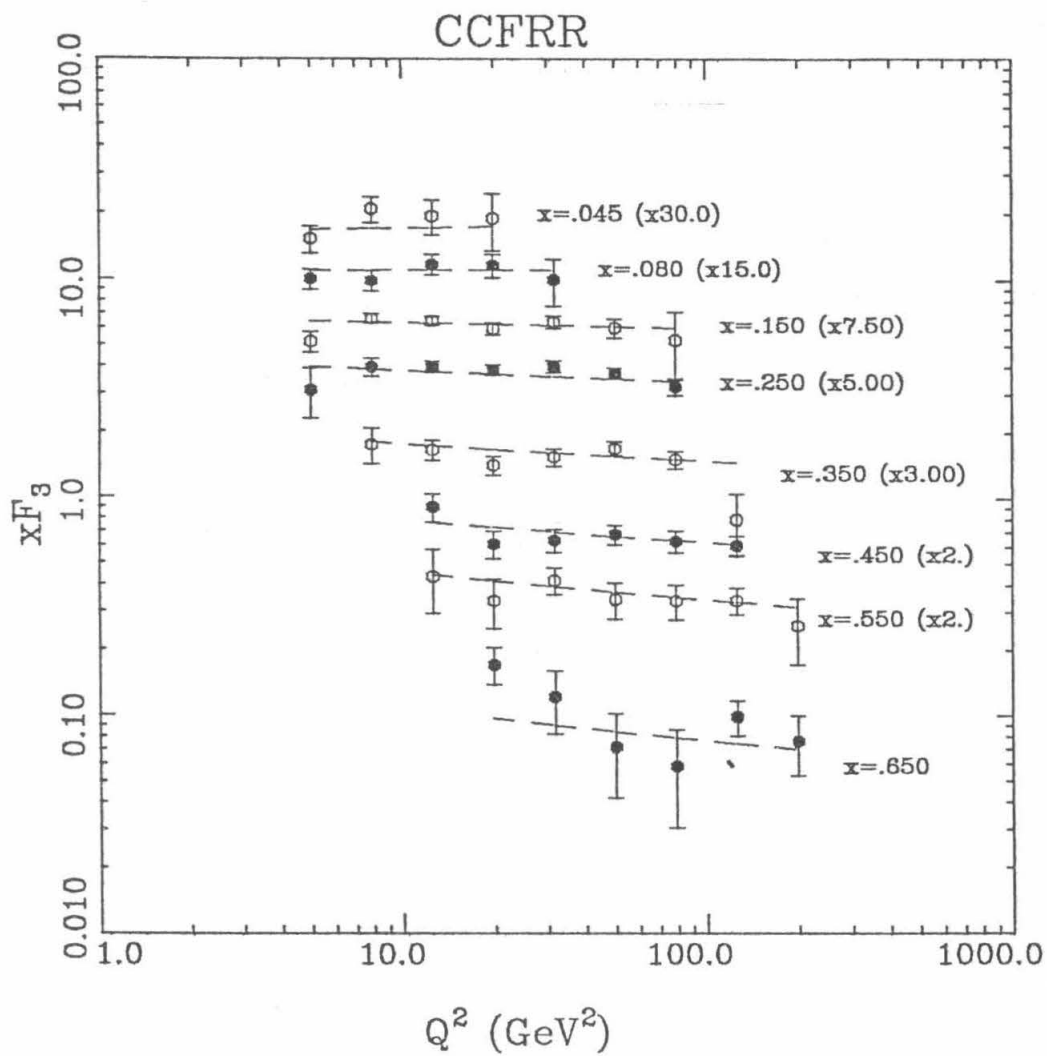


Figure 7.14. xF_3 data with \overline{MS} fit (dashed lines).

7.5.3 Non-singlet Analysis Summary

The hypothesis of no scaling violations ($\Lambda = 0$) is clearly ruled out by all the leading order and second order results (see figs. 7.8, 7.9 and 7.13). Also, an attempt was made to look for higher twist effects by the multiplicative inclusion of the term $(1 + h/Q^2)$ in the xF_3 evolution, but the values of h thus obtained had large errors, with h consistent with zero and no improvement in χ^2 . For example, an \overline{MS} analysis yields $h = 26 \pm 23$.

After Barnett⁽⁹⁸⁾ we have also attempted to look for W^2 dependence in α_S . Our present statistics prevent us from corroborating his evidence that the value of α_S falls if the lower limit for W^2 is raised. The same conclusion is reached with a search for Q^2 dependence (table 7.7).

Q^2 cut (GeV ²)	W^2 cut (GeV ²)	Λ_{LO} (MeV)	χ^2/DF	$\Lambda_{\overline{MS}}$ (MeV)	χ^2/DF
5	10	88 \pm 111	44.2/45	193 \pm 206	43.5/45
5	20	24 \pm 93	34.8/38	67 \pm 163	34.6/38
5	30	131 \pm 254	27.3/32	197 \pm 346	27.5/32
5	10	88 \pm 111	44.2/45	193 \pm 206	43.5/45
10	10	135 \pm 181	31.7/36	144 \pm 197	32.2/36
15	10	62 \pm 115	29.8/29	64 \pm 124	30.1/29
25	10	410 \pm 512	16.7/21	327 \pm 477	17.5/21

Table 7.7

Variation in Λ_{LO} and $\Lambda_{\overline{MS}}$ due to Q^2 and W^2 cuts. The \overline{MS} values are for the technique of Duke et al. The errors are quadratic errors; despite appearances they do not really permit $\Lambda = 0$, e.g., the true errors for the leading order value in the first row are ± 163 MeV and -78 MeV.

We conclude that the determination of Λ from xF_3 is presently limited by statistics. Higher statistics experiments will need more precise flux calibrations as the uncorrelated error on ν and $\bar{\nu}$ fluxes leads to significant uncertainties in xF_3 .

7.5.4 Singlet Analysis

The QCD analysis of F_2 is the subject of another thesis⁽¹⁰⁾; we merely summarize the situation here. The evolution of F_2 depends on the gluon distribution, and its extracted values depend on the value of R and the strange fraction of the sea, particularly at low x . By using the momentum sum rule:

$$\int_0^1 G(x, Q^2) dx = 1 - \int_0^1 F_2(x, Q^2) dx \quad (7.82)$$

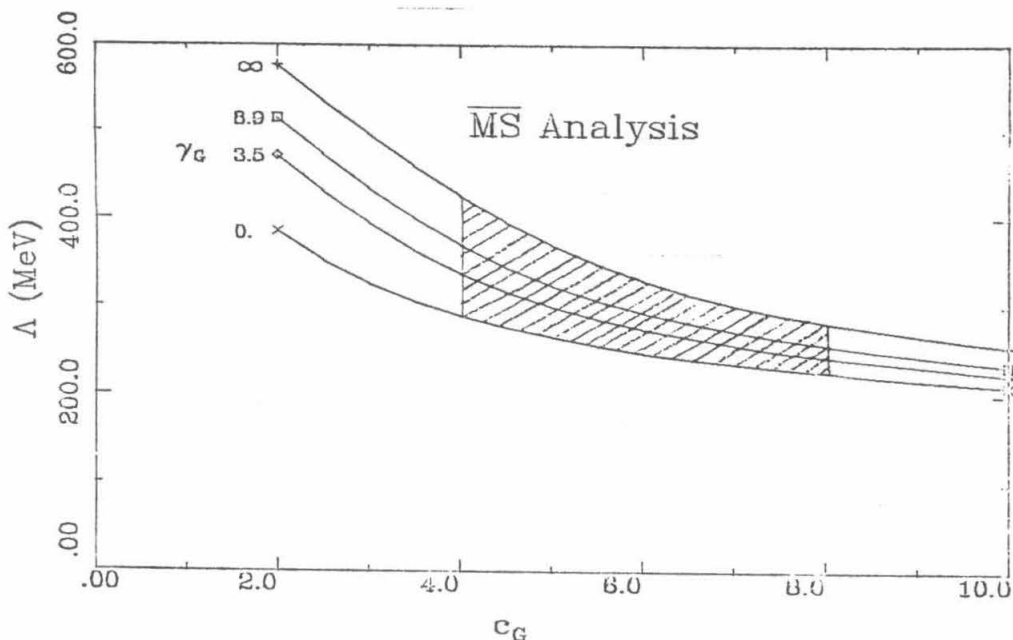


Figure 7.15

Best fit points in the Λ - c_G plane, for different values of γ_G . The shaded area indicates the reasonable range of values for the parameters c_G and γ_G .

we put a powerful constraint on the gluon distribution. The regions used for the F_2 analysis in x and Q^2 are the same as those for xF_3 except we eliminate $x < .1$ and thus decrease the sensitivity to R and the strange sea. Λ remains highly correlated to other parameters, especially to c_G which is poorly determined.

The statistical precision and lower sensitivity of F_2 to scale errors enable us, however, to extract a value of Λ for various assumptions about the gluon distribution. The reasonable assumptions $\gamma_G \geq 0$ and $4 \leq c_G \leq 8$ lead us to a range of values for Λ with different R assumptions (table 7.8). Figure 7.15 shows the correlation between parameter values and Λ for $R = R_{QCD}$ and helps delineate the allowed range.

The best fit Λ values for the three different R assumptions are listed in table 7.8. As noted earlier, most systematic errors on Λ are smaller for F_2 — the values in leading order are ± 25 MeV for the flux smoothing procedure, ± 30 MeV from flux level uncertainties, ± 10 MeV from the beam dispersion and ± 15 MeV each from the hadron and muon energy calibration errors. However, as evidenced from table 7.8, the uncertainty from the gluon distribution is estimated at ± 50 MeV. In future a more precise value of Λ from xF_3 could be used in the F_2 analysis to measure the gluon distribution. At present, our value implies, albeit weakly, a high value for c_G i.e., a soft gluon distribution. Using the CDHS measurement of \bar{q} , we find that the value and error on Λ do not change significantly, but a much better determination of

the gluon distribution is possible. The gluon distribution now has no freedom beyond $x = .25$, and is essentially the same as the CDHS distribution in that region, but the difference in the F_2 integrals from the two experiments forces their gluon distribution to be much larger at low- x .

	Λ_{LO}	$\Lambda_{\overline{MS}}$
$R = 0.0$	$360 \pm 100 \text{ MeV}$	$390 \pm 110 \text{ MeV}$
$R = 0.1$	$200 \pm 90 \text{ MeV}$	$230 \pm 100 \text{ MeV}$
R_{QCD}	$300 \pm 100 \text{ MeV}$	$340 \pm 110 \text{ MeV}$

Table 7.8. F_2 fits with $c_G = 4.6$, $\gamma_G = 9.0$

7.5.5 Comparison with Other Experiments

Other experiments have attempted to measure Λ (see table 7.9), notably EMC⁽⁸⁵⁻⁸⁷⁾ who obtain $\Lambda_{\overline{MS}} = 173_{-98}^{+184}$ MeV from F_2 using iron data, in good agreement with our result from xF_3 . CDHS⁽⁸¹⁾ obtain a value of $\Lambda_{\overline{MS}} = .2_{-0.1}^{+0.2}$ GeV, from a non-singlet analysis of their xF_3 , again for iron and also in good agreement with our result. Clearly, the values for Λ from F_2 lie within errors of the xF_3 results, perhaps because of the somewhat large errors. We can however rule out the older high Λ values obtained by BEBC⁽⁸⁸⁾ at lower Q^2 ($\Lambda_{LO} = .74_{\pm .05}$ GeV) and the older CDHS Buras-Gaemers style analysis⁽⁸⁹⁾ which led to $\Lambda_{LO} = .47_{\pm .1} \pm .1$ GeV. In fact, at the 90% confidence level, using statistical errors, we can state from our xF_3 analysis that

$$.2 < \Lambda_{LO} < 420 \text{ MeV}$$

The BFP muon experiment⁽⁸²⁾ at Fermilab, also in our Q^2 -range, reports a preliminary result with leading order Λ values between 160 MeV and 230 MeV, depending on assumptions made. The CHARM collaboration has done a fit^(110,111) of the non-singlet structure function and obtain a leading order result that is consistent with ours: $\Lambda = 187_{-110}^{+130} \pm 70$ MeV.

Recent results from angular energy correlations in e^+e^- experiments indicate values of Λ in the same range: the Mark-J group reports⁽⁹⁰⁾ $\Lambda_{\overline{MS}} = 180_{-40}^{+60}$ MeV and $\Lambda_{\overline{MS}}$ from two-photon scattering has a comparable value⁽⁹¹⁾: $\Lambda_{\overline{MS}} \approx .2_{\pm .1}$ GeV. The Mark-J result depends on Monte Carlo assumptions about fragmentation, however. Thus it appears that the high-statistics neutrino and muon experiments outside the low- Q^2 region all have values of Λ in the 100 - 300 MeV range, an encouraging sign. Values of Λ from neutrino and muon experiments agree to a remarkable level and singlet and non-singlet analyses lead to the same result within errors. The e^+e^- results are similarly heartening, especially the higher Q^2 result, but error bars prevent us from concluding that the similarity in Λ values from different experiments at different Q^2 values implies that perturbative QCD has been proven beyond doubt.

Experiment	Order	Λ (MeV)
BEBC, ⁽⁸⁸⁾ lower Q^2	LO	740 ± 50
CDHS, ⁽⁸⁹⁾ old result	LO	$470 \pm 100 \pm 100$
CCFRR, ⁽¹⁰⁾ F_2	\overline{MS}	340 ± 110
CCFRR, $x F_3$	LO	$88_{-78}^{+183} \pm_{-70}^{+113}$
CCFRR, $x F_3$	\overline{MS}	193_{-156}^{+272}
EMC, ⁽⁸⁷⁾ iron data	\overline{MS}	173_{-98}^{+164}
CDHS, ⁽⁸¹⁾ $x F_3$	\overline{MS}	200_{-100}^{+200}
BFP, ⁽⁸²⁾ preliminary	LO	160 to 230
CHARM ^(110,111) , $x F_3$	LO	$187_{-110}^{+130} \pm 70$
Mark-J ⁽⁹⁰⁾	\overline{MS}	180_{-40}^{+60}
Two-photon ⁽⁹¹⁾ (JADE)	\overline{MS}	200 ± 100

Table 7.9

Comparison of Λ values from different experiments with emphasis on values from non-singlet distributions. The two older values (first two columns) are higher than recent results which all agree within errors. Our \overline{MS} value is for the Duke et al. method, with statistical errors only.

§7.6 Extraction of R

7.6.1 R from y -dependence of Differential Cross-sections

The dependence of the differential cross-sections on R is not very strong (6.1). Further, F_2 and R enter as one term, identical for both neutrinos and antineutrinos, and the small value of R makes it harder to measure. We have to utilize the different y -dependence of R and F_2 in (6.1) for extraction. A simple technique would be to fit a second order polynomial to y -distributions in x and Q^2 bins and extract F_2 , R and $x F_3$ from the coefficients of the powers of y . Given the level of our statistics, we have chosen the maximum likelihood technique instead, which is essentially an extension of the structure function extraction method.

Each x and Q^2 bin is now further divided into 20 y bins, and the number of neutrino and antineutrino events in every such bin is accumulated and corrected for resolutions, as before. If there are n_i neutrino events in the i^{th} y -bin and \bar{n}_i antineutrino events, then

$$\begin{aligned}
 n_i &= a_i F_2 + b_i 2x F_1 + c_i x F_3 + d_i \\
 \bar{n}_i &= \bar{a}_i F_2 + \bar{b}_i 2x F_1 + \bar{c}_i x F_3 + \bar{d}_i
 \end{aligned}
 \tag{7.83}$$

a , b , c and d have to be obtained, as in the structure function case, by integrating over the appropriate coefficients (see 6.11). The integration would require even more CP time to maintain the same accuracy in these integrals as before, since we have carved out 20 bins out of each x and Q^2 bin. This becomes impossible to handle by simple techniques and therefore we resorted to a Monte Carlo integration. The integration uses stratified sampling with partitioning to reduce variance. We have verified that summing the integrals over the y bins returns the integrals in each x and Q^2 bin evaluated for structure function extraction.

We now form a likelihood for the numbers of ν and $\bar{\nu}$ events in y bins and maximize it by varying F_2 , $2xF_1$ and xF_3 . R is then extracted using (7.23). We check to ensure that xF_3 thus obtained agrees with xF_3 extracted with an assumption about R (as it should because of its independence of R). The results still suffer from poor statistics and it is impossible to detect any meaningful Q^2 dependence of R in an x -bin (see fig. 7.16). Averaging R over Q^2 , we obtain the values listed in table 7.10. The errors are still large. We can only say that R appears lower in the $x > .4$ region than in the $x < .4$ region — the averages for $0 < x < .1$, $.1 < x < .4$ and $.4 < x < 1$. are $.12 \pm .08$, $.16 \pm .09$ and $-.65 \pm .13$. Averaged over all x , we obtain $R = -.01 \pm .05$.

x -bin	R (stat. errors)
$0 < x < .03$	$.04 \pm .15$
$.03 < x < .06$	$.27 \pm .16$
$.06 < x < .1$	$.08 \pm .12$
$.1 < x < .2$	$.30 \pm .13$
$.2 < x < .3$	$.20 \pm .16$
$.3 < x < .4$	$-.12 \pm .17$
$.4 < x < .5$	$-.21 \pm .27$
$.5 < x < .6$	2.7 ± 5.7
$.6 < x < .7$	$-.77 \pm .14$
$.7 < x < 1$.	1.7 ± 10.3

Table 7.10

Values of R in x bins are averaged over Q^2 . The errors are statistical only.

Of course, we have completely ignored systematic effects in obtaining the above numbers. They may therefore be misleading. R is sensitive to anything that affects y -distributions. Therefore flux levels and the energy dependence of cross-sections have to be better understood. We shall leave this task to some future student.

Lacking an estimate of systematic errors, it is improper to draw conclusions from a comparison of our R value with other measurements in the same Q^2 -range; suffice it to say that the values from CHIO⁽¹⁰⁵⁾, SLAC⁽¹⁰⁶⁾, EMC⁽⁶¹⁾ and CDHS⁽⁶²⁾ lie between 0 and .5 and are consistent with each other because of large errors (see fig7.17).

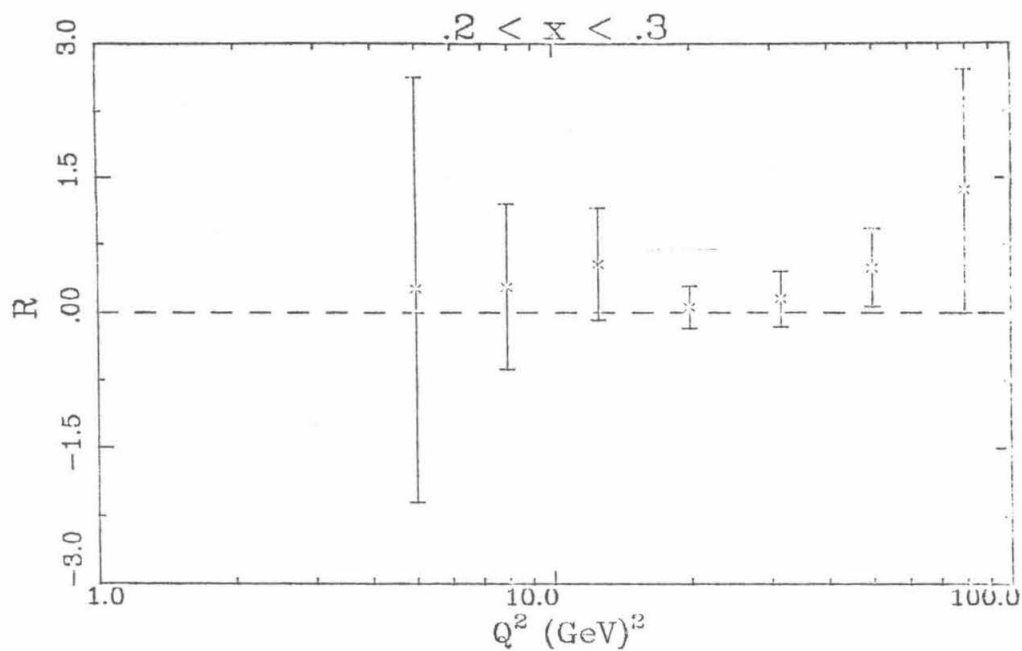


Figure 7.16

R in the bin $.2 < x < .3$ as an illustration of the fluctuations and errors.

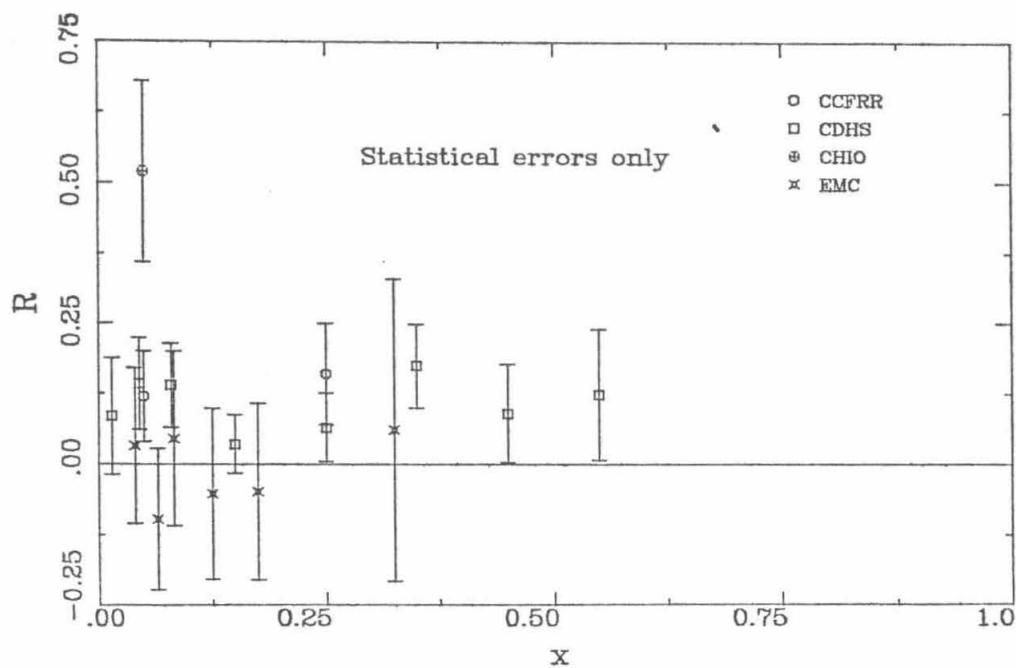


Figure 7.17. R from various experiments.

7.6.2 Limit on R

An attempt was made to obtain an upper limit on R from the condition that $\bar{q}(x) \geq 0$. If $\bar{q}(x)$ is set to zero, only two unknowns remain in every x and Q^2 bin viz., xF_3 and R. Ignoring correction terms and using (7.79), equation 6.1 gives

$$\frac{d^2\sigma^{\nu,\bar{\nu}}}{dx dy} = \frac{G^2 m_p E}{\pi} \left\{ \frac{(1-y)(1+R)}{(1+4m_p^2 x^2/Q^2)} + \frac{y^2}{2(1+2m_p^2 x^2/Q^2)} \pm \frac{(1-(1-y)^2)}{2} \right\} xF_3 \quad (7.84)$$

Integrating over flux and acceptance, the left hand side represents the number of ν and $\bar{\nu}$ events in a bin. The rest of the procedure follows the details of the structure function extraction technique. xF_3 , as before, comes from the difference of the numbers of ν and $\bar{\nu}$ events:

$$n_\nu - n_{\bar{\nu}} = k \langle (1 - (1 - y)^2) \rangle xF_3 \quad (7.85)$$

where k is the overall constant and $\langle \rangle$ denotes integration over bin limits. Along with the equation that comes from summing neutrinos and antineutrinos, we get

$$\left(\frac{n_\nu + n_{\bar{\nu}}}{n_\nu - n_{\bar{\nu}}} \right) \langle (1 - (1 - y)^2) \rangle - \langle (1 + (1 - y)^2) \rangle + \langle y^2 \rangle = \frac{2m_p^2 x^2}{Q^2} = \frac{2R \langle (1 - y) \rangle}{(1 + 4m_p^2 x^2/Q^2)} \quad (7.86)$$

Now the left hand side is almost zero, since R is small, leading to large errors on the extracted limit for R. Thus we are again limited by statistics — the limit, if averaged in the region $x > .4$ is .55 at the 90% confidence level. The CDHS collaboration⁽⁸¹⁾ used narrow-band and wide-band data in the region $.4 < x < .7$ to obtain $R \leq .04 \pm .03$. We conclude that the measurement of R has serious statistical and systematic problems that require further investigation and content ourselves for the present with extracting structure functions with three different assumptions about R (6.10), all of which are consistent with our attempt to extract R.

§7.7 Conclusions

Data were taken during the run of experiment 616 at Fermilab using neutrino and antineutrino dichromatic beams at five momentum settings: 120, 140, 165, 200 and 250 GeV/c. The flux of neutrinos was monitored, allowing a normalized measurement. The absolute level of fluxes was calibrated to 3% with further uncorrelated uncertainties of 1.4% and 3.2% for neutrinos and antineutrinos respectively. With 5.9×10^{18} protons on target, we measured a total of 150000 neutrino and 23000 antineutrino charged current events using the Lab E detector. The 640 ton instrumented target was used to measure the angle of the outgoing muon and the energy of the hadron shower. Downstream, a toroidal spectrometer measured the muon momentum.

After making model independent acceptance corrections the data were analyzed to extract the structure functions F_2 and xF_3 of nucleons in iron (with no Fermi motion corrections) under three different assumptions about the value of R. We covered the range $0 < x < .7$

and $1 < Q^2 < 250 \text{ GeV}^2$. Corrections were made for resolutions, the strange sea, the onset of charm production, radiative effects, and a correction for the mildly non-isoscalar nature of the target nuclei. Statistical and systematic errors on the result have been studied. Statistical errors dominate uncorrelated systematic errors for both xF_3 and F_2 . Correlated flux systematic errors are 3.2% but do not affect determinations of quantities that come from a combined analysis of all bins, e.g., of Λ .

The major conclusions from analysis of the structure functions can be summarized as follows:

- (1) Both $F_2(x, Q^2)$ and $xF_3(x, Q^2)$ have been compared with results from other experiments. Apart from level differences expected from total cross-section differences, the low- x behaviour of the structure function F_2 is markedly different from the CDHS measurement, but is in agreement with that of the EMC and BFP collaborations. In a comparison of xF_3 as a function of x , only the HPWF results show a striking dissimilarity.
- (2) Being the best experiment to measure the GLS sum rule we find

$$\int_0^1 F_3 dx = 2.83 \pm .15 \pm .09 \pm .10$$

at $Q^2 = 3 \text{ GeV}^2$. This is consistent with the quark-parton model value of 3 and QCD expectations with $\Lambda < 525 \text{ MeV}$.

- (3) The QCD evolution of xF_3 , which is independent of R and the strange sea, does not depend on the gluon distribution and fits yield

$$\Lambda_{LO} = 88_{-78}^{+163} \text{ }_{-70}^{+113} \text{ MeV}$$

The systematic errors are smaller than the statistical errors. Second order fits give somewhat different values of Λ , although α_S (at $Q_0^2 = 12.6 \text{ GeV}^2$) is not so different.

- (4) A fit using the better determined F_2 in place of xF_3 for $x > 0.4$ i.e., assuming $\bar{q} = 0$ in that region, gives

$$\Lambda_{LO} = 266_{-104}^{+114} \text{ }_{-79}^{+85} \text{ MeV}$$

Again, the statistical errors are larger than the systematic errors.

- (5) QCD fits to F_2 with a particular choice of the gluon distribution and R give⁽¹⁰⁾

$$\begin{aligned} \Lambda_{LO} &= 360 \pm 100 \text{ MeV} \\ \Lambda_{\overline{MS}} &= 340 \pm 110 \text{ MeV} \end{aligned}$$

Variations in the gluon distribution parameters indicate an additional rms variation of $\sim 50 \text{ MeV}$. The combined systematic uncertainty from the flux and from assumptions about R is comparable to the statistical error. Using the constraint $\bar{q} \approx 0$ for $x > .4$ enables us to make a significant determination of the gluon distribution.

- (6) An attempt to measure R was made. The value of R suffers from serious statistical and systematic uncertainties. The value is shown in figure 7.17 as a function of x . The upper limit on R from the condition $\bar{q}(x) \geq 0$ is 0.55 at the 90% CL in the region $x > 0.4$.

During the course of this analysis there has been an ongoing effort to upgrade the Lab E detector. Drift chambers will replace the spark chambers used in E616. This will permit a higher data taking rate, with the detector essentially not limited by deadtime ($\sim 10 \mu\text{sec}$ per trigger) at projected trigger rates.

With the availability of a 1000 GeV proton beam it will become possible to study the neutrino and antineutrino cross-sections at higher energies. Another high-statistics dichromatic run is planned (E652). The higher energy will make possible an accurate measurement of the GLS rule in a high Q^2 region for the first time. The most interesting question will be the Q^2 dependence of structure functions — has Λ changed with the increase in Q^2 ? It will be important to measure flux levels with higher precision for F_2 comparisons. Higher statistics will improve the Λ value from xF_3 .

A better value of Λ in the present energy range is needed to be able to draw any conclusion about a change in its value as one goes to Tevatron energies. Since our numbers are statistically limited, an extra four to five times the present data will be very useful. An experiment to measure neutrino oscillations with the Lab E detector⁽¹⁰⁹⁾ and the same beam collected roughly an equal number of events during 1981–1982. Further, a wide-band run at the Tevatron (which will mean neutrinos between 100 GeV and 300 GeV) can add an extra million or so events. Such a data set will have to use either our cross-sections or cross-sections measured in the future using a dichromatic beam. Even so, the systematic errors on Λ from xF_3 will come mainly from the cross-sections, and therefore not be the limiting factor until several times the present number of events have been collected.

Appendix A
Beam Kinematics

The flux of neutrinos at Lab E is a function of position and energy setting. As mentioned in the main text, for a dichromatic beam, there is a correlation between radius and neutrino energy; here we derive this and other illustrative quantities.

Most of the decays are 2-body decays ($\pi^\pm \rightarrow \mu^\pm \bar{\nu}_\mu$; $K^\pm \rightarrow \mu^\pm \bar{\nu}_\mu$). The few 3-body decays that produce, on the average, somewhat lower energy muon neutrinos are a small correction. For a 2-body decay, the energy of the neutrino in the zero-momentum frame is given by

$$E^* = p^* = \frac{m_M}{2} \left(1 - \left(\frac{m_\mu}{m_M} \right)^2 \right),$$

where m_M = the mass of the parent meson. For pions, p^* is 29.79 MeV, for kaons it is 235.53 MeV. The lab energy of neutrinos depends, of course, on the energy of the decaying meson in the lab frame and the centre-of-mass decay angle of the neutrino. Defining the z-axis to be the direction of the meson momentum, let θ^* be the angle the neutrino makes with the z-axis in the zero-momentum frame. Then,

$$\left. \begin{aligned} E &= \gamma p^* (1 + \beta \cos \theta^*) \\ p_z &= \gamma p^* (\beta + \cos \theta^*) \\ p_\perp &= p_\perp^* \end{aligned} \right\}$$

Clearly, the maximum and minimum lab energies of the neutrino will be

$$\begin{aligned} E_{min} &= \gamma p^* (1 - \beta) \\ \text{and } E_{max} &= \gamma p^* (1 + \beta), \end{aligned}$$

spanning almost the whole range from zero to $2\gamma p^*$. The lab angle θ corresponding to θ^* given by

$$\cos \theta^* = \frac{\cos \theta - \beta}{1 - \beta \cos \theta}; \quad \phi^* = \phi. \quad (\text{A.1})$$

Thus, at a fixed radius at Lab E,

$$\begin{aligned}
 E &= \gamma p^* (1 + \beta \cos\theta^*) \\
 &= \frac{E_M}{m_M} \frac{m_M}{2} \left(1 - \left(\frac{m_\mu}{m_M} \right)^2 \right) \left(\frac{1 - \beta^2}{1 - \beta \cos\theta} \right) \\
 &= \frac{E_M}{2} \left(1 - \left(\frac{m_\mu}{m_M} \right)^2 \right) \left(\frac{m_M^2 / E_M^2}{1 - \beta \cos\theta} \right)
 \end{aligned}
 \tag{A.2}$$

The maximum radius attainable for a neutrino occurs when $\theta = 0$, giving in the limit $p_M \gg m_M$,

$$E_{max} = E_M \left(1 - \left(\frac{m_\mu}{m_M} \right)^2 \right). \tag{A.3}$$

The factor $\left(1 - \left(\frac{m_\mu}{m_M} \right)^2 \right)$ is 42.7% for pions and 95.4% for kaons, clearly showing that kaon neutrinos have larger energies. Equation (A.2) also clearly establishes an energy versus radius relationship for neutrinos at Lab E. If the beam were infinitely thin, monochromatic and decayed at a point, fixed $\cos\theta$ would correspond to a fixed energy E at Lab E, and so energy would fall off with radius (r). Such an ideal E vs. r plot is shown in figure A.1 for all our secondary energy settings. Continuing with this simplification for a moment, let R be the distance of the decay point from Lab E. If the dimensions of Lab E are always small compared to R ,

$$\cos\theta = \frac{R}{\sqrt{R^2 + r^2}} \approx 1 - \frac{r^2}{2R^2}.$$

Substituting this in (A.2) it is not hard to show that

$$E = \frac{E_{max}}{1 + (r/R)^2 \gamma^2}, \tag{A.4}$$

which gives us the energy vs. radius expression. Notice the characteristic r -dependent fall-off which comes from the $(1 - \beta \cos\theta)$ term in (A.2). The full width at half-maximum is given by

$$r_{FWHM} = \frac{2R}{\gamma}. \tag{A.5}$$

Since pions are lighter than kaons, they have larger γ , and thus their energy falls off much more rapidly with radius.

The other important factor in the kinematics is the flux variation as a function of angle. Since both pions and kaons are spin-zero (there would be no spin selection anyway) the decays in the rest frame are isotropic. If $C(\theta, \phi)$ is the probability density for decay in $[\theta, \theta + d\theta]$

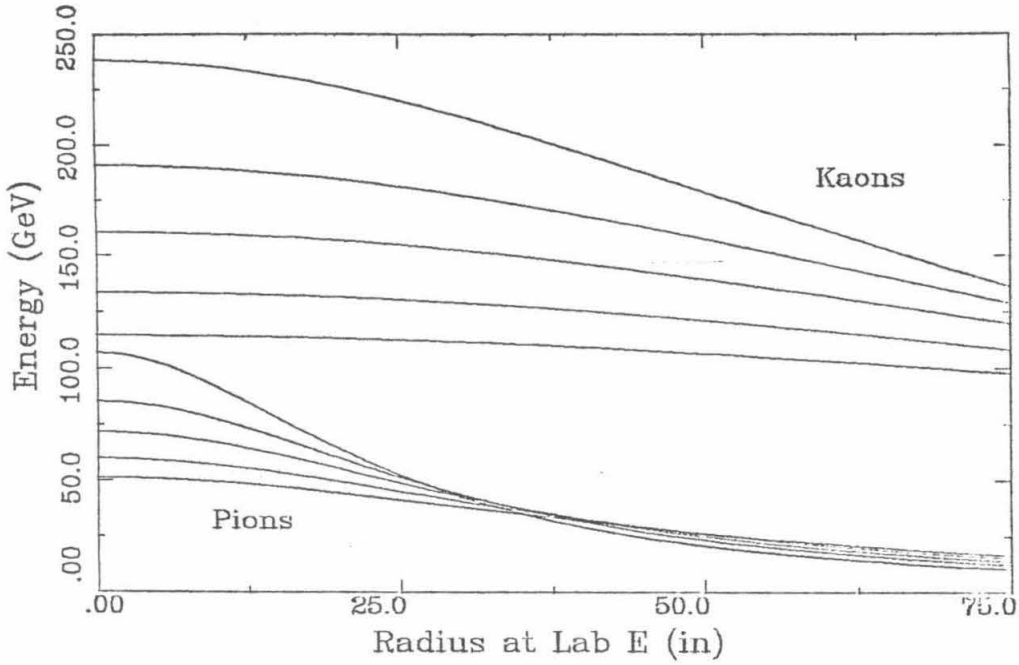


Figure A.1. Ideal Energy-radius relationship at Lab E

and $[\phi, \phi + d\phi]$ (spherical polar coordinates), then

$$C^*(\theta^*, \phi^*) = \frac{1}{4\pi}. \quad (\text{A.6})$$

$$\text{Combining } C^*(\theta^*, \phi^*) \sin\theta^* d\theta^* d\phi^* = C(\theta, \phi) \sin\theta d\theta d\phi \quad (\text{A.7})$$

with (A.1) and (A.6) gives

$$C(\theta, \phi) = \frac{(1 - \beta^2)}{4\pi(1 - \beta \cos\theta)^2}. \quad (\text{A.8})$$

The quantity $(1 - \beta \cos\theta)$ occurs twice in the denominator as opposed to once in (A.2); thus the flux falls off even faster with radius at Lab E. Indeed, rewriting (A.8) as

$$F(r) = \frac{F(0)}{(1 + (r/R)^2 \gamma^2)^2}, \quad (\text{A.9})$$

we see that the FWHM of the flux occurs when

$$\tau_{\text{FWHM}} = (2\sqrt{\sqrt{2} - 1}) \frac{R}{\gamma} = \frac{1.29R}{\gamma}. \quad (\text{A.10})$$

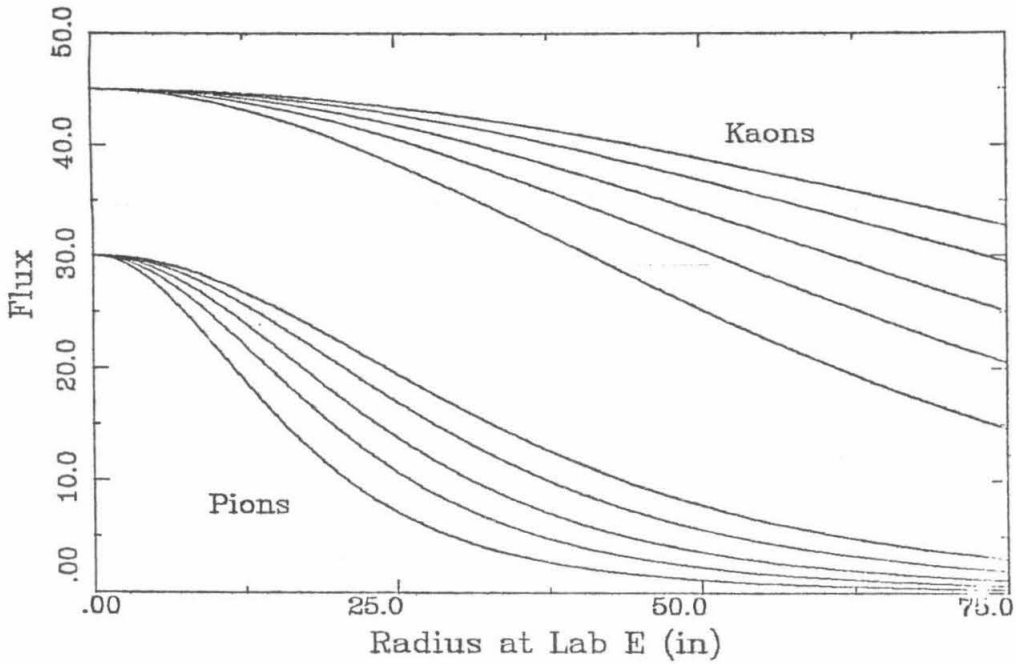


Figure A.2. Ideal Flux-radius relationship at Lab E

A plot of flux vs. radius for an ideal beam is shown in figure A.2.

The real neutrino beam differs from the one described above in four major respects:

- (i) The beam decays over an extended region in z , in fact the decay pipe is 351.5m long and at a mean distance of 1113.7m from Lab E. A factor $e^{-(z-z_2)/\gamma\lambda^*}$ must be multiplied into the flux expressions above and integrated over the z -limits (z_1, z_2) of the decay pipe. λ^* is the centre-of-mass decay length. In fact, the R in above expressions is now z -dependent. In as much as the z -dependence can be separated, the fraction of particles that decay in the decay pipe are $(1 - e^{-(z_2-z_1)/\gamma\lambda^*})$. The fiducial volume of Lab E itself has a spread in z of 12.7m, small compared to the above dimensions. λ^* for pions is 7.804m and is 3.709m for kaons. Listed in table A.1 are various interesting parameters for the beam. Since the decay pipe length is a significant fraction of the distance to Lab E, there will now be a range of energies at any radius r at Lab E instead of a fixed energy as given by (A.4). This fractional spread in energy is easily shown to depend on the fractional z -spread ($=351.5/1113.7$) as

$$\frac{\Delta E}{E} = \frac{\Delta R}{R} \cdot \frac{2}{1 + R^2/r^2\gamma^2}. \quad (\text{A.11})$$

Thus this effect introduces a $\Delta E/E$ from zero at $r = 0$ to 37% for pions at 250 GeV and $r = 30$ in . Similarly, (A.9) may be differentiated to give

$$\frac{\Delta F}{F} = \frac{\Delta R}{R} \cdot \frac{4}{1 + R^2/r^2\gamma^2} \quad (\text{A.12})$$

- (ii) The beam has a momentum spread of $\pm 9\%$. The effect on the radius and flux is straightforward: E as obtained in (A.4) develops the same $\pm 9\%$ spread, the flux spread is less than $\pm 1\%$.
- (iii) The beam has an angular spread of between .1 and .2 milliradians. Clearly this affects both the energy and flux relations. For kaon neutrinos at 250 GeV the flux FWHM angle (see table A.1) is 2.55 mrad, large compared to the angular dispersion, and consequently the effect is small for kaons. For pions, this effect begins to become significant at the higher energies. Differentiating (A.9) it is easy to show that

$$\frac{\Delta F}{F} \approx \frac{\Delta \theta}{\theta} \frac{4}{1 + R^2/r^2\gamma^2} \quad (\text{A.13})$$

and differentiating (A.4),

$$\frac{\Delta E}{E} \approx \frac{\Delta \theta}{\theta} \frac{2}{1 + R^2/r^2\gamma^2} \quad (\text{A.14})$$

- (iv) Two major background sources exist: the background of muon neutrinos from $K_{\mu 3}$ decays and from the wide band background. The latter is described in section 3.1. The decay $K^\pm \rightarrow \mu^\pm (\bar{\nu}_\mu) \pi^0$ has a branching fraction of 3.2% and contributes a small number of low energy neutrinos that are estimated by the beam Monte Carlo (see chapter 3).

Table A.1 of secondary beam related quantities

Energy settings for secondary beam: 120, 140, 168, 200, 250 GeV.

Momentum acceptance $\approx \pm 9.4\%$.

Angular divergence, horizontal $\approx \pm 0.15$ mrad

vertical $\approx \pm 0.19$ mrad

Length of decay pipe = 351.5m

\Rightarrow Gaussian width = 101.47m.

Mean distance to Lab E = 1113.7m.

E_{SET} = Energy setting

$r_{E,FWHM}$ = FWHM radius for the energy versus radius at Lab E.

$r_{F,FWHM}$ = FWHM radius for the flux versus radius at Lab E.

$\theta_{F,FWHM}$ = FWHM angle for the flux versus angle distribution.

The following spreads are computed at a radius of 30 in for neutrinos from pion decays and 70 in for neutrinos from kaon decays (the limits of acceptance cuts).

$(\Delta E/E)_z$: fractional energy spread due to finite decay length.

$(\Delta E/E)_\theta$: fractional energy spread due to angular dispersion of beam, assumed to be 0.18 mrad.

$(\Delta F/F)_\theta$: fractional flux spread due to angular dispersion of beam, assumed to be 0.18 mrad.

E_{SET}	Neutrinos from π decays								
(GeV)	$\tau_{B.FWHM}$	$\tau_{F.FWHM}$	$\theta_{F.FWHM}$	$(\Delta E/E)_z$	$(\Delta E/E)_\theta$	$(\Delta F/F)_\theta$	γ	E_{max}	DF
	(inches)	(inches)	(mrad)	(%)	(%)	(%)		(GeV)	(%)
120	102.0	65.64	1.50	4.68	13.53	27.05	859.8	51.2	5.10
140	87.4	56.26	1.28	5.83	16.85	33.70	1003.1	59.8	4.39
165	74.2	47.74	1.09	7.21	20.81	41.62	1182.2	70.4	3.74
200	61.2	39.38	0.90	8.93	25.79	51.58	1433.0	85.4	3.09
250	49.0	31.51	0.72	10.94	31.59	63.17	1791.3	106.7	2.48

E_{SET}	Neutrinos from K decays								
(GeV)	$\tau_{B.FWHM}$	$\tau_{F.FWHM}$	$\theta_{F.FWHM}$	$(\Delta E/E)_z$	$(\Delta E/E)_\theta$	$(\Delta F/F)_\theta$	γ	E_{max}	DF
	(inches)	(inches)	(mrad)	(%)	(%)	(%)		(GeV)	(%)
120	360.8	232.2	5.30	2.39	2.95	5.90	243.1	114.5	32.29
140	309.2	199.0	4.54	3.10	3.84	7.67	283.6	133.6	28.41
165	262.4	168.9	3.85	4.04	5.00	10.00	334.2	157.4	24.69
200	216.5	139.3	3.18	5.37	6.65	13.30	405.1	190.8	20.86
250	173.2	111.4	2.54	7.20	8.91	17.83	506.4	238.5	17.07

Consider the diagram below.

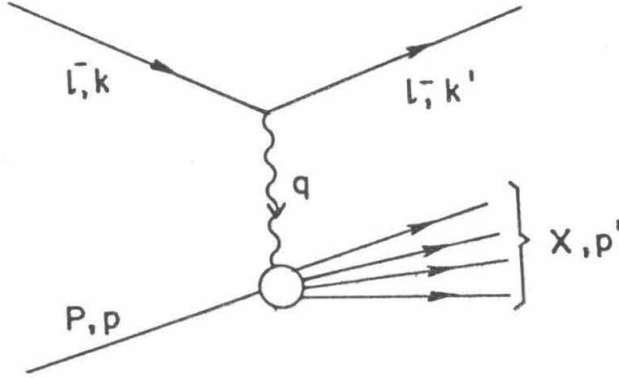


Figure B.1. Charged current process

The 4-momentum of the incident neutrino is k and that of the outgoing muon, k' . The proton is initially p , the final hadron shower p' .

$$\Rightarrow \left. \begin{aligned} k &= (E_\nu, 0, 0, E_\nu) \\ k' &= (E_\mu, p_\mu \sin\theta_\mu \cos\phi_\mu, p_\mu \sin\theta_\mu \sin\phi_\mu, p_\mu \cos\theta_\mu) \\ p &= (m_p, 0, 0, 0) \\ p' &= (m_p + E_\nu - E_\mu, -p_\mu \sin\theta_\mu \cos\phi_\mu, -p_\mu \sin\theta_\mu \sin\phi_\mu, E_\nu - p_\mu \cos\theta_\mu) \\ &= (E_h, p_h \sin\theta_h \cos\phi_h, p_h \sin\theta_h \sin\phi_h, p_h \cos\theta_h) \end{aligned} \right\} \text{(B.1)}$$

$$s = (p + k)^2 = m_p^2 + 2m_p E_\nu \approx 2m_p E_\nu \quad \text{(B.2)}$$

$$\nu \equiv p \cdot (k - k') = m_p(E_\nu - E_\mu) = m_p(E_h - m_p) \quad (B.3)$$

$$\begin{aligned} Q^2 &\equiv -(k - k')^2 = 2E_\mu E_\nu - 2E_\nu |\mathbf{p}_\mu| \cos\theta_\mu - m_\mu^2 \approx 2E_\nu E_\mu (1 - \cos\theta_\mu) \\ &= 4E_\mu E_\nu \sin^2 \frac{\theta_\mu}{2} \approx E_\mu E_\nu \theta_\mu^2 \end{aligned} \quad (B.4)$$

$$y \equiv \frac{\nu}{p \cdot k} = \frac{m_p(E_h - m_p)}{m_p E_\nu} \approx \frac{E_h}{E_\nu} \approx 1 - \frac{E_\mu}{E_\nu} \quad (B.5)$$

If the struck quark has negligible mass but produces another quark with possibly significant mass m_q ,

$$\begin{aligned} (q + xp)^2 &= m_q^2 \\ \text{or, } -Q^2 + 2xq \cdot p + x^2 m_p^2 &= m_q^2. \end{aligned}$$

$$\text{Neglect } x^2 m_p^2 \text{ to give } x \approx \frac{Q^2 + m_q^2}{2q \cdot p} = \frac{Q^2 + m_q^2}{2m_p(E_h - m_p)}. \quad (B.6)$$

$$\text{Neglecting } m_q, m_p \text{ gives } x \approx \frac{Q^2}{2m_p E_h} \quad (B.7)$$

$$\text{or } Q^2 \approx sxy \quad (B.8)$$

Also, from (B.1),

$$\begin{aligned} \cos\theta_h &= \frac{E_\nu - p_\mu \cos\theta_\mu}{\sqrt{E_\nu^2 + |\mathbf{p}_\mu|^2 - 2E_\nu |\mathbf{p}_\mu| \cos\theta_\mu}} \\ \Rightarrow \sin\theta_h &= \frac{|\mathbf{p}_\mu| \sin\theta_\mu}{\sqrt{E_\nu^2 + |\mathbf{p}_\mu|^2 - 2E_\nu |\mathbf{p}_\mu| \cos\theta_\mu}} \end{aligned} \quad (B.9)$$

Thus, or directly from (B.1),

$$\sin\theta_h = \frac{|\mathbf{p}_\mu|}{|\mathbf{p}_h|} \sin\theta_\mu \approx \frac{1-y}{y} \sin\theta_\mu. \quad (B.10)$$

It is easy to see that

$$(1-y) = \frac{(1 + \cos\theta^*)}{2}.$$

This follows trivially if we assume that all centre-of-mass energies are equal to ϵ and all particles are massless. If γ be the boost from the centre-of-mass to the lab frame,

$$\begin{aligned} E_\mu &= \gamma\epsilon + \gamma\epsilon \cos\theta^* \\ E_\nu &= \gamma\epsilon + \gamma\epsilon, \end{aligned} \quad (B.11)$$

from which and (B.5) the result is obvious.

Differential Cross-sections

Presented here is the expression for the differential cross-sections for neutrino and anti-neutrino scattering off nucleons, central to extraction of structure functions. A brief explanation precedes the formula.

The total cross section for a neutrino-quark collision, barring spin considerations, is

$$\frac{2G^2s}{\pi} \quad (\text{C.1})$$

Both the neutrino and the quark are spin-1/2 particles, giving rise to 4 possible situations. However, standard theory tells us that only left-handed neutrinos exist, and at high energies, interact only with left-handed quarks and right-handed antiquarks. We also consider the possibility of spin-zero constituents of nucleons. So all possible situations can be summarized as in fig. C.1.

As shown in appendix B,

$$(1 - y) = \frac{(1 + \cos\theta^*)}{2} \quad (\text{C.2})$$

If x be the fraction of the nucleon momentum carried by the struck quark, the differential cross-section for neutrino quark collisions is

$$\frac{d^2\sigma^\nu}{dx dy} = \frac{G^2s}{\pi} \cdot x \cdot q(x) \quad (\text{C.3})$$

The s in (C.1) must be replaced by sx , the square of the centre-of-mass energy for the neutrino-quark system as opposed to that of the neutrino-nucleon system. Since only left-handed quarks can interact, a factor of 1/2 appears. $q(x)dx$ is the probability of finding a quark with momentum fraction in $[x, x + dx]$. Because $J = 0$, there is no y factor in this case. In general though, one must include the appropriate power of $(1 + \cos\theta^*)/2$ or equivalently, of $(1 - y)$. For example, the antineutrino quark cross-section can be written

$$\frac{d^2\sigma^{\bar{\nu}}}{dx dy} = \frac{G^2s}{\pi} \cdot x q(x) \cdot (1 - y)^2 \quad (\text{C.4})$$

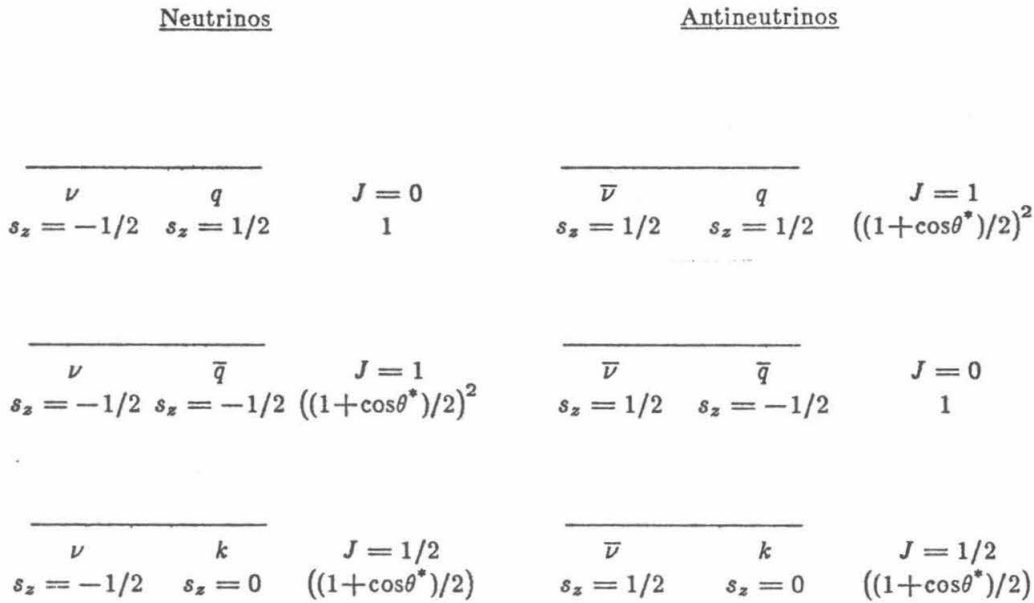


Figure C.1. Spin considerations diagram

Let u, d, s and c represent x times the probability density of finding a u, d, s or c quark in $[x, x + dx]$. The subscript v refers to valence quarks only. The superscripts p, n and N refer to the proton, neutron and nucleon respectively. $k(x)dx$ is x times the probability that a spin-zero object lies in the interval $[x, x + dx]$. Since the target is not exactly isoscalar, we introduce

$$f = \left\langle \frac{Z}{A} \right\rangle. \quad (C.5)$$

$$\left. \begin{array}{l} \text{We assume } c^N = \bar{c}^N = 0, \\ u_v^p = d_v^n, d_v^p = u_v^n \end{array} \right\} \quad (C.6)$$

$$\text{and } \bar{u}^p = \bar{u}^n = \bar{d}^p = \bar{d}^n. \quad (C.7)$$

Also, the strange sea is expected to have the same x dependence as \bar{u} and \bar{d} , therefore

$$s = \bar{s} = \frac{t}{2+t} \cdot \bar{q}, \quad (C.8)$$

where t is a constant expressing the fraction of "SU(3) symmetric" content due to the strange sea.

$$(\bar{u} = \bar{d} = \frac{1}{2+t} \bar{q}) \quad (C.9)$$

$$\text{For a "half SU(3) symmetric" sea, } t = 1/2 \quad (C.10)$$

Ignoring charm mass corrections for the moment, we then get

$$\frac{d^2\sigma^\nu}{dx dy} = \frac{G^2 s}{\pi} \cdot \left\{ (d^N + s^N) + (1-y)^2 \bar{u}^N + (1-y)k \right\}, \quad (\text{C.11})$$

$$\frac{d^2\sigma^{\bar{\nu}}}{dx dy} = \frac{G^2 s}{\pi} \cdot \left\{ (\bar{d}^N + \bar{s}^N) + (1-y)^2 u^N + (1-y)k \right\} \quad (\text{C.12})$$

$$\text{Clearly, } d^N = f(d_v^p + \bar{d}^p) + (1-f)(d_v^n + \bar{d}^n) = f d_v^p + (1-f)u_v^p + \bar{d}^p \quad (\text{C.13})$$

$$u^N = f(u_v^p + \bar{u}^p) + (1-f)(u_v^n + \bar{u}^n) = f u_v^p + (1-f)d_v^p + \bar{u}^p \quad (\text{C.14})$$

Defining

$$\left. \begin{aligned} 2xF_1 &\equiv q + \bar{q} = u_v^p + d_v^p + 2\bar{d}^p + 2s^p \\ F_2 &\equiv q + \bar{q} + 2k = u_v^p + d_v^p + 2\bar{d}^p + 2s^p + 2k \\ xF_3 &\equiv q - \bar{q} = u_v^p + d_v^p \end{aligned} \right\} \quad (\text{C.15})$$

we can reduce (C.13) and (C.14) to

$$d^N = \frac{u_v^p + d_v^p}{2} + (1-2f)\frac{(u_v^p - d_v^p)}{2} + \bar{d}^p = \frac{xF_3}{2} + (1-2f)\frac{(u_v - d_v)}{2} + \bar{d}^p \quad (\text{C.16})$$

$$\text{Similarly, } u^N = \frac{xF_3}{2} - (1-2f)\frac{(u_v - d_v)}{2} \quad (\text{C.17})$$

Using (C.15) and (C.16) we may rewrite (C.11) as

$$\begin{aligned} \frac{d^2\sigma^\nu}{dx dy} &= \frac{G^2 s}{2\pi} \left\{ xF_3 + (1-2f)(u_v - d_v) + \left\{ \frac{2xF_1 - xF_3}{2} + s^N \right\} \right. \\ &\quad \left. + (1-y)^2 \left\{ \frac{2xF_1 - xF_3}{2} - s^N \right\} + (1-y)(F_2 - 2xF_1) \right\} \\ &= \frac{G^2 s}{2\pi} \left\{ xF_3 \frac{(1 - (1-y)^2)}{2} + F_2(1-y) + 2xF_1 \cdot \frac{y^2}{2} \right. \\ &\quad \left. + (1 - (1-y)^2)s^N + (1-2f)(u_v - d_v) \right\} \end{aligned} \quad (\text{C.18})$$

$$\text{Target mass effects make the } (1-y)F_2 \text{ into } (1-y - mxy/2E)F_2. \quad (\text{C.19})$$

Thus, since R is defined by

$$F_2 = \frac{(1+R)}{(1+4m^2x^2/Q^2)} 2xF_1 \quad (\text{C.20})$$

$$\frac{d^2\sigma^{\nu,\bar{\nu}}}{dx dy} = \frac{G^2 s}{2\pi} \left\{ \left(1 - y + \frac{y^2}{2} \cdot \frac{(1 + 2m^2 x^2/Q^2)}{(1+R)} \right) F_2 \pm \frac{(1 - (1-y)^2)}{2} x F_3 \right. \\ \left. \pm (1-2f) \left(\frac{1}{(1-y)^2} \right) (u_v^p - d_v^p) + (1 - (1-y)^2) s^N \right\} \quad (\text{C.21})$$

Also, in reality $m_c \neq 0$, making it necessary to recalculate (C.21). This has been done⁽²⁴⁾ and the prescription is that

- (i) ξ must be used instead of x where $\xi = (Q^2 + m_c^2)/2mE_h$ (see Appendix B).
- (ii) Only the region where $\xi \leq 1$ is allowed.
- (iii) The y distribution coefficients 1 and $(1-y)^2$ become

$$\left\{ (1-y) + \frac{xy}{\xi} \right\} \theta(1-\xi) \quad \text{and} \quad \left\{ (1-y) + \frac{x}{\xi} (y^2 - y) \right\} \theta(1-\xi)$$

respectively.

For our purposes it will be simplest to rewrite (C.21) in such a way that only a "correction term" gets added. In what follows the subscript ξ implies that the quark density in question is a function of ξ , not of x . For example, (C.13) may be written as

$$d^N = (f d_v^p + (1-f) u_v^p + \bar{d}^N) \cos^2 \theta_c + (f d_v^p + (1-f) u_v^p + \bar{d}^N)_\xi \sin^2 \theta_c (1-y + \frac{xy}{\xi}) \theta(1-\xi) \quad (\text{C.22})$$

One can add and subtract $(f d_v^p + (1-f) u_v^p + \bar{d}^N) \sin^2 \theta_c$; the final expression works out to be

$$\frac{d^2\sigma^{\nu,\bar{\nu}}}{dx dy} = \frac{G^2 m_p E_\nu}{\pi(1 + Q^2/m_W^2)^2} \left\{ \left(1 - y + \frac{y^2}{2} \cdot \frac{(1+2m^2 x^2/Q^2)}{(1+R)} \right) F_2 \pm \frac{(1-(1-y)^2)}{2} x F_3 \right. \\ \left. \pm (1-2f) \left(\frac{1}{(1-y)^2} \right) (u_v^p - d_v^p) + (1 - (1-y)^2) s^N \right. \\ \left. + R_{\nu,\bar{\nu}}(x, Q^2, E) + C_{\nu,\bar{\nu}}(x, Q^2, E, m_c) \right\} \quad (\text{C.23})$$

where the isoscalar and strange sea correction terms are explicit, $R_{\nu,\bar{\nu}}(x, Q^2, E)$ is the radiative correction term, and the charm mass correction terms are:

$$C_\nu = 2[-\sin^2 \theta_c (f d_v + (1-f) u_v + \bar{d}_N) + (f d_v + (1-f) u_v + \bar{d}_N)_\xi \sin^2 \theta_c (1-y + \frac{xy}{\xi}) \theta(1-\xi) \\ - \cos^2 \theta_c s_N \quad \quad \quad + s_{N_\xi} \cos^2 \theta_c (1-y + \frac{xy}{\xi}) \theta(1-\xi)] \quad (\text{C.24})$$

and,

$$C_{\bar{\nu}} = 2[-\bar{d}_N \sin^2 \theta_c \quad \quad \quad + \bar{d}_{N_\xi} \sin^2 \theta_c (1-y + \frac{xy}{\xi}) \theta(1-\xi) \\ - \bar{s}_N \cos^2 \theta_c \quad \quad \quad + \bar{s}_{N_\xi} \cos^2 \theta_c (1-y + \frac{xy}{\xi}) \theta(1-\xi)] \quad (\text{C.25})$$

The $1/(1+Q^2/m_W^2)^2$ in (C.23) comes from the W-boson propagator which we neglected in earlier expressions for simplicity. Notice that here we neglect W_4 and W_5 since they come in as $\sim \left(\frac{m_\mu}{m_p}\right)^2$.

Multiple Scattering

Multiple scattering enters both the track fitting procedures – in the determination of p_μ and of θ_μ at the vertex. The two are quite different problems; the physics and logic is discussed in Chapter 5.

Here we present the mathematical mechanics starting with the simpler case of θ_μ . Both problems are linearized i.e., the displacements (or, in general, measurements), written in vector form as \mathbf{y} , are linearly related to the parameters \mathbf{c} by

$$\mathbf{y} = \mathbf{A}\mathbf{c} \quad (\text{D.1})$$

If we knew the true set of parameters $\hat{\mathbf{c}}$, $\boldsymbol{\epsilon}$ would be the 'error' vector where

$$\boldsymbol{\epsilon} = \mathbf{y} - \mathbf{A}\hat{\mathbf{c}} \quad (\text{D.2})$$

The covariance matrix of the measurements \mathbf{y} is

$$\sigma_{ij} = \text{E}(\epsilon_i \epsilon_j) \quad (\text{D.3})$$

For the general case of correlated errors and unequal weights, σ_{ij} is a symmetric matrix and the problem is to minimize

$$S = (\mathbf{y} - \mathbf{A}\mathbf{c})^T (\boldsymbol{\sigma}^{-1}) (\mathbf{y} - \mathbf{A}\mathbf{c}) \quad (\text{D.4})$$

with respect to the parameters \mathbf{c} . This minimization is satisfied by

$$\hat{\mathbf{c}} = (\mathbf{A}^T \boldsymbol{\sigma}^{-1} \mathbf{A})^{-1} \mathbf{A}^T \boldsymbol{\sigma}^{-1} \mathbf{y} \quad (\text{D.5})$$

In the shower penetration case (θ_μ), we merely use (5.2), (5.3) and (5.4) along with

$$\mathbf{y}_i = y_0 + s_y z_i + \sum_{k=1}^i (\delta_k + \theta_k z_{ki}) \quad (\text{D.6})$$

where y_0 = the y-view intercept
 s_y = the y-view slope
 z_i = the z-coordinate for the i^{th} scattering centre
 δ_k = k^{th} multiple scattering induced displacement
 θ_k = k^{th} multiple scattering induced angle
 z_{ki} = distance between scattering centres k and i ,

to get

$$\sigma_{ij} = \langle (y_i - y_i^0)(y_j - y_j^0) \rangle = \langle \sum_{k=1}^i \sum_{l=1}^j (\delta_k + \theta_k z_{ki})(\delta_l + \theta_l z_{lj}) \rangle \quad (D.7)$$

$$= \sum_{k=1}^i \sigma_0^2 \left[\frac{L_k^2}{3} + \frac{L_k}{2} (z_{kj} + z_{ki}) + z_{ki} z_{kj} \right] \quad (D.8)$$

L_k is the thickness of the k^{th} scattering centre, z_{kj} is 0 if $k > j$ and y^0 is the (straight line) path without multiple scattering. The parameters are merely y_0, s_y, x_0 and s_x ; no attempt is made to recover all the δ_k and θ_k . A is thus a trivial 2×2 matrix and the main problem is to invert σ . Calculating σ_0^2 , including dE/dx losses, is easy since p_μ is known.

For the muon momentum tracking, we need not only the slopes and intercepts but also all the δ_k, θ_k and the muon momentum. As mentioned in section 5.1, the problem is first linearized by iteratively using the last estimate of $|p|$. The matrix A is enormous – it couples, in general, 36 angles, 36 deltas, and all the sparks in both views to the slopes, intercepts, $1/|p|$, and the 36 angles and 36 deltas (there are 18 scattering centres). Most of the CP time is spent in matrix multiplication of A in spite of some of its blocks being diagonal. It is necessary to obtain all δ_k, θ_k because the magnetic field is a function of position and good tracking helps get the correct magnetic kicks and eliminate bad sparks.

Note that for both fits an intrinsic spark resolution, s^2 , is added to the diagonal elements σ_{ii} . For the linearized problem, one application of (D.5) gives the best estimates of the parameters. In the case of θ_μ , we repeat the procedure getting closer to the vertex by adding one plane at a time, as described in section 5.2. For p_μ , there is no hadron shower to contend with, but we iterate to improve p_μ (the problem is artificially linearized).

Event Counting for Total Cross-sections

In this appendix we describe the separation of events into various categories for evaluating cross-sections. For events with $E_h < 10$ GeV, we can calculate a maximum angle.

$$\begin{aligned} \theta^2 &\sim 2mx \frac{y}{1-y} \frac{1}{E_\nu} \\ \Rightarrow \theta^{max} &= \left(2m \frac{(10/E_\nu^{min})}{1 - (10/E_\nu^{min})} \frac{1}{E_\nu^{min}} \right)^{1/2} \end{aligned} \quad (E.1)$$

$$\text{But } E_\nu^{min} = 28.5 \text{ GeV} \quad \Rightarrow \quad \theta^{max} \approx 189 \text{ mrad.} \quad (E.2)$$

The angle beyond which the muon trigger efficiency cannot be geometrically recovered is the angle a line from the apparatus centre at $z=-167$ in (closest event to the toroids) to a corner of T2 (55 in square, $z=142.5$ in) makes with the apparatus axis; this is 251 mrad. Hence (E.1) indicates that for $E_h < 10$ GeV, all events fire the muon trigger and the muon energy is measured. At every radius, an energy E_{sep} can be defined that separates neutrinos from pion and kaon decays. One can safely assume that if $E_h > .85 E_{sep}$, the event is from a neutrino from kaon decay. This leaves the region $10 \text{ GeV} < E_h < .85 E_{sep}$ in which to distinguish pion and kaon induced events. In this region it is possible to show using the energy versus radius expressions outlined in appendix A, that at every radius the maximum possible muon angle from kaon-decay-neutrinos is smaller than the maximum needed for full geometrically corrected acceptance. Consequently, events with $E_\nu > E_{sep}$ are identified by S1 as kaon-decay-neutrino events. For $R_{beam} < 30$ in and $R_{beam} > 30$ in , their muon trigger geometric weights (WMUZ) can be added up to give the total kaon-decay-neutrino events. The penetration trigger geometric weights (WPEN) are summed up for all S3 events with $R_{beam} < 30$ in . We can thus make 6 categories of events:

No.	Category	Weight summed
1	$E_h < 10 \text{ GeV}, R < 30 \text{ in}, E < E_{sep}, S1$	WMUZ
2	$E_h < 10 \text{ GeV}, E > E_{sep}, S1$	WMUZ
3	$10 < E_h < .85E_{sep}, R < 30 \text{ in}, S3$	WPEN
4	$10 < E_h < .85E_{sep}, R < 30 \text{ in}, E > E_{sep}, S1$	WMUZ
5	$10 < E_h < .85E_{sep}, R > 30 \text{ in}, E > E_{sep}, S1$	WMUZ
6	$E_h > .85E_{sep}, S3$	WMUZ

Table E.1. Event categories for cross section analysis.

Clearly,

$$\begin{aligned} \text{neutrinos from pions} &= \sum \text{Cat.1} + \sum \text{Cat.3} - \sum \text{Cat.4} \\ \text{neutrinos from kaons} &= \sum \text{Cat.2} + \sum \text{Cat.4} + \sum \text{Cat.5} + \sum \text{Cat.6} \end{aligned}$$

A few words about corrections to cross-sections:

The correction for unsampled regions described in §6.2 is typically $\sim 1\%$ and is never larger than 2.6%. The basis for our Monte Carlo is a parametrization of structure functions which is also used to make the isoscalar correction ($\sim -1.7\%$ for neutrinos, $+1.1\%$ for antineutrinos). The wideband events are directly eliminated by using events from closed slit runs scaled to the correct number of open slit protons. The assumptions made for the wide band background are that it has no position dependence and that, because of the way the beam is dumped, it is the same for all antineutrino settings but different for neutrino settings. Table E.2 lists various features of this background.

Momentum Setting (GeV/c)	$\sum WBB$	N_{CR}	$\sum WBB - N_{CR}$	$\sum WBB - N_{CR}$ Rescaled to Open slit Protons	\sum Open slit With WBB cuts	WBB Fraction (%)
-250	38.8 ± 6.9	$.125 \pm .125$	38.7 ± 6.9	462.5 ± 82.5	3066	15.1 ± 2.7
-200	12.1 ± 4.0	$.5 \pm .25$	11.6 ± 4.0	262.3 ± 90.4	3664	7.2 ± 2.5
-165	10.3 ± 3.9	0.	10.3 ± 3.9	188.2 ± 71.3	3607	5.2 ± 2.0
-140	20.0 ± 5.2	$.15 \pm .15$	18.8 ± 5.2	227.3 ± 62.9	2949	7.7 ± 2.1
-120	9.4 ± 3.4	$.16 \pm .16$	9.2 ± 3.4	117.5 ± 43.4	2054	5.7 ± 2.1
120	80.3 ± 10.3	13.8 ± 7.8	66.5 ± 12.9	504.1 ± 97.8	11496	4.4 ± 0.9
140	30.9 ± 5.9	22.7 ± 10.5	8.2 ± 12.0	109.0 ± 159.5	14479	0.8 ± 1.1
165	56.6 ± 8.7	20.7 ± 9.2	35.9 ± 12.7	597.7 ± 211.5	23123	2.6 ± 0.9
200	176.2 ± 15.0	55.3 ± 17.1	120.9 ± 15.6	876.5 ± 113.1	27998	3.1 ± 0.4
250	189.0 ± 15.9	50.3 ± 14.5	138.7 ± 21.5	1550.0 ± 241.0	33338	4.6 ± 0.7

Table E.2. Wide band background fraction analysis.

Using the cosmic ray gates, we find less than $\sim 0.1\%$ of fast spill events are due to

cosmic rays. Neutrinos during slow spill have a significant cosmic ray background however ($\sim 2.8\%$), which is subtracted for each momentum setting and category using the properly scaled number of cosmic ray events from cosmic ray gates. We know that events are not being double counted because the DSTs contain events in strictly increasing order.

To summarize, table E.3 contains the number of raw events, the corrected number of pion and kaon events, and the predicted number of pion and kaon events with $\sigma/E = 1 \times 10^{-38} \text{ cm}^2/\text{GeV}$. The final result (with statistical averaging alone) is

$$\begin{aligned} \sigma_\nu &= (.691 \pm .0036) \times 10^{-38} \text{ cm}^2/\text{GeV} && \text{(slow spill)} \\ \sigma_\nu &= (.685 \pm .0036) \times 10^{-38} \text{ cm}^2/\text{GeV} && \text{(fast spill)} \\ \text{and } \sigma_{\bar{\nu}} &= (.339 \pm .0034) \times 10^{-38} \text{ cm}^2/\text{GeV}. \end{aligned}$$

This agrees with the detailed calculations involving more correct averaging of energy settings (using the estimated systematic errors) that led to the published result⁽³⁰⁾ of

$$\begin{aligned} \sigma_\nu &= (.669 \pm .003 \pm .024) \times 10^{-38} \text{ cm}^2/\text{GeV} \\ \text{and } \sigma_{\bar{\nu}} &= (.340 \pm .003 \pm .020) \times 10^{-38} \text{ cm}^2/\text{GeV} \end{aligned}$$

Momentum Setting	Neutrino type	Corrected # of events	'Predicted' # of events	Cross section ($\times 10^{-38} \text{cm}^2/\text{GeV}$)
-250	π	2100.13 ± 52.90	6433.05	$.326 \pm .0082$
	K	449.74 ± 23.66	1489.56	$.301 \pm .0158$
-200	π	2453.75 ± 54.70	7283.42	$.336 \pm .0075$
	K	520.46 ± 25.26	1674.97	$.310 \pm .0150$
-165	π	2227.52 ± 51.65	6393.15	$.348 \pm .0080$
	K	542.04 ± 25.50	1661.65	$.326 \pm .0153$
-140	π	1948.66 ± 48.30	5465.21	$.356 \pm .0088$
	K	449.52 ± 23.47	1335.91	$.336 \pm .0175$
-120	π	1339.34 ± 40.23	3673.43	$.364 \pm .0109$
	K	247.56 ± 17.58	761.49	$.325 \pm .0231$
120	π	7268.38 ± 100.16	10540.67	$.689 \pm .0095$
	K	2301.68 ± 56.10	3417.80	$.673 \pm .0164$
140	π	9474.95 ± 122.29	13551.28	$.699 \pm .0090$
	K	3654.11 ± 69.95	5376.74	$.679 \pm .0130$
165	π	14715.43 ± 148.45	21984.93	$.669 \pm .0067$
	K	7638.39 ± 104.36	10851.70	$.703 \pm .0096$
200	π	16777.58 ± 158.68	24805.42	$.676 \pm .0064$
	K	10773.90 ± 124.48	15503.35	$.694 \pm .0080$
250	π	16682.83 ± 156.72	24986.88	$.667 \pm .0062$
	K	15989.53 ± 147.35	21954.82	$.728 \pm .0067$

Table E.9. Events for elementary cross-section analysis.

Models for Fitting Structure Functions

Structure function extraction requires some iteration since the correction terms depend on the structure functions themselves. We have used two models to fit the structure functions and these are described below. In the empirical model, we are motivated by standard forms for $2xF_1$ and xF_3 at fixed Q^2 , namely

$$2xF_1(Q^2 = 10 GeV^2) = d(1 + ex)(1 - x)^f \quad (F.1)$$

$$xF_3(Q^2 = 10 GeV^2) = a(1 + c'_d(1 - x))x^b(1 - x)^c \quad (F.2)$$

In the above, a, b, c, d, e and f are parameters. c'_d reflects the faster $(1 - x)$ fall-off expected for d-quarks⁽³¹⁾. At fixed x , in the restricted regions of Q^2 explored by any experiment, it is reasonable to fit straight lines to $2xF_1$ and xF_3 as functions of $\log Q^2$:

$$2xF_1 \text{ (fixed } x) = a + b \log_{10} Q^2/10 = a(1 + \frac{b}{a} \log_{10} Q^2/10) \quad (F.3)$$

If b/a is plotted as a function of x , one finds in general a parabola with its minimum pointing towards $-x$. Thus, a Q^2 -dependence of the type $(1 + (g - h\sqrt{x}) \log_{10} Q^2/10)$ is used to multiply (F.1) and (F.2) above, giving the forms

$$\left. \begin{aligned} 2xF_1 &= d(1 + ex)(1 - x)^f (1 + (g - h\sqrt{x}) \log_{10} Q^2/10) \\ xF_3 &= a(1 + c'_d(1 - x))x^b(1 - x)^c (1 + (g - h\sqrt{x}) \log_{10} Q^2/10) \end{aligned} \right\} \quad (F.4)$$

where a, b, c, d, e, f, g and h are parameters obtained by a simultaneous fit to $2xF_1$ and xF_3 . We fix c'_d with the requirement that there be twice as many u quarks as d quarks in a proton. This leads to

$$2c'_d = \frac{(\Gamma(b)\Gamma(c+1)/\Gamma(b+c+1))(1+g \log_{10} \frac{Q^2}{10}) - (\Gamma(b+1/2)\Gamma(c+1)/\Gamma(b+c+3/2))h \log_{10} \frac{Q^2}{10}}{(\Gamma(b)\Gamma(c+2)/\Gamma(b+c+2))(1+g \log_{10} \frac{Q^2}{10}) - (\Gamma(b+1/2)\Gamma(c+2)/\Gamma(b+c+5/2))h \log_{10} \frac{Q^2}{10}} \quad (F.5)$$

The constants after the final iteration were, for $R = 0.1$,

$$\begin{aligned}
 a &= 2.083 \pm .218 \\
 b &= 0.482 \pm .421 \\
 c &= 2.459 \pm .134 \\
 d &= 1.654 \pm .203 \\
 e &= 0.283 \pm .190 \\
 f &= 2.440 \pm .106 \\
 g &= 0.445 \pm .038 \\
 h &= 1.043 \pm .075
 \end{aligned}
 \tag{F.6}$$

The other model is a QCD-inspired fit like that of Buras and Gaemers⁽⁴¹⁾, which we have altered slightly in order to keep the number of parameters to a minimum. It should be emphasized that this fit is not an attempt to extract a value for Λ from the data, but rather is just another model used as a basis for the corrections to be applied in structure function extraction. Both models yield a χ^2 of approximately 210 for 152 degrees of freedom for their best fits and thus neither seems intrinsically superior. For our published results we use the 'Buras-Gaemers' model.

In this model the valence quark distribution is approximated by

$$xF_3(x, Q^2) = Ax^{\eta_1(\bar{s})}(1-x)^{\eta_2(\bar{s})}(1+c_d(1-x)) \tag{F.7}$$

where

$$\bar{s} = \ln((\ln Q^2/\Lambda^2)/(\ln Q_0^2/\Lambda^2))$$

and

$$\eta_i(\bar{s}) = \eta_{i0} + \bar{s}\eta_{i1}, \quad i = 1, 2. \tag{F.8}$$

Again, we have chosen to separate the $(1-x)$ dependence of u and d quarks. As before, this implies that

$$c_d(\bar{s}) = \frac{1}{2} \frac{\eta_1(\bar{s}) + \eta_2(\bar{s}) + 1}{\eta_2(\bar{s}) + 1} \tag{F.9}$$

We assume that the gluon distribution has the form

$$xG(x, Q^2 = 12.6 \text{ GeV}^2) = A_G(1-x)^5 \tag{F.10}$$

where A_G is fixed by the momentum sum rule:

$$\int_0^1 dx xG(x, Q^2) + \int_0^1 dx F_2(x, Q^2) = 1 \tag{F.11}$$

The sea of antiquarks and quarks is modeled by two moments as

$$xS(x, Q^2) = P_S \left(\frac{1}{\langle x \rangle_S} - 1 \right) (1-x)^{(1/\langle x \rangle_S) - 2} \quad (\text{F.12})$$

where

$$P_S = \langle S(Q^2) \rangle_2$$

$$\text{and } \frac{1}{\langle x \rangle_S} = \frac{\langle S(Q^2) \rangle_2}{\langle S(Q^2) \rangle_3} \quad (\text{F.13})$$

$\langle S(Q^2) \rangle_n$ are moments of the sea distribution, defined by

$$\langle S(Q^2) \rangle_n = \int_0^1 dx x^{n-1} S(x, Q^2). \quad (\text{F.14})$$

Because of the coupling of the Q^2 evolutions of F_2 and G ,

$$\langle S(Q^2) \rangle_n = \frac{3}{4} D_2^{(n)}(Q^2) + \frac{1}{4} D_1^{(n)}(Q^2) \quad (\text{F.15})$$

where

$$D_1^{(n)}(Q^2) = \langle S(Q_0^2) \rangle_n e^{-\gamma_n^+ \bar{s}}$$

$$D_2^{(n)}(Q^2) = \{ (1 - \alpha_n) \langle q^S(Q_0^2) \rangle_n - \beta_n \langle G(Q_0^2) \rangle_n \} e^{-\gamma_n^+ \bar{s}}$$

$$+ \{ \alpha_n \langle q^S(Q_0^2) \rangle_n + \beta_n \langle G(Q_0^2) \rangle_n \} e^{-\gamma_n^- \bar{s}} - \langle xF_3(Q_0^2) \rangle_n e^{-\gamma_n^- \bar{s}} \quad (\text{F.16})$$

$\alpha_n, \beta_n, \gamma_n^+, \gamma_n^-$ and γ_n^{\pm} are known constants and

$$\langle q^S(Q_0^2) \rangle_n = \langle S(Q_0^2) \rangle_n + \langle xF_3(Q_0^2) \rangle_n \quad (\text{F.17})$$

Thus, the parameters are $\Lambda, A, \eta_{10}, \eta_{11}, \eta_{20}, \eta_{21}, \langle S(Q_0^2) \rangle_2$ and $\langle S(Q_0^2) \rangle_3$.

This model was fit for all three values of R and the final values of the parameters are quoted in table F.1. For this fit we did not throw out points with large systematic errors as in the QCD fits described in the chapter 7; nevertheless, the value of Λ is consistent with our final result.

Parameter	$R = 0.$	$R = 0.1$	$R = .73(1-x)^{3.68} / \ln(Q^2/.24^2)$ (QCD)
Λ (MeV)	202.1 ± 133.6	194.7 ± 126.0	247.4 ± 114.58
A	$1.838 \pm .113$	$1.679 \pm .129$	$1.702 \pm .105$
η_{10}	$0.4382 \pm .0277$	$0.4003 \pm .0341$	$0.4079 \pm .0273$
η_{11}	$-0.1507 \pm .0540$	$-0.2066 \pm .0685$	$-0.2156 \pm .0557$
η_{20}	$2.285 \pm .0648$	$2.271 \pm .0813$	$2.225 \pm .0642$
η_{21}	$1.849 \pm .4278$	$1.861 \pm .4309$	$1.742 \pm .3174$
$\langle S(Q_0^2) \rangle_2$	$0.1671 \pm .0055$	$0.1453 \pm .0056$	$0.1494 \pm .0053$
$\langle S(Q_0^2) \rangle_3$	$0.0202 \pm .0019$	$0.0167 \pm .0011$	$0.0180 \pm .0012$

Table F.1. Best parameters for Buras-Gaemers model; different R values.

R=0.1 Structure Functions

x	Q^2	F_2	ΔF_2	$x F_3$	$\Delta x F_3$
.015	1.259	1.25582	.04923	.17085	.05995
	1.995	1.30798	.05698	.37642	.05721
	3.162	1.49922	.08192	.30911	.07770
	5.012	1.36980	.11360	.43427	.10700
	7.943	1.54774	.26328	-	-
.045	1.259	1.13397	.05011	.44840	.14579
	1.995	1.35019	.04659	.62746	.08976
	3.162	1.34836	.04393	.61455	.06288
	5.012	1.52800	.05793	.51304	.07227
	7.943	1.64677	.07982	.69616	.09385
	12.589	1.51965	.11269	.64685	.11640
	19.953	1.06799	.19609	.63006	.18132
.080	1.259	1.24675	.12790	-	-
	1.995	1.44714	.05451	.62005	.18380
	3.162	1.48609	.04624	.77359	.10383
	5.012	1.46027	.04377	.66828	.07019
	7.943	1.54216	.05127	.65696	.06910
	12.589	1.59194	.06791	.78149	.08531
	19.953	1.58351	.09018	.77123	.09766
	31.623	1.24093	.16773	.66191	.16152
.150	1.995	1.19379	.10906	-	-
	3.162	1.18550	.03639	.73272	.13496
	5.012	1.28368	.02832	.68936	.07349
	7.943	1.24077	.02554	.87819	.04599
	12.589	1.24165	.02834	.85393	.04163
	19.953	1.30537	.03650	.78867	.04845
	31.623	1.29031	.04696	.84621	.05511
	50.119	1.18841	.07711	.79932	.07983
	79.433	0.91729	.26105	.70531	.23941

x	Q^2	F_2	ΔF_2	$x F_3$	$\Delta x F_3$
.250	3.162	1.87372	.72552	-	-
	5.012	1.02767	.03878	.62169	.16070
	7.943	.98905	.02655	.79181	.07607
	12.589	.94128	.02431	.79395	.04792
	19.953	.93629	.02674	.76636	.04233
	31.623	.96817	.03391	.79476	.04956
	50.119	.86187	.03467	.74495	.04222
	79.433	.77668	.05556	.64935	.05738
	125.893	.59753	.29864	-	-
.350	5.012	.88153	.18938	-	-
	7.943	.67718	.02735	.58121	.10778
	12.589	.65216	.02262	.55024	.05929
	19.953	.64518	.02406	.46626	.04723
	31.623	.63736	.02784	.50918	.04765
	50.119	.60015	.02871	.55930	.04092
	79.433	.61857	.03848	.49863	.04520
	125.893	.71853	.08329	.26618	.08603
.450	7.943	.49761	.04115	-	-
	12.589	.42063	.01982	.44968	.06724
	19.953	.39816	.01881	.30443	.04292
	31.623	.38788	.02067	.31655	.03809
	50.119	.35372	.02151	.33689	.03554
	79.433	.38524	.02722	.31495	.03635
	125.893	.29228	.02978	.30254	.03242
	199.526	.30656	.14743	.29994	.14598
.550	12.589	.24130	.01716	.21663	.07035
	19.953	.23222	.01559	.16722	.04326
	31.623	.20861	.01451	.20694	.02921
	50.119	.20174	.01835	.16959	.03231
	79.433	.20319	.02093	.16740	.03059
	125.893	.15649	.02045	.16856	.02440
	199.526	.12753	.04488	.13031	.04641
.650	12.589	.14995	.01762	.16111	.07902
	19.953	.12099	.01048	.17002	.03294
	31.623	.13931	.01519	.12085	.03925
	50.119	.11247	.01471	.07132	.03014
	79.433	.10015	.01641	.05793	.02771
	125.893	.09539	.01427	.09799	.01844
	199.526	.07128	.02238	.07628	.02425

Table G.1. F_2 and $x F_3$ with statistical errors for R=0.1

Tables of Statistical and Systematic Errors

x	Q^2 (GeV ²)	F_2	Stat error (%)	Shape uncorrel (%)	Shape correl (%)	Flat xsec correction (%)	Level error (%)	E_{had} diff (%)
.015	1.3	1.287	3.92	.67	2.22	.69	3.86	-.18
	2.0	1.342	4.35	.57	1.95	.70	3.93	-.12
	3.2	1.536	5.46	.38	1.15	.89	4.00	-.09
	5.0	1.402	8.27	.24	.72	1.31	4.08	-.05
	7.9	1.584	16.97	.37	.90	1.55	4.12	.01
.045	1.3	1.133	4.43	.66	2.11	.71	3.57	-.17
	2.0	1.358	3.45	.76	2.41	.69	3.66	-.16
	3.2	1.363	3.26	.75	2.50	.64	3.73	-.12
	5.0	1.544	3.79	.52	1.70	.64	3.79	-.08
	7.9	1.661	4.84	.26	.74	.99	3.87	-.06
	12.6	1.530	7.41	.29	.83	1.25	3.93	-.01
	20.0	1.070	18.34	.43	.69	1.45	3.92	.03
.080	1.3	1.243	10.29	.64	2.04	.72	3.55	-.09
	2.0	1.444	3.77	.65	2.09	.70	3.51	-.08
	3.2	1.487	3.11	.75	2.37	.68	3.58	-.10
	5.0	1.464	3.00	.79	2.58	.62	3.67	-.07
	7.9	1.544	3.32	.57	1.85	.60	3.73	-.04
	12.6	1.590	4.26	.27	.71	.87	3.79	-.03
	20.0	1.576	5.69	.28	.82	1.12	3.86	-.00
	31.6	1.227	13.50	.47	.77	1.22	3.84	.03
.150	2.0	1.182	9.21	.69	2.21	.76	3.77	.01
	3.2	1.180	3.07	.69	2.19	.70	3.55	.07
	5.0	1.280	2.20	.75	2.39	.66	3.52	.07
	7.9	1.234	2.06	.78	2.55	.60	3.59	.05
	12.6	1.232	2.28	.59	1.91	.56	3.63	.05
	20.0	1.291	2.79	.32	.83	.73	3.68	.06
	31.6	1.269	3.64	.24	.71	.91	3.74	.05
	50.1	1.160	6.49	.44	.85	.85	3.62	.05
	79.4	.888	28.26	.08	-.15	.91	3.43	.04

x	Q^2 (GeV ²)	F_2	Stat error (%)	Shape uncorrel (%)	Shape correl (%)	Flat xsec correction (%)	Level error (%)	E_{had} diff (%)
.250	3.2	1.868	38.73	.74	2.36	.76	3.85	.30
	5.0	1.025	3.77	.71	2.26	.68	3.49	.40
	7.9	.985	2.68	.77	2.44	.63	3.45	.36
	12.6	.933	2.58	.76	2.50	.57	3.54	.28
	20.0	.923	2.85	.57	1.75	.54	3.60	.25
	31.6	.952	3.50	.30	.68	.72	3.65	.25
	50.1	.839	4.02	.24	.73	.81	3.73	.19
	79.4	.747	7.08	.55	.89	.72	3.71	.12
	125.9	.568	49.14	.56	-.84	.78	3.49	.07
.350	5.0	.882	21.46	.77	2.46	.73	3.77	.70
	7.9	.676	4.03	.74	2.36	.64	3.41	.78
	12.6	.648	3.46	.77	2.52	.59	3.44	.68
	20.0	.637	3.73	.66	2.20	.53	3.52	.56
	31.6	.627	4.37	.47	1.18	.59	3.57	.52
	50.1	.587	4.78	.18	.53	.75	3.64	.48
	79.4	.597	6.22	.37	.90	.70	3.73	.32
	125.9	.684	11.13	.52	.56	.69	3.71	.19
.450	7.9	.497	8.26	.75	2.39	.65	3.44	1.28
	12.6	.419	4.71	.76	2.47	.60	3.38	1.23
	20.0	.394	4.72	.70	2.37	.54	3.45	1.04
	31.6	.382	5.33	.54	1.57	.53	3.52	.92
	50.1	.347	6.09	.28	.62	.69	3.57	.89
	79.4	.374	7.07	.23	.70	.72	3.66	.72
	125.9	.279	9.95	.59	.94	.64	3.74	.44
	199.5	.289	45.72	.58	-.83	.77	3.64	.25
.550	12.6	.240	7.11	.75	2.44	.61	3.36	2.00
	20.0	.230	6.72	.72	2.42	.55	3.40	1.79
	31.6	.205	6.96	.57	1.83	.51	3.47	1.57
	50.1	.198	9.10	.37	.82	.63	3.52	1.49
	79.4	.198	10.30	.18	.57	.73	3.60	1.35
	125.9	.149	12.71	.46	.96	.64	3.71	.92
	199.5	.119	33.52	.33	.21	.72	3.72	.56
.650	12.6	.149	11.75	.75	2.44	.60	3.33	3.16
	20.0	.120	8.67	.73	2.43	.55	3.35	2.98
	31.6	.138	10.91	.59	1.99	.51	3.42	2.64
	50.1	.110	13.09	.42	1.02	.59	3.48	2.47
	79.4	.098	16.39	.18	.52	.74	3.55	2.35
	125.9	.092	14.59	.34	.87	.68	3.67	1.77
	199.5	.067	30.26	.57	.66	.67	3.73	1.14

x	Q^2 (GeV ²)	F_2	Stat error (%)	E_μ diff (%)	R error (%)	SU(3) symmetry (%)	Model error (%)	Extraction techniques (%)
.015	1.3	1.287	3.9	0.39	2.10	-1.51	1.67	0.15
	2.0	1.343	4.4	0.42	2.57	-1.74	1.90	1.65
	3.2	1.537	5.5	0.41	2.78	-1.94	1.63	2.38
	5.0	1.402	8.3	0.36	3.19	-2.22	1.08	-0.78
	7.9	1.584	17.0	0.27	3.96	-2.50	0.26	-7.09
.045	1.3	1.134	4.4	0.33	0.24	-0.65	2.04	-1.50
	2.0	1.359	3.5	0.37	0.85	-0.98	1.89	0.55
	3.2	1.363	3.3	0.33	1.60	-1.26	1.92	-0.33
	5.0	1.545	3.8	0.28	1.97	-1.44	1.84	0.22
	7.9	1.662	4.8	0.24	2.19	-1.69	1.51	0.48
	12.6	1.531	7.4	0.16	2.98	-2.01	0.82	0.16
	20.0	1.071	18.3	0.06	3.98	-2.17	0.70	-13.41
.080	1.3	1.244	10.3	0.20	0.31	-0.40	1.82	1.14
	2.0	1.445	3.8	0.16	0.11	-0.49	1.60	-0.42
	3.2	1.487	3.1	0.16	0.51	-0.75	1.50	-0.68
	5.0	1.464	3.0	0.11	1.16	-1.02	1.51	-1.42
	7.9	1.545	3.3	0.04	1.59	-1.19	1.66	-0.22
	12.6	1.591	4.3	0.00	1.74	-1.36	1.65	1.60
	20.0	1.576	5.7	-0.06	2.49	-1.67	1.09	-0.96
	31.6	1.228	13.5	-0.15	3.37	-1.83	0.95	4.31
.150	2.0	1.183	9.2	-0.08	1.12	-0.35	1.51	0.95
	3.2	1.180	3.1	-0.26	0.38	-0.37	1.14	0.40
	5.0	1.280	2.2	-0.34	0.26	-0.51	0.96	0.48
	7.9	1.235	2.1	-0.38	0.72	-0.70	1.09	0.87
	12.6	1.232	2.3	-0.45	1.14	-0.82	1.39	1.04
	20.0	1.292	2.8	-0.50	1.34	-0.93	1.55	1.95
	31.6	1.270	3.6	-0.54	1.91	-1.12	1.24	-0.25
	50.1	1.161	6.5	-0.64	2.72	-1.17	1.00	-2.17
	79.4	0.889	28.3	-0.76	3.37	-1.10	1.03	9.05
.250	3.2	1.868	38.7	-0.82	0.43	-0.23	0.56	4.67
	5.0	1.026	3.8	-1.12	0.23	-0.22	0.43	0.73
	7.9	0.985	2.7	-1.19	0.17	-0.29	0.50	0.72
	12.6	0.933	2.6	-1.18	0.51	-0.41	0.75	0.18
	20.0	0.923	2.9	-1.21	0.86	-0.49	1.15	1.84
	31.6	0.952	3.5	-1.27	1.04	-0.55	1.40	1.73
	50.1	0.840	4.0	-1.25	1.65	-0.68	1.08	1.61
	79.4	0.747	7.1	-1.27	2.57	-0.74	0.81	1.53
	125.9	0.568	49.1	-1.37	3.34	-0.66	0.94	-3.66

x	Q^2 (GeV ²)	F_2	Stat error (%)	E_μ diff (%)	R error (%)	SU(3) symmetry (%)	Model error (%)	Extraction techniques (%)
.350	5.0	0.882	21.5	-1.83	0.45	-0.14	0.22	4.70
	7.9	0.676	4.0	-2.15	0.13	-0.13	0.12	0.23
	12.6	0.649	3.5	-2.15	0.25	-0.18	0.38	3.18
	20.0	0.638	3.7	-2.11	0.55	-0.24	0.73	0.71
	31.6	0.627	4.4	-2.15	0.80	-0.27	1.18	-0.32
	50.1	0.587	4.8	-2.18	1.04	-0.31	1.17	3.60
	79.4	0.597	6.2	-2.08	1.82	-0.38	0.69	2.41
	125.9	0.684	11.1	-2.05	2.70	-0.39	0.41	1.13
.450	7.9	0.498	8.3	-3.33	0.15	-0.06	0.15	1.30
	12.6	0.419	4.7	-3.45	0.16	-0.08	0.05	0.57
	20.0	0.395	4.7	-3.36	0.38	-0.10	0.44	3.13
	31.6	0.382	5.3	-3.34	0.63	-0.12	0.90	0.97
	50.1	0.347	6.1	-3.40	0.81	-0.13	1.20	-1.57
	79.4	0.375	7.1	-3.31	1.29	-0.16	0.77	0.71
	125.9	0.279	10.0	-3.12	2.26	-0.18	0.52	1.47
	199.5	0.290	45.7	-3.11	3.09	-0.16	0.42	5.43
.550	12.6	0.241	7.1	-5.26	0.12	-0.03	0.43	1.60
	20.0	0.231	6.7	-5.22	0.29	-0.04	0.10	2.72
	31.6	0.206	7.0	-5.13	0.51	-0.04	0.62	4.87
	50.1	0.198	9.1	-5.19	0.68	-0.05	0.99	5.75
	79.4	0.199	10.3	-5.16	0.97	-0.06	0.80	9.21
	125.9	0.150	12.7	-4.84	1.81	-0.06	0.46	-6.62
	199.5	0.120	33.5	-4.65	2.78	-0.07	0.42	-3.89
	.650	12.6	0.150	11.8	-8.09	0.07	-0.01	0.75
20.0		0.120	8.7	-8.19	0.22	-0.01	0.27	3.28
31.6		0.138	10.9	-8.05	0.40	-0.02	0.41	0.49
50.1		0.111	13.1	-8.09	0.56	-0.02	0.82	-1.60
79.4		0.098	16.4	-8.15	0.76	-0.02	0.72	-4.64
125.9		0.092	14.6	-7.72	1.39	-0.02	0.32	2.24
199.5		0.068	30.3	-7.29	2.37	-0.03	0.10	-0.56

Table H.1. F_2 errors. See note at end of appendix.

x	Q^2 (GeV ²)	$x F_3$	Stat error (%)	Shape uncorrel (%)	Shape correl (%)	Flat xsec correction (%)	Level error (%)	E_{had} diff (%)
.015	1.3	.1649	35.0	4.01	0.61	4.10	15.35	0.08
	2.0	.3655	15.2	3.23	0.82	3.63	12.85	0.05
	3.2	.3032	25.1	2.01	0.77	4.26	11.80	0.05
	5.0	.4306	24.6	1.04	0.90	5.72	10.82	0.08
.045	1.3	.4401	32.6	4.65	0.54	5.10	18.26	0.28
	2.0	.6198	14.3	3.36	1.33	3.15	11.89	0.19
	3.2	.6081	10.2	2.80	1.77	2.32	9.07	0.12
	5.0	.5084	14.1	2.05	1.26	2.29	8.23	0.07
	7.9	.6929	13.5	0.82	0.69	3.06	7.78	0.08
	12.6	.6460	18.0	0.86	0.88	3.71	6.99	0.08
	20.0	.6307	28.8	1.00	0.84	4.31	6.52	0.07
.080	2.0	.6145	29.7	4.05	0.73	4.37	15.81	0.38
	3.2	.7693	13.4	2.98	1.45	2.74	10.54	0.29
	5.0	.6656	10.5	2.49	2.05	1.92	7.84	0.18
	7.9	.6550	10.5	1.89	1.58	1.81	7.00	0.13
	12.6	.7806	10.9	0.72	0.67	2.30	6.72	0.12
	20.0	.7711	12.7	0.69	0.83	2.75	6.02	0.09
	31.6	.6621	24.4	0.92	0.88	3.09	5.57	0.07
.150	3.2	.7318	18.4	3.47	0.98	3.57	13.16	0.54
	5.0	.6890	10.7	2.72	1.62	2.38	9.38	0.47
	7.9	.8785	5.2	2.22	2.17	1.65	7.02	0.33
	12.6	.8548	4.9	1.63	1.79	1.43	6.10	0.25
	20.0	.7903	6.1	0.74	0.81	1.63	5.79	0.23
	31.6	.8471	6.5	0.49	0.73	1.88	5.27	0.18
	50.1	.7993	10.0	0.74	0.93	1.82	4.73	0.12
	79.4	.7040	33.9	0.15	-0.05	1.88	4.36	0.06
.250	5.0	.6230	25.9	3.26	1.25	3.14	11.80	0.89
	7.9	.7938	9.6	2.57	1.86	2.10	8.47	0.79
	12.6	.7965	6.0	2.03	2.34	1.45	6.38	0.59
	20.0	.7697	5.5	1.39	1.80	1.23	5.55	0.47
	31.6	.7988	6.2	0.57	0.71	1.40	5.26	0.45
	50.1	.7473	5.7	0.43	0.71	1.42	4.74	0.34
	79.4	.6504	8.7	0.75	0.96	1.33	4.31	0.19

x	Q^2 (GeV ²)	xF_3	Stat error (%)	Shape uncorrel (%)	Shape correl (%)	Flat xsec correction (%)	Level error (%)	E_{had} diff (%)
.350	7.9	.5836	18.6	2.93	1.62	2.55	9.92	1.29
	12.6	.5528	10.8	2.29	2.22	1.69	7.18	1.10
	20.0	.4687	10.1	1.69	2.24	1.27	5.75	0.87
	31.6	.5124	9.3	0.98	1.30	1.16	5.23	0.76
	50.1	.5628	7.3	0.32	0.51	1.35	4.87	0.71
	79.4	.5003	9.1	0.54	0.93	1.14	4.37	0.47
	125.9	.2657	31.1	0.62	0.63	1.09	4.03	0.25
.450	12.6	.4522	15.0	2.58	2.04	2.00	8.14	1.75
	20.0	.3063	14.1	1.94	2.35	1.41	6.21	1.45
	31.6	.3188	12.0	1.25	1.72	1.16	5.38	1.23
	50.1	.3395	10.5	0.52	0.68	1.29	5.04	1.17
	79.4	.3168	11.5	0.37	0.68	1.18	4.50	0.95
	125.9	.3026	10.5	0.71	1.01	0.99	4.11	0.56
	199.5	.3015	46.2	0.63	-0.78	0.98	3.81	0.31
.550	12.6	.2177	32.6	2.87	1.92	2.29	9.11	2.60
	20.0	.1683	25.9	2.19	2.32	1.60	6.81	2.29
	31.6	.2086	14.1	1.48	1.95	1.25	5.66	1.96
	50.1	.1711	19.1	0.73	0.95	1.25	5.22	1.82
	79.4	.1688	18.3	0.31	0.54	1.29	4.71	1.66
	125.9	.1695	14.0	0.60	1.01	1.01	4.22	1.10
	199.5	.1298	33.9	0.38	0.27	0.96	3.92	0.66
.650	12.6	.1628	49.1	3.05	1.88	2.45	9.58	3.83
	20.0	.1714	19.4	2.43	2.25	1.80	7.47	3.56
	31.6	.1217	32.4	1.70	2.08	1.37	6.03	3.11
	50.1	.0720	42.1	0.92	1.18	1.28	5.44	2.86
	79.4	.0584	47.8	0.34	0.51	1.40	4.97	2.72
	125.9	.0989	18.4	0.51	0.91	1.11	4.37	2.02
	199.5	.0764	30.6	0.67	0.74	0.96	4.02	1.28

x	Q^2 (GeV ²)	xF_3	Stat error (%)	E_μ diff (%)	R error (%)	SU(3) symmetry (%)	Model error (%)	Extraction techniques (%)
.015	1.3	.1649	35.0	0.67	2.20	0.48	3.26	-35.16
	2.0	.3655	15.2	0.67	1.05	0.47	1.60	6.75
	3.2	.3032	25.1	0.63	1.77	0.35	2.34	-12.16
	5.0	.4306	24.6	0.59	0.64	0.18	1.06	-2.19
.045	1.3	.4401	32.6	0.42	0.10	0.41	1.11	18.87
	2.0	.6198	14.3	0.46	0.37	0.41	1.06	-0.43
	3.2	.6081	10.2	0.47	0.61	0.41	1.13	2.32
	5.0	.5084	14.1	0.44	1.26	0.40	1.99	-8.77
	7.9	.6929	13.5	0.41	0.69	0.21	1.40	3.96
	12.6	.6460	18.0	0.38	0.36	0.06	0.41	-3.12
	20.0	.6307	28.8	0.34	0.13	0.01	0.10	8.55
.080	2.0	.6145	29.7	0.11	0.06	0.27	1.59	12.34
	3.2	.7693	13.4	0.15	0.20	0.28	1.02	8.14
	5.0	.6656	10.5	0.20	0.48	0.29	1.07	0.13
	7.9	.6550	10.5	0.19	0.78	0.29	1.53	-0.31
	12.6	.7806	10.9	0.16	0.63	0.20	1.51	1.36
	20.0	.7711	12.7	0.16	0.34	0.05	0.50	-7.05
	31.6	.6621	24.4	0.14	0.16	0.00	0.08	-15.51
.150	3.2	.7318	18.4	-0.35	0.05	0.17	1.64	0.72
	5.0	.6890	10.7	-0.36	0.13	0.16	1.34	-1.16
	7.9	.8785	5.2	-0.29	0.23	0.17	0.91	1.89
	12.6	.8548	4.9	-0.29	0.38	0.16	1.19	0.97
	20.0	.7903	6.1	-0.32	0.48	0.11	1.49	-2.09
	31.6	.8471	6.5	-0.30	0.24	0.02	0.72	-3.79
	50.1	.7993	10.0	-0.33	0.09	-0.01	0.15	2.18
	79.4	.7040	33.9	-0.40	0.07	-0.01	0.00	-24.75
.250	5.0	.6230	25.9	-1.24	0.08	0.09	2.33	-1.65
	7.9	.7938	9.6	-1.24	0.04	0.09	1.22	1.61
	12.6	.7965	6.0	-1.11	0.15	0.09	0.99	-2.49
	20.0	.7697	5.5	-1.07	0.27	0.10	1.25	-0.35
	31.6	.7988	6.2	-1.11	0.29	0.07	1.49	2.40
	50.1	.7473	5.7	-1.03	0.17	0.03	0.69	3.35
	79.4	.6504	8.7	-0.97	0.06	-0.01	0.17	3.89

x	Q^2 (GeV ²)	$x F_3$	Stat error (%)	E_μ diff (%)	R error (%)	SU(3) symmetry (%)	Model error (%)	Extraction techniques (%)
.350	7.9	.5836	18.6	-2.34	0.08	0.04	1.86	-0.42
	12.6	.5528	10.8	-2.24	0.05	0.05	1.30	-1.30
	20.0	.4687	10.1	-2.09	0.19	0.05	1.29	0.13
	31.6	.5124	9.3	-2.07	0.27	0.05	1.55	1.48
	50.1	.5628	7.3	-2.09	0.23	0.03	1.35	-6.07
	79.4	.5003	9.1	-1.90	0.14	0.01	0.48	-0.01
	125.9	.2657	31.1	-1.81	0.09	0.00	0.26	-2.97
.450	12.6	.4522	15.0	-3.72	0.06	0.02	1.36	9.00
	20.0	.3063	14.1	-3.52	0.08	0.03	1.47	-2.60
	31.6	.3188	12.0	-3.41	0.20	0.03	1.49	2.04
	50.1	.3395	10.5	-3.45	0.19	0.02	1.58	5.10
	79.4	.3168	11.5	-3.30	0.19	0.01	0.86	-0.05
	125.9	.3026	10.5	-3.02	0.06	0.00	0.25	-3.50
	199.5	.3015	46.2	-2.96	0.02	0.00	0.16	5.76
.550	12.6	.2177	32.6	-5.72	0.21	0.01	2.39	-1.31
	20.0	.1683	25.9	-5.56	0.07	0.01	1.72	6.19
	31.6	.2086	14.1	-5.37	0.09	0.01	1.33	7.84
	50.1	.1711	19.1	-5.38	0.24	0.01	1.85	-9.71
	79.4	.1688	18.3	-5.33	0.22	0.01	1.24	-0.92
	125.9	.1695	14.0	-4.89	0.08	0.00	0.34	3.02
	199.5	.1298	33.9	-4.63	0.03	0.00	0.19	-3.67
.650	12.6	.1628	49.1	-8.73	0.17	0.00	1.77	31.12
	20.0	.1714	19.4	-8.72	0.09	0.00	1.22	10.41
	31.6	.1217	32.4	-8.46	0.07	0.00	1.33	15.51
	50.1	.0720	42.1	-8.42	0.17	0.00	1.77	17.35
	79.4	.0584	47.8	-8.47	0.31	0.00	1.76	-26.72
	125.9	.0989	18.4	-7.91	0.12	0.00	0.46	6.09
	199.5	.0764	30.6	-7.36	0.05	0.00	0.12	0.26

Table H.2. $x F_3$ errors.

The errors on some quantities were obtained as rms values after generating 26 data sets (see text in §6.6). The rest were obtained by subtracting the base data set from one obtained after shifting the relevant quantity by $\pm 1\sigma$; hence the signs. The errors in all bins are only the diagonal terms, i.e., no bin-to-bin correlations are quoted.

List of Collaborators

R.E. Blair¹, Y.K. Chu, D.B. MacFarlane, R.L. Messner²,
D.B. Novikoff³, M.V. Purohit
California Institute of Technology, Pasadena, CA 91125

F.J. Sciulli, M.H. Shaevitz
Columbia University, New York, NY 10027

H.E. Fisk, Y. Fukushima⁴, B.N. Jin⁵, Q.A. Kerns
T. Kondo⁴, P.A. Rapidis, S.L. Segler,
R.J. Stefanski, D.E. Theriot, D.D. Yovanovitch
Fermilab, Batavia, IL 60510

A. Bodek, R.N. Coleman⁶, W.L. Marsh⁶
University of Rochester, Rochester, NY 14627

O.D. Fackler, K.A. Jenkins
Rockefeller University, New York, NY 10021

-
1. Now at Columbia University, New York, NY 10027.
 2. Now at SLAC, Stanford, CA 94305.
 3. Now at Hughes Aircraft Co., El Segundo, CA 90245.
 4. Now at the National Laboratory for High Energy Physics, Tsukuba-gun, Ibaraki-ken 305, Japan.
 5. Now at the Institute for High Energy Physics, Peking, P.R. China.
 6. Now at Fermilab, Batavia, IL 60510.

References

- 1.) H. Frauenfelder and E.M. Henley, '*Subatomic Physics*', Prentice-Hall Inc., Englewood Cliffs, N.J., 1974.
- 2.) J.I. Friedman and H.W. Kendall, *Ann. Rev. of Nucl. Sci.*, 22 (1972) 203.
- 3.) R.P. Feynman, '*Photon-Hadron Interactions*', W.A. Benjamin Inc., Reading, Mass., 1972.
- 4.) J.D. Bjorken and E.A. Paschos, *Phys. Rev.* 185 (1969) 1975.
- 5.) F. Sciulli et al., 'Neutrino Physics at very high energies', *Fermilab Proposal 21*, FNAL (1970).
- 6.) V. Peterson, 'A Monochromatic Neutrino Beam from a High Intensity 200 BeV Proton Synchrotron', *LRL Report UCID-10028*, (1964).
- 7.) B. Barish et al., *Phys. Rev. Lett.* 35 (1975) 1316.
B. Barish et al., *Phys. Rev. Lett.* 39 (1977) 1595.
- 8.) R. Blair, 'A Total Cross Section and Y Distribution Measurement for Muon Type Neutrinos and Antineutrinos on Iron', *Ph. D. Thesis*, Caltech (1982).
- 9.) J.R. Lee, 'Measurements of νN Charged Current Cross Sections From $E_\nu = 25$ GeV to $E_\nu = 260$ GeV', *Ph. D. Thesis*, Caltech (1981).
- 10.) D.B. MacFarlane, 'Nucleon Structure from Neutrino Interactions in an Iron Target with a Study of the Singlet Quark Distribution', *Ph. D. Thesis*, Caltech (1984).
- 11.) F.J. Sciulli, 'Neutrinos and Neutrino Interactions', *Proceedings of the SLAC Summer Institute on Particle Physics, 1980*.

- 12.) H.E. Fisk and F.J. Sciulli, *Ann. Rev. of Nucl. and Part. Sci.*, 32 (1982) 499.
- 13.) H.W. Atherton et al., 'Precise Measurements of Particle Production by 400 GeV/c Protons on Beryllium Targets.' CERN 80-07 (1980).
- 14.) R. Blair et al., 'Monitoring and Calibration System for Neutrino Flux Measurement in a High Energy Dichromatic Beam', *Nucl. Instr. and Methods*, (to be published).
- 15.) A very similar beam and its characteristics are described in W.F. Baker et al., 'Production of π^\pm , K^\pm , p and \bar{p} by 400 GeV/c protons', Fermilab 78/79-EXP.
- 16.) R.L. Anderson and J.A. Grant, *Nucl. Instr. and Methods*, 135 (1976) 267.
- 17.) M.V. Purohit, 'Effect of dust in a Čerenkov counter', *E616 internal memo*.
- 18.) A. Bodek et al., *Z. Phys.* C18 (1983) 289.
- 19.) K.A. Jenkins, *E616 internal memos on the Čerenkov counter*.
- 20.) S. Chandrasekhar, 'Stochastic Problems in Physics and Astronomy', *Rev. of Mod. Phys.*, 15 (1943) 1.
- 21.) E. Fermi, *Nuclear Physics*, The University of Chicago Press, Chicago, 1950.
- 22.) This procedure was first brought to our attention by M. Strovink.
- 23.) H. Abramowicz et al., *Nucl. Instr. and Methods*, 180 (1981) 429.
- 24.) H. Georgi and H.D. Politzer, *Phys. Rev.* D14 (1976) 1829.
- 25.) F.E. Close, *Rep. Prog. Phys.*, 42 (1979) 1285.
- 26.) T.M. Yan, *Ann. Rev. Nucl. Sci.*, 26 (1976) 199.
- 27.) A.J. Buras, *Rev. Mod. Phys.*, 52 (1980) 199.
- 28.) W.B. Atwood, 'Lepton Nucleon Scattering', *SLAC Summer Institute on Particle Physics*, 1979.
- 29.) F.E. Close, '*An Introduction to Quarks and Partons*', Academic Press, New York, N.Y., 1979.
- 30.) R. Blair et al., *Phys. Rev. Lett.* 51 (1983) 343.
- 31.) J.F. Gunion, *Phys. Rev.* D10 (1974) 242.
- 32.) J. Kiskis, *Phys. Rev.* D8 (1973) 2129.
- 33.) A. de Rújula et al., *Nucl. Phys.* B154 (1979) 394.
- 34.) H. Abramowicz et al., *Z. Phys.* C15 (1982) 19.
- 35.) W. Smith, private communication. Paper in preparation.
- 36.) W.B. Atwood and G.B. West, *Phys. Rev.* D7 (1973) 773.
- 37.) A. Bodek and J.L. Ritchie, *Phys. Rev.* D23 (1981) 1070.
A. Bodek and J.L. Ritchie, *Phys. Rev.* D24 (1981) 1400.

- 38.) J.J. Aubert et al., *Phys. Lett.* 123B (1983) 275.
- 39.) A. Bodek et al., *Phys. Rev. Lett.* 51 (1983) 534.
A. Bodek et al., *Phys. Rev. Lett.* 50 (1983) 1431.
- 40.) R.L. Jaffe, *Phys. Rev. Lett.*, 50 (1983) 228.
- 41.) A.J. Buras and K.J.F. Gaemers, *Nucl. Phys.* B132 (1978) 249.
- 42.) R. Blair, private communication.
- 43.) D.H. Perkins, '*Introduction to High Energy Physics*', Addison-Wesley, Reading, Mass., 1972.
- 44.) I.J.R. Aitchison and A.J.G. Hey, '*Gauge Theories in Particle Physics*', Adam Hilger Ltd., Bristol, 1982.
- 45.) G. Arnison et al., *Phys. Lett.* 122B (1983) 103.
G. Banner et al., *Phys. Lett.* 122B (1983) 476.
- 46.) G. Arnison et al., *Phys. Lett.* 126B (1983) 398.
- 47.) Particle Data Group, *Phys. Lett.* 111B (1982) 1.
- 48.) E. Fermi, *Nuovo Cimento* 11 (1934) 1.
- 49.) E. Fermi, *Z. Phys.* 88 (1934) 161.
- 50.) T.D. Lee and C.N. Yang, *Phys. Rev.* 104 (1956) 254.
- 51.) C.S. Wu et al., *Phys. Rev.* 105 (1957) 1413.
- 52.) N. Cabibbo, *Phys. Rev. Lett.* 10 (1963) 531.
- 53.) S.L. Glashow, *Nucl. Phys.* 22 (1961) 579.
- 54.) S. Weinberg, *Phys. Rev. Lett.* 19 (1967) 1264.
- 55.) A. Salam in '*Elementary Particle Theory*' edited by N. Svartholm (Stockholm: Almqvist, Forlag A and B), p. 367 (1968).
- 56.) S.L. Glashow, J. Iliopoulos and L. Maiani, *Phys. Rev.* D2 (1970) 1285.
- 57.) G. 't Hooft, *Nucl. Phys.* B35 (1971) 167.
- 58.) M. Kobayashi and K. Maskawa, *Prog. Theor. Phys.* 49 (1973) 652.
- 59.) J.D. Bjorken, *Phys. Rev.* 179 (1969) 1547.
- 60.) E.M. Riordan et al., SLAC PUB 1634 (1975), SLAC, Stanford, California.
- 61.) J.J. Aubert et al., *Phys. Lett.* 121B (1983) 87.
- 62.) H. Abramowicz et al., *Phys. Lett.* 107B (1981) 141.
- 63.) H. Caprasse, *Phys. Rev.* D24 (1981) 185.
- 64.) J.D. Bjorken, '*Elements of Quantum Chromodynamics*', SLAC PUB 2372 (1979), SLAC, Stanford, California.

- 65.) S.J. Brodsky, 'Quantum Chromodynamics and Hadronic Interactions at Short Distances', *Proceedings of the 1981 SLAC Summer Institute on Particle Physics*, SLAC, Stanford, California.
- 66.) G. Altarelli, *Phys. Rep.* 81 (1982) 1.
- 67.) A.J. Buras, *Rev. Mod. Phys.* 52 (1980) 199.
- 68.) E. Reya, *Phys. Rep.* 69 (1981) 195.
- 69.) A.J. Buras, 'Seven Topics in Perturbative QCD', Fermilab-Conf-80/79-THY.
- 70.) A.J. Buras, 'A Tour of Perturbative QCD', Fermilab-Conf-81/69-THY.
- 71.) R.D. Field, 'Perturbative QCD and Applications to Large Momentum Transfer Processes', CALT-68-739.
R.D. Field, 'Applications of Quantum Chromodynamics', CALT-68-696.
- 72.) G.C. Fox, 'The Physics of Inclusive Charged Current Neutrino Reactions', CALT-68-658.
G.C. Fox, *Nucl. Phys.* B131 (1977) 107.
G.C. Fox, *Nucl. Phys.* B134 (1978) 269.
- 73.) E.L. Berger, 'Case Studies in Perturbative Quantum Chromodynamics', ANL-HEP-CP-79-51.
- 74.) G. Altarelli and G. Parisi, *Nucl. Phys.* B126 (1977) 298.
- 75.) R.T. Herrod and S. Wada, *Phys. Lett.* 96B (1980) 195.
- 76.) W.A. Bardeen et al., *Phys. Rev.* D18 (1978) 3998.
- 77.) H. Georgi and H.D. Politzer, *Phys. Rev. Lett.* 36 (1976) 1281
and *Phys. Rev. Lett.* 37 (1976) 68.
- 78.) A. Bodek et al., *Phys. Lett.* 113B (1982) 77.
- 79.) J.L. Ritchie et al., *Phys. Lett.* 126B (1983) 499.
- 80.) A. Bodek et al., paper in preparation.
- 81.) H. Abramowicz et al., *Z. Phys.* C17 (1983) 283.
- 82.) A.R. Clark et al., 'Measurement of the Nucleon Structure Function in Iron Using 215 and 93 GeV Muons', LBL-16286 (1983). Submitted to the 1983 Lepton-Photon Conference.
- 83.) A. Devoto et al., *Phys. Rev.* D27 (1983) 508.
- 84.) L.F. Abbott and R.M. Barnett, *Annals of Physics* 125 (1980) 276.
- 85.) J.J. Aubert et al., *Phys. Lett.* 105B (1981) 315.
- 86.) J.J. Aubert et al., *Phys. Lett.* 105B (1981) 322.
- 87.) J.J. Aubert et al., *Phys. Lett.* 114B (1982) 291.
- 88.) P.C. Bosetti et al., *Nucl. Phys.* B142 (1978) 1.
- 89.) J.G.H. de Groot et al., *Z. Phys.* C1 (1979) 143.

- 90.) B. Adeva et al., *Phys. Rev. Lett.* 50 (1983) 2051.
- 91.) D.L. Burke, 'Proceedings of the 21st International Conference on High Energy Physics', Paris, 1982, p.513.
- 92.) G. Altarelli and G. Parisi, *op. cit.*
- 93.) E.G. Floratos et al., *Phys. Lett.* 98B (1981) 89.
- 94.) G. Curci et al., *Nucl. Phys.* B175 (1980) 27.
- 95.) A. Bialas and A.J. Buras, *Phys. Rev.* D21 (1980) 1825.
- 96.) R.M. Barnett, 'Proceedings of the 1979 SLAC Summer Institute on Particle Physics', SLAC, Stanford, California.
- 97.) W.A. Bardeen et al., *op. cit.*
- 98.) R.M. Barnett, *Phys. Rev. Lett.* 48 (1982) 1657.
- 99.) R.M. Barnett and D.M. Schlatter, *Phys. Lett.* 112B (1982) 475.
- 100.) R.T. Herrod et al., *Z. Phys.* C9 (1981) 351.
- 101.) W. Furmanski and R. Petronzio, *Z. Phys.* C11 (1982) 293.
- 102.) D.W. Duke, J.F. Owens and R.G. Roberts, *Nucl. Phys.* B195 (1982) 285.
- 103.) R.M. Barnett, *Phys. Rev.* D27 (1983) 98.
- 104.) R. Barbieri et al., *Nucl. Phys.* B117 (1976) 50.
- 105.) B.A. Gordon et al., *Phys. Rev.* D20 (1979) 2645.
- 106.) M.D. Mestayer et al., *Phys. Rev.* D27 (1983) 285.
- 107.) T. Bolgnese et al., *Phys. Rev. Lett.* 50 (1983) 224.
- 108.) H.D.I. Abarbanel, M.L. Goldberger and S.B. Treiman, *Phys. Rev. Lett.* 22 (1969) 500.
- 109.) C.Haber et al., 'A Search for Inclusive Oscillations of Muon Neutrinos in the Mass Range, $20 < \Delta m^2 < 900 \text{eV}^2$ ', Nevis Labs preprint R1290. *Contributed paper to EPS meeting, Brighton, England* (1983).
- 110.) J.K. Panman, 'A Study of Inclusive Neutrino Interactions in a Marble Target', Ph.D. Thesis (unpublished), NIKHEF, Amsterdam, The Netherlands (1981).
- 111.) F. Bergsma et al., *Phys. Lett.* 123B (1983) 269.